FACTORS AFFECTING SURFACE TOPOGRAPHY IN DIAMOND TURNING

FACTORS AFFECTING SURFACE TOPOGRAPHY IN DIAMOND TURNING

By
ALEX YIP, B. Eng
(McMaster University, Canada)

A Thesis
Submitted to the School of Graduate Studies
in Partial Fulfilment of the Requirements
for the Degree
Master of Applied Science

McMaster University

Ultraprecision, single point diamond turning (SPDT) is a tool based machining technology that allows the ability to produce high quality surface finishes on the order of nanometers while meeting tight form tolerances on the order of micrometers. It is generally agreed that surface finish in SPDT is primarily affected by four factors: Tool edge quality, relative vibration between the tool and workpiece, material properties and microstructure, and tool geometry (nose radius and machining parameters) machining. To the author's knowledge, no work has been done to combine all the factors to study their effect on surface generation in SPDT. This is important given that the factors are highly interdependent. Two diamond tools with nose radius of 12mm were used; however, one of them was chemically honed. Results suggest that the honed tool provides a much better surface finish with a significantly reduced amount of running-in stage tool wear. The cutting edge radius of the diamond tools was measured using a novel 3D confocal laser microscope to analyze the chemical honing process and to measure tool wear. The presence of built-up edge (BUE) is more prominent on the honed tool earlier in its life which results in unpredictable surface roughness to appear sooner than on the regular tool. To understand the dynamics of the machine, a redesign of the tool holder bracket was done to increase stiffness. Modal tests were then performed on it to verify performance improvement. With an understanding of the vibration and its effect on the cutting force, a 400Hz disturbance frequency was detected in the cutting forces. From a 3D scan of the surface, a total of 24 undulations on the surface of the part were observed when the spindle speed was set to 1000RPM The machine was instrumented and a rotordynamic investigation was carried out to determine the cause and nature of the vibration in an effort to reduce it and in so doing improve surface form accuracy.

Acknowledgements

I would like to express my gratitude and thanks to Dr. Stephen C. Veldhuis for the opportunity and his guidance throughout my research career. I would also like to give special thanks to Dr. Mohammed Tauhiduzzaman, and Mr. Maneesh Khanna for their continued support and guidance and feedback in developing the design of experiments.

I would also like to thank the staff and technicians of the Mechanical Engineering Department, including Mr. Ron Lodewyks, Mr. Michael Lee, Mr. Mark MacKenzie and Mr. Joe Verhaeghe. Thanks to Dr. German Fox-Rabinovich, Dr. Julia Dosbaeva, Mrs. Glynis de Silveira and Mr. Chris Butcher for sharing their expertise in microscopy and metrology and Mr. Terry Wagg for his expertise in machining and fabrication.

Finally, author would also like to thank the Natural Sciences and Engineering Research Council of Canada (NSERC), Olympus Canada for their in-kind assistance and Brian Creber at B-Con Engineering for their financial support of this research.

Table of Contents

List of Figures

List of Tables

List of all Abbreviations and Symbols

R_a – Arithmetic mean roughness

SPDT – Single Point Diamond Turning

BUE – Built-Up Edge

t – Uncut chip thickness

φ – Shear plane angle

α – Tool rake angle

V – Cutting speed

ζ – Tool clearance angle

R_{th}, PV – Peak-To-Valley Roughness

f – Tool feed rate, in μm/rev

R_n – Tool nose radius

WLI – White Light Interferometer

SCD – Single Crystal Diamond

P_{peak} – Chuck position with peak acceleration, in degrees from spindle index position

T_{peak} – Number of seconds from spindle index position to time of peak acceleration

T_{index} – Time of spindle passing index position

P_{trial} – Trial location of test weight on spindle, in degrees from spindle index position

P_{lag} – Adjustment lag, in degrees

a_e – Effective rake angle

R_c – Tool cutting edge radius

OD – Outer diameter of workpiece

ID – Inner diameter of workpiece

$s(\theta)_{total}$– Total length of cut in facing operation

p_{height} – Y-position of plotted parabolic approximation of tool profile

$p_{position}$ – X-position of plotted parabolic approximation of tool profile

M – Mass of rotor-shaft system

C – Damping of rotor-shaft system

K – Stiffness of rotor-shaft system

G – Gyroscopic damping of rotor-shaft system

B – Gyroscopic effect of rotor-shaft system

$Lshaft$ - Distance between bearings for calculating shaft stiffness

f_{vib} – External force vector causing vibration

ω – Rotational frequency, in Hz

E – Young's modulus

FFT – Fast Fourier Transform

FRF – Frequency Response Function

Declaration of Academic Achievement

The main contribution of this thesis is the development of a detailed experimental analysis which explains the formation of radial undulations on the surface of an optical part. In addition, a standard diamond tool was compared to a chemically etched tool to determine the effect of edge preparation on the tool life and performance. Long standing questions on observed undulations and tool edge preparation have been addressed as part of this study.

Chapter 1. Introduction

Ultraprecision, single point diamond turning (SPDT) is a tool based machining technology which is used for the manufacture of computer disks and optical components as well as precision molds. SPDT is unique in its capability in producing components with optical-quality surface finish with tight, micrometer-level form tolerances. The purpose of improving the surface finish in diamond turned surfaces is to reduce the cost of rotationally-symmetric optical components by reducing or eliminating costly manual polishing and lapping. It is generally agreed that surface finish in SPDT is primarily affected by the cutting parameters and quality of the tool's cutting edge, the workpiece's material microstructure, and the relative vibration between the tool tip and workpiece. Typical diamond turned surfaces are of very high quality, having an average surface roughness of about 1-10nm R_a and surface form error on the order of 50-100nm.

The ultraprecision machine centers used to produce these smooth, mirror-like surfaces are dedicated machines with positional resolution on the order of ±1~10nm. In contrast, a conventional machine tool will typically have a positional resolution on the order of ±100nm. In addition these machine tools must be very stiff as any deflection on the order of nanometers can cause aberrations on the generated surface.

The diamond tools used in diamond turning are honed to a very sharp edge, while the ultraprecision machine center allows very shallow depths of cut and fine feed rate control that can be used to generate an optical quality surface finish. This tool material is chosen for its high hardness, thermal conductivity, and ability to be honed to a very sharp edge and retain this edge under cutting loads [1]. Typical cutting parameters are 2μm depth of cut and 5μm/rev feed rate in SPDT. The extremely sharp tool together with precise and conservative cutting parameters affect the shape of the uncut chip, changes the cutting physics and ultimately, the final generated surface.

The tool edge is important to the surface generation in SPDT. Diamond tools are sharpened using a mechanical grinding and lapping process, which can create a sub-micron cutting edge radius. However, due to sub-micron uncut chip thickness, the tool cannot be considered to be perfectly sharp due to relative scale of uncut chip thickness in comparison to the edge roundness. In this study, two tools were used to understand how the edge roundness affects the cutting mechanics, surface finish and tool life. One tool was sharpened and honed to extreme precision using traditional methods and the other tool was chemically etched to provide an intentionally blunted edge. Both the tools were chip and defect free at 800X magnification as certified by the suppliers.

Measuring the cutting edge radius of diamond tools has always been a challenge as there were no commercial systems available with the required measurement resolution. In this study, a novel laser confocal microscope technology, LEXT system from Olympus was explored and the radius of the sharp tool was measured to be around 90nm. The chemically etched tool was also measured and its profile was analyzed to approximate a 105nm edge radius. Both the tools were then compared by machining with them and measuring the surface roughness and cutting forces. It was observed that the chemically blunted tool had a minimum running in stage of tool wear; however, tool life as measured by acceptable surface finish produced on the workpiece was shorter when compared to the sharp tool. Tool life in SPDT of aluminum was also noticed to be dependent on adhesion (build up edge, BUE) of the aluminum on the tool, compromising the cutting edge quality deteriorates the surface quality. The BUE can be described as a piece of workpiece material adhered to the cutting edge of the tool. This is observed as a rainbow appearance on the surface of the workpiece. The BUE is harder than the bulk workpiece material since it contains material that has been strain hardened. This creates periodic groves that result in a diffraction grating pattern that causes the rainbow appearance when light is shone on it. Cutting force also increases due to the interaction between the BUE and bulk workpiece material. Interestingly cutting edge radius for both the tools was approximately 295nm near the end of tool life where BUE formation was very frequent.

The workpiece material must be chosen carefully such that they have the correct mechanical properties for the desired application, as well as good cutting characteristics. It has been found that materials with a fine grained microstructure [2] that are free of defects contribute to excellent surface finish. For this reason, rapidly solidified aluminum (RSA) – 6061 was used in this study. It is also used commercially in the optics industry. RSA 6061 is a commercially developed material produced by a melt-spinning process. This material has grain sizes on the order of 2µm to 5µm. A 99.87% pure aluminum workpiece was also machined with an average grain size of 300µm for comparison.

The machine tool's spindle and movement of the machine axes can generate relative vibrations through the machine's structure between the tool and workpiece. Surface finish can be affected by excessive relative vibration between the tool and the workpiece, causing errors in surface finish and final machined form [3]. With careful consideration of the dynamic properties of the fixture, spindle, and machine structure, surface finish can be improved. It was observed in this study that there is a strong synchronous error present on the surface in the form of radial spokes radiating from the center of the workpiece. Such errors are termed as “spindle star” due to their appearance.

The spindle star error was observed to be an integer harmonic of the rotational frequency of the spindle. It is also dependent on the natural frequency of the spindle rotor. This error was found to have unusual characteristics, which can be explained by constructing a Campbell diagram, a technique typically used for high speed turbine shafts. The rotating body vibrates due to gyroscopic effects. To compensate for this, the rotating body undergoes air hammer instability, a condition created by the cross coupling between differing stiffness across the air bearing journal. In externally pressurized air bearing journals, assisted air hammer instability is present, causing the excitation of natural frequencies even though the spindle rotational frequency is well below the natural frequency. The reason for this is due to the difference in cross-coupling stiffness of air bearings, and a non-linear spring rate. This results in a different natural frequency for the first and second half-cycle of vibration representing the tension and compression phase of a single cycle of vibration. The resulting motion is thus no longer simple harmonic motion but can be represented by a Fourier series based on multiples of the circular frequency of a full cycle. In a physical sense, a shaft with a rotating imbalance will thus cause it to vibrate at the rotational frequency as well as its harmonic frequencies. This forces the number of spindle star lobes present on the surface of the part to be an integer.

In this thesis, these factors will be studied to gain an understanding of how all of these factors affect the final form and surface finish of the machined part to determine its topography. The objective of this study is to determine the effect and relationship between the workpiece microstructure, machine vibration characteristics, and tooling. The scope of this study is restricted to mechanical ultraprecision machining using diamond tools for the creation of rotationally-symmetric workpieces with an optical grade mirror quality surface finish.

Chapter 2 will provide a detailed literature review on ultraprecision SPDT. Fundamental physics of SPDT will be highlighted. Rotodynamic analysis on rotating bodies will also be discussed. Chapter 3 describes the experimental setup, equipment and procedure in detail. Chapter 4 describes the machine modification done in this study with detailed analysis and reasoning provided to support the modifications. Chapter 5 introduces the supporting theory and focuses on the results and discusses the tool edge roundness effect, material properties and dynamics in surface topography in SPDT. Chapter 6 focuses on the conclusions from this study and Chapter 7 presents potential future work.

LabVIEW, MATLAB, and other computer codes used in this study and a case study of fabricating a Fresnel lens are presented in the appendices A1 and A2 respectively.

Chapter 2. Literature Review

The term ultraprecision machining is generally used to describe a material removal process with tolerances of less than 1µm and surface finishes on the order of nanometers, producing shiny, mirror-like surfaces. There has been considerable interest in the field of Computerized Numerical Controlled (CNC) single point diamond turning (SPDT) to produce final surfaces with tight form accuracy which requires no further manual polishing to meet product specifications.

2.1 Introduction to Single Point Diamond Turning (SPDT)

SPDT is a precision engineering manufacturing process with tolerances smaller than 1µm, and surface finishes on the order of nanometers. The "Taniguchi Curve" as shown in Figure 2.1 graphically shows the relative precision and accuracy of machining technologies and how they have changed over time. SPDT can be categorized as an ultra-precision machining technology.

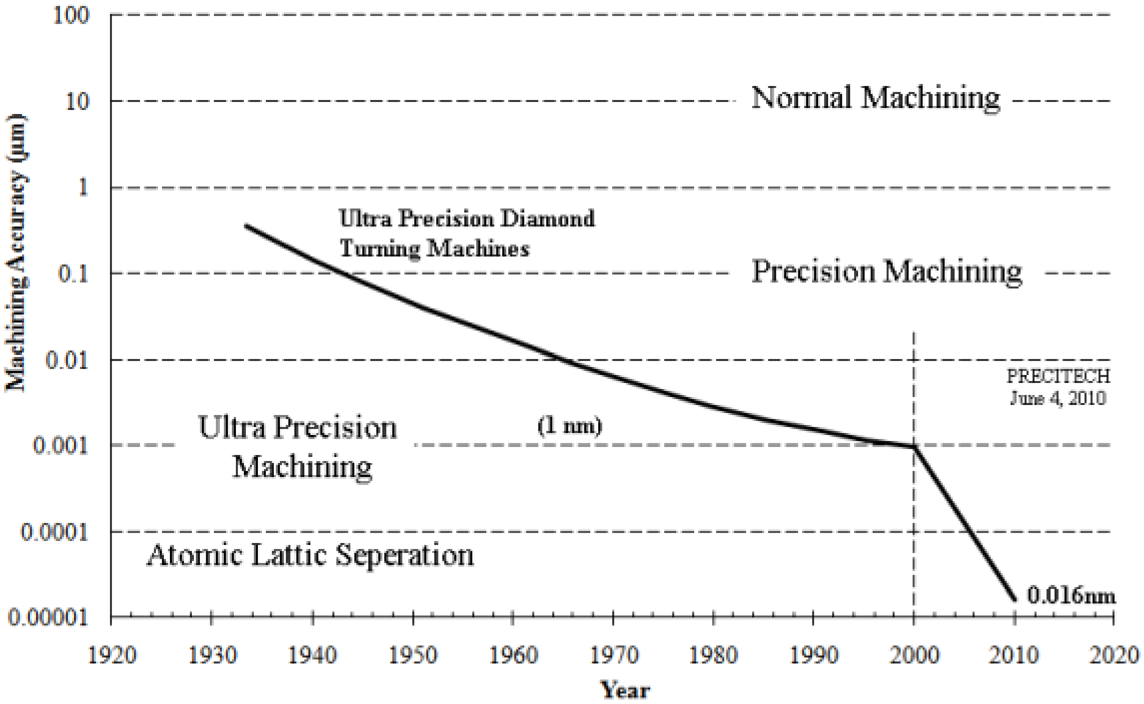

Figure 2.1 Taniguchi Curve [4] [After Tauhiduzzaman (2011)]

There are many similarities between SPDT and conventional turning, but at the micrometer and nanometer level scale that SPDT operates, it requires the consideration of several issues that are often not relevant in conventional turning.

SPDT holds many advantages compared to other precision machining techniques, such as mechanical grinding, focused ion beam, and manual lapping and polishing. Mechanical grinding is limited by the fact that in soft metals, the abrasive wheel can drag or smear hard particles in the metal, reducing the surface quality [5]. Focused ion beam, lapping and polishing techniques are costly and more time consuming compared to SPDT. They can achieve the desired surface finish but are not able to control form or practically produce a large surface area like SPDT can. In the fabrication of precision optics, there has been a push to reduce component cost, a focus on reducing manufacturing cycle time since hand finishing operations associated with manual polishing can be very costly. Common applications of SPDT include the creation of lens molds, ultra fast and ultra light metallic aerospace optics, infrared optics, and laser focusing optics. It is also the technique of choice for creating prismatic, aspheric, and Fresnel type lenses as the surface finish left behind requires minimal or no post polishing.

It is generally agreed that there are four major factors that affect the surface finish in SPDT, outlined by Sohn et. Al [6] and by Tauhiduzzaman and Veldhuis [7].

- Material properties and microstructure
- Tool Geometry
- Cutting tool edge quality
- Relative vibration between tool and workpiece

The objective of this thesis is to outline the effects of these factors and to address them to improve part tolerances and machine limits. It is not possible to disregard any of these four factors as they all contribute in different ways to the form and surface roughness of the finished, generated surface. It has been concluded that the workpiece's material microstructure and unwanted machine vibration are the two factors that contribute most to the surface topography of a diamond turned surface [7].

2.1.1 Material Microstructure in SPDT

When a material is machined, a shear plane is formed at the tool tip between the chip and the workpiece. This is called the primary shear zone, shown in Figure 2.2. The shearing process is heavily dependent on the material microstructure, ultimately affecting the final surface topography of the workpiece.

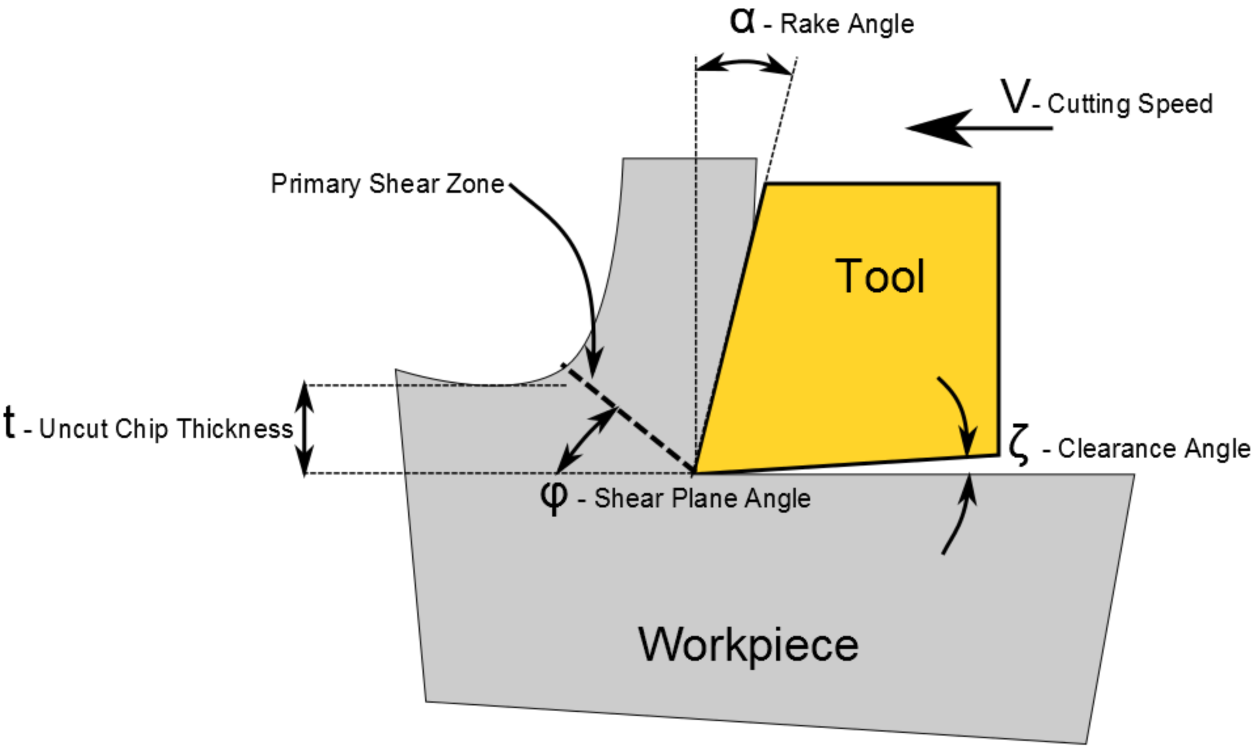

Figure 2.2 Metal Chip Flowing Over Tool

In diamond turning, the material plays a large role in the resultant surface finish of the part due to the size effect. Figure 2.3 shows the relative scale of the uncut chip thickness, material microstructure and cutting tool. The size effect is considerable when the uncut chip thickness of the machining parameters approaches the average grain size of the tool and the cutting edge radius. In conventional machining, the depth of cut in face turning varies from 1mm to 0.1mm for roughing and finishing operations. The material behavior is similar to the properties obtained using bulk mechanical testing in the macro scale. However, in SPDT, the uncut chip thickness in face turning can be up to 10µm in roughing operations and can be as small as 1µm in finishing operations. At this scale, the material behaves differently, as material voids, segregations, and grain boundary densities must be considered. During finishing operations in SPDT, the uncut chip thickness can be smaller than the average grain size of the material. The cutting process physics changes again, as the tool is effectively cutting single crystals of material. This is similar to a tool cutting through single, ideal crystals of the workpiece material. This phenomenon is termed as “size effect” in metal cutting. It has been observed that the surface finish of a finished part will depend on the material microstructure of the workpiece [8] [7].

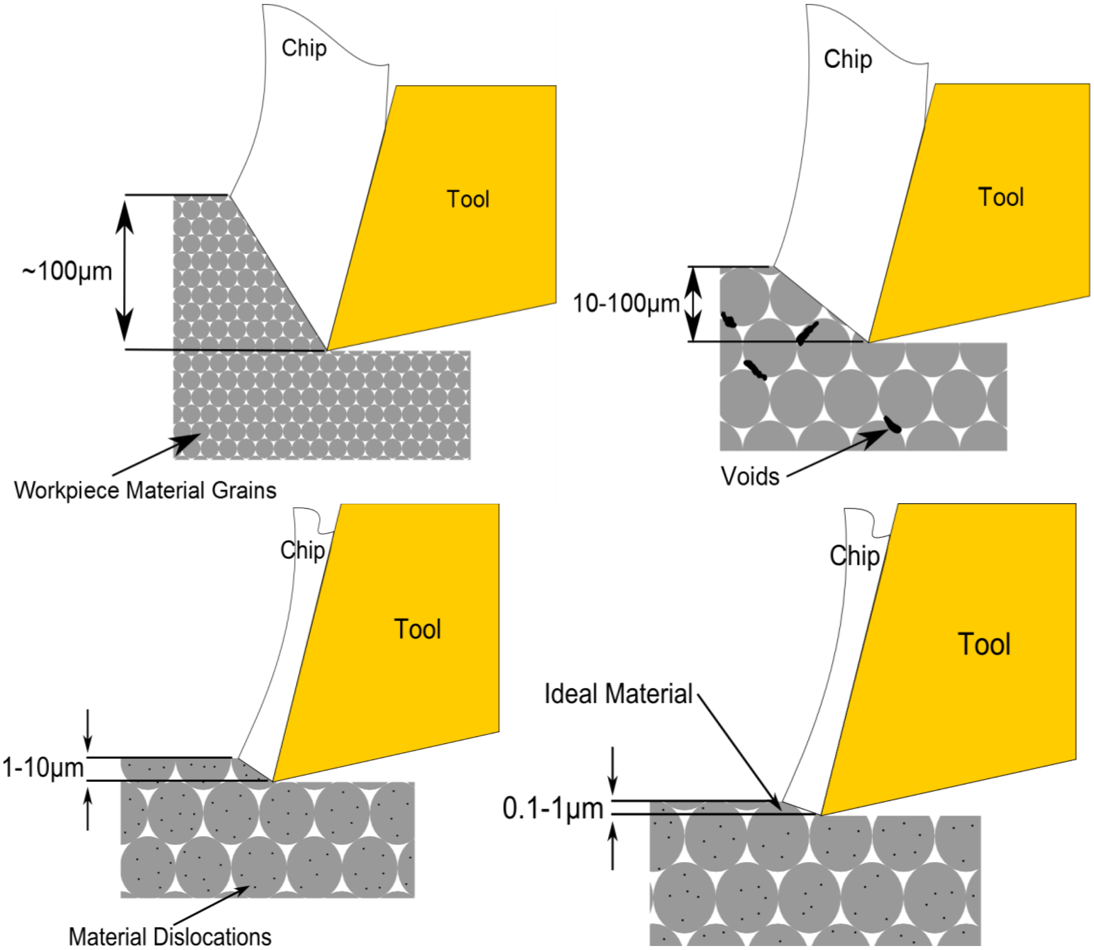

Figure 2.3 Material Behavior as machining size reduces. (a) Continuous material. (b) Effects of grain boundary. (c) Effects of dislocation and (d) Ideal material. [9] [Adapted After Sugita et al., (1984)]

S.To et al. [10] has observed in their study of single crystal aluminum workpieces that the surface roughness of the workpiece is dependent on the orientation of the crystal. This is due to the anisotropy of a single crystal. Depending on the orientation that a crystal is being cut, there will be directions where it is preferential for a slip plane to easily form, causing the material to plastically deform. In the study by S.To et al. [10], they found that the cutting force in a single crystal of aluminum depended on its orientation to the cutting tool. In a polycrystalline material, a similar property applies. The mechanical properties of the workpiece will change depending on the crystallographic orientation of the grain being cut [11] during that instant. It has also been concluded that the passing of the tool over grain boundaries will create discontinuities in cutting force [12]. Different cutting forces will be encountered in each grain, causing uneven plastic and elastic stress. The grains will be cut at different heights and negatively affect the surface roughness, creating grain boundary induced roughness. As the tool shears through the workpiece material, the grains making up the newly generated surface spring back due to the thrust forces and plastic deformation. Each grain is randomly oriented, causing changes in thrust force, causing surface roughness. In a study by Tauhiduzzaman [2], a polycrystalline material that has been diamond turned exhibited grain boundary induced roughness. Examples of spring back and grain boundary induced roughness are shown in Figure 2.4 and Figure 2.5.

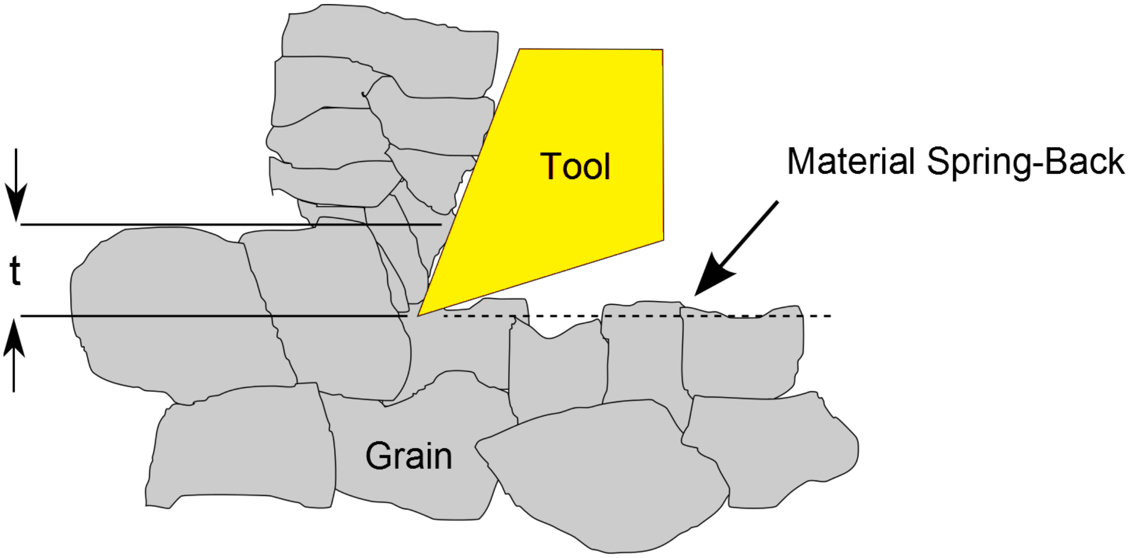

Figure 2.4 Example of Material Spring-Back

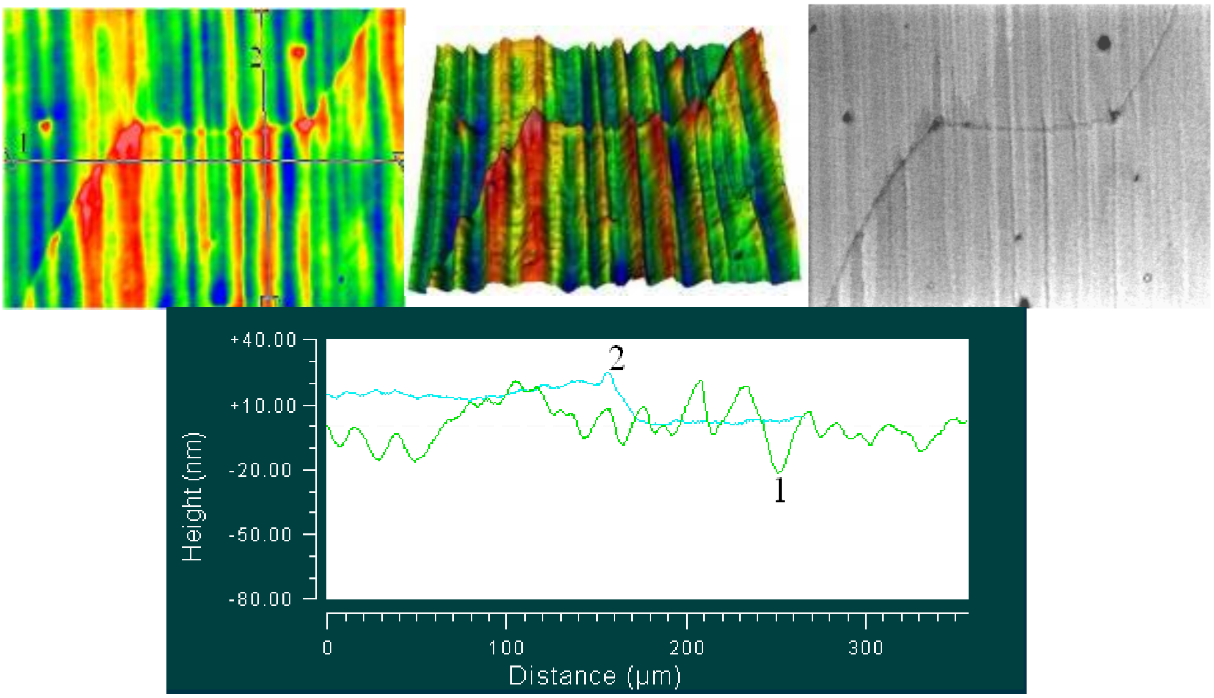

Figure 2.5 Grain Boundary Induced Roughness on Furnace Cooled 99.97% Aluminum [2] [After Tauhiduzzaman et al. (2011)

Again, materials with a large number of inclusions, such as hard particles and voids will also negatively impact the surface finish. These hard particles can smear, be dragged along the surface of the workpiece creating scratches, or be pulled out of the surface creating holes [11] [2]. Using energy-dispersive x-ray spectroscopy (EDS) by Tauhiduzzaman [2], the hard particles were found to be made of silicon and iron, alloying elements in aluminum 6061 as shown in Figure 2.6.

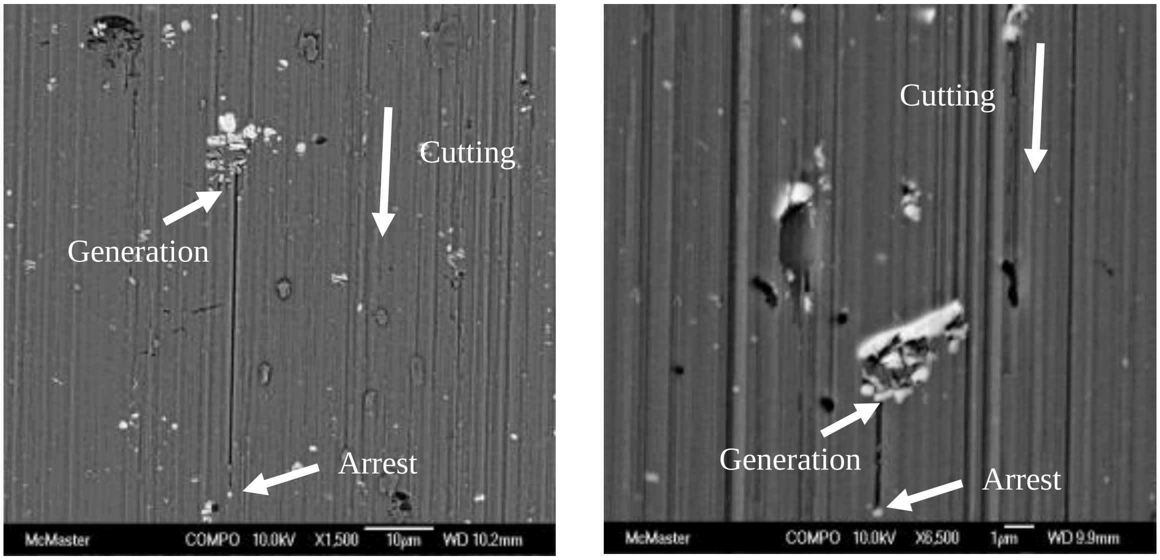

Figure 2.6 Back-Scattered Electron (BSE) image of Aluminum 6061 Showing Brittle Fracture, Hard Particle Smears, and Dimple Formation [2] [After Tauhiduzzaman (2011)]

Another important aspect to define a material's mechanical behavior and chip formation is dislocation density [7]. Under low shear stresses the dislocation density in a material increases [13]. This occurs near the edge of the primary shear zone, shown in Figure 2.2. Grain boundaries in a material act as barriers to prevent the travel of dislocations, increasing tensile strength and hardness. Tauhiduzzaman [2] concluded that a friction-stir processing (FSP) method can be applied to aluminum workpieces to improve their surface finish by mechanically working the material to increase dislocation density, reducing grain sizes to nanometer level and removing strong grain boundaries.

Friction stir processing (FSP) is a related process to friction stir welding (FSW). FSW is a solid state welding process in which the material is not melted but mechanically stirred. This process was created by The Welding Institute (UK) in 1991 and patented in 1995 [14]. The FSW process starts with two workpieces that are butted against each other to create a joint and are clamped in place. The tool, known as a bobbin, is a specially shaped pin with a large shoulder. The bobbin, rotating between 180 and 300RPM is forced into the material. Friction between the workpiece and bobbin softens the material. As the bobbin is fed through the workpiece, pressure from the clamps forces the softened material to be forged together [15], creating the welded joint. FSP uses the same bobbin and tooling as FSW, only that the process is not used to join two workpieces, but is instead used to create an area of re-forged metal in the worked region of the workpiece. The FSP process is shown in Figure 2.7. FSP, when applied to aluminum, decreases the grain size and increases the density of material defects creating an alloy with a small average grain size and finely dispersed hard particles. The re-forged metal behind the bobbin is churned, undergoes dynamic recrystallization and recrystallizes with a microstructure that has a high dislocation density [16]. The dislocation-dense crystals also serve as nucleation sites for slip planes to form when the material is deformed and sheared. Figure 2.8 shows and compares the microstructures of 99.87% aluminum in furnace cooled state and after FSP. The grain sizes have been dramatically reduced using this method.

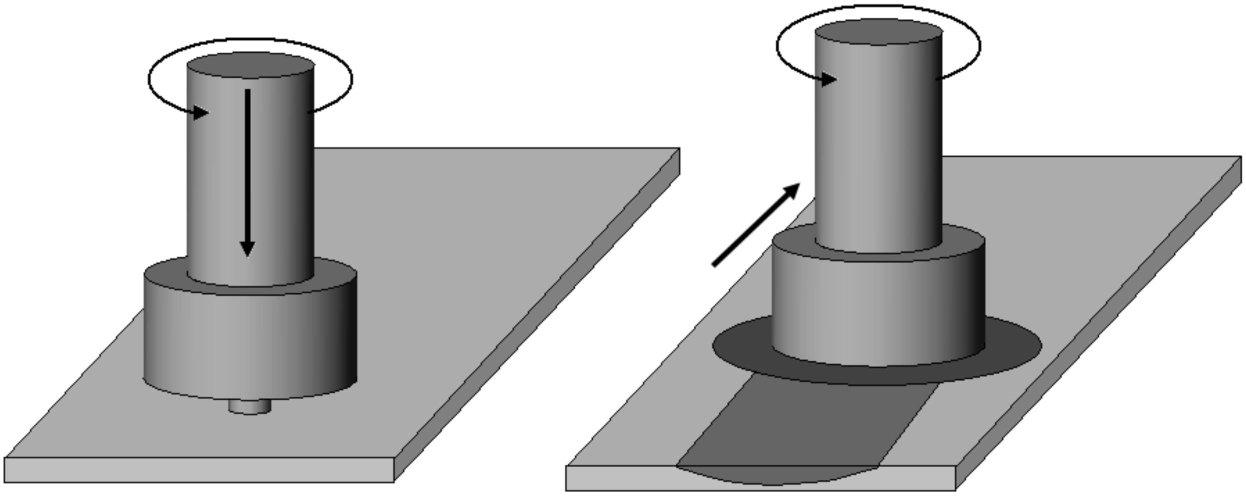

Figure 2.7 Friction Stir Process [17] [After Tauhiduzzaman (2011)]

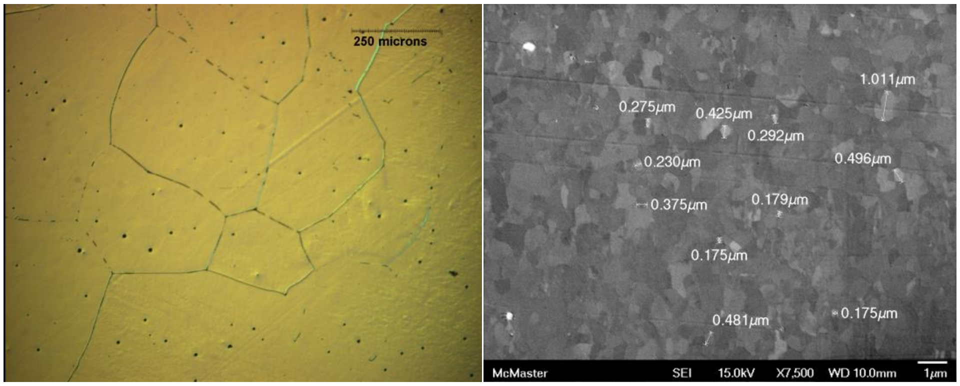

Figure 2.8 Comparison of Optical Microscope and SEM Images of 99.87% pure Aluminum Workpieces Before And After FSP respectively (Note different scales) [2] [After Tauhiduzzaman (2011)]

Rapidly Solidified Aluminum (RSA-6061) is a similar material produced by RSP-Technology which uses a proprietary meltspinning process to create a 6061-series aluminum alloy [18]. RSA-6061 and FSP alloys both feature a microstructure with an average grain size of under 2μm and a fine dispersion of insoluble hard particles in the solidified ingot. This alloy is commonly used in the diamond turning industry for producing focusing mirrors.

By using a material with an appropriate microstructure such as RSA-6061, the effects of hard particle scratches, and grain boundary roughness, can be minimized. These alloys minimize the number of hard particle scratches as the hard alloying particles are finely dispersed throughout the aluminum matrix. The decreased grain size reduces the impact of the size effect at the low depths of cut typically used in SPDT. This causes the tool to cut material that has a material property more similar to the bulk material, rather than the material property of that of a perfect, single crystal metal. The increased density of grain boundaries in RSA or FSP treated material strengthens the bulk workpiece material, but will also reduce the effect of grain-boundary induced roughness. This is due to the greater number of active slip planes in adjacent grains in RSA or FSP treated alloys.

2.1.2 Tool Geometry

The geometry of a cutting tool significantly impacts surface finish at higher feed rates as it determines the shape of the tool marks on the finished surface. At high enough feed rates, the surface roughness will be close to the theoretical limit of surface roughness as captured in Equation 2.1.

$$R_{th} = \frac{f^2}{8\ R_n}$$

Equation 2.1 Theoretical Surface Roughness

In Equation 2.1, the peak-to-valley roughness (R_{th}) is dependent on the feed per revolution (f), and the nose radius of the tool (R_n). This theoretical limit only holds true if the tool is a perfect circular arc and only if an exact imprint of the tool is left on the generated surface. Equation 2.1 implies that higher feed rates and tools with smaller nose radii will create surfaces with higher roughness. This conventional wisdom is applicable when diamond turning at higher feed rates during roughing operations. In a study by Childs et al. [8], they found that for a sharper tool, the achievable surface roughness approaches a minimum. Edge sharpness is one of many factors that affect the R_{th} of a diamond turned surface.

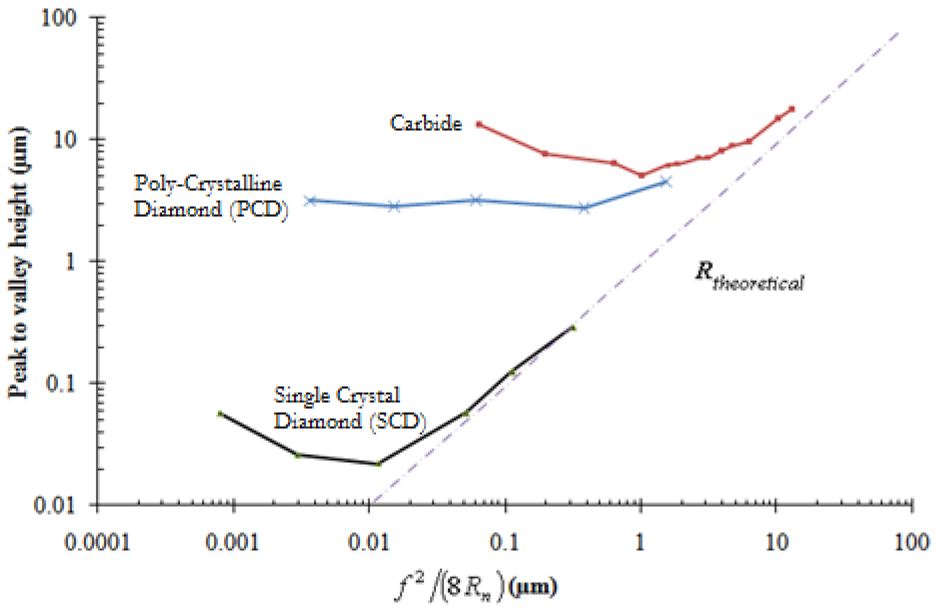

Figure 2.9 Roughness Data on Turning and Facing [8] [After Childs et al., (2008)]

When the feed rate is decreased, the feed marks are obscured by the magnitude of tiny vibrations in the machine and by microscopic defects in the workpiece. To demonstrate this phenomenon, Figure 2.10 was produced in this study where a 0.5mm nose radius tool was used to machine a surface at different feed rates. At a relatively high feed rate of 50µm/rev, the surface profile is dominated by the scallop-shaped tool marks and machine vibration can be neglected. In this case, Equation 2.1 will provide a close estimate to the peak-to-valley (R_{th}) roughness of the generated surfaces. When the feed rate is lowered to 20µm/rev, the measured R_{th} will be affected by both the size of the scallops created by the tool as well as minute machine vibration. When the feed rate is lowered again to 5µm/rev, the kinematic equation suggests a value of R_{th} = 6.25nm where the measured R_{th} is actually 61.89nm, as the feed marks are obscured by machine vibration.

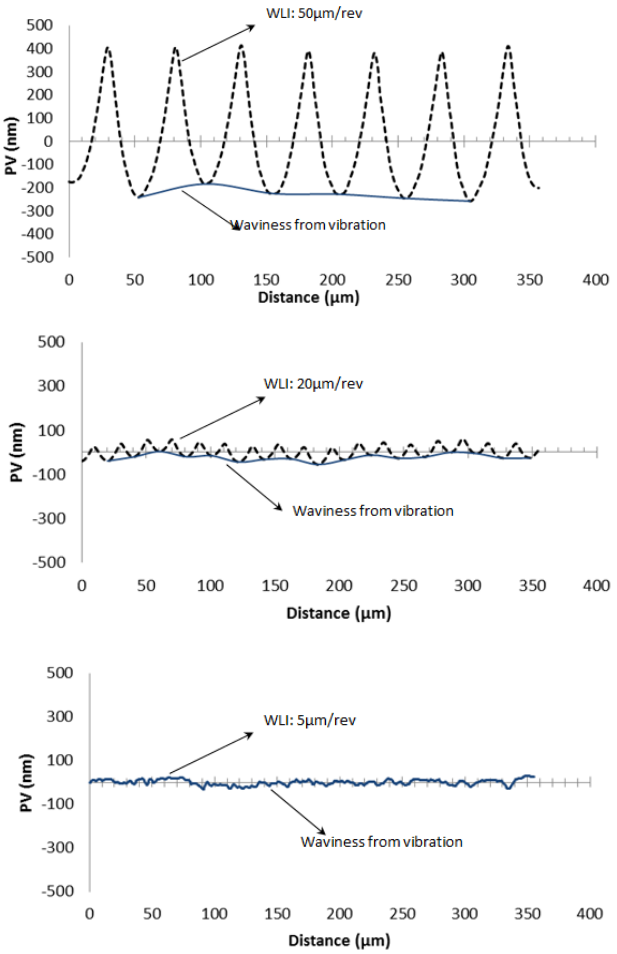

Figure 2.10 **Comparison of Measured Peak-To-Valley (PV) Surface Roughness From White Light Interferometer (WLI) and Waviness at Different Feed Rates**

It is difficult to determine the point at which vibration and other factors will dominate over the feed marks on the generated surface as it is highly dependent on the machine capability, material microstructure, and tool geometry. A detailed analysis to explain the interplay between material microstructure, cutting parameters and edge roundness is provided in Chapter 5.1.

2.1.3 Cutting Tool Edge Quality

In conventional machining, edge preparation can help with the tool life and surface quality of the turned part. A blunted cutting edge has the advantage of being stronger when cutting through hardened materials as it has more material to support the cutting edge. It can also be used as a method of increasing friction between the tool and workpiece, creating process damping and reducing the severity of vibration [19].

In SPDT, the cutting edge quality plays a large role in generating the new surface on the workpiece. Intuitively, the sharp diamond tools with high edge quality will generate surfaces with better surface finish. In practice, it is not possible to use perfectly sharp tools for diamond turning. Any damage or aberrations in the tool profile, such as ragged edges due to improper honing and chips or notches on the cutting edge will cause similar damage within the feed marks on the workpiece’s surface. This highlights the importance of cutting edge quality. Commercial quality SCD tools are inspected with an optical microscope at 800X magnification to ensure that the cutting edge is free of chips, cracks, and defects.

Tool wear in machining typically follows a pattern. The plot of tool wear vs. the length of cut generated by a tool can be split into three distinct stages: wear-in, stable wear, and rapid wear as shown in Figure 2.11.

The break-in stage is characterized by low cutting forces, moderate surface quality, and rapid deterioration of the cutting edge. The cutting edge erodes as it is prepared for the stable wear stage. The erosion of the cutting edge also introduces the possibility of subsurface damage to the tool substrate where the mechanisms involved are not well known. The amount of subsurface damage and erosion required for the cutting edge to reach the stable wear stage will affect the fatigue strength and consequently, the total tool life.

The stable wear stage is characterized by high surface quality and consistent cutting forces for a long period of time. The tool is subjected to high cutting forces and temperatures, causing a gradual breakdown of the tool. In a conventional turning operation, the cutting tool is considered to be worn if the flank wear exceeds 300µm. This standard is not applicable to SPDT due to the small depths of cut and feed rates involved.

The final rapid wear stage is characterized by a sudden increase of cutting forces from the stable wear stage and a decrease in surface quality. Typical indications of the rapid wear stage include chipping, cracking, or erosion of the rake face, flank face, or cutting edge. Coated tools typically wear rapidly after coating failure or delamination.

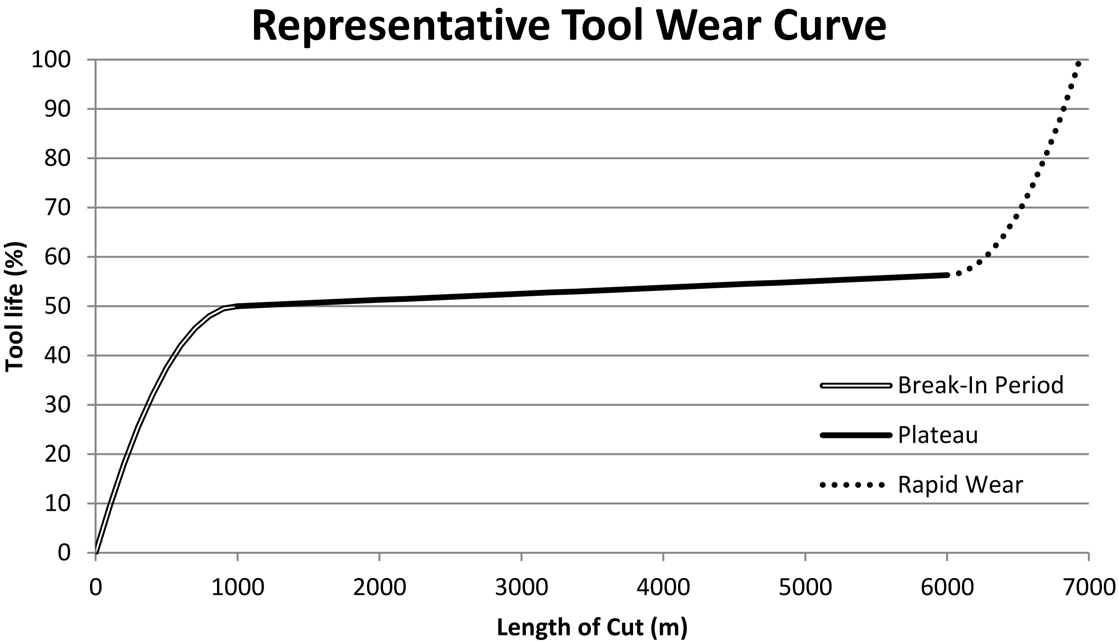

Figure 2.11 Representative Tool Wear Curve

Edge preparation and honing are well studied in conventional machining. A study was performed with a flyhobbing technique [20] to study the differences between various edge preparation methods and edge radii on PM-HSS tools with an aluminum-titanium-nitride

(AlTiN) coating. The workpiece tested was 27MnCr5. It was found that a tool with a cutting edge radius of 10-20µm provided the largest number of gears produced. A similar study [21] was performed for PM-HSS inserts for a milling operation and found that an optimum cutting edge radius of 14µm was most appropriate for milling a case hardening steel, 27MnCr5. Another study was performed to study the optimal cutting edge radius of diamond-coated tungsten carbide tools for cutting lightweight abrasive alloys [22]. In conventional machining, edge preparation has typically been used to extend the tool life or improve stability in the machining of difficult materials.

In the field of ultraprecision machining, there has been research on the influence of cutting edge radius on the stability of the micromilling process [23], with the conclusion that a cutting tool with 4.5µm cutting edge radius is more stable than a tool with a 1µm cutting edge radius. A study performed on a chamfered tool found that tool life and surface quality improved when using a chamfered tool instead of a tool with a conventional diamond bit [24] when machining tungsten carbide. There has also been research on the effect of a chamfered, sharp edge on the diamond turning of hard materials, such as a silicon crystal [25]. To the author’s knowledge, there has not been any research on the effect of an intentionally blunted edge on a single crystal diamond tool.

In SPDT, there are two primary causes of tool wear. The first is the breakdown and erosion of the cutting edge. The second source of tool wear is wear through formation and breaking of built-up-edge (BUE). Other types of wear, such as flank wear, crater wear, and stress fractures are less likely to occur due to the relatively low temperatures in the cutting zone in

SPDT. M.Masuda and Y.Maeda (1989) investigated the mechanism in which surfaces are generated using worn diamond tools [26]. They found that for a flat-nosed, sharp SCD tool, better surface finish is achieved when the cutting edge is worn slightly and recedes. This allows for a burnishing effect by the tool's trailing edge when placed at a positive tool setting angle. A specially designed flat-nosed tool with specially radiused corners was developed by Tauhiduzzaman and Veldhuis [2] to minimize plastic side flow and to encourage burnishing.

Lucca, Seo, et al. [27] studied the effect of tool edge geometry in the ultraprecision flycutting of Te-Cu alloy and found that SCD tools primarily wear by erosion of the cutting edge. An atomic force microscope (AFM) was used to measure the cutting edge radius of the SCD tools. The cutting edge radius was found to be 0.25µm on a new tool and was measured to be 1µm for a worn tool. It was also found that the tool thrust force was higher on a worn tool for uncut chip thicknesses below 8µm. Thrust force between both tools were similar beyond 8µm.

The tooling can be modified by irradiating the SCD tool using a focused ion beam (FIB) process, a method studied by Kawasegi et al. [28]. When machining aluminum alloys, the FIB-treated tool showed increased adhesion of the work material to the tool, decreasing the surface quality. When the FIB treated tools are heat treated, the adhesion problem does not appear, opening the applicability of using FIB treated tools in SPDT. This work is important as it highlights the possibilities of modifying SCD tools with highly controlled geometries. The high economic cost and training required to use FIB may limit its adoption in industry.

A study was performed by Zareena and Veldhuis [29] to improve tool life in the ultraprecision machining of titanium alloys by applying a polymer coating to the SCD tool, blocking chemical interactions between the titanium and diamond tool. The polymer coating also served to form a lubricious layer between the tool and workpiece as evidenced by lower cutting forces. This shows that it is possible to apply tool coatings to SCD tools, but the selection is limited as the coatings must be extremely thin and adhere well to the SCD.

In this thesis, a chemical etching process was performed on a diamond tool to prematurely wear the tool to reduce the length of the wear-in period and to extend tool life by reducing subsurface damage generated during the wear in stage. There have been many studies performed in the past to enhance the SCD tools used in diamond turning, such as the use of a chamfered sharp cutting edge, tool geometry changes to encourage burnishing, treatment through FIB, and thin polymer tool coatings. To the author’s knowledge, there has not been a study performed on the effect of a chemically etched and blunted tool in SPDT.

2.1.4 Relative Tool-Workpiece Vibration

This is an important topic in the field of SPDT as relative tool-workpiece vibration accounts for the form error in the resulting part. There has been research in off-line and in-process metrology to develop new technologies in order to compensate for these errors.

Tool-workpiece vibration in SPDT is commonly observed, even in dedicated machines with vibration isolation systems in place. Vibration in ultra-precision machine centers can cause various form and surface errors, directly influence the form of the resulting part. The cause of machine vibration can be attributed to a combination of the machine spindle and linear drives as well as outside influences such as disturbances in the compressed air supply or disturbances transmitted through the ground. In a production environment, it is sometimes not technically or economically feasible to completely isolate the machine tool from outside disturbances.

A pioneering work from Takasu et al. [3], assumed that a simple harmonic motion existed between the tool and workpiece and that it had a low frequency with small amplitude. Equations were presented to describe the peak-to-valley of the generated surface with consideration to the effects of tools with different nose radii for fly-cutting. This analysis was further developed by Fawcett [30] who measured relative tool to workpiece vibrations (while out-of-cut) in the in-feed direction using a capacitive gage. This allowed the development of a fast, low-amplitude tool servo to compensate for these errors during SPDT. The equations [3] were then used by Cheung and Lee [31] [32] [33] with a capacitive displacement probe to predict the peak-to-valley roughness (R_t) and mean arithmetic roughness (R_a) to values measured on machined workpieces. In these works, [32] [33] use a surface roughness evaluation length of 0.5mm, which may not capture the total form error in the part.

The excitations to the machine structure, whether from outside sources or from the machine itself, will cause a machine tool's components to vibrate at their natural frequency. Fawcett et al. [30] analyzed their ultraprecision machine center and found that the z-axis slide vibrates at its natural frequency when cutting and used a fast tool servo to compensate. The diamond tool itself was analyzed by Zhang et al. [34]. By using experimental data and computational models, the natural frequency of the tool shank tip, diamond tip, and tool tip were determined. Meyer et al. [35] performed modal tests using a set of accelerometers and force hammers to determine the natural frequency of various machine structural components. With this information, the frequency of vibration during cutting can be attributed to a specific machine component.

Regenerative chatter is a common problem when machining with high depths of cut. In diamond turning however, the possibility of chatter has been ruled out by Cheung and Lee [33] as the depth of cut is too small in relation to the system stiffness for the regenerative effect to occur. There has been some evidence of high frequency components (12-14kHz) being present in the cutting force signal and surface roughness profile, which is believed to be from tool-tip vibration [36] in SPDT. Many of these articles do not explain the source of these vibrations, especially those that contribute heavily to form error.

Bittner et al. [37] simulated all possible sources of error and their effects on the generated surface when diamond turning optical elements. His simulations covered not only physical errors from decentering of the tool with respect to the center of rotation and tilting of the machine slide relative to the spindle, but also periodic errors like variable shift between tool and spindle, periodic structures by thermal effects or tool wear and vibration of the axis of rotation which produce a spindle star pattern. Variable shift between tool and spindle occurs due to slow variable and oscillating position errors caused by thermal effects, uneven cooling of the tool or the carrier or from uneven cutting tool wear. Kim and Kim [38] analyzed and compensated the thermal growth spindle error in real time using a fast tool servo along with a capacitive displacement sensor and were able to bring the form error down to 0.1µm in a 100mm diameter specimen. Finally, vibrations of the spindle perpendicular to the workpiece can result in azimuthal ripples on the surface forming the spindle star pattern. Simulated appearance of such errors is shown in Figure 2.12. The spindle star was described as a type of form error that is characterized by azimuthal ripples in the surface or straight, radial spokes in the surface when viewed in an interferometer [37]. This error is generally attributed to the spindle and should not occur in an ideal turning process. In the results of this research, it is shown that flat planar surfaces with good surface finish will still have this problem. The star error of an ultraprecision machine center is of particular interest as it contributes greatly to the remaining form error measured on a finished part. Given other process improvements this level of error is now a dominant one which needs to be addressed to further improve lens performance.

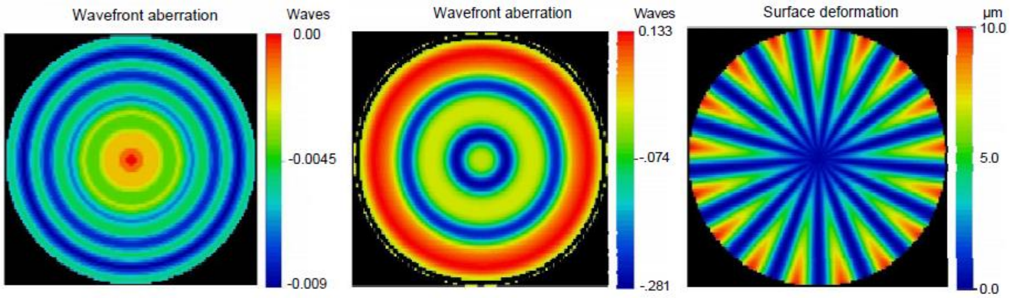

Figure 2.12 Variable Shift Between Tool and Spindle, Periodic Structures by Thermal Effects or Tool Wear and Vibration of the Axis of Rotation (Spindle Star Error) [37] [After Bittner et al. (2007)]

Jurgens, Shepard III, and Schafer [39] suggested that the spindle star has a weak effect on the RMS wavefront error and that the error originates from imbalance and the air bearing orifices of the spindle. They also stated that a properly designed spindle generally should produce little to no spindle star. The size, location, and shape of air bearing orifices in an aerostatic bearing can cause oscillations of the spindle. Newer air bearing spindles using continuous slots with porous graphite pads have claimed to eliminate this type of error. However, spindle shaft imbalance will always exist as it is impossible to produce an error-free part. It is not possible to perfectly compensate for imbalance using adjustment screws as they can only act upon a single plane of the spindle shaft, while the actual location of the imbalance can exist anywhere along the shaft, making perfect balance impossible. Khanfir [40] has also observed the spindle star and stated that the error is due to resultant axial and radial motion of the machine spindle. By using a spindle with active magnetic bearings, Khanfir et al. was able to filter out the fifth harmonic vibration of the spindle, eliminating the five lobed spindle star, and leaving a surface with a seven lobed spindle star pattern instead. Although the vibration amplitude decreased when the active magnetic bearings were modified, the pattern continues to exist. Zhang et al. [41] created a mathematical model (with five degrees of freedom) of an aerostatic spindle and analyzed how its movements affect the surface topography of a machined surface in SPDT. In this study, the mathematical model was successful in predicting the surface topography of a machined surface. However, the source of the spindle tilting frequency was not identified. The effects of the tilting frequency that they found contributes to the spindle star error at the center of the part. Excessive spindle star error can cause an optical component to fail inspection. This is because the human eye is very effective at spotting regularly spaced aberrations in optical components.

In diamond turning, form error can be categorized into 3 types: eccentricity, higher order synchronous motion, and asynchronous error motions. When a disturbance frequency is a harmonic or multiple of the rotating spindle frequency, it is a synchronous error motion. When the disturbance frequency is independent, it is termed as asynchronous error motion. Reducing eccentricity can be addressed by proper bearing alignment and spindle balancing. Reducing synchronous and asynchronous errors requires attention to the airflow and geometry of the aerostatic bearing. One way to reduce asynchronous error is to ensure that the incoming air supply is free from pressure pulses and contaminants. Improvements in aerostatic bearing design and manufacture have enabled error to be reduced from 200nm to 50nm over the last twenty years [42]. Figure 2.13 shows a cross section of an aerostatic bearing and how deflections in the spindle are countered by the air pressure.

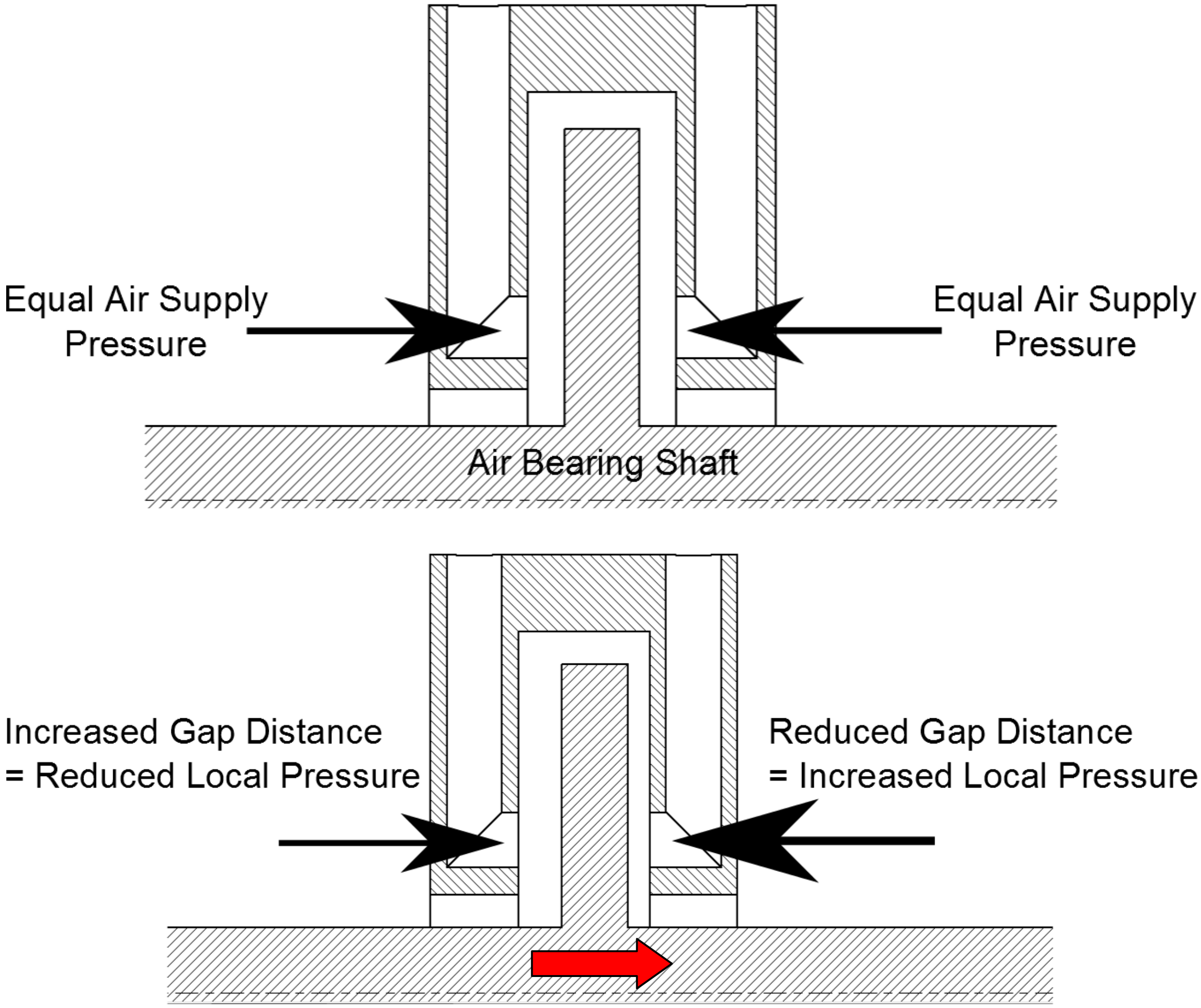

Figure 2.13 Example of an Air-Bearing Machine Spindle, Showing Self-Centering Effect [43] [Adapted after Alfred Jäger GmBH (2011)]

There have been several proposed methods to mitigate unwanted tool-workpiece vibration in order to improve surface finish and decrease the form error. Many of these methods require some modification of the machine, such as the use of actively compensating magnetic bearings [40]. Many other methods require the use of a fast tool servo, a feature that is not standard on all ultraprecision machine tools. Extensive modifications to ultraprecision machines may not be feasible for manufacturing businesses that cannot justify the economic cost of new machine parts and machine downtime. In order to study the vibration between the tool and workpiece, an understanding can be gained by performing rotordynamic studies, analyzing the assisted air-hammer instability of the air-bearing spindle, and investigating the impact of structural vibration. These three factors are interdependent in the formation of spindle star. A detailed rotordynamic analysis to explain spindle star phenomenon is provided in Chapter 5.2.

2.2 Measurement of Cutting Edge Radius

The measurement of the cutting edge radius of a Single Crystal Diamond (SCD) tool is extremely difficult, given the nature of the material and small size of the radius. A study was performed to determine the influence of cutting edge radius on the stability of a micromilling process using a carbide end mill [23]. The cutting edge radii of the tools used ranged from 4.5µm to 1µm. The small size of these micromilling cutters represents some of the sharpest commercially available carbide tools. SCD tools however, are expected to have smaller cutting radii of under 1µm.

There are several techniques and technologies available that can detect and resolve the small features on a diamond tool that are on the order of nanometers. The most common technologies used are scanning electron microscopy (SEM) imaging, atomic force microscopy (AFM), and confocal laser scanning (CLS) microscopy.

Optical microscopes are traditionally used to measure and characterize wear on a cutting tool in conventional machining. There has been a study on the surface generation of worn diamond tools [26] in 1989 where the amount of wear was quantified using optical micrographs to show the flank wear on the tools. This represents one of the first attempts to quantify the wear on an SCD tool. Optical microscopes cannot measure the cutting edge radius of a diamond tool due to the lack of resolution and the fact that the images produced are two dimensional – any misalignment of the diamond tool will result in an inaccurate measurement.

A scanning electron microscope (SEM) produces two dimensional images of a sample by scanning it with a focused beam of electrons. The sample is placed in a vacuum chamber with detectors inside. These detectors scan the scattered electrons from the electron beam, producing an image of the sample [44]. It is difficult to produce images of SCD tools in an SEM due to edge effects and charging [45]. Points and edges, such as the cutting edge of a diamond tool, produce more electrons as the electrons preferentially discharge from sharp edges and peaks, creating a ‘glow’ on the tool edge. SCD tools also produce charging artifacts. This is why diamond tools require a sputtered-gold coating before being placed in a vacuum chamber for SEM scanning. Proper fixturing of the diamond tool is important as the SEM produced two-dimensional images. Any slight misalignment of the tool to the detector will cause the image to be distorted, as the cutting edge will be seen from an oblique angle. Despite these limitations, there has been some success in using an SEM to measure the cutting edge radius of an SCD tool. Figure 2.14 shows the photograph of a high resolution SEM.

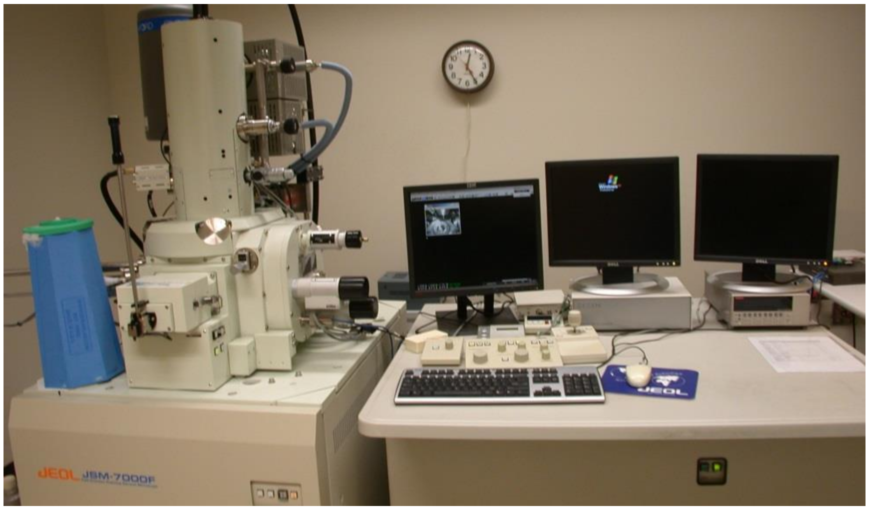

Figure 2.14 JEOL JSM-7000F Scanning Electron Microscope at McMaster University

Asai et al. [46] constructed a new SEM with two detectors, allowing them to measure the small cutting edge radius of diamond tools. They found that their diamond tools had an edge radius of 20nm to 45nm. The authors have attempted to measure the cutting edge radius of a diamond tool using an SEM, but the resulting picture was blurred by charging artifacts as shown in Figure 2.15. There was also difficulty in ensuring alignment between the tool and detector, leading to inaccurate measurements of the cutting edge radii.

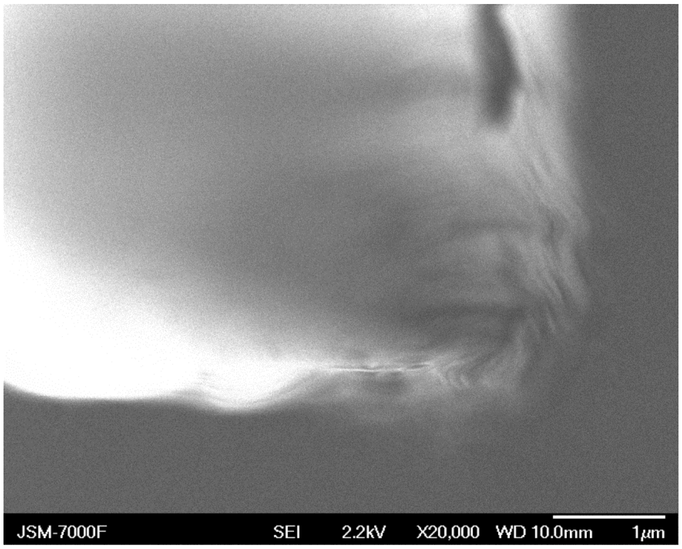

Figure 2.15 SEM Image of Diamond Tool Under 20000X Magnification

AFM is a technique in which a sharp, cantilever probe is moved or tapped over a sample. The cantilever probe typically has a small radius of curvature, on the order of nanometers. There are tiny deflections in the cantilever due to a variety of forces, such as mechanical contact force, van-der-waals forces, or electrostatic forces. The deflections in the cantilever probe are measured using either an interferometer, by piezoelectric sensing elements or by capacitive sensors [47]. By combining an accurate positioning system with the cantilever probe, a three-dimensional point cloud of the scanned surface or object can be made, creating a map of the tool's cutting edge. AFM cantilevers are limited by their low durability of the tip and their small working distance. The cantilever will not work if its displacement is too large. The AFM probe, being made of a softer material than diamond, can be easily damaged. Figure 2.16 shows a typical AFM instrument.

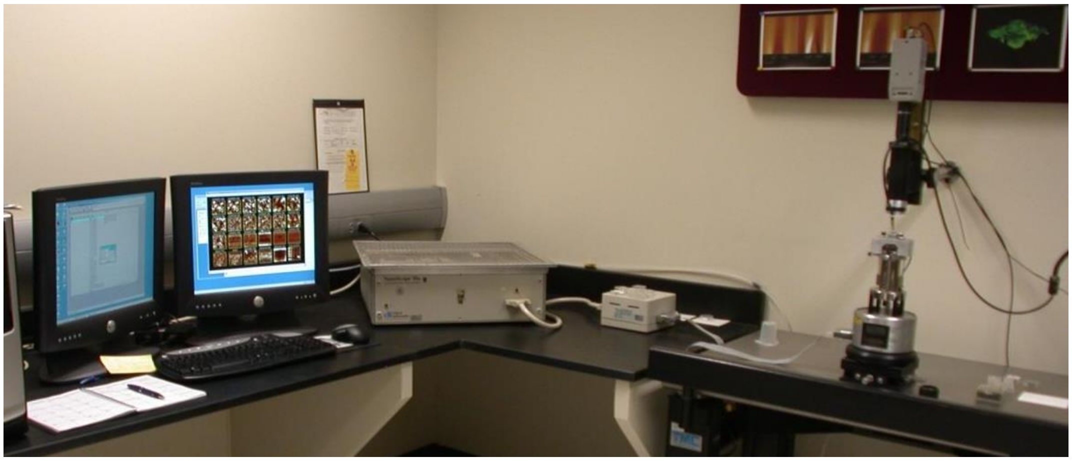

Figure 2.16 NanoScope IIIa Atomic Force Microscope at McMaster University

Despite these limitations, AFM has been successfully used to measure the cutting edge radius of an SCD tool by many laboratories. An early work by Lucca et al. [27] used an AFM to measure the cutting edge radius of an SCD tool by placing it into the stage at an inclined angle. The cutting edge radius for a new tool was estimated to be about 0.25μm. The AFM technique was improved by Gao et al. [48] by using an optical sensor to align the cantilever probe to the tool tip. The cutting edge radius was found to be 0.22µm for a worn tool and was 0.09µm for a new tool. This alignment technique was placed inside an ultraprecision machine center to allow for online measurement of tool wear by Asai et al. [49]. They found that the cutting edge radius of a diamond tool is between 0.056µm to 0.143µm with the measurement heavily dependent on the condition of the AFM probe.

The AFM was used again by Brinksmeier et al. [50] and the cutting edge radius of a new diamond tool was found to be 0.04µm. The cutting edge radius of a new SCD tool from these publications was measured to be between 0.09µm to 0.25µm. It has been shown to be a good method for determining the cutting edge radius of a diamond tool as it produces a 3D scan of the tool. However, using an AFM to measure the cutting edge radius of a diamond tool requires high operator skill to prevent breakage of the AFM probe. The probe tip radius can also cause the measurements to be inaccurate as shown in Figure 2.17.

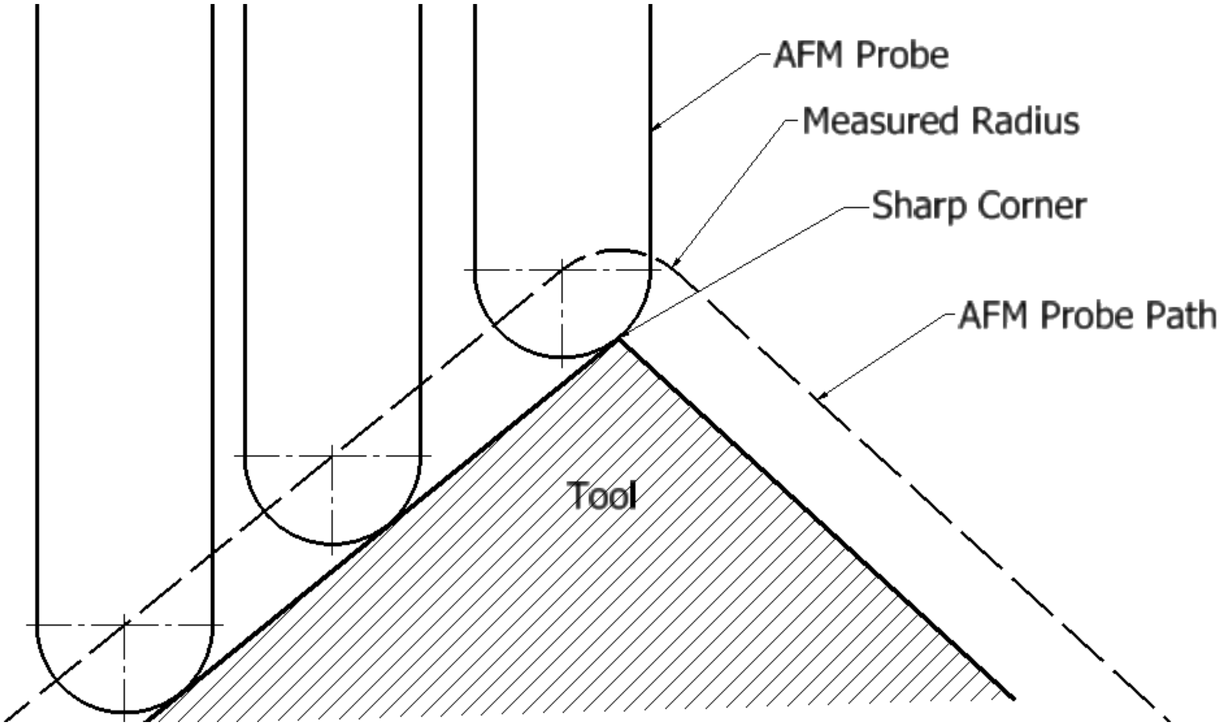

Figure 2.17 Relatively Large AFM Probe To Tool Cutting Edge Radius, Causing Larger Measured Value

Finally, the confocal laser scanning microscope is typically used in the biological and medical sciences. Its advantage is that it can capture images from selected depths using a very limited depth of focus. A laser is focused and reflected through the objective lens of the microscope to illuminate the sample. The sample reflects diffracted light back through the objective lens. The laser beam then travels through a pinhole to create a sharp focus as it is conjugate to the focal point of the objective lens [51]. Behind the pinhole is a detector. Electronically controlled mirrors can change the path of the laser beam to scan different points on the surface of the sample. A computer with the appropriate software can use the laser to scan points on the surface of the sample and move the focal plane to allow for optical sectioning [52]. With this technique, a 3D map of the surface can be constructed.

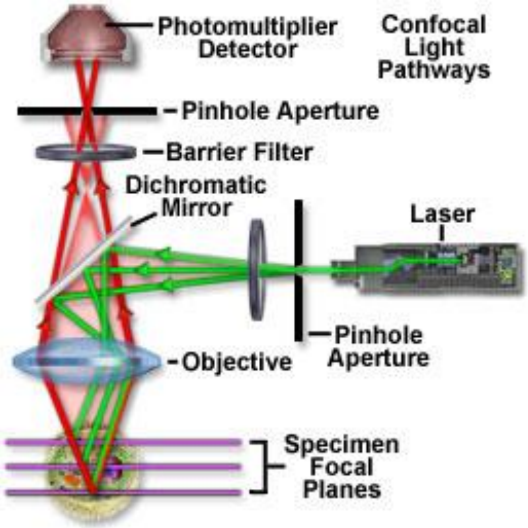

Figure 2.18 Schematic Diagram of Confocal Laser Scanning Microscope [53] [After Fellers and Davidson(2009)]

To the author’s knowledge, there are no published results of the measurement of the cutting edge radius of an SCD tool with a confocal laser scanning microscope. This is because of the sharp cutting edge radius of the diamond tool and the limited lateral resolution of the CLS microscopes. Recent advancements in CLS technology have allowed them to achieve a lateral resolution at the nanometer level thus facilitating accurate inspection and measurement of SCD tools.

Chapter 3. Experimental Setup & Procedure

3.1 Single Crystal Diamond (SCD) Tools

Diamond is a nearly ideal tool material for ultraprecision machining due to its high hardness, strength, thermal conductivity, and its ability to be honed to a very sharp edge and retain this edge while machining. Table 3.1summarizes the properties of diamond. Its only shortcoming is that diamond has chemical affinities with certain materials like iron and the fact that it breaks down under high temperatures.

Table 3.1 Properties of Diamond [54]

Symbol	**C**
Atomic Number	6
Atomic weight (amu)	12.011
Hardness	7000 Knoop Hardness (WC=2100 Knoop Hardness)
Density	3.51 g/cm^3
Most Common Valance	+4
Electron Configuration	$1s^2 2s^2 2p^2$
Melting Point	>3550 ^{0}C
Bonding type and energy	Covalent; 713 *kJ/mol*
Mechanical Properties	E= 1035 GPa
Electrical Conductivity	10^{-14} [(Ω-m)$^{-1}$]
Thermal conductivity	2000-2500 *W/m-K*

Four diamond tools were used in this study. Two were used for experiments and two were used for cleaning and preparing workpieces. The tools with a 12mm nose radius were produced by DiamTech SCD Tool Technology, located in Quebec, Canada. Two more tools with a 1.5mm and a 0.5mm nose radius were supplied by K&Y Diamond, also located in Quebec. The four tools used in this study are:

- 12mm nose radius tool with honed, sharp edge
- 12mm nose radius tool with chemically etched and blunted edge
- 1.5mm nose radius tool with honed, sharp edge
- 0.5mm nose radius tool with honed, sharp edge

The tools with sharp edges are commercially available but the tool with a chemically etched edge was specially ordered by B-Con Engineering in Ontario, Canada. The tools were inspected with an optical microscope with at least 800X magnification to ensure that the tool's cutting edges are sharp and chip-free, a standard industrial practice. The tools are wiped using isopropyl alcohol and cleaned using air jets before inspection. Effort was made to ensure that the diamond was not exposed to oil such as from ones hands and coolant was not allowed to dry on the tool surface. The sharp edge of the diamond tool is particularly sensitive to chemical attack.

In order to compare tools of different nose radii, the measurements of cutting force will be expressed in force per unit contact length, N/µm. The geometric contact length is dependent on the depth of cut and nose radius of the tool as shown in Figure 3.1. The contact length was computed using Autodesk Inventor 2013 and presented in Table 3.2

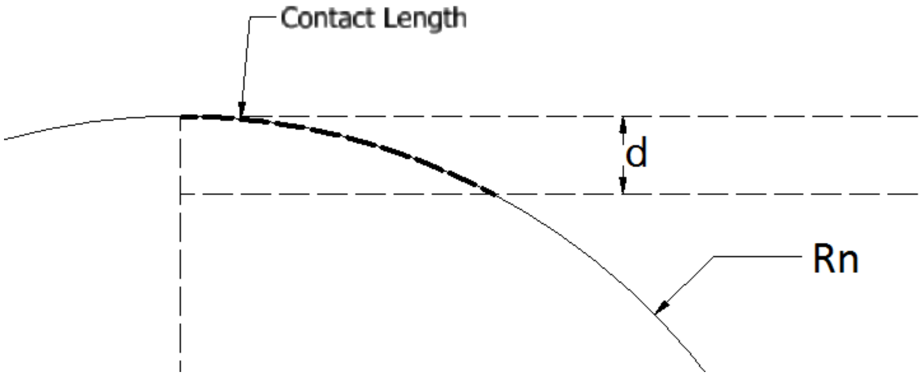

Figure 3.1 Geometric Contact Length of Round-Nosed Cutting Tool

Table 3.2 Geometric Contact Length of SCD Tools

Nose Radius, R_n	**Depth of Cut, d**	**Contact Length**
12 mm	2 µm	0.21909 mm
1.5 mm	2 µm	0.07747 mm
0.5 mm	2 µm	0.04474 mm

3.2 Workpiece: RSA-6061 and holders

The workpiece used for the majority of the cutting tests was an aluminum 6061 workpiece made of Rapidly Solidified Aluminum (RSA-6061). It is 60mm in diameter and 15mm thick. It was mounted to a workpiece-holding aluminum disk in order for it to be held by the vacuum chuck of the machine tool with the help of a dowel pin followed by precision dialing within ±1μm run out. The workpiece mounted on the aluminum disk and SEM image of the microstructure is shown in Figure 3.2. Grain sizes of the RSA 6061 aluminum is observed to be around 2μm to 5μm where the alloying elements are finely distributed on the matrix. The micro-hardness of the RSA-6061 workpiece showed that its hardness was 144HV. The micro-hardness test was also completed at 25gf load with 10 seconds of dwell time on a CLIMEX CMT 5.0 micro-indentation tester.

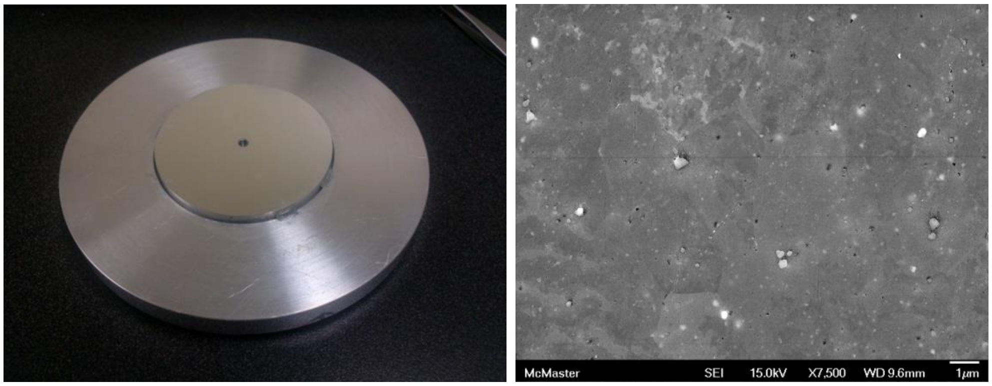

Figure 3.2 RSA-6061 Workpiece (left center) and microstructure (right)

The RSA-6061 workpiece was also placed into a large steel holder weighing 4kg. This steel workpiece holder was used to test the dynamics of the machine with a heavier workpiece without changing the material being cut. The photograph of the 4kg workpiece holder is shown in Figure 3.3.

Figure 3.3 Steel Workpiece Holder for RSA-6061 Workpiece, 4kg Mass

3.3 Machine Tool: Precitech Freeform 700G

The Precitech Freeform 700G machine is a high performance, ultra-precision machine tool with computer numerical control. It is suitable for the production of optical and mechanical components. The machine tool has three linear axes (X, Y, Z) as well as one rotational axis (B) as shown in Figure 3.4.

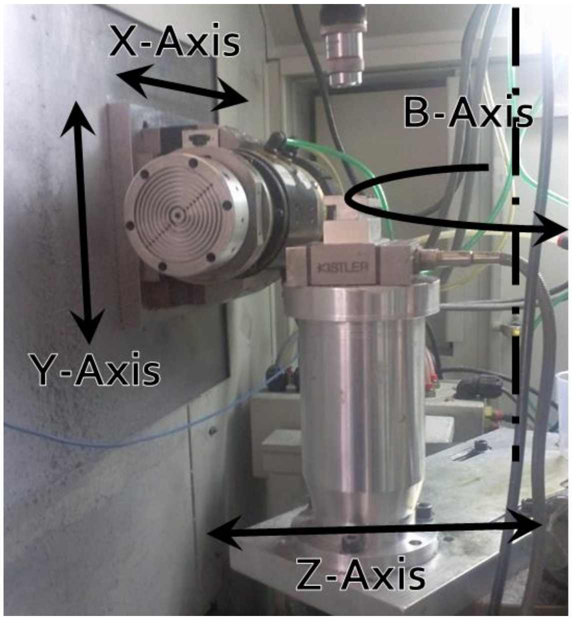

Figure 3.4 Precitech Machine Tool Setup and Machine Axes

The linear axes are guided by hydrostatic oil slide ways and controlled by multi-phase linear motors. The home position of these linear motors is sensed by a Linear Variable Differential Transformer (LVDT) transducer. Positional feedback is given by laser holographic linear encoders athermally mounted to these slideways. The X and Y axis encoders have a resolution of 8.6nm, while the Z axis encoder has a resolution of 1.4nm [42]. The straightness of these X, Y, and Z slideways is within 0.5 µm per 150mm length [42].

The machine is controlled by the use of the Precitech Ultrapath^{TM} digital signal processing-based control system. The machine is mounted to a sealed natural granite base and is leveled and isolated from the ground using a pressurized air system [42] that isolates the machine from high frequency vibrations from the ground. An air-bearing spindle with a vacuum chuck 4" in diameter holds the workpiece. This spindle has a maximum speed of 10,000 RPM. The maximum spindle speed used in this study did not exceed 3600 RPM. The photograph of the spindle is shown in Figure 3.5 with the workpiece mounted on the vacuum chuck.

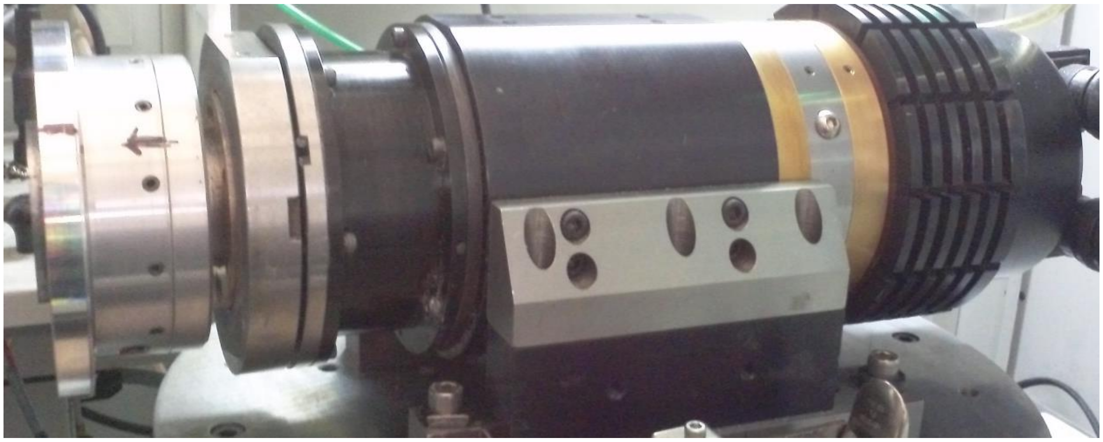

Figure 3.5 Precitech SP-90 Spindle

The machine enclosure is connected to a stand-alone heater/cooler in order to control the machine temperature. This heater/cooler uses a closed-loop temperature controller with a

Programmable Logic Controller (PLC) and Resistance Temperature Detector (RTD) and can hold a temperature to within 0.1°C [42]. The room temperature is maintained at 20 +/- 1°C. The machine axes are stiff enough to keep deflection within single nanometer levels when cutting with sub-newton forces. The machine axes are designed to be very stiff for the purpose of diamond turning. The stiffness values are outlined in

Table 3.3.

Table 3.3 Precitech Machine Stiffness [42]

Axis	Direction	Stiffness (N/µm)
X (Linear)	Vertical/Horizontal	438N/µm / 438N/µm
Y (Linear)	Vertical/Horizontal	263N/µm / 263N/µm
Z (Linear)	Z-Direction/X-Direction	438N/µm / 438N/µm
B (Rotary)	Axial/Radial	1750N/µm / 525N/µm
Spindle (RPM)	Axial/Radial	70N/µm / 26N/µm

3.3.1 Machine Operating Procedure

The Precitech Freeform 700G is an extremely accurate and precise machine. Care must be exercised to ensure consistent results.

Step 1:

The machine brakes are released and servos are activated by disengaging the “Emergency Stop” and resetting the controller. The homing sequence is performed (“RESET” phase motor and then “HOME” axes)

Step 2:

The Precitech machine is placed through a ‘warmup’ program that will run the spindle and move the X, Y, and Z axes through their range of motion for 30 minutes. This warmup cycle is also repeated every day before cutting tests are performed to ensure thermal uniformity within the machine.

Step 3a:
Workpiece is mounted on the spindle’s vacuum chuck.

The workpiece is centered to minimize eccentricity of mass. Eccentric loading will cause the spindle to vibrate, creating errors in the finished surface. More severe eccentricity will cause imbalance and radial runout, compromising the safety of the operator and equipment.

Step 3b:
A mark is placed on the vacuum chuck and on the workpiece to ensure that the workpiece is mounted in the same orientation with respect to each other. The outer circumference of the workpiece is assumed to be square with the back face of the workpiece.

A runout of no more than 2.45µm is recommended [42]. The workpiece is centered by setting the vacuum chuck to the “LOW” position. A dial gauge with a resolution of 2µm is used to measure radial runout. The workpiece is tapped on the spindle until the dial gauge records a maximum runout of less than 2µm and the vacuum chuck is then set to the “HIGH” position.

Step 4:
The cutting tool is mounted into the tool holder. The tool holder is fixed to a force dynamometer to measure the cutting forces generated by the tool. Depending on the machine setup, the tool holder can be mounted to the B-axis or on the X/Y-axis.

Step 5:
If the tool is mounted on the B-axis table, the B-axis is rotated to allow cutting with a desired portion of the tool. If the tool is mounted in the X/Y-axis, the B-axis is rotated to a desired angle to minimize misalignment between the spindle’s rotational axis and the Z-axis.

3.3.2 Machine Balancing Procedure

The Precitech's SP-90 work-holding spindle must be balanced before use. The chuck allows for single-plane balancing using 12 set screws placed around the vacuum chuck. The SP-90 is equipped with a 1000-line optical encoder with indexing pulse that can be used as part of the balancing procedure. The balancing procedure is limited by the arrangement of the balancing screws as only single plane of balancing can be performed. The true location and magnitude of the shaft imbalance is unknown and cannot be fully compensated using the balancing screws alone.

Step 1:
Several instruments need to be mounted to the machine to allow for single-plane balancing.

The index pulse from the SP-90 optical encoder is attached to an opto-isolator breakout board. The one used here is a SparkFun Model BOB-09118 equipped with ILD213T opto-isolator chip.

A Kistler Type 8640A5 accelerometer was mounted to the SP-90 spindle in the radial direction near the chuck to measure vibration. The PCB Piezotronics Model 480D06 power unit was used to amplify the signal from the accelerometer.

These two devices were connected to a data acquisition system consisting of a National Instruments NI PCI-6023E and BNC-2110. A key feature of this data acquisition system is that it supports hardware triggering. A LabView 7.1 VI was used to capture the accelerometer data using the signal from the opto-isolator to trigger the data recording. The hardware trigger ensures that the data acquisition system begins recording at the index pulse of the spindle rotation each time. 40960 samples were collected at a rate of 40.960kS/sec for each measurement.

Step 2:

The Precitech ‘warmup’ cycle is performed. This program will move all three linear axes, X, Y, and Z throughout their full range of motion for 30 minutes. The spindle is set to run at 1000RPM during this time.

Step 3:

After the warmup cycle, the spindle is run at 1000RPM with the instrumentation inside the machine. At 1000RPM, the rotational frequency is 16.667Hz. The LabView VI uses a bandpass filter with a lower frequency of 16Hz and upper frequency of 18Hz to retain only the rotation dependent content. The LabView VI also measures the peak-to-peak value of this filtered signal to assess the quality of balance.

Step 4:

The filtered signal is displayed on the screen for one revolution. A trial mass is hot-glued to the spindle at a selected position. This is done to determine the number of degrees of lag between the peak recorded acceleration to the position of adjustment.

At 16.667Hz, one rotation will take 0.06 seconds. The time of peak acceleration, T_{peak} is recorded. This peak acceleration occurs at some *nth* rotation of the spindle since the data acquisition system started. The time of the index pulse corresponding to this *nth* rotation, T_{index}, is also recorded. An equation is used to determine the position where the trial mass should be mounted.

$$P_{peak} = \frac{T_{peak} - T_{index}}{(\frac{60}{RPM})} * 360°$$

Equation 3.1 Formula Used To Determine Trial Mass Position

The spindle is set to run at 1000RPM again and the new T_{peak} and T_{index} values are recorded. Using Equation 3.1, a new P_{peak} can be calculated, called P_{trial}. The lag between the peak acceleration and adjustment position can be calculated.

$$P_{lag} = P_{trial} - P_{peak}$$

Equation 3.2 Formula To Determine Adjustment Lag

The trial mass is removed.

Step 5:

The spindle is set to run at 1000RPM. The position for adjustment is determined by a modification to Equation 3.1.

$$P_{peak} = \frac{T_{peak} - T_{index}}{(\frac{60}{RPM})} * 360° + P_{lag}$$

Equation 3.3 Formula To Determine Adjustment Position

The selected set screw for adjustment is determined by finding the closest set screw to the position found using Equation 3.3. The peak-to-peak value of the filtered signal is recorded.

Step 6:

The selected set screw is screwed inwards by half a turn. The spindle is set to run at 1000RPM for 30 seconds. A measurement is taken again with the data acquisition system.

If the filtered peak-to-peak acceleration is smaller than the value found in Step 5, repeat Step 5 again.

If the filtered peak-to-peak acceleration is larger than the previous step, then the spindle is stopped, and the selected set screw is screwed outwards by one full turn.

Run the spindle at 1000RPM for 30 seconds and measure again. If the filtered peak-to-peak acceleration is still larger than the value found in Step 5, then turn the set screw inwards by one half turn and move onto the next step.

Step 7:
Repeat step 6, but replace all half-turns with quarter-turns, and all full-turns with half-turns of the set screw. Repeat until the filtered peak-to-peak acceleration is minimized within the physical limitations of adjusting the set screws.

3.4 Data Acquisition System

The forces encountered by a cutting tool are important as they reflect the quality and condition of the tool, machine, fixture, and sometimes even the finished surface. The use of a force dynamometer is critical and allows for easy monitoring of the cutting process. The data acquisition system (DAQ) consists of a MiniDyn 3-component dynamometer (Kistler 9256B1), a dual-mode three-channel charge amplifier (Kistler Type 5010), and a USB data acquisition system with four input channels (NI compactDAQ-9172, NI 9215 and NI 9234). A PC using National Instruments' (NI) LabView software is used to collect and analyze the force data.

3.4.1 Force Dynamometer: Kistler 9256B1

The cutting tool is mounted to the force dynamometer. Its specifications are taken from the data sheet included with the dynamometer, listed in the Table 3.4 below. Figure 3.6 shows the dynamometer with the tool holding fixture mounted.

Table 3.4 Kistler 9256B1 Specifications [55]

	Notation	Unit	Type 9256B1
Measuring Range	F_x, F_y, F_z	N	-250/250
Overload	F_x, F_y, F_z	N	-300/300
Crosstalk		%	≤±2
Rigidity	c_x, c_z	N/ µm	>250
	c_y	N/ µm	>300
Operating Temperature range		°C	0 … 70
Natural frequency	f_{nx}	KHz	5.1
	f_{ny}		2.5
	f_{nz}		5.6
Sensitivity	X	pC/N	11.2
	Y		13.7
	Z		11.7

Figure 3.6 Kistler 9256B1 Dynamometer with Tool Holding Clamp Installed

The diamond cutting tools were installed on the Kistler 9256B1 with the X, Y, and Z, directions of measurement corresponding to the tool's thrust, feed, and cutting force, respectively as shown in Figure 3.7.

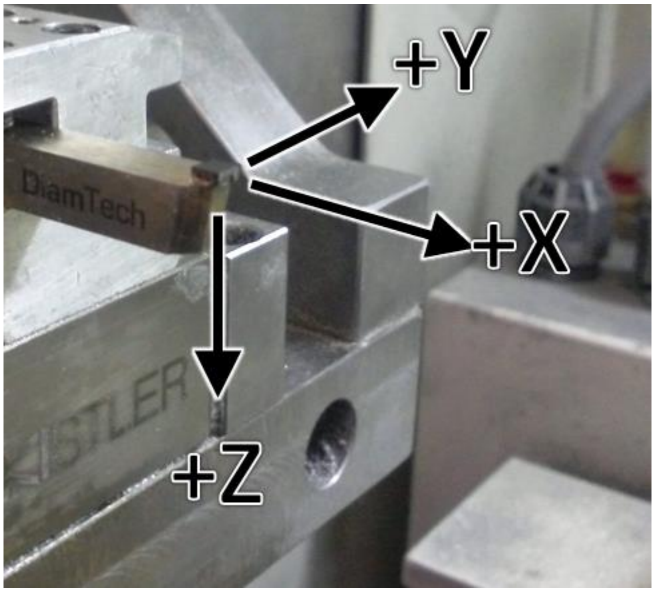

Figure 3.7 Tool and Force Dynamometer Coordinate System

3.4.2 Charge and Voltage Amplifier: Kistler Type 5010 and PCB Piezotronics Model 480D06

A charge amplifier is necessary for the DAQ to record force from the force dynamometer. The Kistler Type 5010 converts the charge signal from the dynamometer to a voltage proportional to the input. This amplifier is capable of producing an output signal from -10V to +10V. Sensitivity of the three channels was chosen according to Table 3.4, and the amplifier’s sensitivity was set to be the signal to 1 pC/N. The LabView software has the ability to scale the results according to the force dynamometer’s sensitivity manually. Due to the sub-newton forces involved, high sensitivity is important. The time constant is set to “short” to sense high frequency changes in cutting force are detected. The charge amplifier used in this study is shown in Figure 3.8.

Figure 3.8 Kistler Type 5010 dual mode, three-channel charge amplifier

For the balancing procedure, a voltage amplifier is required to measure the signals from an accelerometer. PCB Piezotronics Model 480D06 was used to attach an accelerometer to the unpowered PCI-based data acquisition system. This amplifier is capable of producing an output signal of +/- 10V. The gain on the amplifier was set to 1 for all measurements. The instrument is shown in Figure 3.9.

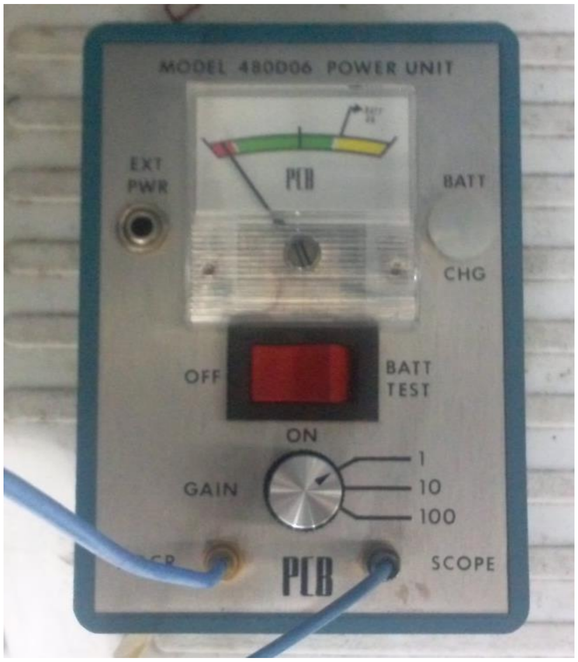

Figure 3.9 PCB Piezotronics Model 480D06 Voltage Amplifier

3.4.3 Accelerometer: Kistler Type 8730A500M1 and Kistler Type 8640A5

The 8730A500M1 accelerometers (Shown in Figure 3.10) used in this study use quartz sensing elements and have low mass which makes them ideal for precision measurement of light weight structures. It has a measuring range of +/- 500g and a sensitivity of about 9.5mV/g [56]. These accelerometers were attached to various parts of the machine tool using hot glue.

Figure 3.10 Kistler Type 8730A500M1 Accelerometer

The Kistler Type 8640A5 is a lightweight single axis accelerometer (Shown in Figure 3.11) with a ceramic beam sensing element, also ideal for analyzing lightweight elements. It has a measuring range of +/- 5g, a sensitivity of 990mV/g [57]. It also has a resonant frequency of 17kHz.

Figure 3.11 Kistler Type 8640A5 Accelerometer

3.4.4 Impulse Hammer: PCB Piezotronics Model 086B01 & Kistler 9726A5000

The PCB Piezotronics Model 086B01 is a small impulse hammer used to strike the machine structure as shown in Figure 3.12. When the structure is instrumented with accelerometers, the information from the impulse hammer and the accelerometers can be used to find the natural frequency and dominant vibration modes of the structure. This impulse hammer has a frequency response of 10kHz and has a sensitivity of 12mV/N [58]. The hard tip is used to create a sharp spike of excitation force.

Figure 3.12 PCB Piezotronics Model 085B01

The Kistler 9726A5000 is a larger impulse hammer used to excite larger structures than the smaller PCB Piezotronics hammer. This impulse hammer has a frequency response of 1kHz and a sensitivity of 1.138 mV/N. Again, the hard tip was used to create a sharp excitation force. The hammer is shown in Figure 3.13.

Figure 3.13 Kistler 9726A5000

3.4.5 USB Data Acquisition System

There are two components to the data acquisition system. The first is the NI cDAQ-9172 chassis [Figure 3.14] with USB connection to the PC with 8 module slots. It has a power input of 11 to 30 VDC at 15W. This chassis can hold many types of modules, but the one used is the general purpose NI 9215 [Figure 3.15] to measure cutting force. This module operates at +/- 10VDC with an accuracy of 0.003V and can sample at a maximum of 100kS/sec [59].

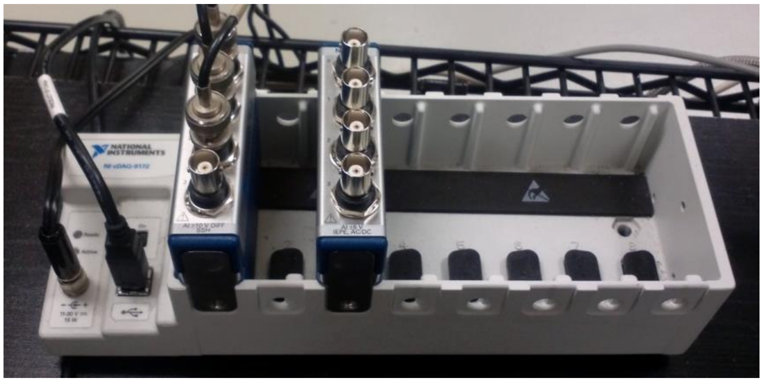

Figure 3.14 National Instruments NI cDAQ-9172

Figure 3.15 National Instruments NI 9215 Module

The NI 9234 module is used to record accelerometer data. This module operates at +/- $5V_{pk}$ and can sample at a maximum of 51.2kS/sec [60] as shown in the Figure 3.16.

Figure 3.16 National Instruments NI 9234 Module

This system is attached to a PC with the NI LabView software. A LabView program is used to process and record the data. A fast Fourier transform (FFT) can also be performed on the data to extract frequency-domain data. For the purposes of this study, a sampling rate of 1.0240 kS/sec was used and each measurement consisted of 20480 samples. This system is used for acquiring data from cutting and vibration tests.

3.4.6 PCI Data Acquisition System

A PCI-based data acquisition system is used exclusively for the balancing procedure. A National Instruments PCI-6023E PC card as shown in Figure 3.18 was used in conjunction with the National Instruments BNC-2110 (Shown in Figure 3.18). The BNC-2110 serves as an attachment point for instruments with BNC connections. The PCI-6023E operates at +/- 10VDC with an accuracy of 0.008V and can sample at a maximum of 200kS/sec [61]. It also has a hardware triggering capability, allowing it to be triggered by the index pulse of a rotary encoder. This system is used for acquiring data for spindle balancing.

Figure 3.17National Instruments PCI-6023E Data Acquisition Card

Figure 3.18 National Instruments BNC-2110 Shielded Connector Block

3.4.7 Data Acquisition Software: LabVIEW 7.1

The National Instruments LabVIEW is an acronym for Laboratory Virtual Instrument Engineering Workbench. It is a visual programming language used in this study for data acquisition and monitoring. The programs created by LabVIEW are called VI, or virtual instruments.

For data acquisition, the DAQ Assistant was used to match the physical channels from the USB or PCI data acquisition system to input channels in the VI. For FFT calculations, the Spectral Measurements VI was used to measure the power spectrum of a signal, using a Hanning window and linear output. For balancing, the Filter VI was used with a band-pass, third order infinite impulse response filter.

For reading the saved measurements from the data acquisition program, the same program is used by replacing the DAQ Assistant VI with the Read LVM File VI.

3.5 Modal Testing Software: CutPro 9

The software used for modal tests is produced by the Manufacturing Automation Laboratories Corporation in B.C., Canada. The MalTF program is an extremely fast and easy to use program that uses an impulse hammer and accelerometer to extract the transfer function of a vibrating structure. The program can be used to predict the natural frequency, damping ratio, modal mass and modal stiffness of each mode in the machine structure [62].

3.6 Mapping & Measurement of Surface Topography

3.6.1 White Light Interferometer: Zygo NewView 5000

Surface finish was inspected using a Zygo NewView 5000 white-light interferometer. It can be used to scan a surface and returns a graphical representation of the surface and a 3D point cloud showing the surface topography. The interferometer does this optically, without touching or disturbing the surface. This system consists of two parts: a microscope and a computer. Depending on the resolution settings, the vertical resolution ranges from 0.1nm to 20nm.

The microscope is mounted on a granite base and stable gantry column and has a 20X internal magnification. An internal lens can be changed to allow for magnification from 0.4 to 2.0, with a selection of 1X, 10X, and 50X objective lenses. The microscope is also equipped with a 4 axis stage with X and Y linear axes with roll and pitch. Images are captured and transferred to the PC using a CCD camera having a resolution of 640x480 pixels. The Zygo Corporation also provides the MetroPro software for analyzing the scanned surface.

For surface finish inspections, the 50X/Mirau objective lens was used in combination with 20X internal magnification and a 1.0X internal zoom. This gave a total 1000X magnification with a spatial resolution of 0.22μm. The spatial resolution varies with the field of view (FOV) and magnification as shown in Table 3.5. This setting was chosen as it can effectively measure the small machining tool marks and the shape of these tool marks on the finished surface. The Microscope application in the MetroPro software was used to measure the surface finish. No filtering options were used.

Table 3.5 Zygo NewView 5000 Specifications [63]

Internal Zoom Lenses	Field of View (FOV) (mm X mm)			Spatial Resolution (µm)		
	1X/Mich	**10X/Mirau**	**50X/Mirau**	**1X/Mich**	**10X/Mirau**	**50X/Mirau**
0.5X	14.5 X 10.9	1.41 X 1.06	0.28 X 0.21	22.70	2.21	0.44
0.75X	9.10 X 6.82	0.94 X 0.70	0.19 X 0.14	14.22	1.47	0.29
1.0X	7.18 X 5.38	0.70 X 0.53	0.14 X 0.11	11.22	1.10	0.22
1.5X	5.37 X 4.03	0.47 X 0.35	0.09 X 0.07	8.39	0.73	0.15
2.0X	3.57 X 2.68	0.35 X 0.27	0.07 X 0.05	5.59	0.55	0.11

For inspections of form error, the 1X/Mich objective lens was used with an internal magnification of 20X and an internal zoom of 0.5X. This gave a spatial resolution of 22.70µm. This reduced spatial resolution allowed the machine to essentially ‘ignore’ surface roughness and measure larger undulations and waves in the finished surface. To organize data across multiple scans the stitching feature within the MetroPro software was used. This feature can take multiple scans of the surface, and stitch them together into one large scan. For these measurements, no filtering options were selected and a stitching overlap of 15% was used.

3.6.2 3D Laser Confocal Microscope: Olympus OLS4000 LEXT

The measurement of the cutting edge radius of SCD tools requires measurement with very high resolution. A confocal laser scanning microscope uses a laser and detector to create very high resolution images. The laser is focused through the objective lens on the specimen. Reflected and scattered light is picked up by the objective lens and fed to a detector. This technique, when combined with a computer, can be used to produce 3D height maps of a surface.

Olympus Corporation performed measurements of the cutting edge of the single crystal diamond tools using an Olympus OLS4000 3D laser confocal microscope as shown in Figure 3.19. This microscope was chosen as it was designed for nanometer-level imaging, 3D measurements, and roughness measurement. It uses a 405nm laser with dedicated objective lenses to image slopes up to 85 degrees, a feature that is perfect for measuring and analyzing the edge preparation of a sharp diamond tool. The OLS4000 is also unique in its performance specifications as outlined in Table 3.6.

Figure 3.19 Olympus LEXT OLS4000 Laser Confocal Microscope

Table 3.6 Olympus LEXT OLS4000 Performance Specifications

Planar Measurement		**Height Measurement**	
Repeatability	Accuracy	Repeatability	Accuracy
0.02µm (100x)	+/- 2%	0.012µm (50x)	(0.2 + L / 100)µm or less (where L=Measuring Length, µm)

The SCD tools measured using the maximum magnification available, at 17280X. The objective lens was a 100X objective M PlanApo N LEXT with a zoom factor of 8X. The image size was 1024 by 256 pixels, using the XYZ fine scan mode. Laser intensity was 80%. No filtering or other modifications to the 3D point cloud were used. Under these conditions, the field of view was 16µm x 4µm. The spatial resolution in the X and Y direction was 0.0156µm.

3.7 Workpiece Material and Cutting Parameters

The aluminum alloy used exclusively in this study is a rapidly solidified aluminum (RSA) 6061 alloy. It was chosen as it is well suited to diamond turning due to its ability to be cut easily with diamond tools to leave an optical finish without the use of nickel plating. The physical properties of RSA-6061 are shown in Table 3.7.

Table 3.7 Physical Properties of RSA 6061 [18]

Property	Units	Value
Density	kg/m^3	2700
Hardness, Brinell	HB	110
Ultimate Tensile Strength	MPa	330
Yield Strength	MPa	300
Elastic Modulus	GPa	70.0
Coefficient of Thermal Expansion	µm/m-°C	23.0
Thermal Conductivity	W/m-K	160

The workpiece is mounted to the spindle and a facing operation is performed. A schematic of this operation is shown in Figure 3.20.

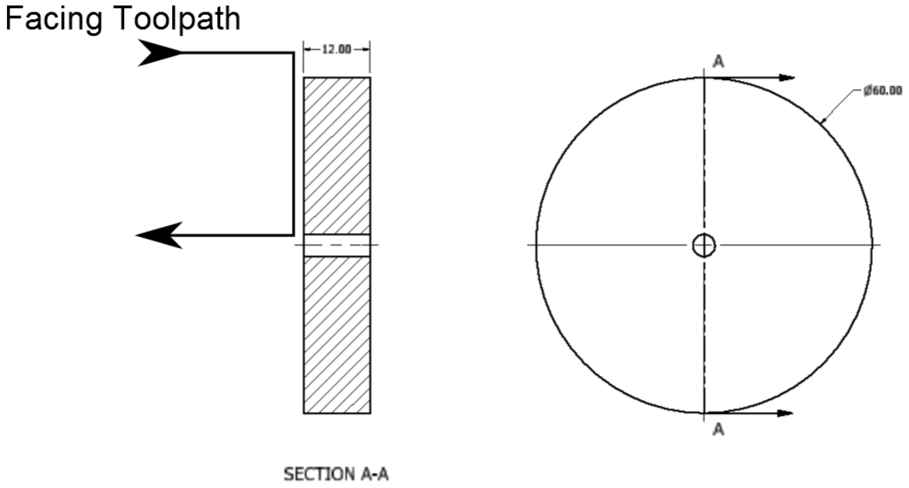

Figure 3.20 Facing Operation and Workpiece Drawing

In order to compare the two 12mm nose radius tools, one cutting parameter was chosen. The spindle speed will be 1000 RPM and the tool will be fed at a speed of 5µm/rev. The depth of cut is 2µm. These cutting parameters are widely accepted speeds and feeds for the finishing of optical surfaces in aluminum alloys. For vibration analysis, the spindle speed has been varied from 400rpm to 3600rpm, but the feed rate of 5µm/rev and a depth of cut of 2µm remain unchanged.

Chapter 4. Machine Tool Modification & Analysis

To produce the best surface finish, the machine’s deflections due to cutting forces should be minimized. This can be done by designing tool-holding fixtures that are stiff and work in a way such that the cutting forces act against the stiffest machine axes. The older machine setup was not well suited to diamond turning due to the design of the tool-holding fixture as it lacked stiffness and versatility. The resulting surface finish was not very good as it relied on both the B-axis and less accurate X-axis for controlling the depth of cut into the workpiece. The previous machine setup is shown in Figure 4.1. The revised tool-holding fixture will rearrange the machine such that only the most accurate and stiffest Z-axis will be used to control the depth of cut.

Figure 4.1 Tool-Holding Fixture, Before Modifications

4.1 Fixture Design

The fixture was designed to be as compact and as stiff as possible to reduce the severity of vibration during machining. The fixture was also built out of a combination of stainless steel 304 for corrosion resistance and some parts with high carbon 4140 steel to allow the attachment of magnetic stands and coolant spray nozzles. The rendered view of the fixture as shown in Figure 4.2 was designed and modeled in Autodesk Inventor 2013.

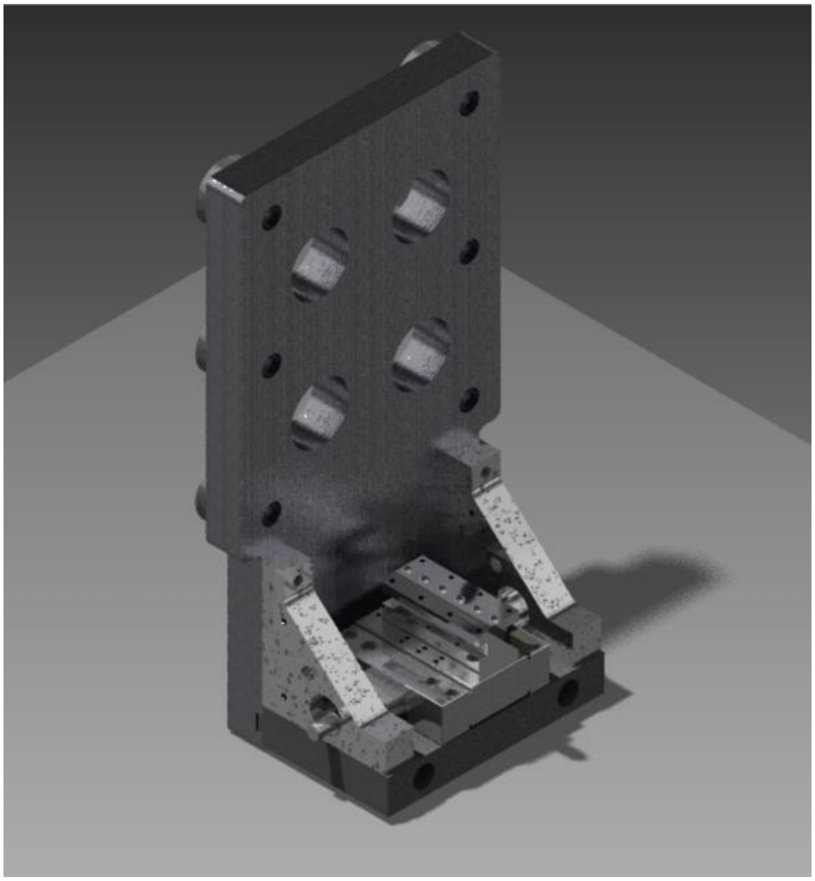

Figure 4.2 Render of New Tool-Holding Fixture

Using Autodesk Inventor, the model was analyzed for static deflection under 1N of load at the tool tip which is a typical cutting force in SPDT. The maximum deflection will be at the tool shank, with a deflection of 20nm. A software probe was placed on the base of the tool holder, showing a deflection of 8nm. Figure 4.3 shows the results with adjusted colors to exaggerate the deflection of the fixture.

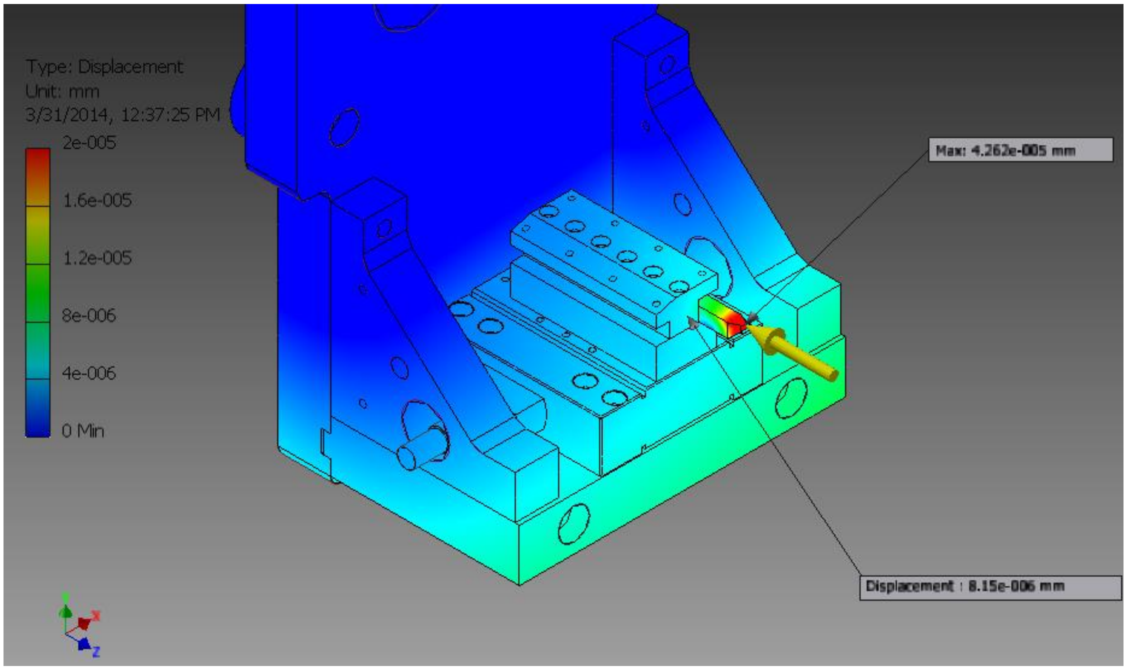

Figure 4.3 Static FE Analysis of Tool-Holding Fixture, with adjusted colors for clarity

With the help of the McMaster Manufacturing Research Institute (MMRI) and technicians, the fixture was built using a water jet abrasive cutter and an Okuma 3-Axis CNC machining center. It is now installed in the Precitech 700G machine tool on X/Y axes stage as shown in Figure 4.4 and Figure 4.5.

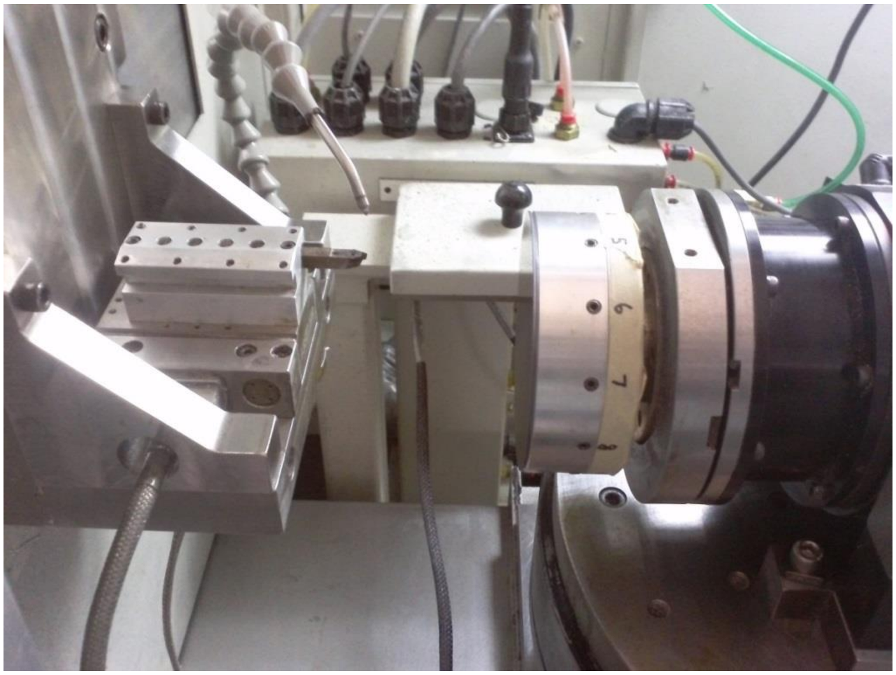

Figure 4.4 Fixture Installed in Precitech Ultraprecision Machining Center

The new fixture also places the tool and workpiece in a different orientation with respect to the machine axes. The machine X and Z axis now correspond with the feed and thrust direction of the tool, respectively.

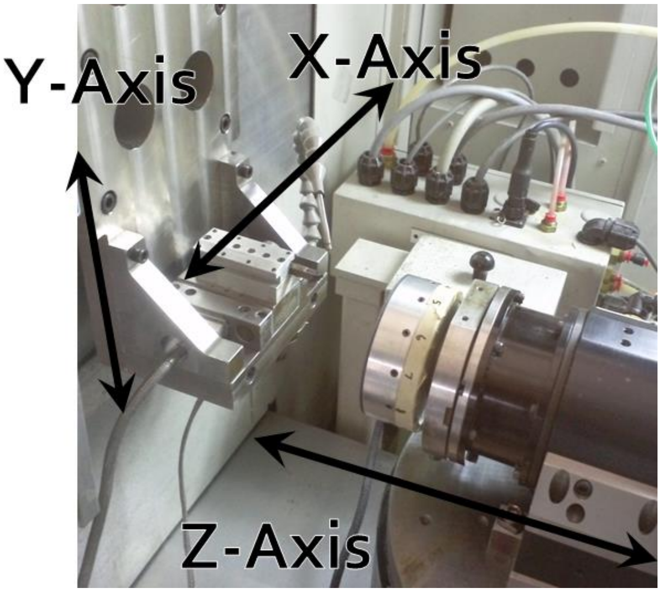

Figure 4.5 Machine Axes with New Tool-Holding Fixture

4.2 Fixture Modal Test

A modal test was used to determine the natural frequencies of vibration in the structure. By instrumenting a structure with accelerometers and using an instrumented hammer to give an impact force and analyzing the input to the output signals from the instruments, one can determine the natural frequency, dynamic stiffness and mass of the system.

4.2.1 Modal Test Procedure

The new fixture was tested while it was mounted on the Precitech machine tool to test its vibration characteristics. Fixture stiffness is important in the thrust direction of the tool as reduced vibration here will decrease form and surface finish errors. The instruments used in this experiment are listed below in Table 4.1.

Table 4.1 Equipment Used for Fixture Modal Test

Instrument Type	Model
Force Hammer	Kistler 9726A5000
Force Hammer	PCB Piezotronics 086B01
Accelerometer	Kistler 8730A500M1
Data Acquisition	National Instruments NI 9234
Data Acquisition to USB Interface	National Instruments NI cDAQ 9172

The fixtures were instrumented with an accelerometer on the front flat surface of the tool holder. The PCB Piezotronics force hammer was struck in-plane to the front of the fixture. This smaller hammer is suited to exciting smaller structures. Five taps were used for each test, with the results analyzed by the MalTF software included with CutPro 9. Both fixtures were tested three times. The data acquisition system and CutPro software was used to determine the natural frequency, dynamic stiffness and damping ratio of the fixtures.

4.2.2 Modal Test Signal Coherence

The coherence graphs in Figure 4.6 and Figure 4.7 represents the relationship between the input signal from the force hammer to the output signal sensed by the accelerometer for unmodified and modified fixtures respectively. It was used to determine the accuracy of the result. In this study, only frequencies found with signal coherence higher than 0.8 were considered valid. Three measurements were done on each setup conditions. Coherence was reasonably good (generally above 0.8) for all three sets of measurements in the 200Hz to 1000Hz frequency range. Coherence at this level in this frequency range is justified, since the natural frequency of the fixture was within this range.

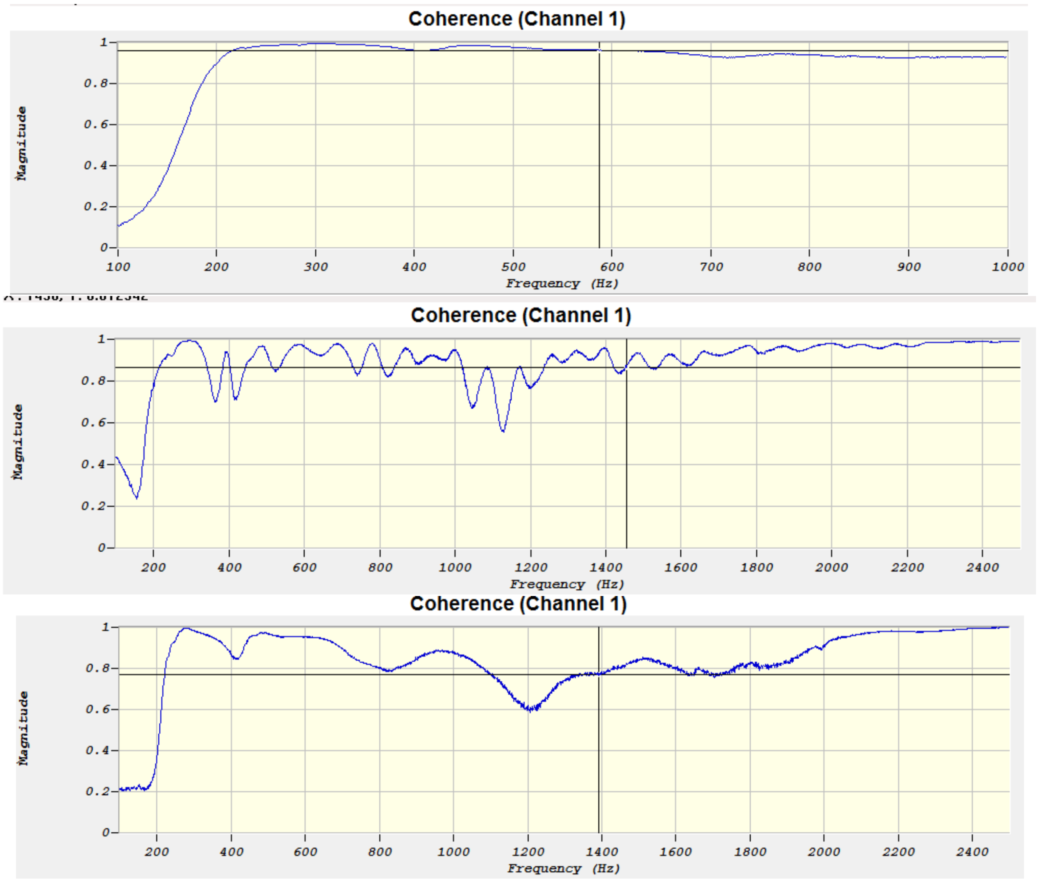

Figure 4.6 Signal Coherence for Tests 1, 2, 3 on Unmodified Tool-Holding Fixture

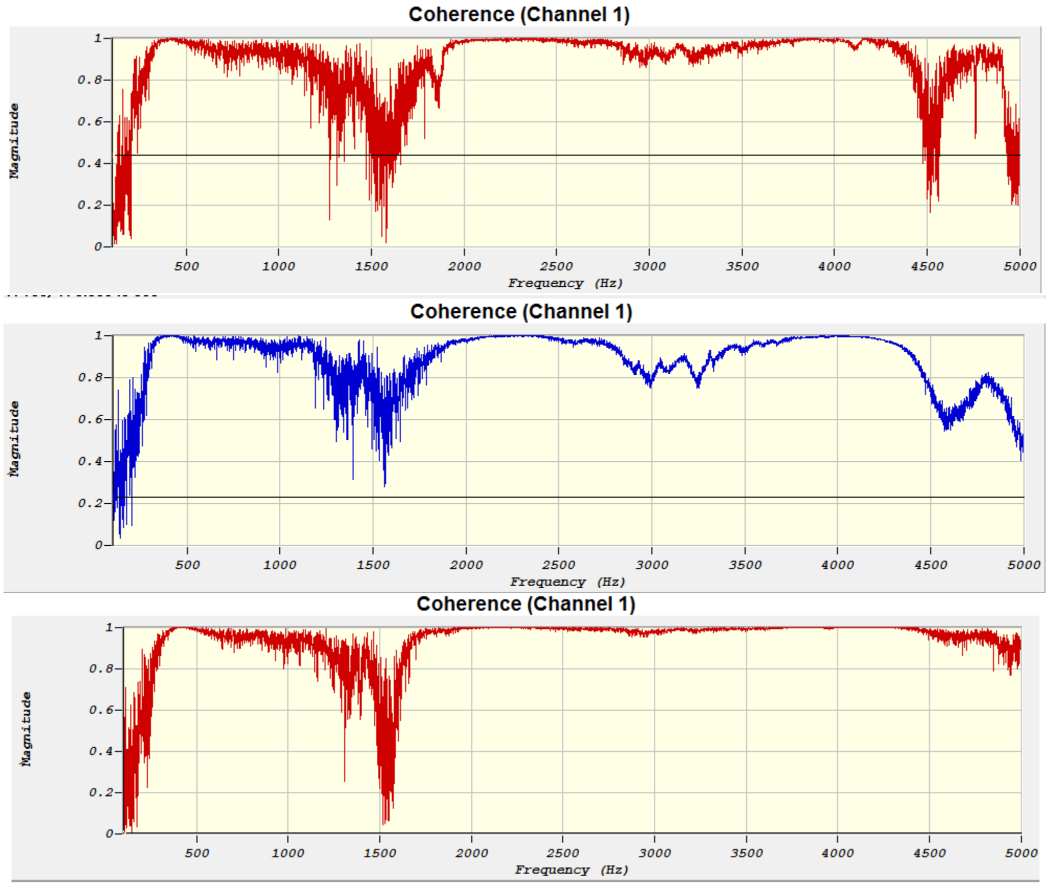

Figure 4.7 Signal Coherence for Tests 1, 2, 3 on Modified Tool-Holding Fixture

4.2.3 Modal Test Frequency Response Function (FRF) and Results

The accelerometer and force hammer signals are processed using the included MalTF software to produce a frequency response function (FRF) of the tested system. The program then identifies the modes of vibration. The identified frequencies were referred back to the signal coherence graphs to ensure that the coherence is above 0.8 at that particular frequency. The modal test results are tabulated in Table 4.2 and Table 4.3 for both set of tests suggesting that the natural frequencies lie in the range of 200Hz to 450Hz.

Table 4.2 Modal Test Results of Tool-Holding Fixture, Before Modifications

	Natural Frequency (Hz)	Dynamic Stiffness (N/µm)	Damping Ratio (%)
Test 1	279.2965	6.8519	5.276
Test 2	279.6869	8.9923	4.266
Test 3	279.8092	8.6149	4.400
Average	279.5975	8.1530	4.647

Table 4.3 Modal Test Results of Modified Tool-Holding Fixture

	Natural Frequency (Hz)	Dynamic Stiffness (N/µm)	Damping Ratio (%)
Test 1	408.0913	80.488	4.670
Test 2	399.5783	80.018	5.640
Test 3	419.8525	90.372	4.198
Average	409.1740	83.626	4.836

The result of the modification was that the new fixture has a much higher stiffness and higher natural frequency. This will be advantageous in reducing vibration amplitude in the machine. A face turning, cutting test was performed at a spindle speed of 1000RPM, feed rate of 5µm/rev, and a depth of cut of 2µm. The surface finish was measured using the Zygo white-light interferometer (WLI) at 200X magnification. The same 0.5mm nose radius tool was used for both tests. Zygo WLI screenshot of the generated surfaces are shown for an unmodified setup in Figure 4.8 and for a modified setup in Figure 4.9.

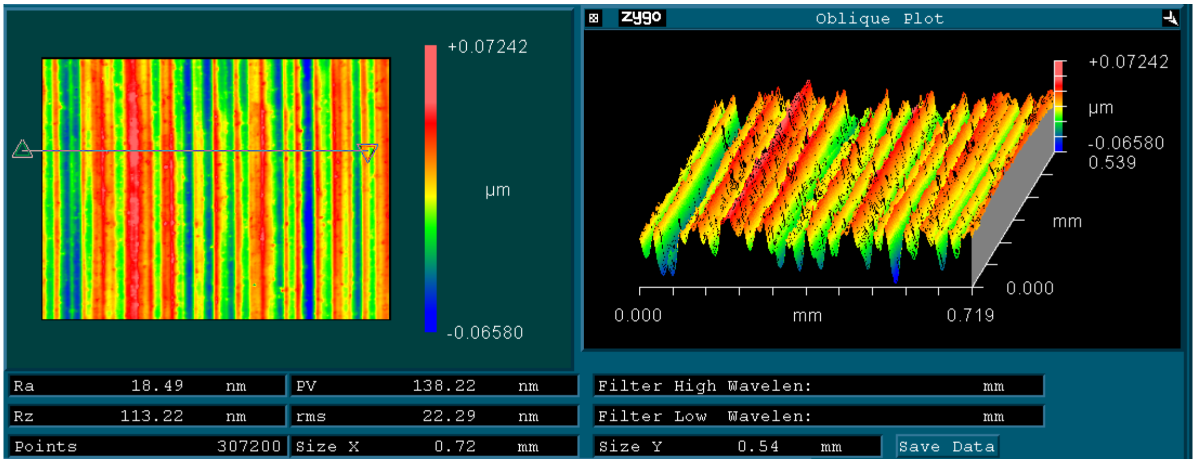

```
Ra      18.49   nm   PV      138.22   nm   Filter High Wavelen:        mm
Rz     113.22   nm   rms      22.29   nm   Filter Low  Wavelen:        mm
Points     307200    Size X    0.72   mm   Size Y     0.54    mm
```

Figure 4.8 Surface Roughness of Commercial 6061 Workpiece, Machined Using Unmodified Setup, 200X Magnification

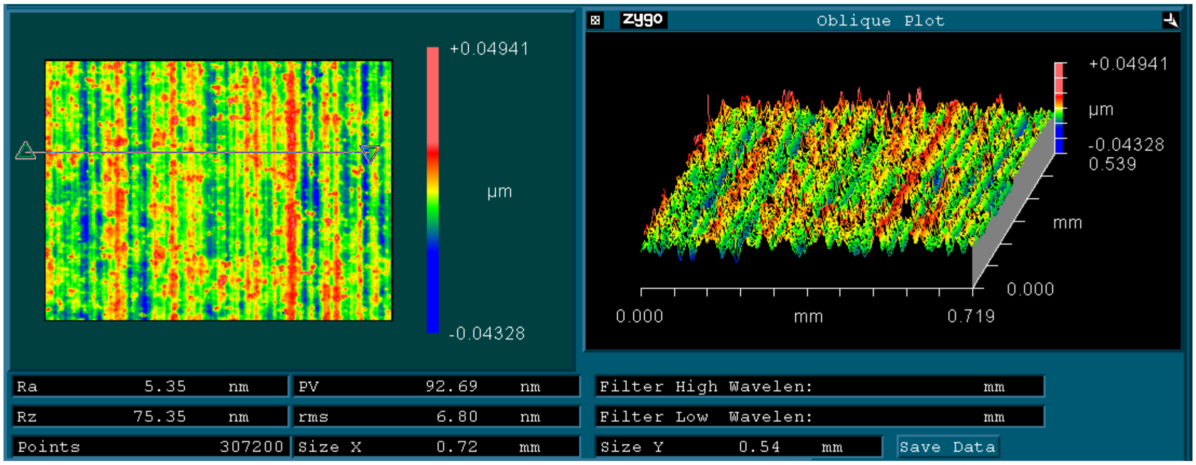

Ra 5.35 nm
PV 92.69 nm
Filter High Wavelen: mm
Rz 75.35 nm
rms 6.80 nm
Filter Low Wavelen: mm
Points 307200
Size X 0.72 mm
Size Y 0.54 mm

Figure 4.9 Surface Roughness of Commercial 6061 Workpiece, Machined Using Modified Setup, 200X Magnification

The changed setup allowed the machining of much better surface (*PV* area improvement by 33%; *PV* line improvement by 50%) finish on an ordinary commercial aluminum 6061 sample. The results are summarized in Table 4.4.

Table 4.4 Comparison Of Surface Roughness Profile From Change in Machine Setup

Machine Setup	Arithmetic Mean $_{\text{Area}}$, R_a (nm)	Peak-To-Valley $_{\text{Area}}$, PV (nm)
Unmodified	18.49	138.22
Modified	5.35	92.69

Chapter 5. Experimental Results and Discussion

5.1 Effect of Edge Preparation in Diamond Turning

When the uncut chip thickness is low, such as those used in SPDT, the size effect begins to affect the surface roughness of the workpiece. The size effect affects both the material microstructure from the apparent cutting edge radius.

Typically, in SPDT, round nosed (R_n) tools are used as they can be used to create many types of geometries. When cutting a plano surface, the tool leaves behind scalloped tool marks. Due to the shape of the tool, the uncut chip thickness changes across the tool. Figure 5.1 shows the cross section of the chip's cross section over the tool rake face.

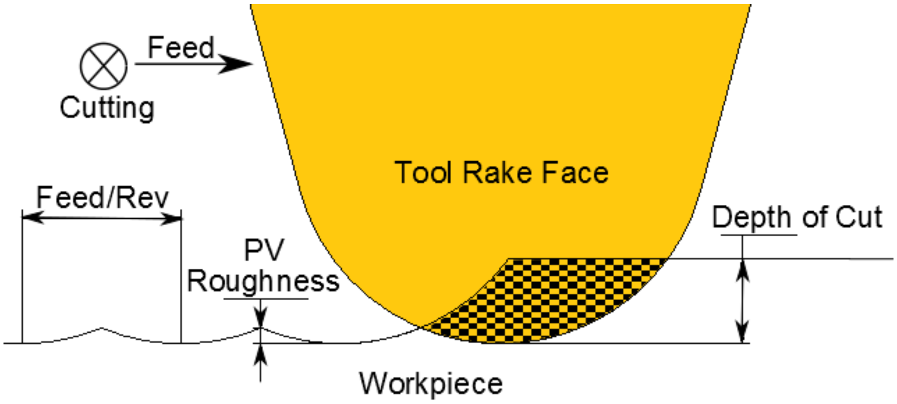

Figure 5.1 Profile of Uncut Chip in SPDT

The uncut chip thickness is nearly zero at the edge of the tool profile, where the finished surface is generated. When the uncut chip thickness is small, the tool can no longer be assumed to be perfectly sharp. The cutting edge of the diamond tool is on the order of 50nm and thus acts like a rounded tool [64]. Figure 5.2 shows a tool that normally has a 0 degree rake angle, but due to the small uncut chip thickness, the effective rake angle (R_c) is negative. There are many mathematical models available to model the chip formation of the tool as it passes through the workpiece to remove material, such as the Merchant's Circle and the Lee-Shaffer model [65]. These models serve as reasonable approximations in conventional machining, but are not accurate in SPDT as these models assume that the tools are perfectly sharp. An exaggerated schematic of the tool-chip contact zone is shown in Figure 5.1 where the chip section is higher near the free surface and essentially zero near the trailing edge of the tool. The effective rake angle will be not be constant across the entire cutting edge. It will be negative near the trailing edge which will cause a higher thrust force as shown in Figure 5.2.

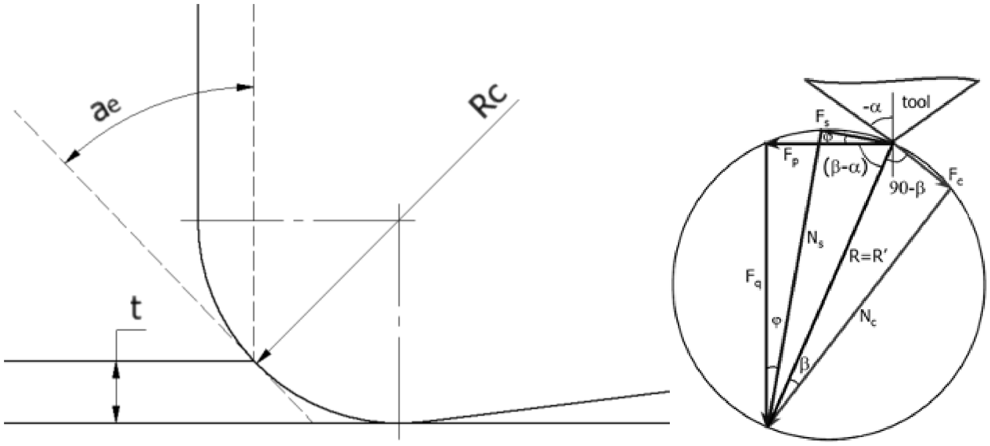

Figure 5.2 Changes in Tool Thrust and Cutting Force Due to Effective Rake Angle for Small Uncut chip Thickness

The small uncut chip thickness, now smaller than the average grain size on some regions of the tool, is now effectively cutting through single crystals, ideal material. This can be seen in Figure 5.3, where section b of the tool is effectively cutting through single crystals of material, while section e is not.

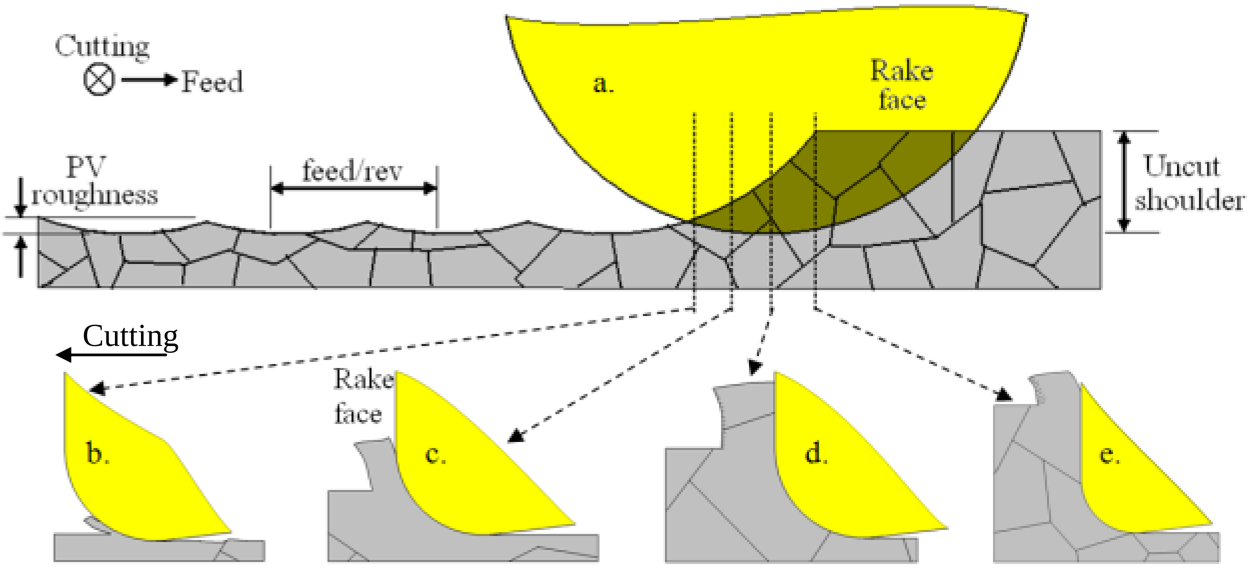

Figure 5.3 Change In Cutting Behavior Across Tool Face [2] [After Tauhiduzzaman et al. (2011)]

In machining, there is a minimum chip thickness that determines whether or not a tool will remove material from a workpiece. If the chip thickness is smaller than the minimum chip thickness criterion, the tool will cause the ploughing of material on the surface of the workpiece rather than shearing and material removal. The minimum chip thickness criterion was first proposed by Sokolowski in 1955 [66]. The value of the minimum chip thickness depends on the radius of the cutting edge, cutting speed, and machine system stiffness. In a series of hard turning tests, Kishawy and Elbestawi (1999) [67] observed that the material is plastically deformed instead of being cut and removed, and is pushed out to the secondary edge of the tool. This phenomenon is known as plastic side flow or ploughing, and occurs opposite to the feed direction. The build-up of material causes an increase in surface roughness in SPDT, called plastic side flow induced roughness [Figure 5.4].

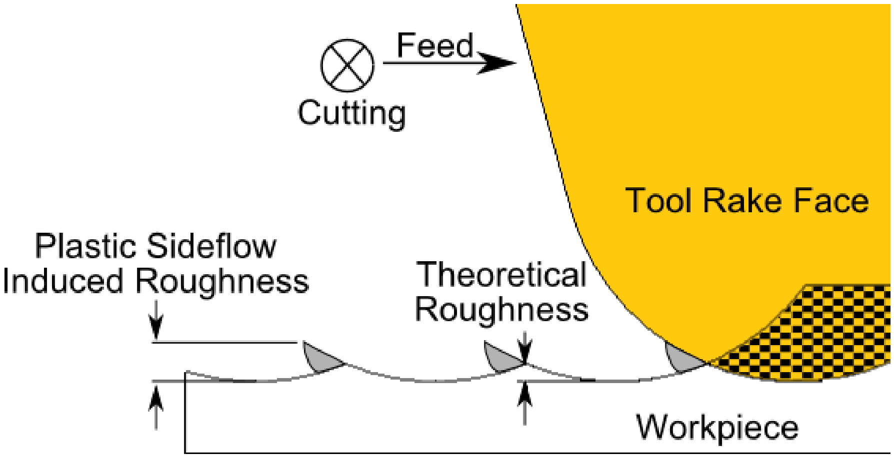

Figure 5.4 Figure Showing Plastic Sideflow Induced Roughness [68] (Adapted After Liu, Melkote et al., 2006)

The plastic side flow is caused by the edge of the tool that generates the new surface, caused by the uncut chip thickness being smaller than the minimum chip thickness. This can be seen in Figure 5.3, where sections b and c are cutting through single grains of the polycrystalline workpiece material. The severity of plastic side flow can be minimized by limiting the amount of ploughing that occurs. This can be done by changing the tool geometry, such that the uncut chip cross section limits the area that is below the minimum chip thickness. Liu et al. [69] built an analytical model for the prediction of minimum chip thickness in micromachining, and validated this with cutting tests using carbon steel and aluminum. They found that the criterion for transitioning from ploughing to microcutting is dependent on the effective flow stress generated during cutting and the shear strength of the adhesive junction at the chip-to-tool interface. The shear flow stress is dependent on the strain, strain rate, and temperature difference between room and chip interface. The shear strength of the adhesive junction at the chip-to-tool interface is dependent on several material properties, such as latent heat of melting and melting point of the material.

Tauhiduzzaman [2] and Kishawy et al. [67] observed that plastic side flow can be detected by observing the chips from the machining processes in diamond turning and hard turning processes, respectively. Plastic side flow is characterized by chips having the appearance of a serrated edge. Figure 5.5 represents the chips generated by a 1.5mm nose radius tool while machining 99.87% cold rolled aluminum. It is clear from this figure that a sharp tool produces less edge serration while a worn tool results in severe edge serration due to more edge rounding and size dependent effects.

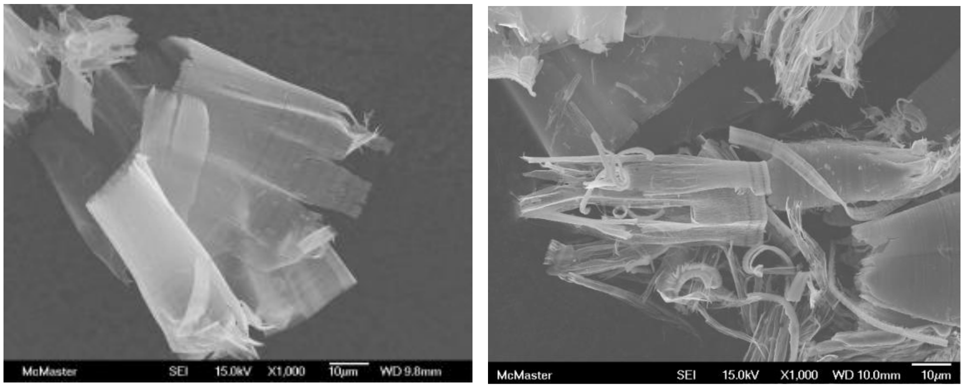

Figure 5.5 Chip Serration Due to Chip Thinning Using a 1.5mm Nose Radius Tool; left: new tool, right: worn tool

Two tools were used to compare the effect of a rounded cutting edge. Both of these tools are single crystal diamond (SCD) tools with a 12mm nose radius. One has been treated chemically to round the cutting edge, while another tool has not been modified.

These tools were both tested in a face turning operation. From Merchant’s circle, a tool with a larger negative rake angle is expected to have a higher thrust force during machining, all other factors being equal. A cutting tool at low depths of cut cannot be assumed to be perfectly sharp. This creates an effectively negative rake angle. The honed tool with its larger cutting edge radius should have a more negative effective rake angle. This statement is schematically shown in Figure 5.6 to aid in understanding.

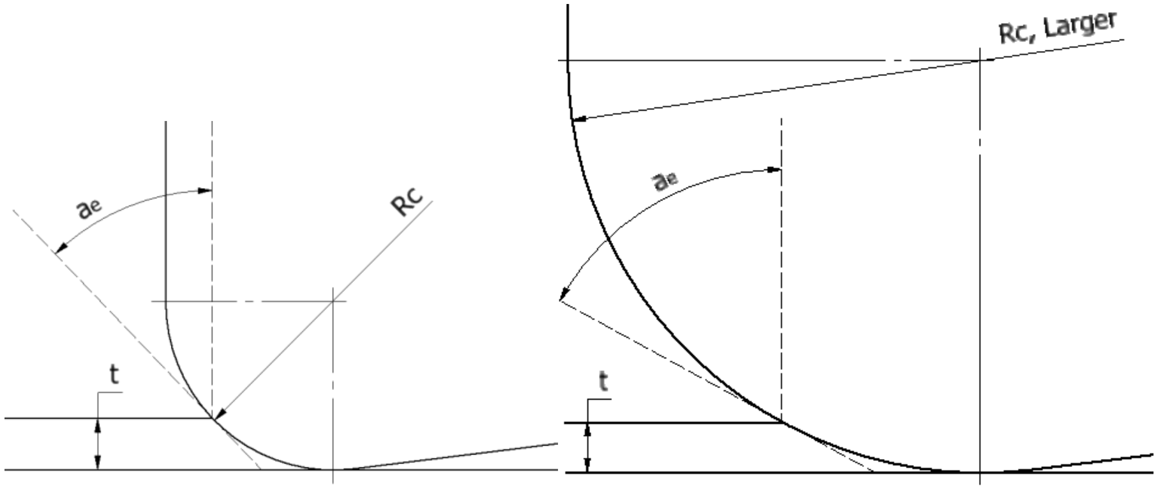

Figure 5.6 Change in Effective Rake Angle for Blunt Tool in SPDT

As a cutting tool is used, its cutting edge erodes and the cutting edge radius becomes larger during the wear-in period. This wear-in period erodes the tool, potentially causing subsurface damage and possibly shortening the lifetime of the tool. By using a chemical etching process, one can chemically erode the tool edge to simulate the break-in period without undergoing plastic deformation or chipping. This can cause reduced tool life due to subsurface damage and unfavorable residual stresses in the tool substrate.

5.1.1 Workpiece Material Selection

One of the most common materials used in SPDT products are aluminum alloys. Tauhiduzzaman [2] performed many cutting tests and material analysis studies to determine which factors in an aluminum alloy will make it best suited for SPDT. They concluded that a 99.9% pure aluminum workpiece with a fine microstructure produced the best surface finish when compared to all other workpieces. 99.9% pure aluminum is impractical for industrial uses, as it is easily scratched and has very poor mechanical properties. Instead, for higher tensile strength, hardness, and lower cost, aluminum 6061 alloys are more commonly used. These alloys, unlike commercially pure aluminum billets, contain alloying hard particles that can be pulled out, dragged, or smeared on the surface causing surface defects. Figure 5.7 and Figure 5.8 shows examples of voids and dragged particles due to imperfections in the RSA-6061 material.

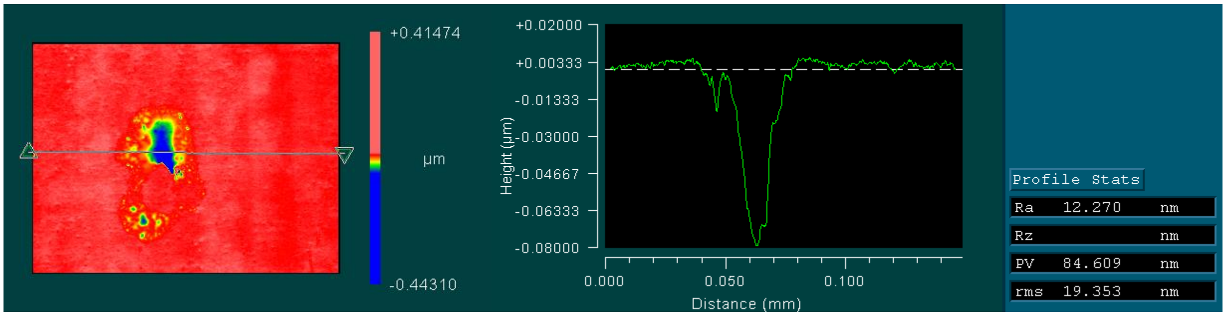

Profile Stats
Ra 12.270 nm
Rz nm
PV 84.609 nm
rms 19.353 nm

Figure 5.7 Example of a Pull-Out of Alloying Particle in RSA-6061Aluminum Workpiece

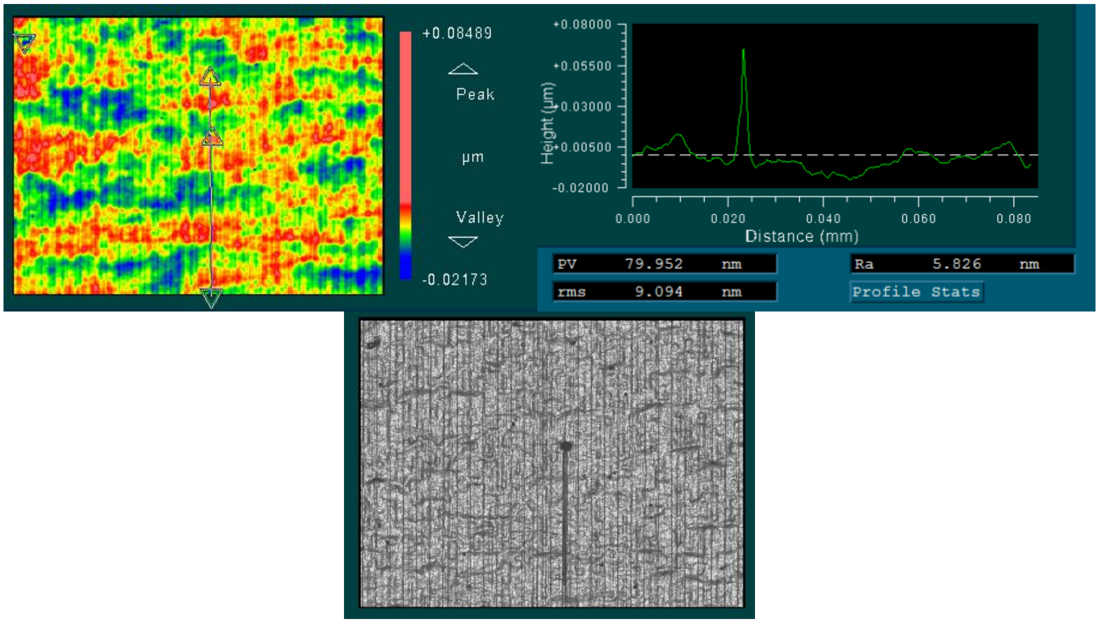

PV 79.952 nm
rms 9.094 nm
Ra 5.826 nm
Profile Stats

Figure 5.8 Example of a Dragged Alloying Particle in RSA 6061 Aluminum Workpiece

If a 99.9% pure aluminum sample can be made more suitable for diamond turning by refining the grain structure, then a similar trend should exist for Aluminum-6061. A cylindrical bar of commercially available Al-6061 alloy was procured and annealed in a furnace to return the bar to a known state. The bar was annealed as its condition, strain hardening characteristics, and exact heat treatment of the commercially available alloy was unknown. The oven was set to heat the aluminum sample at 775°F (413°C) for 2 hours. Then, the oven cooled at 10°F/hour (approximately 5.6°C/hour) until it had reached 500°C (260°C). Afterwards, the oven was shut off and the sample was left to be air cooled until it has reached ambient temperature.

When the material being cut has an uncut chip thickness on the micrometer scale, the mechanisms that cause it to shear are in the nanometer scale. The probability that the cutting tool will encounter a void, dislocation, or defect in the workpiece is decreased. Otherwise, there is more probability that the tool will not cut and plough through material instead. Ploughed material that is not removed is deformed instead, causing material swelling and spring-back. Increasing the density of defects in the material, such as by strain hardening, can help mitigate this effect.

Grain boundaries typically slow, or even stop the movement of dislocations from travelling through a material, effectively increasing its tensile strength. This accumulation of dislocations and defects moving towards the grain boundary hardens it, increasing its coefficient of friction when a nano-scratch test was performed, discovered by Kim et al. [70]. When a material is strain hardened, the dislocation density increases and the grain shape changes. During diamond turning, when the tool encounters a grain boundary, there is a higher probability that there will be dislocations on the opposite side of the grain boundary, allowing cutting to take place. Figure 5.9 shows an example of surface roughness due to grain boundary induced roughness, caused by anisotropy of the individual grains of material. However, such grain boundary induced roughness was not observed while machining RSA alloy as shown in Figure 5.11.

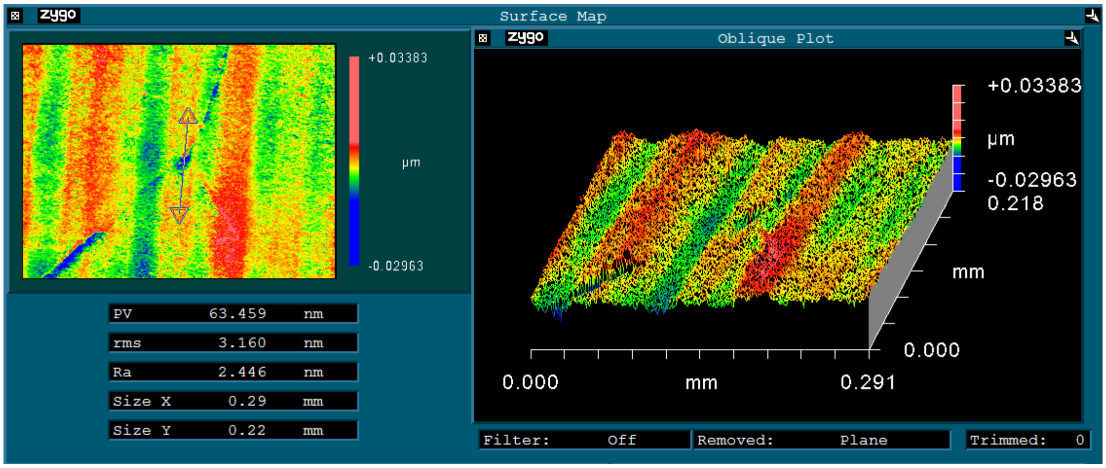

PV 63.459 nm
rms 3.160 nm
Ra 2.446 nm
Size X 0.29 mm
Size Y 0.22 mm

Filter: Off
Removed: Plane
Trimmed: 0

Figure 5.9 Example of Grain Boundary Induced Roughness, in 54% Cold Rolled 99.9% Pure Aluminum (500X Magnification)

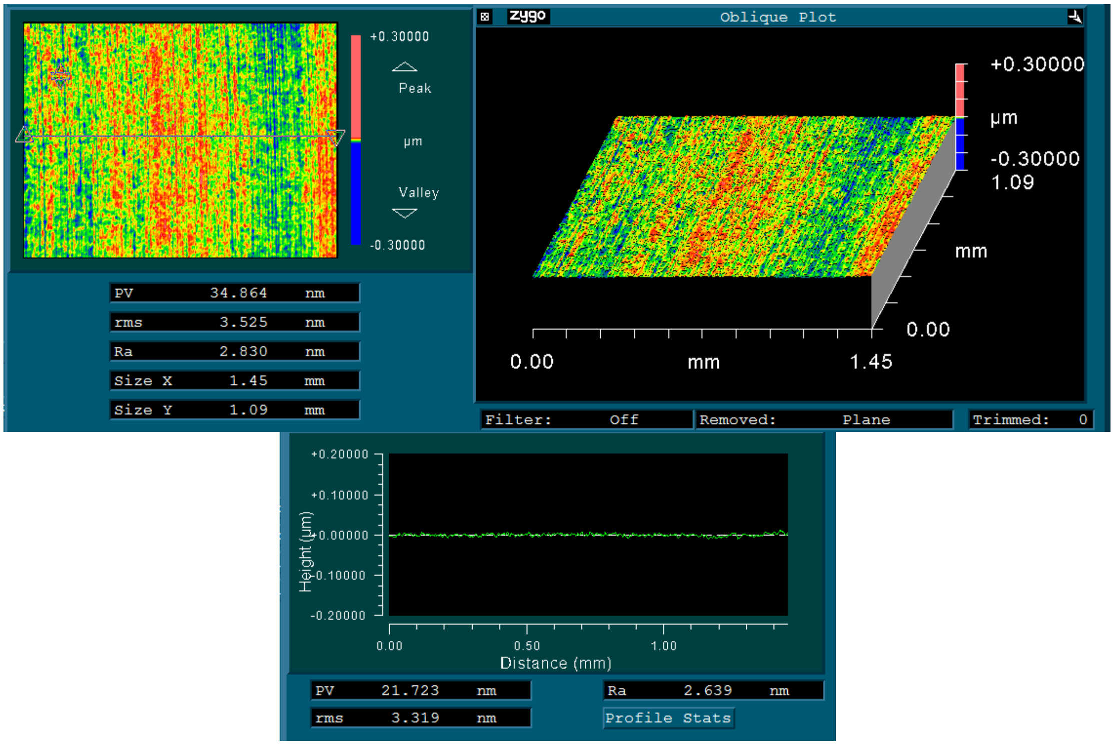

PV 34.864 nm
rms 3.525 nm
Ra 2.830 nm
Size X 1.45 mm
Size Y 1.09 mm

Filter: Off
Removed: Plane
Trimmed: 0

PV 21.723 nm
rms 3.319 nm
Ra 2.639 nm
Profile Stats

Figure 5.10 Interferometer Scan of Machined Surface, Rapidly Solidified Aluminum 6061, 100X Magnification

Materials can be cold rolled in order to strain harden it. Three samples were cold rolled using a cold rolling mill. Samples were cold rolled to 32%, 50%, and 76% reduction of thickness. One sample was subjected to friction stir processing. A simple cutting test was performed on these samples using the original, unmodified machine setup (See 0 for details). An SCD tool with 0.5mm nose radius was used, cutting with a spindle speed of 1000RPM, feed rate of 1µm/rev, and a depth of cut of 2µm. After cutting, the machined surface was inspected using a white light interferometer. The materials that are expected to have the best surface finish are the materials with the highest dislocation density and smallest average grain size.

The resulting surfaces, shown in Figure 5.11 to Figure 5.15 vary by a high amount in terms of roughness, this is consistent with severe scratching. The FSP alloy showed a better surface finish when compared to the other samples as summarized in Table 5.1.

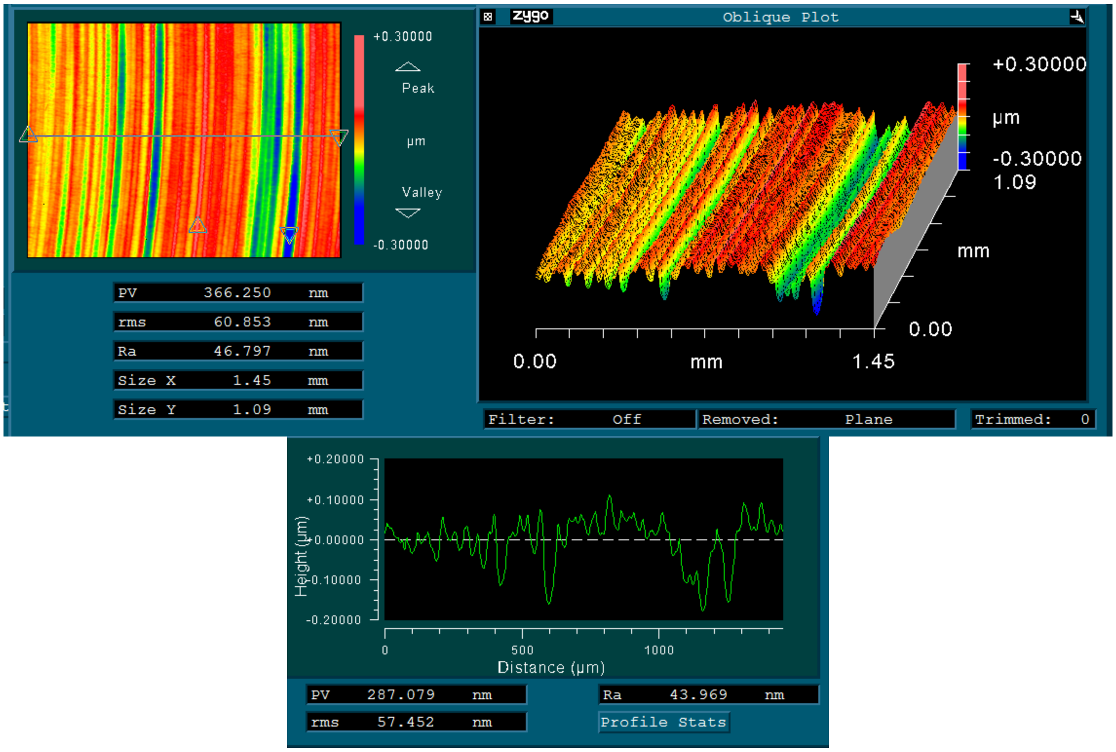

PV 366.250 nm
rms 60.853 nm
Ra 46.797 nm
Size X 1.45 mm
Size Y 1.09 mm

Filter: Off
Removed: Plane
Trimmed: 0

PV 287.079 nm
rms 57.452 nm
Ra 43.969 nm

Figure 5.11 Interferometer Scan of Machined Surface, 32% Cold Rolled Aluminum 6061, 100X Magnification

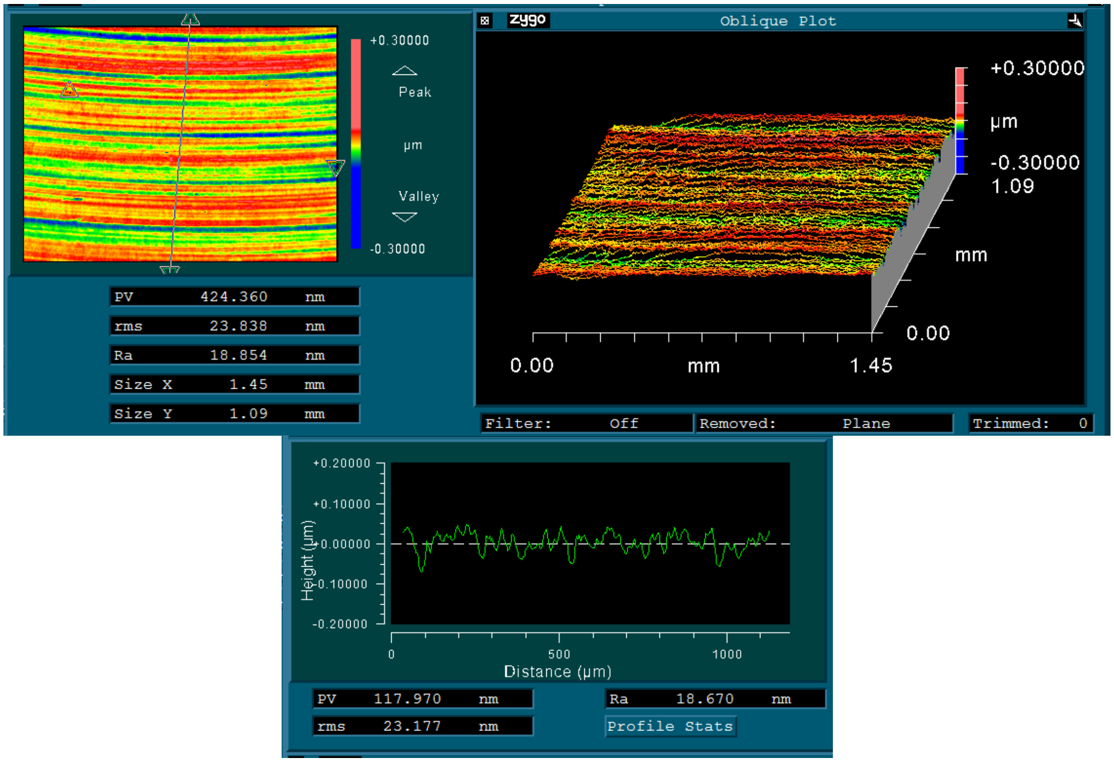

PV 424.360 nm
rms 23.838 nm
Ra 18.854 nm
Size X 1.45 mm
Size Y 1.09 mm

Filter: Off
Removed: Plane
Trimmed: 0

PV 117.970 nm
rms 23.177 nm
Ra 18.670 nm

Figure 5.12 Interferometer Scan of Machined Surface, 50% Cold Rolled Aluminum 6061, 100X Magnification

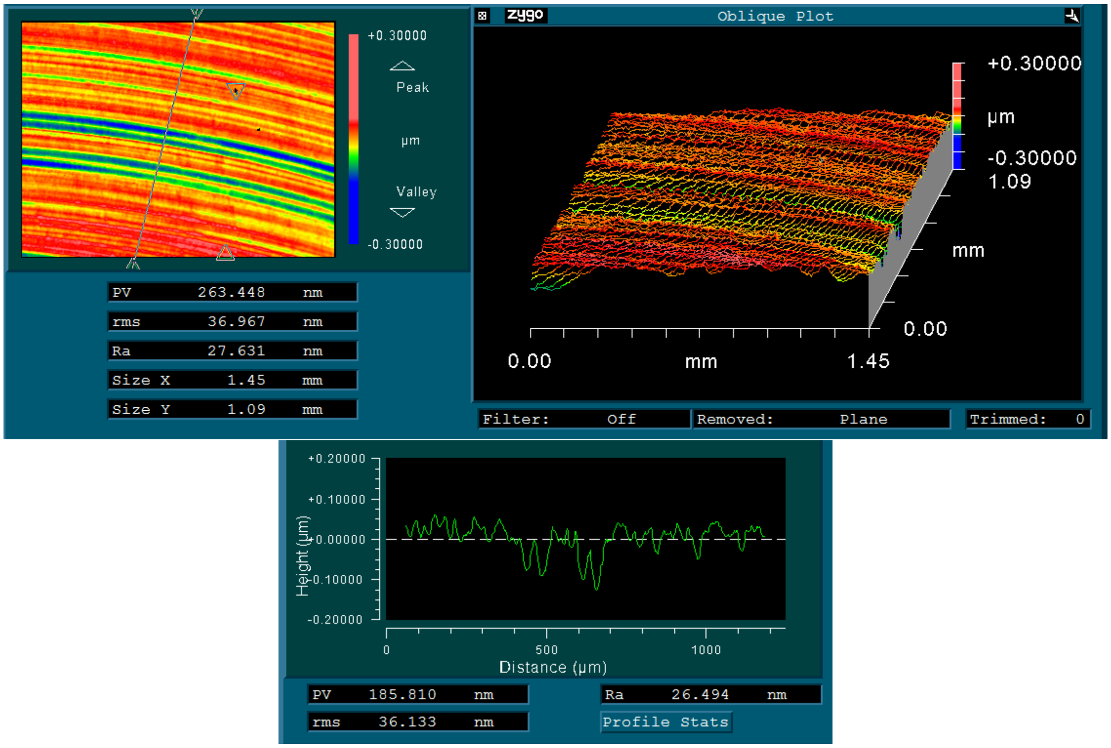

PV 263.448 nm
rms 36.967 nm
Ra 27.631 nm
Size X 1.45 mm
Size Y 1.09 mm

Filter: Off
Removed: Plane
Trimmed: 0

PV 185.810 nm
rms 36.133 nm
Ra 26.494 nm

Figure 5.13 Interferometer Scan of Machined Surface, 76% Cold Rolled Aluminum 6061, 100X Magnification

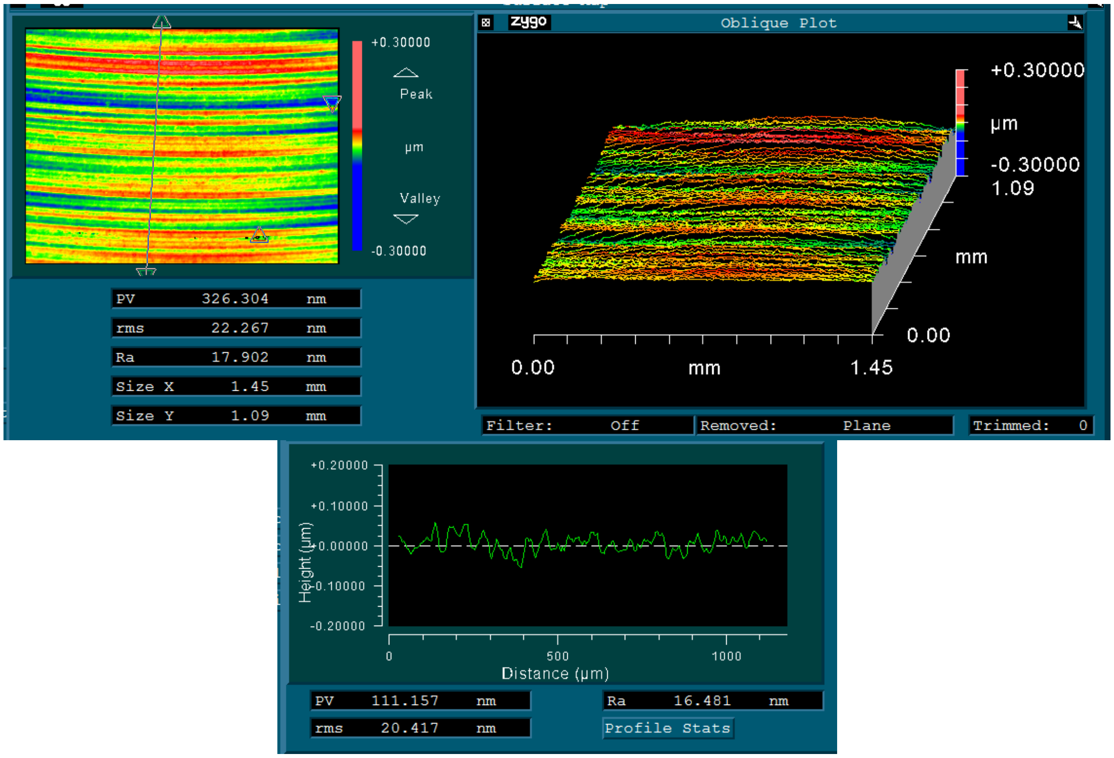

PV 326.304 nm
rms 22.267 nm
Ra 17.902 nm
Size X 1.45 mm
Size Y 1.09 mm

Filter: Off
Removed: Plane
Trimmed: 0

PV 111.157 nm
rms 20.417 nm
Ra 16.481 nm

Figure 5.14 Interferometer Scan of Machined Surface, Annealed Aluminum 6061, 100X Magnification

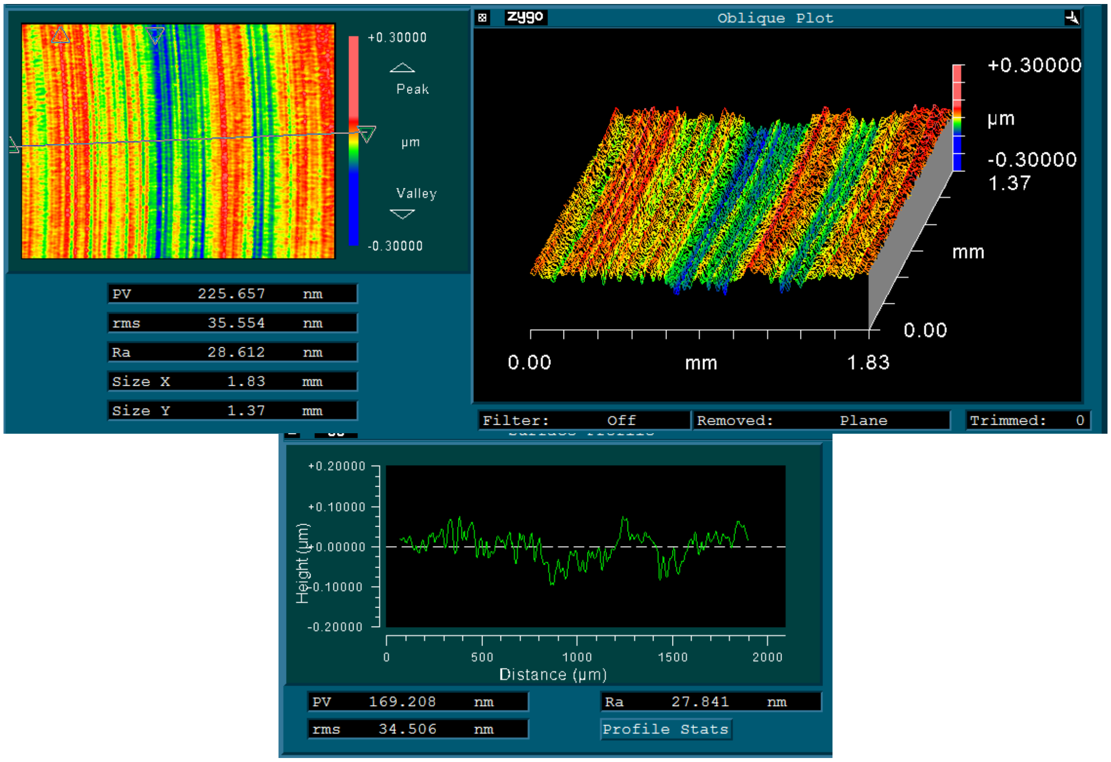

PV 225.657 nm
rms 35.554 nm
Ra 28.612 nm
Size X 1.83 mm
Size Y 1.37 mm

Filter: Off
Removed: Plane
Trimmed: 0

PV 169.208 nm
rms 34.506 nm
Ra 27.841 nm

Figure 5.15 Interferometer Scan of Machined Surface, Friction Stir Processed Aluminum 6061, 100X Magnification

Table 5.1 Summary of Cutting Test Results For Different Materials in SPDT

Aluminum 6061 Alloy Condition	Line PV (nm)	Line R_a (nm)
32% Cold Rolled	287.079	43.969
50% Cold Rolled	117.970	18.670
76% Cold Rolled	185.810	26.494
Friction Stir Processed	169.208	27.841
Annealed	111.157	16.481

5.1.2 Measurement of Cutting Edge Radius

In order to properly study the effect of edge preparation on an SCD tool, the cutting edge must be measured before the cutting test. The sharpness of the tool must be known, as well as the effect of the chemical etching process. A 3D laser confocal microscope, the Olympus OLS4000 LEXT was used to scan the tools before and after cutting. Figure 5.16 and Figure 5.17 shows the measurement done on the fresh edge of two tools using this technique.

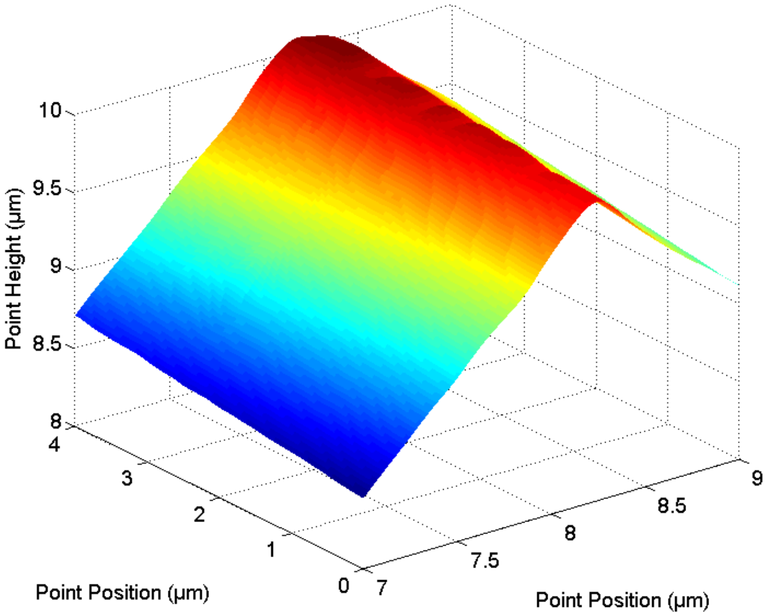

Figure 5.16 3D Confocal Laser Scan of Unmodified Tool, New

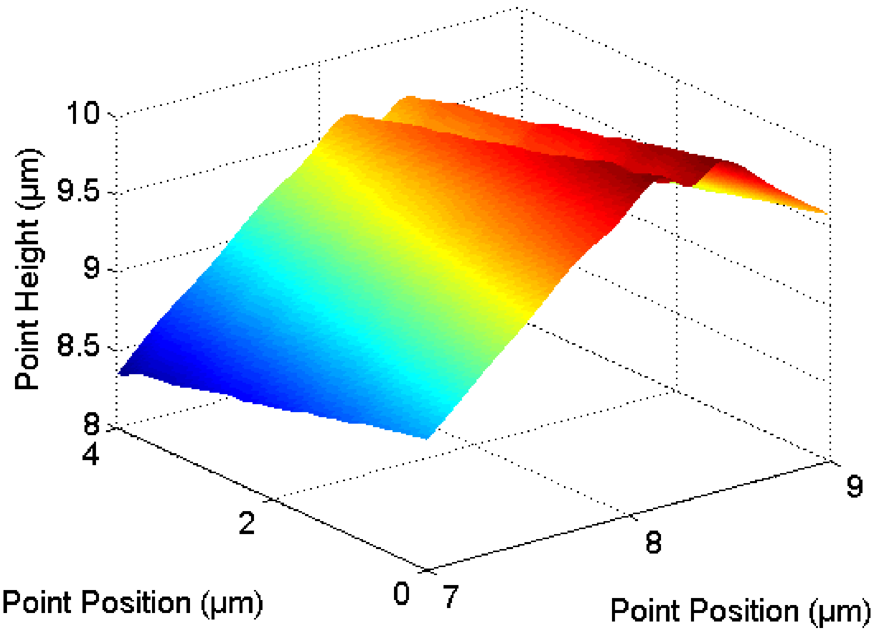

Figure 5.17 3D Confocal Laser Scan of Chemically Etched Tool, New

The output of the 3D confocal laser microscope is a point cloud with a pixel resolution of 15.625nm. To measure the cutting edge radius, a line across the cutting edge was taken out of the point cloud and plotted. Points were isolated from this selected line to make up the cutting edge. These points are carefully chosen as they must only be part of the cutting edge. The selected points on red color are shown in Figure 5.18 and Figure 5.19.

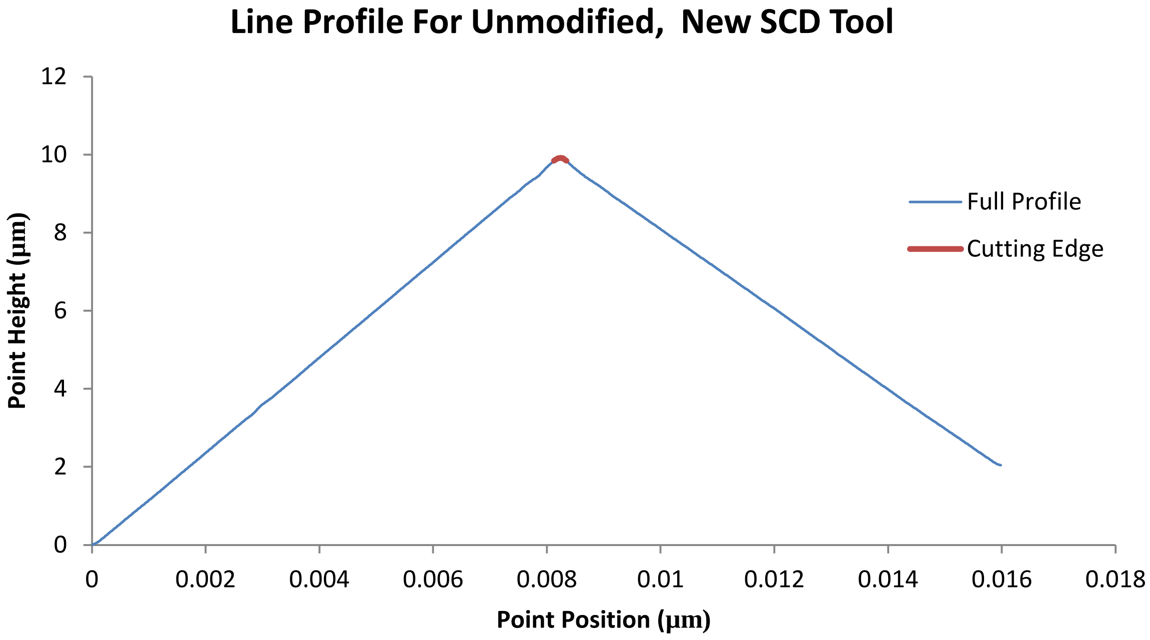

Figure 5.18 Line Profile For Unmodified, New SCD Tool

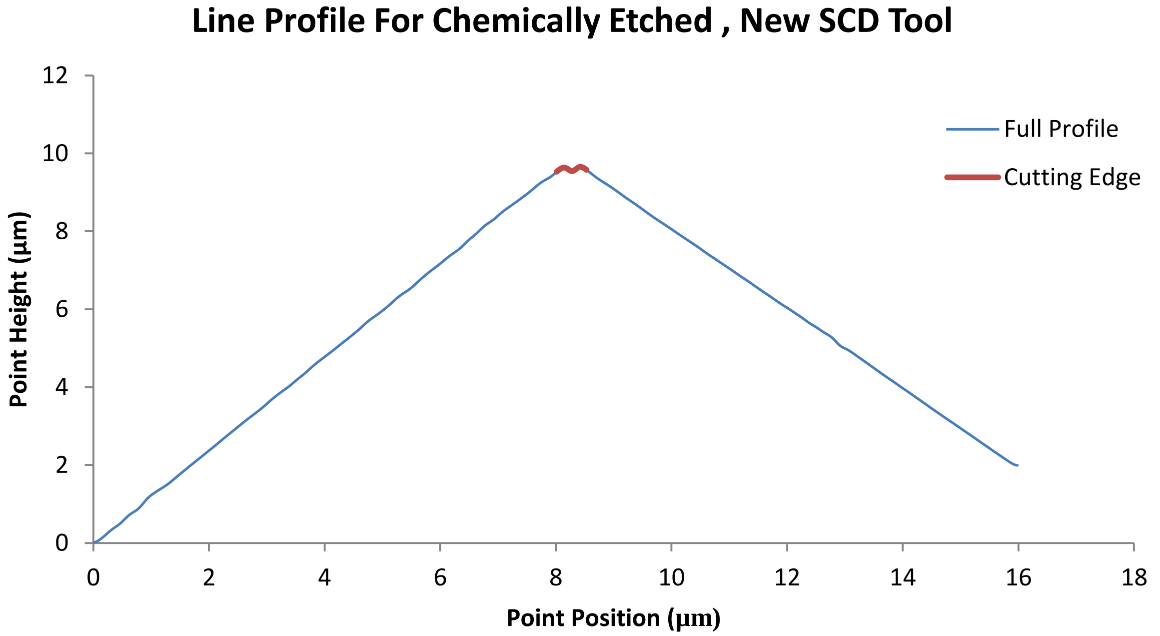

Figure 5.19 Line Profile For Chemically Etched, New SCD Tool

The microscope revealed that the sharp tool is in the expected range of radius of 50-100nm (Figure 5.20). The chemically etched tool did not have the expected edge preparation. Instead of eroding the edge and creating a rounded cutting edge, the chemical etching attacked the edge and created a step-like profile instead (Figure 5.21)The highlighted points were imported into a MATLAB circle-fitting program to determine the cutting edge radius. The circle fitting code was based on code from MATLAB Central, by Izhak Bucher [71].

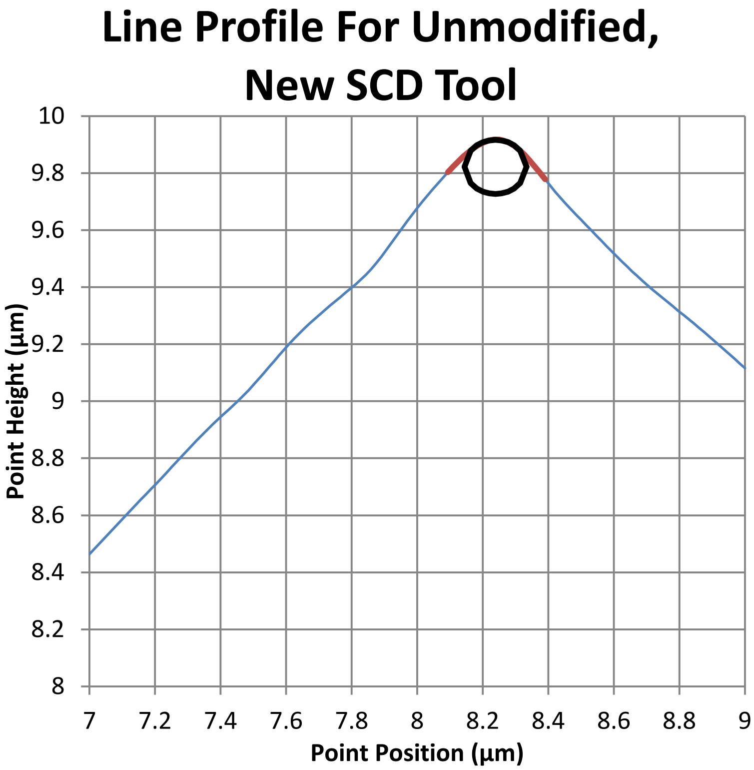

Figure 5.20 Circle Fit for Unmodified, New SCD Tool

The MATLAB code indicated that the cutting edge radius of the unmodified SCD tool was 94.8nm. The chemically etched tool had a cutting edge with a stepped profile. Fitting a circle to these points will not provide useful information. Figure 5.21 is presented below to show the stepped cutting edge in greater detail.

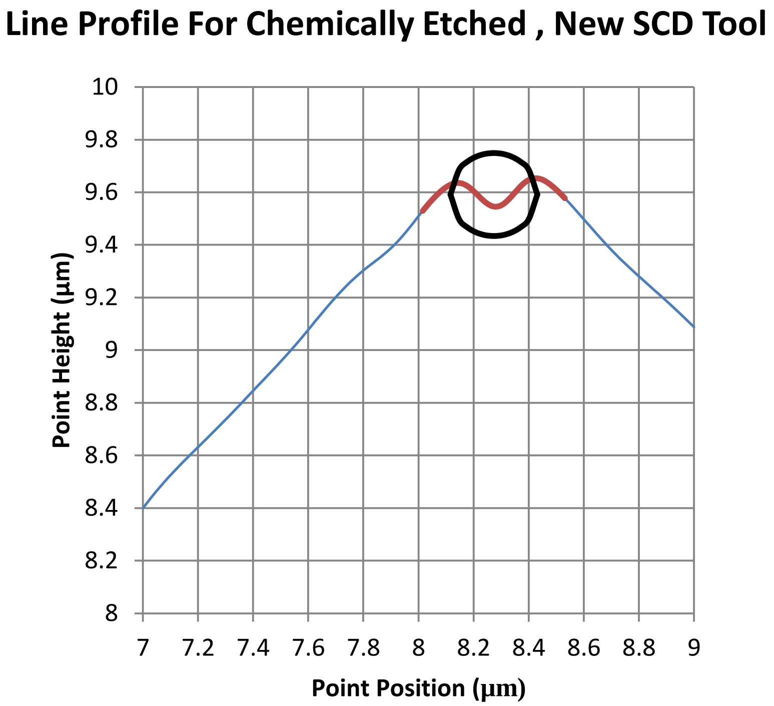

Figure 5.21 Circle Fit for Chemically Etched, New SCD Tool

Due to the stepped cutting edge profile of the chemically etched tool, it is difficult to judge which points will constituent the cutting edge. The cause for this stepped effect can possibly be due to the acid preferentially attacking areas with high residual stress and large surface area. In this case, the MATLAB circle-fitting code reported that the fitted circle has a radius of 157.6nm. Instead, one of the corners of the ‘cutting edge’ was isolated, and the cutting edge radius was fitted from those points as shown in Figure 5.22.

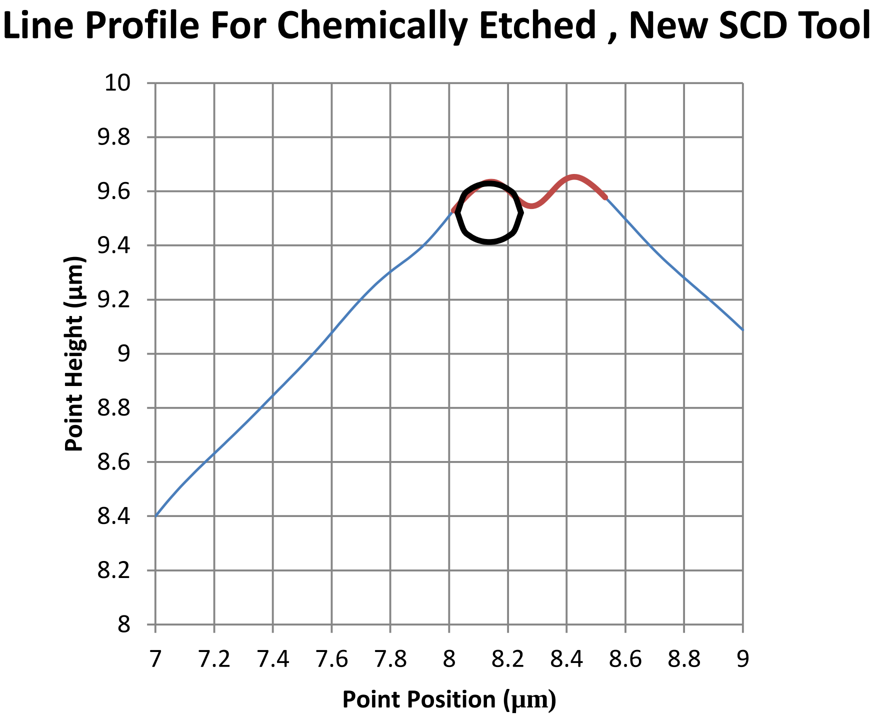

Figure 5.22 Circle Fit for Chemically Etched, New SCD Tool, Isolated Points

The cutting edge radius of part of the stepped edge of the chemically etched tool was 108.1nm. An example of the MATLAB code used here can be found in the appendix. All the measured edge radiuses of fresh, new tool edges are shown in

Table 5.2.

Table 5.2 Summary Of Cutting Edge Measurements, New Tool

SCD Tool	Cutting Edge Radius (nm)
Unmodified Tool	95
Chemically Etched Tool	158
Chemically Etched Tool, Partial Section	108

5.1.3 Cutting Test Results

A cutting test was performed with both tools in face turning, where the tool is assumed to trace an Archimedean spiral with equal spacing for each successive rotation. The cutting length can be calculated given the feed rate per revolution and the inner and outer diameter of the generated surface. The arc length of an Archimedean spiral is shown below in Equation 5.1, where the variable *f* is the spacing between each successive rotation of the spiral, and θ is the number of turns in the spiral in radians.

$$s(\theta) = 0.5\, f\, \left(\theta\sqrt{1+\theta^2} + \sinh^{-1}\theta\right)$$

Equation 5.1 Arc Length of Archimedean Spiral [72]

The number of turns in a generated surface, given its outer diameter can be found using the equation below. D_{outer} represents the outer diameter of the generated surface.

$$\theta = 2\pi * \left(\frac{D_{outer}}{f}\right)$$

Equation 5.2 Number of Turns in a Generated Circular Surface, in Radians

The workpiece used in this study is annular, as it contains a hole at its center. The cutting length is calculated by first finding the arc length of the surface generated based on the outer diameter, and subtracting the arc length of the surface left behind, based on the inner diameter of the generated surface.

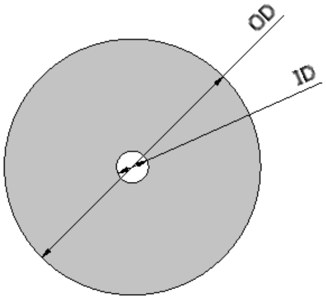

Figure 5.23 Annular Surface on Workpiece, with Inner and Outer Diameters

The cutting length is then calculated combining Equation 5.1 and Equation 5.2.

$$s(\theta)_{Tot} = s(\theta)_{OD} - s(\theta)_{ID}$$

Equation 5.3 Cutting Length of a Generated Surface in SPDT

Tool life is typically characterized by three stages; a break-in stage where surface finish and cutting forces vary, a stable region where cutting forces and surface finish is consistent, followed by catastrophic failure. This pattern is generally seen in conventional machining as well. The break-in period involves the breakdown of the fresh cutting edge by rounding the edge and eroding it.

The honed tool showed a much shorter break-in period than the unmodified tool as shown in Table 5.3. For reference, the cutting length of a flat, plano surface that is 60mm in diameter is approximately 2000m.

Table 5.3 Break-in Period of Honed and Unmodified SCD Tool

Tool	Cutting Length to Acceptable Finish (m)	Surface Finish (Peak-To-Valley, nm)	Approximate number of parts
Chemically Etched	13266.2	20.121	7
Unmodified	19912.1	17.81	10

The surface quality was measuring using the Zygo white-light interferometer. Surface quality was judged using the peak-to-valley, or PV taken from the scanned area. The chemically etched tool showed slightly better consistency in producing high quality surfaces. (

Table 5.4)

Table 5.4 Basic Statistics of Chemically Etched and Unmodified SCD Tool

Tool	Average PV (nm)	Variance of PV (nm)	Standard Deviation of PV (nm)
Chemically Etched	16.495	18.228	4.269
Unmodified	17.226	19.693	4.467

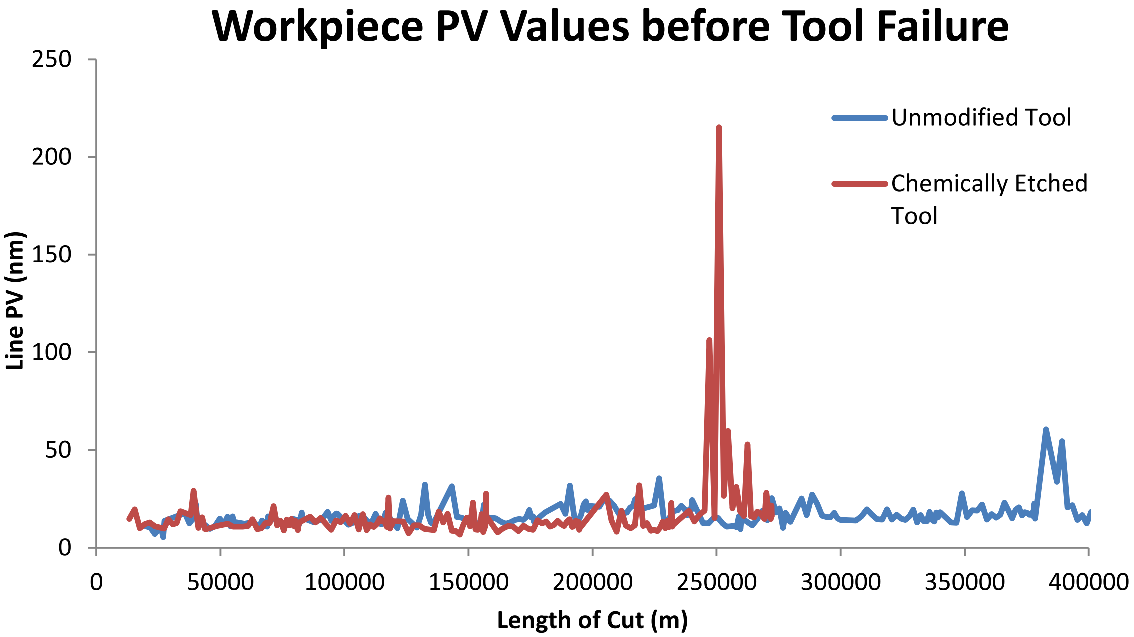

Figure 5.24 Peak-To-Valley Values for Generated Surfaces of Honed and Unmodified SCD Tool

The tools were considered to be worn once several parts exhibited a PV of over 50nm. It is difficult to categorize and determine when a tool is worn out. Visible light has an average wavelength of approximately 500nm [73]. The tool was considered to be worn once the PV reached 50nm, as it represents approximately one tenth of the wavelength of light. Although the tools returned to producing surfaces with acceptable PV after they were considered to be worn, they consistently generated unacceptable surfaces with deep scratch marks, producing an undesirable ‘rainbow-color’ or diffraction grated pattern on the part surface. An example of this type of defect is shown below in Figure 5.25.

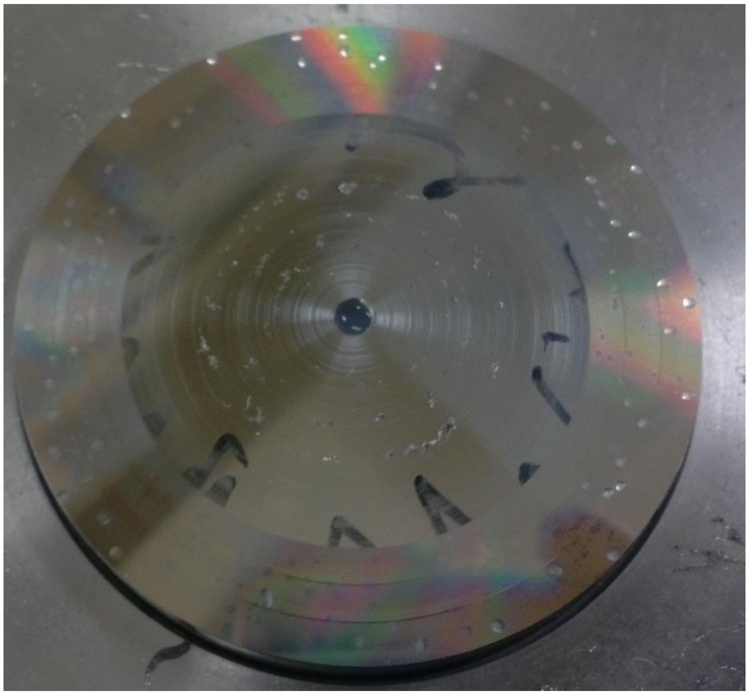

Figure 5.25 Example of Diffraction Grated Surface on Workpiece

The chemically etched tool has a much shorter tool life. This was attributed to the higher cutting forces in the thrust direction when compared to the unmodified tool, shown in Figure 5.26. The chemical honing creates a tool with a stepped cutting edge, increasing cutting forces and consequently, increasing the wear rate of the tool. Forces in the cutting direction of both tools were similar (Figure 5.27). However, the unmodified tool experienced a large increase in cutting force near the end of its useful life.

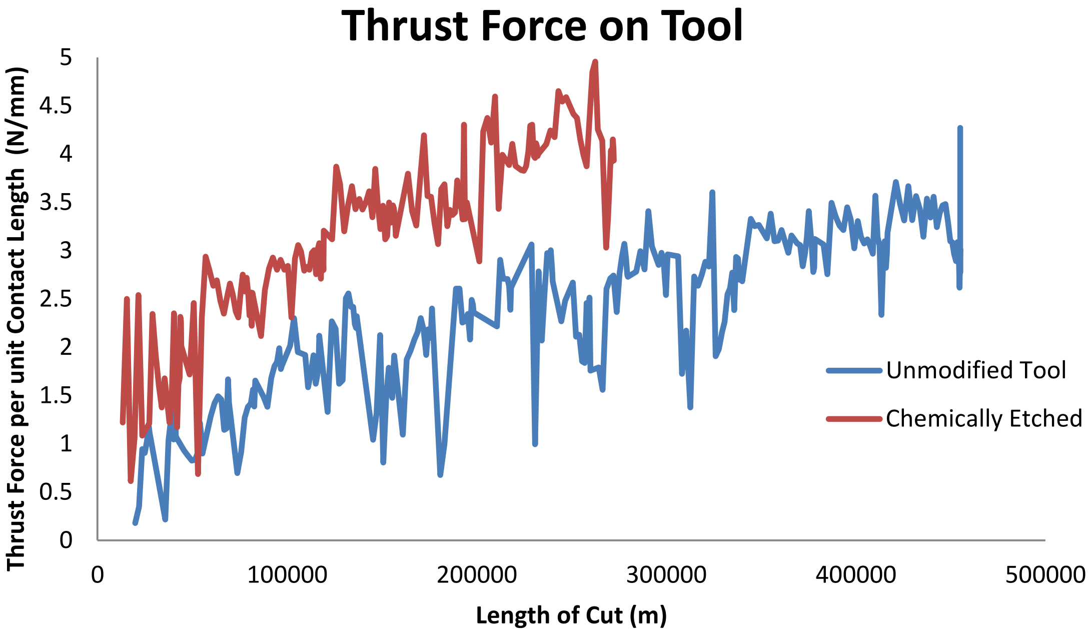

Figure 5.26 Thrust Force on Tool of Chemically Etched and Unmodified SCD Tool

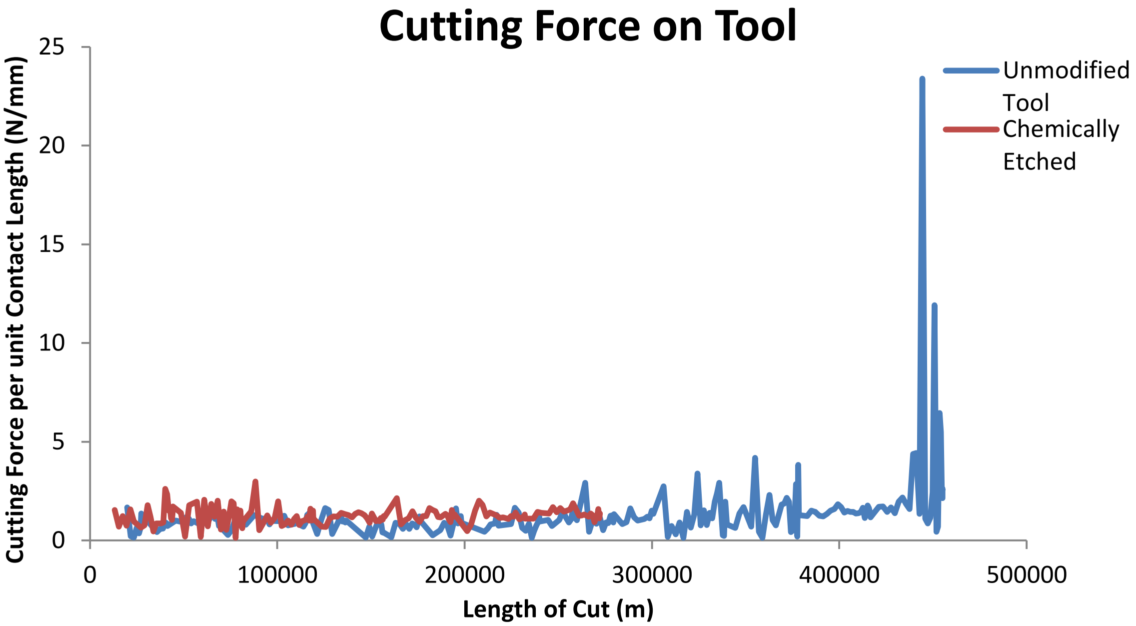

Figure 5.27 Cutting Force on Tool With Chemically Etched and Unmodified SCD Tool

For both tools, thrust forces increased with cutting length. Cutting forces however, stayed relatively constant. The ratio of thrust force over the cutting force can be an indicator of tool wear as a larger cutting edge radius will create a more negative effective rake angle.

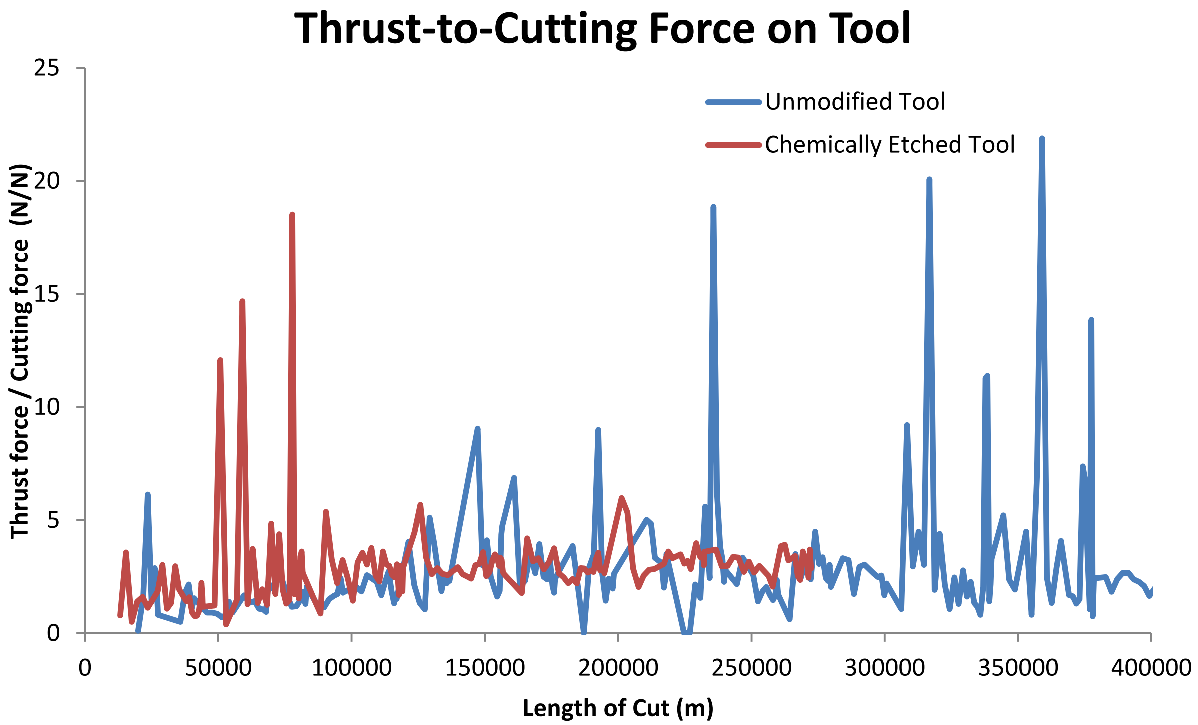

Figure 5.28 Ratio of Thrust Force to Cutting Force of Chemically Etched and Unmodified SCD Tool

During the break-in period, both tools produced surfaces with very good surface finish and similar topography. The tool marks from machining are very faint during the break-in stage, leading to very good surface finish. New, sharp tools are less prone to the size effect near the edge of the tool, creating less plastic side flow.

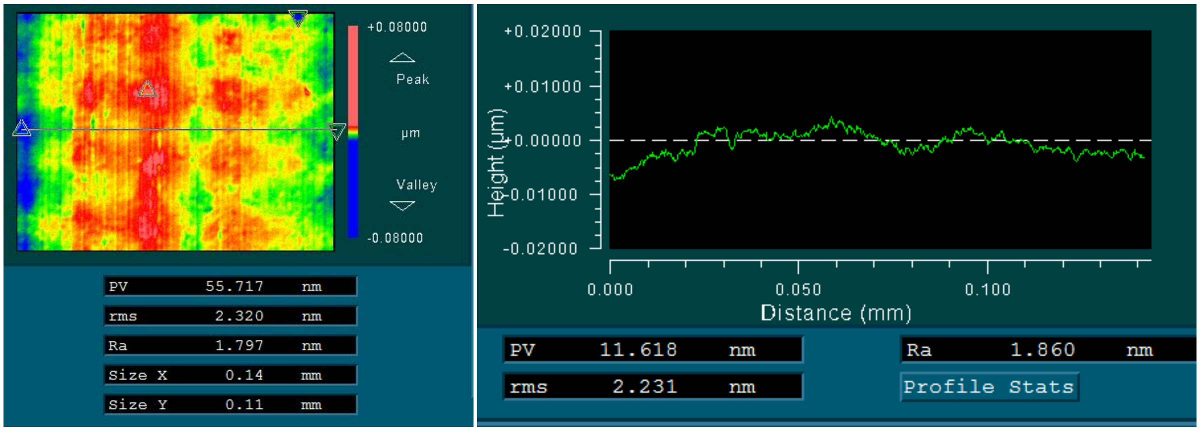

PV 55.717 nm
rms 2.320 nm
Ra 1.797 nm
Size X 0.14 mm
Size Y 0.11 mm

PV 11.618 nm
rms 2.231 nm
Ra 1.860 nm

Figure 5.29 Interferometer Scan of RSA Workpiece, Unmodified Tool, Break-In Stage (1000X Magnification)

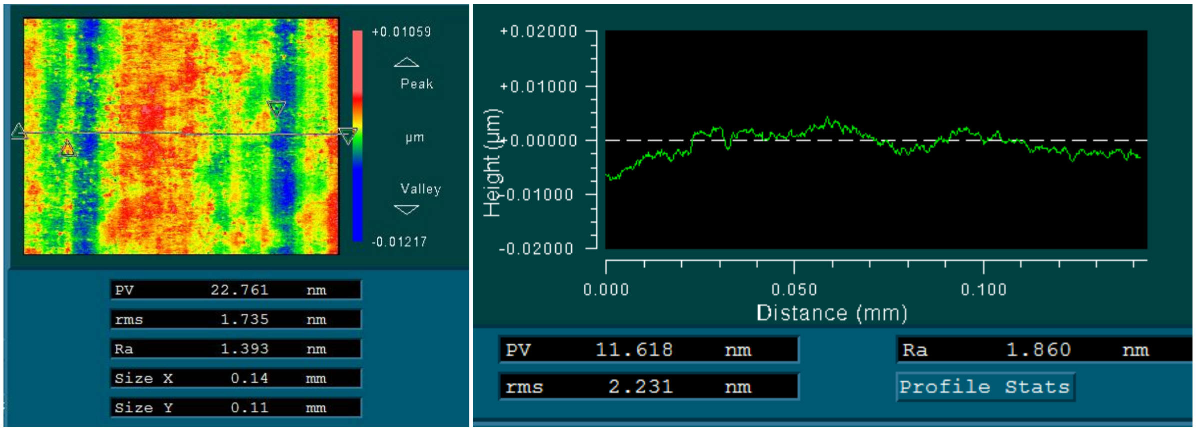

PV 22.761 nm
rms 1.735 nm
Ra 1.393 nm
Size X 0.14 mm
Size Y 0.11 mm

PV 11.618 nm
rms 2.231 nm
Ra 1.860 nm

Figure 5.30 Interferometer Scan of RSA Workpiece, Chemically Etched Tool, Break-In Stage (1000X Magnification)

As the tools wear out, they enter the stable wear stage. This is characterized by a long period of stable cutting. The feed marks are clearer as the eroded, larger cutting edge radius is less prone to cutting and creates more plastic side flow.

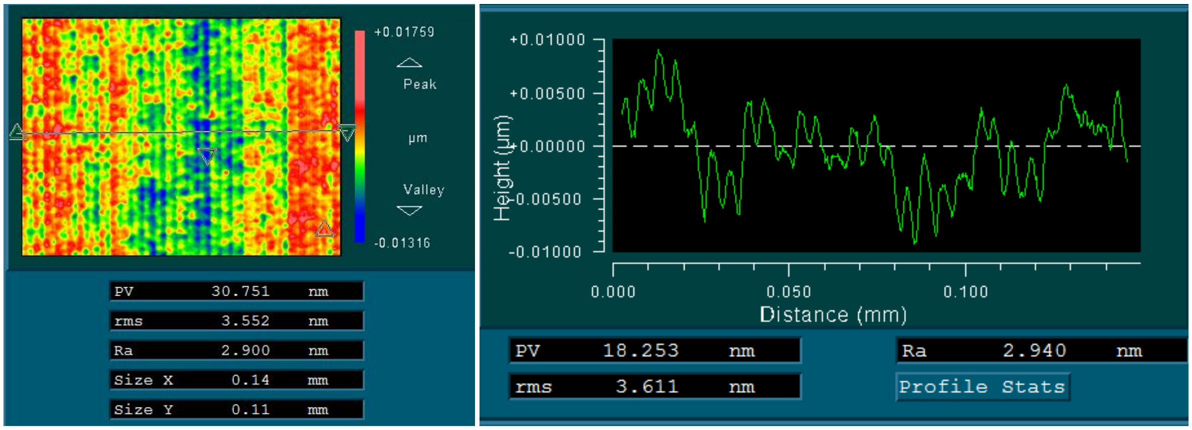

PV 30.751 nm
rms 3.552 nm
Ra 2.900 nm
Size X 0.14 mm
Size Y 0.11 mm

PV 18.253 nm
rms 3.611 nm
Ra 2.940 nm

Figure 5.31 Interferometer Scan of RSA Workpiece, Unmodified Tool, Stable Wear Stage (1000X Magnification)

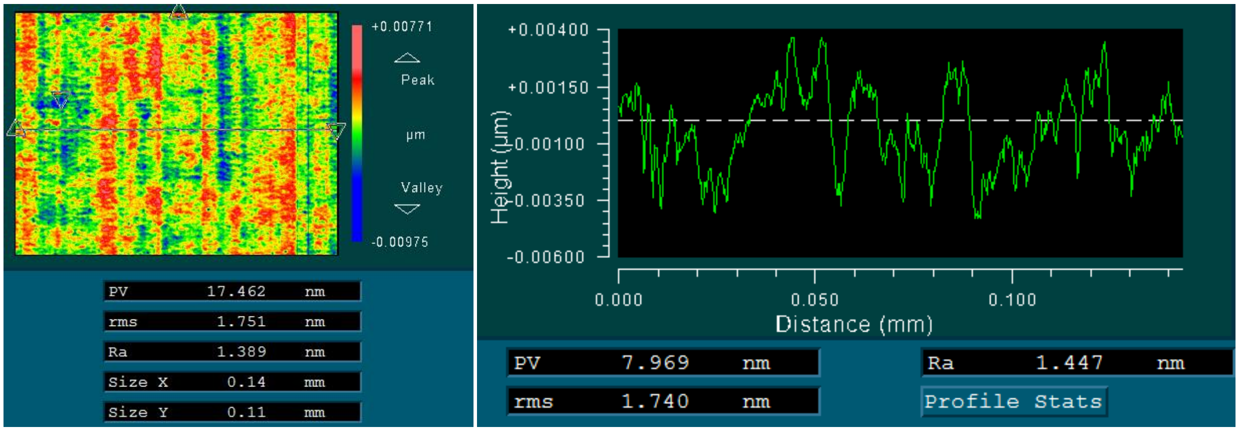

PV 17.462 nm
rms 1.751 nm
Ra 1.389 nm
Size X 0.14 mm
Size Y 0.11 mm

PV 7.969 nm
rms 1.740 nm
Ra 1.447 nm

Figure 5.32 Interferometer Scan of RSA Workpiece, Chemically Etched Tool, Stable Wear Stage (1000X Magnification)

After the tools were considered to be worn, they both began to generate surfaces that were unacceptable as they had diffraction grated surfaces. These diffraction grated surfaces did not have a PV of over 50nm, but were unacceptable due to their appearance.

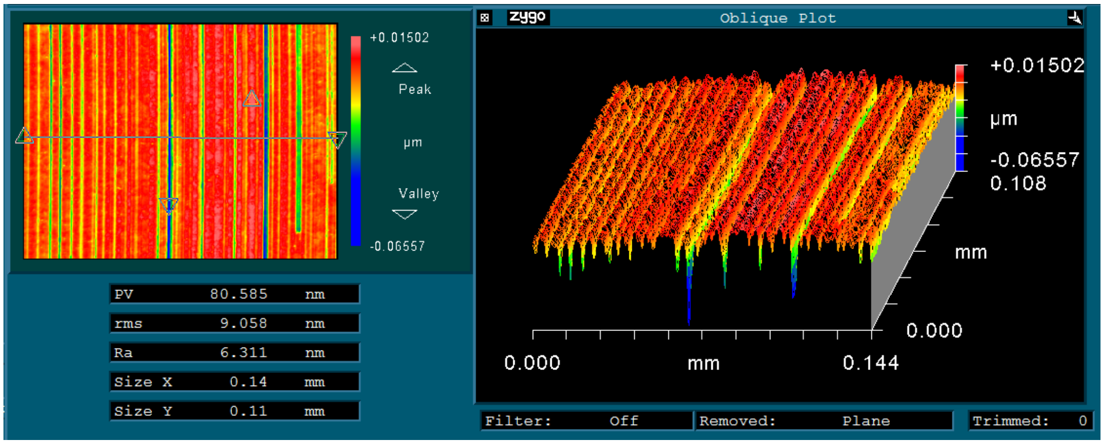

PV 80.585 nm
rms 9.058 nm
Ra 6.311 nm
Size X 0.14 mm
Size Y 0.11 mm
Filter: Off
Removed: Plane
Trimmed: 0

Figure 5.33 Interferometer Scan of RSA Workpiece, Unmodified Tool, Worn (1000X Magnification) Rainbow appearance from diffraction gratings

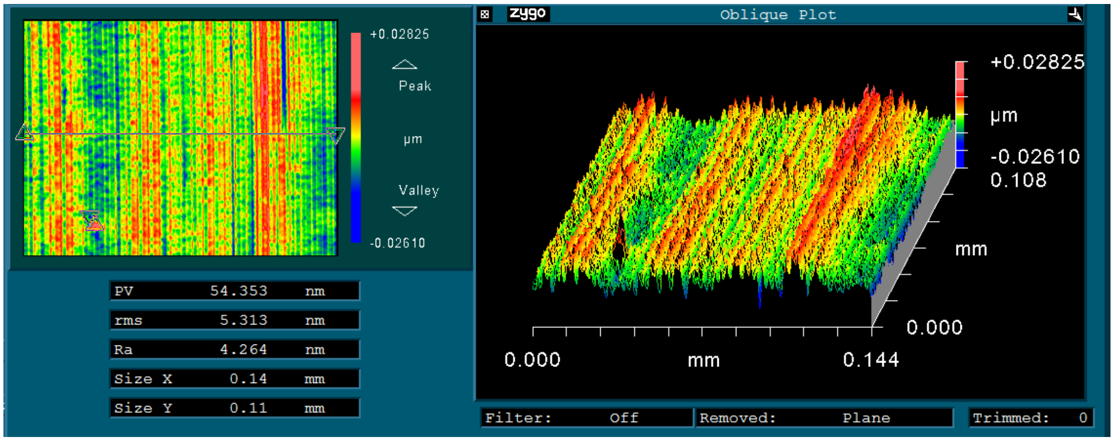

PV 54.353 nm
rms 5.313 nm
Ra 4.264 nm
Size X 0.14 mm
Size Y 0.11 mm
Filter: Off
Removed: Plane
Trimmed: 0

Figure 5.34 Interferometer Scan of RSA Workpiece, Chemically Etched Tool, Worn (1000X Magnification)

The use of RSA virtually eliminates grain boundary induced roughness and scratches from hard particles due to its fine grain structure and finely dispersed hard alloying particles. Both tools also exhibited an increase of thrust force with cutting length, indicating a rounding of the cutting edge. The presence of BUE does not seem to be reflected by an increase in cutting force. The cutting forces for both tools remained relatively constant, and followed similar trends.

Rounded cutting edges, due to the size effect, creates a more negative effective rake angle. The tools also showed increased plastic side flow with wear, contributing to surface roughness.

Although the chemically etched tool created surfaces of extremely high quality, the tool wore out more quickly than the unmodified tool. This is confirmed by the relatively higher thrust force than that which the chemically etched tool produces.

5.1.4 Diffraction Grated Surfaces and Built-Up Edge

Occasionally, the tools will produce a surface with deep scratch marks with even spacing, causing a ‘rainbow-pattern’, or diffraction grated effect. This effect occurred periodically during the stable wear stage of the cutting test. During the worn-out stage of the cutting test, the tools consistently generated diffraction grated surfaces. This effect was seen when machining with the chemically etched and unmodified tools.

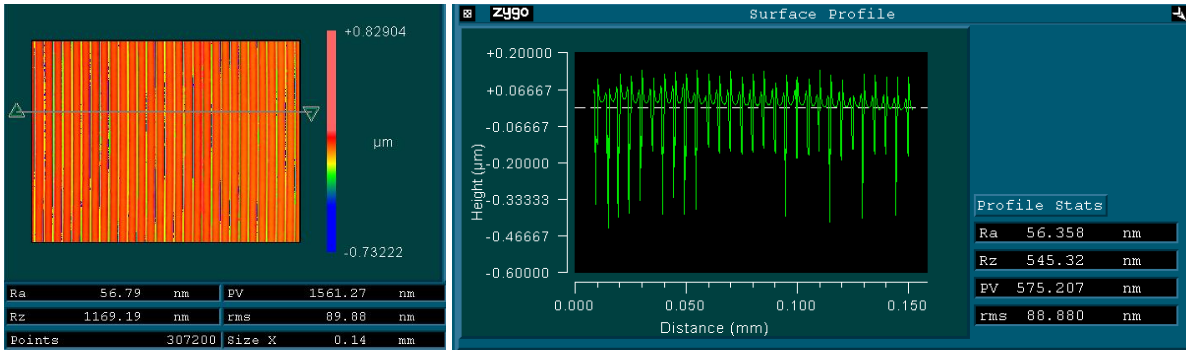

Ra	56.79	nm	PV	1561.27	nm
Rz	1169.19	nm	rms	89.88	nm
Points	307200		Size X	0.14	mm

Profile Stats

Ra	56.358	nm
Rz	545.32	nm
PV	575.207	nm
rms	88.880	nm

Figure 5.35 Diffraction Grated Surface Created Using Unmodified Tool

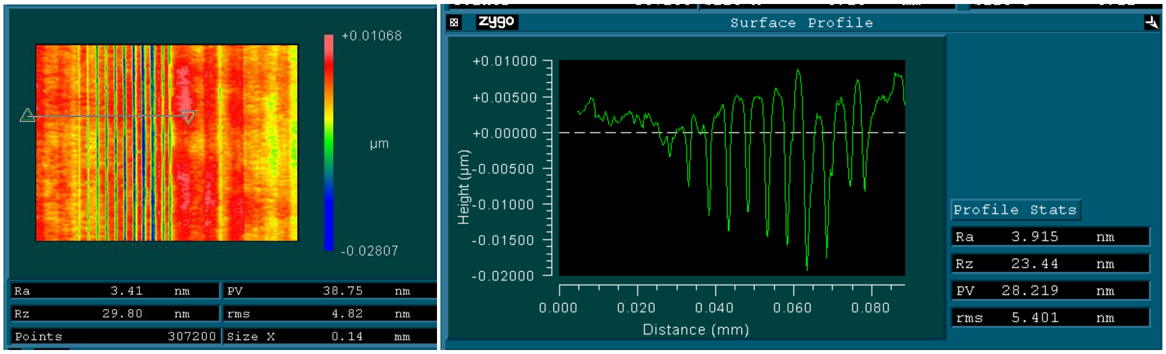

Ra 3.41 nm
PV 38.75 nm
Rz 29.80 nm
rms 4.82 nm
Points 307200
Size X 0.14 mm

Ra 3.915 nm
Rz 23.44 nm
PV 28.219 nm
rms 5.401 nm

Figure 5.36 Diffraction Grated Surface Created Using Chemically Etched Tool

The scratch marks have a deep and sharp profile to them, unlike the nose radius of the tool. The effect will also appear as periodic bands near the center of the part and will appear occasionally without pattern. This is due to the presence of a built-up-edge (BUE). Although cutting forces and cutting temperatures are low when compared to conventional machining, the material can stick to the diamond tool due to pressure on the rake face. This was confirmed by scanning the tools in a white light interferometer after cutting and gentle cleaning.

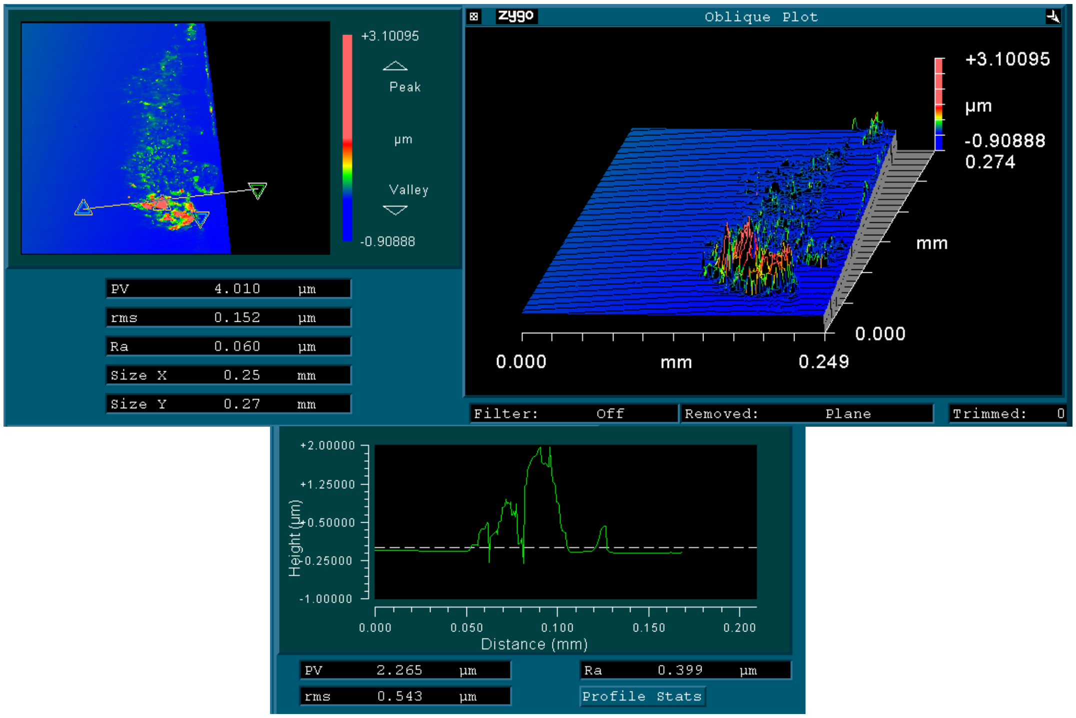

PV 4.010 µm
rms 0.152 µm
Ra 0.060 µm
Size X 0.25 mm
Size Y 0.27 mm

Filter: Off
Removed: Plane
Trimmed: 0

PV 2.265 µm
Ra 0.399 µm
rms 0.543 µm

Figure 5.37 BUE on Unmodified SCD Tool

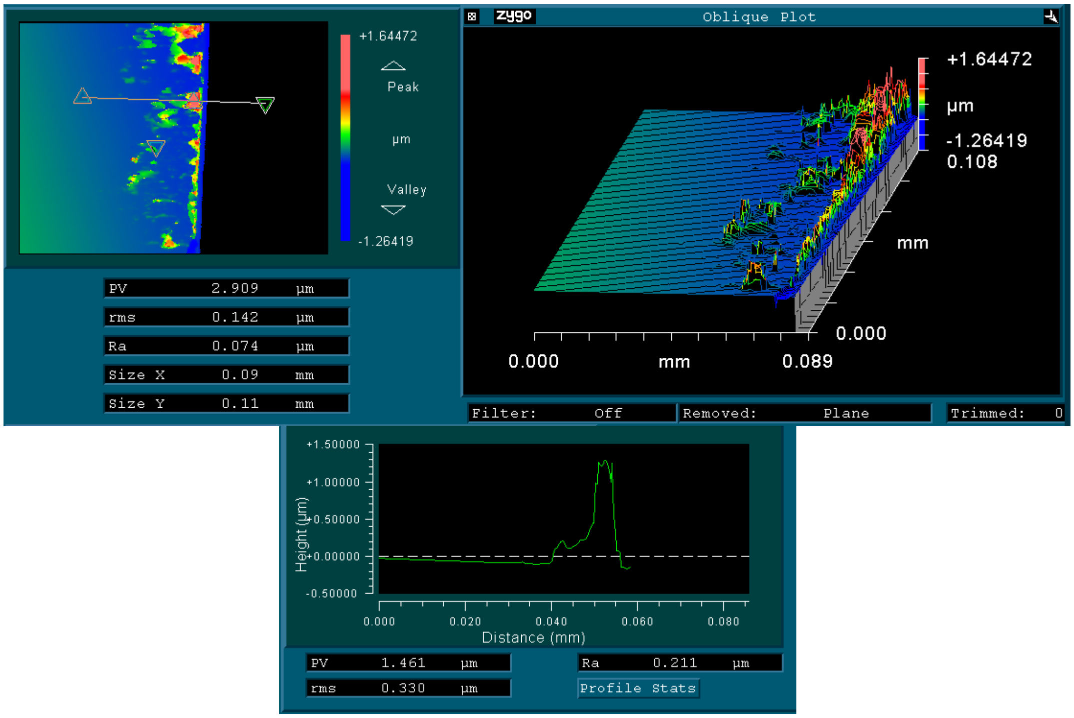

PV 2.909 µm
rms 0.142 µm
Ra 0.074 µm
Size X 0.09 mm
Size Y 0.11 mm

Filter: Off
Removed: Plane
Trimmed: 0

PV 1.461 µm
rms 0.330 µm
Ra 0.211 µm

Figure 5.38 BUE on Honed SCD Tool

The combination of pressure and adhesion of aluminum on the tools worsened as the tools were worn down. The adhesion of aluminum to the tool also occurs on the flank face, negatively affecting surface finish.

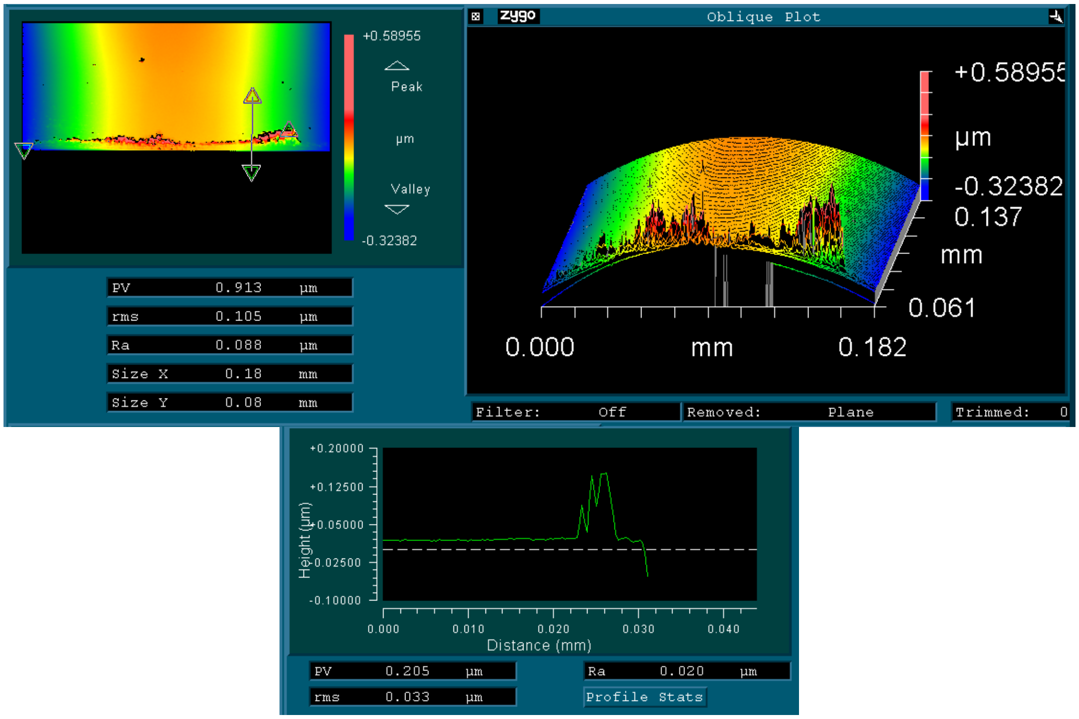

PV 0.913 µm
rms 0.105 µm
Ra 0.088 µm
Size X 0.18 mm
Size Y 0.08 mm
Filter: Off
Removed: Plane
Trimmed: 0
PV 0.205 µm
rms 0.033 µm
Ra 0.020 µm

Figure 5.39 BUE on Flank Face of Unmodified Tool (1000X Magnification)

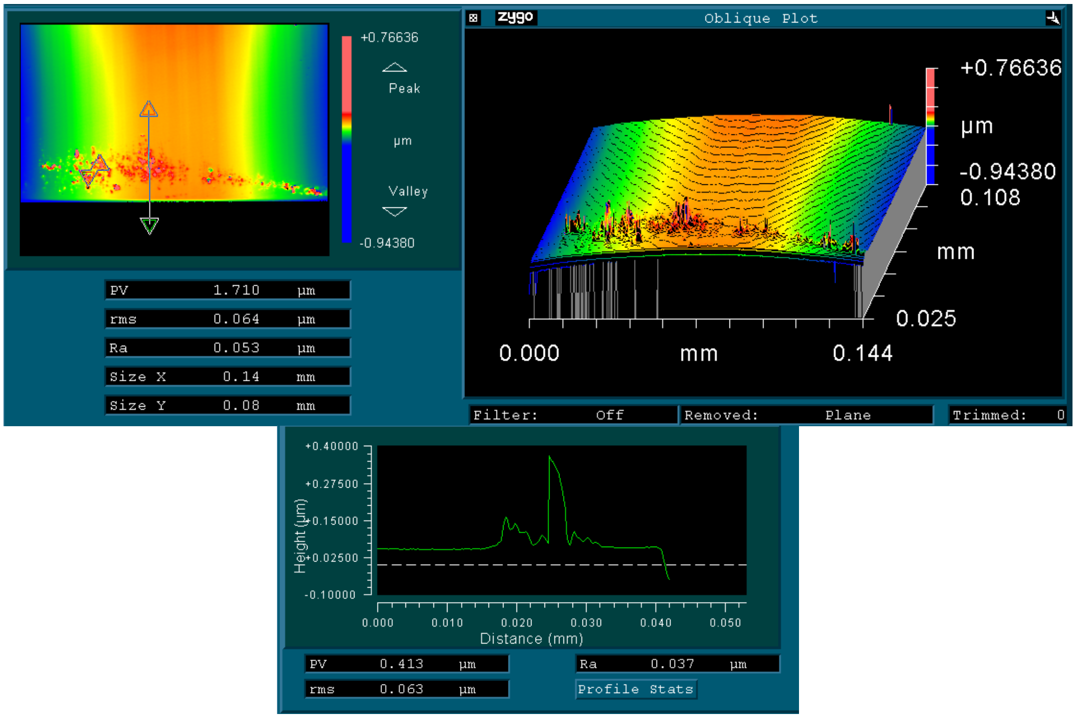

PV 1.710 µm
rms 0.064 µm
Ra 0.053 µm
Size X 0.14 mm
Size Y 0.08 mm
Filter: Off
Removed: Plane
Trimmed: 0
PV 0.413 µm
rms 0.063 µm
Ra 0.037 µm

Figure 5.40 BUE on Flank Face of Chemically Etched Tool (1000X Magnification)

This can be confirmed by drawing the tool profile over the grooves of a diffraction grated surfaces. The surface profile was extracted from the scan shown in Figure 5.36. The tool marks indicate that a sharp protrusion from the tool caused the regular-spaced scratches on the surface. Following an equation by Takasu et al. [3], tool profiles can be approximated using a parabola with the equation:

$$p_{height} = \frac{p_{position}{}^{2}}{2\ r_n}$$

Equation 5.4 Tool Profile Approximation

Where P_{height} is the height of the profile, in the Y-axis and $P_{position}$ is the position of a point in the X-axis. The variable r_n represents the nose radius of the tool. In Figure 5.41, the tool was fed from the positive X-direction to the origin of the graph. The scratches on the surface due to BUE are obvious as there is no imprint that clearly follows the surface profile.

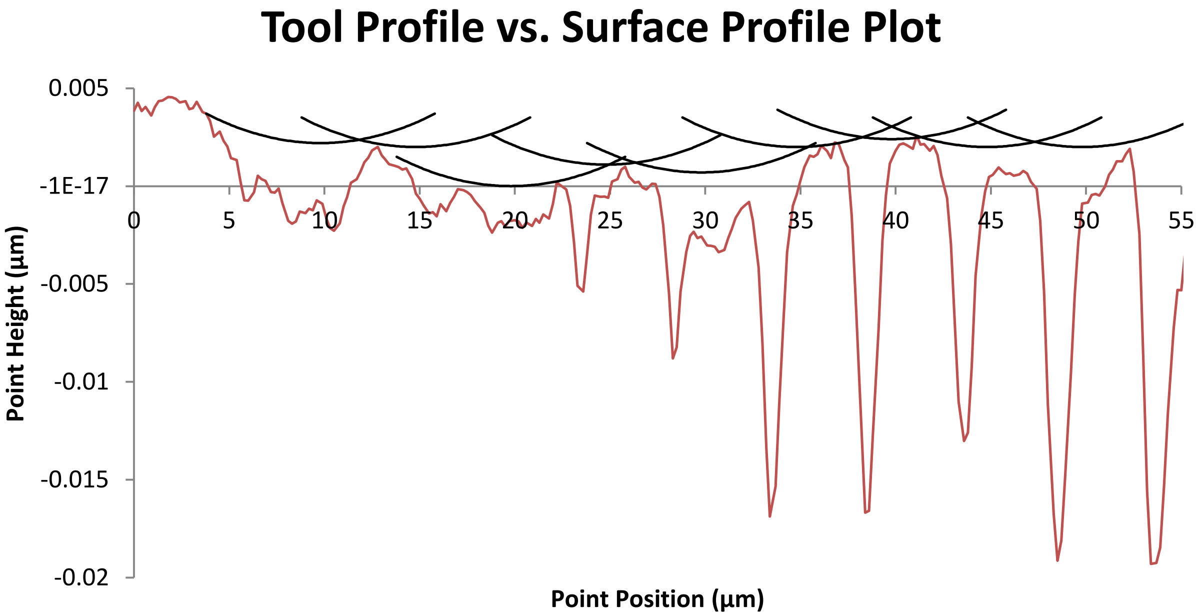

Figure 5.41 Surface Profile Showing Scratches From BUE

After machining and finding the presence of diffraction grated patterns on the workpiece, the SCD tools were removed from the machine and scanned using the white light interferometer. Sticking of material on both the rake and flank faces of the tools was detected. After the tools were cleaned, the surface finish became acceptable again, until workpiece material began to stick to the tool, creating BUE and creating a poor finish. The creation and breaking-off of BUE on the tool will cause tool wear and inconsistent surface finish. The main mechanism of wear of these SCD tools in face turning flat surfaces was found to be wear through BUE formation.

5.1.5 Measurement of Worn Cutting Edge of SCD Tools

After the tools were worn out, measurements of the cutting edge were performed again using the 3D confocal laser microscope, Olympus OLS4000 LEXT. Before measuring, the tools were cleaned in acetone using a cotton swab, and then placed in a bath of 0.5M sodium hydroxide solution to dissolve any remaining aluminum BUE. The measurement procedure was previously outlined in Chapter 5.1.2.

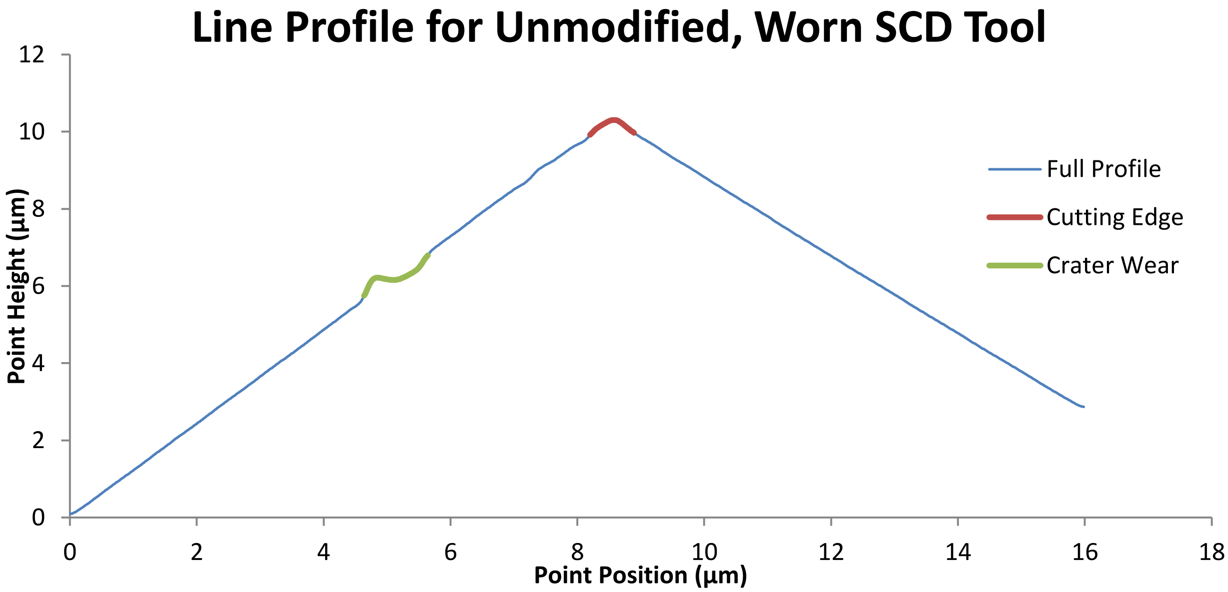

Figure 5.42 Line Profile For Unmodified, Worn SCD Tool

From the full profile across the tool, there has been obvious crater wear on the rake face of the unmodified tool. There has been some rounding of the cutting edge, creating a larger cutting edge radius.

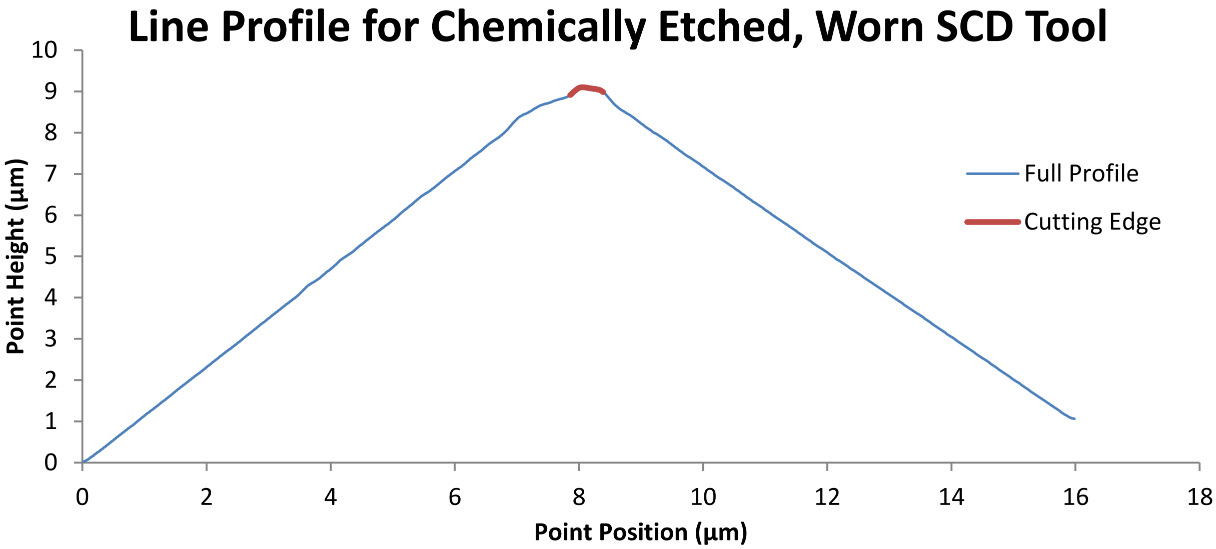

Figure 5.43 Line Profile For Chemically Etched, Worn SCD Tool

For the chemically etched tool, the stepped cutting edge has been eroded to a rounded cutting edge profile with the ‘step’ on the rake face having given way to a tool with a beveled edge instead. The highlighted points from Figure 5.42 and Figure 5.43 were selected to be fitted to a circle for cutting edge measurement.

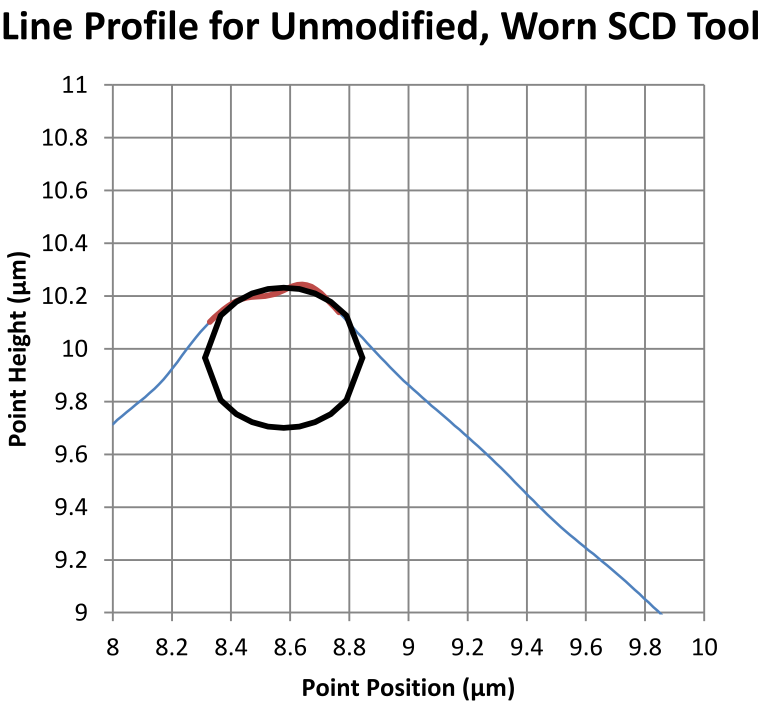

Figure 5.44Circle Fit for Unmodified, Worn SCD Tool

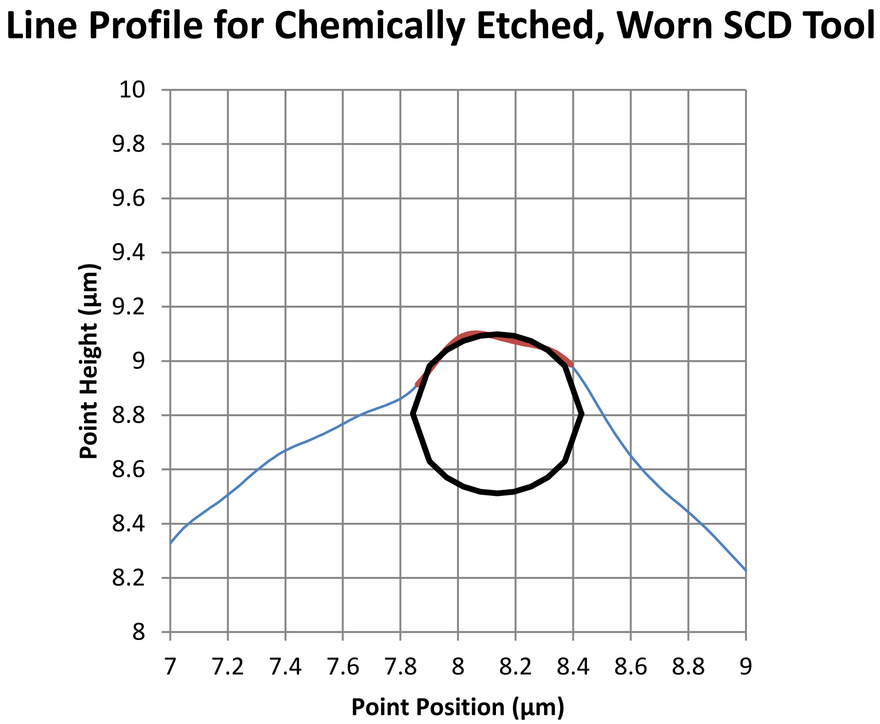

Figure 5.45 Circle Fit for Chemically Etched, Worn SCD Tool

Table 5.5 Summary of Cutting Edge Measurements, Worn Tool

SCD Tool	Cutting Edge Radius (nm)
Unmodified Tool, Worn	266
Chemically Etched Tool, Worn	293

The measurements show that both tools exhibit the same amount of tool wear after the cutting test. However, the length of cut for the unmodified tool is much longer than that of the chemically etched tool. Although the chemically etched tool did not require a long break-in period, its useful tool life is shorter than that of the unmodified tool.

5.2 Spindle Star Error in Diamond Turning

In the diamond turning process, the proper combination of good workpiece quality, sharp, controlled waviness tools, and a high quality positioning system will create a part with high accuracy and optical surface quality. Now that the surface quality is very high, the form error in the part becomes distinguishable from the surface roughness.

The largest source of error in the diamond turning process comes from vibration in the air-bearing spindle. The vibration can be due to minute imbalances and torque ripple from the brushless DC motor that powers the spindle. The air bearings in the spindle itself can also cause vibration from phenomena such as air hammer instability, and inconsistent compressed air supply. Finally, the rotating imbalance in the shaft can cause it to vibrate at its rotational frequency and its harmonic frequencies.

In spindle analysis and in the analysis of rotating machinery, there are two types of vibrations: synchronous and asynchronous. Synchronous vibration is defined as a vibration that is equal to an integer multiple of the rotating frequency. Asynchronous vibration is defined as a vibration that is at a frequency that is other than an integer multiple of the rotational frequency.

This study will confirm that the spindle star is the primary cause of form error in SPDT. To the author’s knowledge, no work has been done to address the spindle star formation and its detailed analysis to date. In this thesis, the author took the first attempt to describe this phenomenon using rotordynamic analysis and a Campbell waterfall diagram, techniques which are typically used in the high-speed turbine industry. The spindle star error was detected using the force dynamometer during tool testing. It is a consistent disturbance frequency at approximately 400Hz. Further investigation resulted in the discovery of a large error on the surface of the part, on the order of 80nm peak-to-valley. This investigation also revealed the true nature of the spindle star error and its synchronous and asynchronous components.

The spindle star error is not limited to the machine tool and spindle used for this thesis. Two diamond turned components from different manufacturers were scanned under the white light interferometer to confirm that spindle star error is endemic to the diamond turning process.

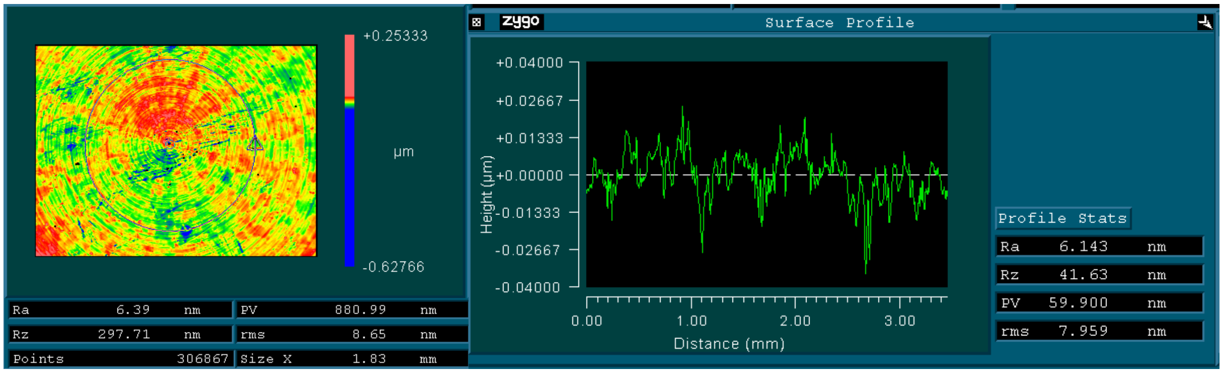

Ra	6.39 nm	PV	880.99 nm
Rz	297.71 nm	rms	8.65 nm
Points	306867	Size X	1.83 mm

Profile Stats

Ra 6.143 nm
Rz 41.63 nm
PV 59.900 nm
rms 7.959 nm

Figure 5.46 WLI Scan of Large Concave Telescope Mirror, produced using SPDT, 80X Magnification

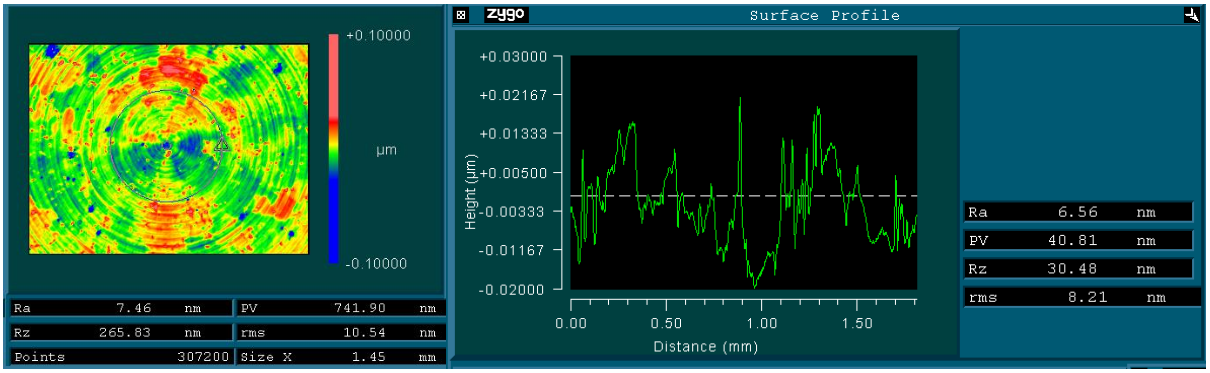

Ra	7.46 nm	PV	741.90 nm
Rz	265.83 nm	rms	10.54 nm
Points	307200	Size X	1.45 mm

Ra 6.56 nm
PV 40.81 nm
Rz 30.48 nm
rms 8.21 nm

Figure 5.47 WLI Scan of Small Concave Mirror, produced using SPDT, 100X Magnification

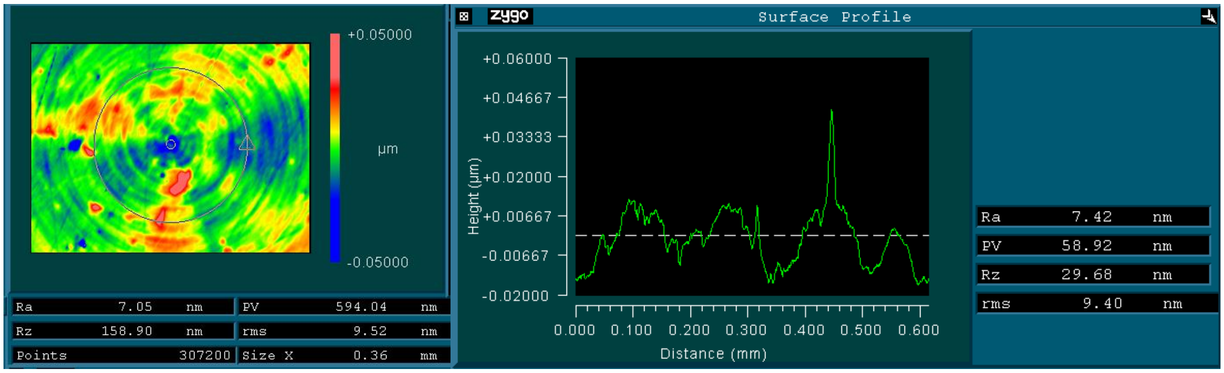

Ra	7.05 nm	PV	594.04 nm
Rz	158.90 nm	rms	9.52 nm
Points	307200	Size X	0.36 mm

Ra 7.42 nm
PV 58.92 nm
Rz 29.68 nm
rms 9.40 nm

Figure 5.48 WLI Scan of Small Concave Mirror, produced using SPDT, 400X Magnification

These off-the-shelf optical components all show signs of wear, such as scratches and pitting from handling. However both components show clear signs of spindle star error. By taking a circular surface profile, it can be characterized by large, regularly spaced undulations.

5.2.1 Rotordynamics: Theory and Analysis

Rotordynamics is the study of vibration in axially symmetric, rotating structures. It is typically applied to high-speed pumps, turbines, motors, and disk drives. At high speeds, care must be taken to prevent the inertial and gyroscopic effects of the shaft, masses, and bearings from creating large vibrations that can shake the machine apart. This type of analysis will be applied to diamond turning in order to study the vibration in the air bearing spindle. Although vibrations in the spindle are relatively low in amplitude and will not cause damage, excessive vibration will still cause unacceptable form errors in the finished part.

In general, the equation for vibrating mechanical components is dependent on the masses in the system, damping, and spring constants [74] and takes the form of a second order ordinary differential equation (Equation 5.5).

$$[M]\{\ddot{x}\} + [C]\{\dot{x}\} + [K]\{x\} = \{f\}$$

Equation 5.5 General Second-Order Equation for Mechanical Vibrations

The variables in Equation 5.5 represent the following: *M* is the mass matrix, *C* is the damping matrix, *K* is the matrix of spring constants and *f* represents the external force vector. In the case of rotating machinery, the equation gains additional components from the gyroscopic effect and gyroscopic damping, shown in Equation 5.6.

$$[M]\{\ddot{x}\} + ([G] + [C])\{\dot{x}\} + ([B] + [K])\{x\} = \{f_{vib}\}$$

Equation 5.6 Dynamic Equations for Jeffcott-Laval Rotor [75]

G is a skew-symmetric gyroscopic matrix, dependent on rotational velocity. *B* is the skew-symmetric rotating damping matrix, also heavily dependent on rotational velocity. It will modify the apparent stiffness of the structure and can cause instability [76]. The matrices *G* and *B* are dependent on the polar moment of inertia of the rotor and traverse moment of inertia, both of which are dependent on the mass and distribution of mass in the rotor. These moments of inertia will determine the response that the spinning shaft and rotor will have to a tilt or perturbation.

When machining, there will always be a perturbation on the machine spindle due to the cutting forces generated by the cutting tool. In a physical shaft-rotor system, there will always be some degree of mass eccentricity that will cause a perturbation or tilt in the shaft-rotor system. This is because a physical shaft-rotor system also cannot be made to be perfectly axially symmetric. These two sources of vibration together will cause the air bearing spindle to undergo precession or whirling. Figure 5.49 shows a schematic of a spindle shaft and the modes of vibration that the shaft can undergo.

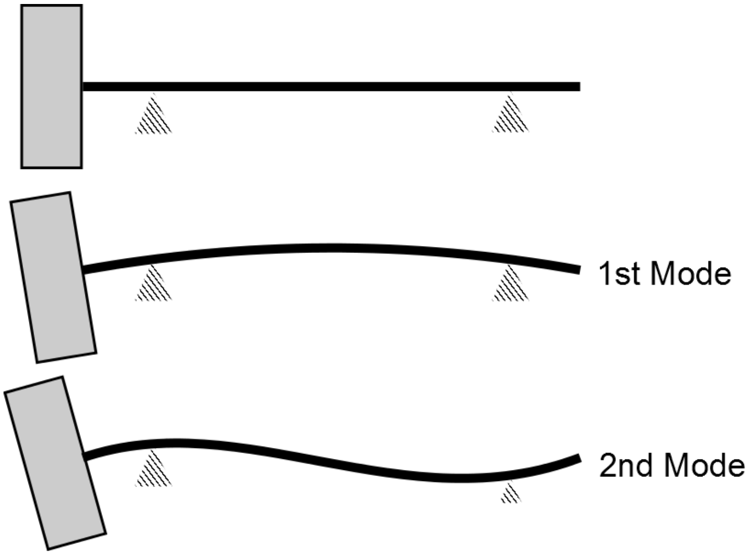

Figure 5.49 Example of Bending Modes Of Spindle Shaft [77] [Adapted After Van Osch and Van Esch (2006)]

When the machine shaft is not rotating, it will act similar to a stationary beam. It is affected by its mass, stiffness, and damping. There will be many modes of vibration. When the system's bearings are modeled as stiff pivots, the bearings will act as nodal points for the first mode of vibration. The point of largest displacement for this mode will be the midpoint between the two bearings and the cantilevered ends. Once the machine is rotating, the modes are no longer planar. Assuming radially symmetric bearings, the masses in the system will trace a circle [75]. The displacement will also be at its highest at the midpoints between bearings (anti-node). For diamond turning, the cantilevered end of the shaft, where the vacuum chuck and workpiece is located, is of interest.

If we assume the air bearings to be flexible and the shaft to be perfectly rigid, there will be two motions in which the shaft can move that will affect the depth of cut. Diagrams of these motions are shown in Figure 5.50. The first motion is vibration of the spindle in the axial direction. The second motion is a motion where the vibration of the front bearing is out of phase with the rear bearing, creating a conical pattern when in motion. The third motion is a cylindrical orbit, where the front and rear bearings both vibrate with the same phase.

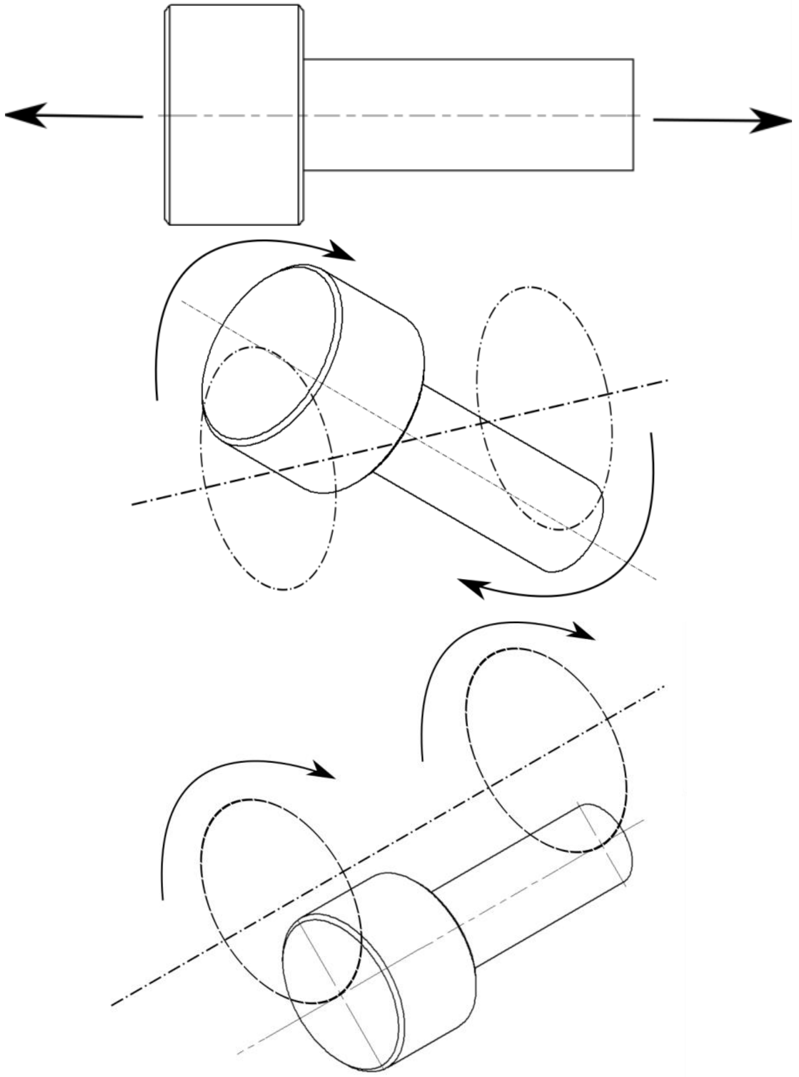

Figure 5.50 Examples Of Different Spindle Shaft Vibration Motions With Flexible Bearings

The cylindrical mode is commonly associated with a phenomenon called whirling. The Jeffcott-Laval rotor in Figure 5.51 is often used to explain shaft whirling. It consists of a point mass (m) at the midpoint of a rotating, long, massless shaft. The eccentricity of the point mass is e while the shaft rotates at a constant speed ω. In this example, the shaft ends are mounted on stiff bearings.

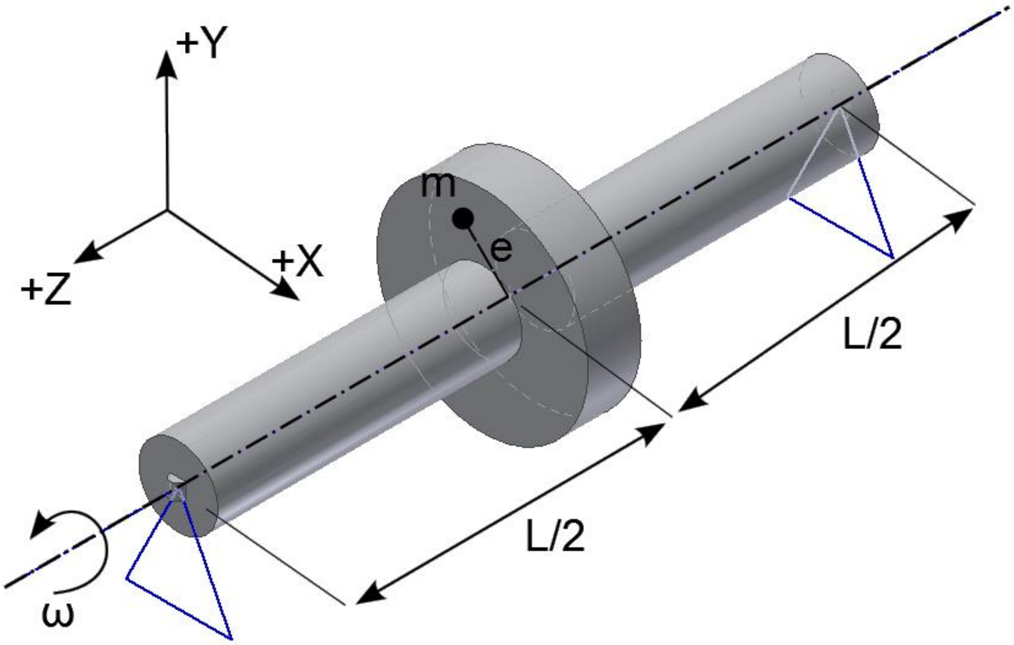

Figure 5.51 Jeffcott-Laval Rotor

Should the eccentricity of mass be zero, the shaft will bow outwards due to the inertia of the spinning mass. If the eccentricity of mass is more than zero, the dynamics of the system are strongly affected and the shaft will bow outwards more strongly. In this model, assume that the rotor disk in the center does not affect the stiffness of the shaft. The bending stiffness (*K_s*) of the shaft is given by Equation 5.7, where *E* is the Young's modulus of the shaft, *L* is the length between the bearings, and *I* is the second moment of area.

$$k_s = \frac{48EI}{{L_{shaft}}^3}$$

Equation 5.7 Stiffness of a Uniform Beam [74]

For a circular shaft, the second moment of area is related to its diameter *D*, given by Equation 5.8.

$$I = \frac{\pi D^4}{64}$$

Equation 5.8 Second Moment of Area of a Circular Shaft [78]

It can be assumed that the shaft also has a small amount of damping, c_s. The rotor dynamics of a Jeffcott-Laval rotor will be governed by Figure 5.8.

$$m\ddot{x} + k_s x + c_s \dot{x} = m\, e\, \omega^2 \cos(\omega t)$$
$$m\ddot{y} + k_s y + c_s \dot{y} = m\, e\, \omega^2 \cos(\omega t)$$

Equation 5.9 Equations of Motion of a Jeffcott-Laval Rotor [75]

The eccentric center of mass, while rotating, will tend to be pushed outwards from the rotational axis due to inertial forces, causing it to vibrate back and forth on the shaft, as shown in Figure 5.52.

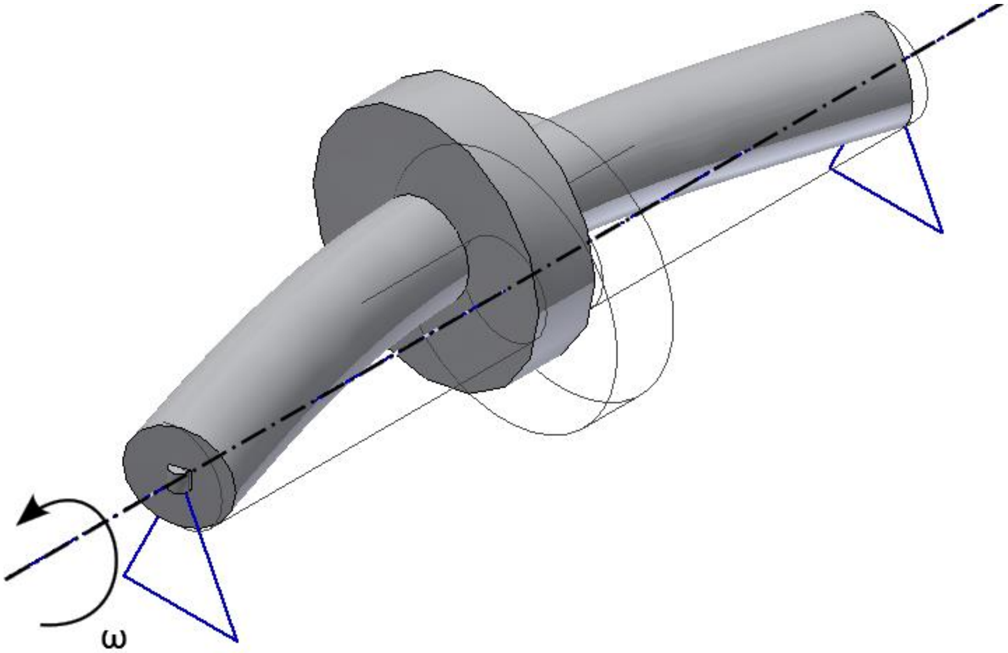

Figure 5.52 Jeffcott-Laval Rotor With Exaggerated Deformation

At the same time that the rotor is tracing a cylindrical orbit as it is also spinning with a constant angular velocity, ω. If the direction of the orbit is the same direction as the shaft rotation, it is known as forward whirl. If the orbit direction is reversed from the direction of shaft rotation, it is known as backward whirl [79]. A visual representation of forward and backward whirling is shown in Figure 5.53.

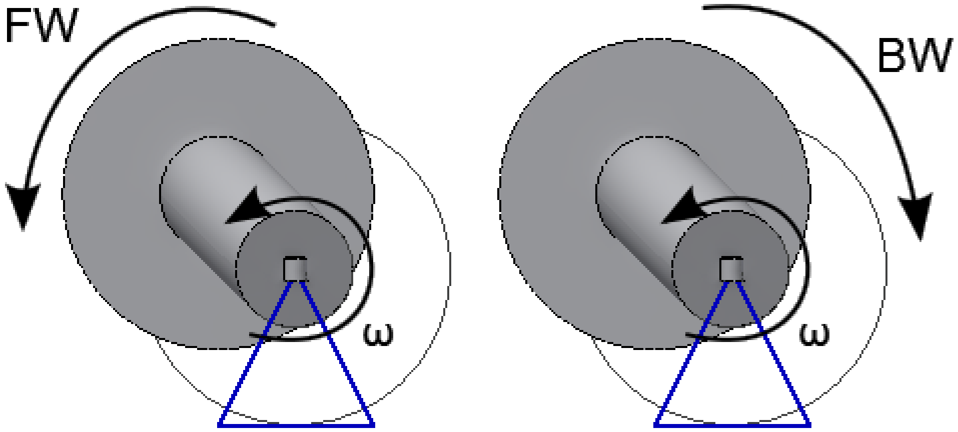

Figure 5.53 Example of Forward Whirl (FW) and Backward Whirl (BW) on Jeffcott-Laval Rotor

Although a cylindrical orbit does not directly affect the depth of cut in the case of the face turning of a flat piece, it may be a source of excitation for the other modes of vibration. It can also cause vibration marks when machining workpieces with different geometry, such as spherical lenses.

The conical orbit is commonly associated with the precession of a rotating object. The machine tool spindle consists of a shaft supported by air bearings with a vacuum chuck and workpiece on the cantilevered end. The mass of this workpiece will always create a bending moment in the shaft due to gravity. An example of this can be seen in Figure 5.54.

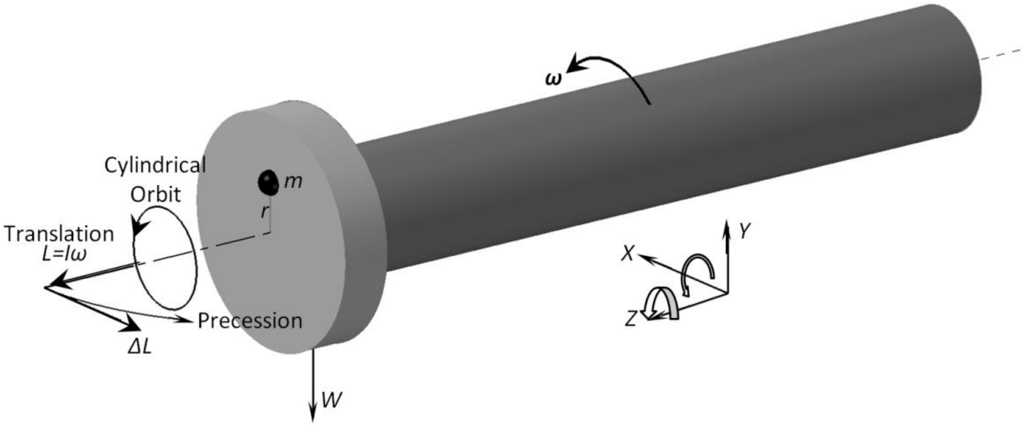

Figure 5.54 Example of Precession

This bending moment will always be perpendicular to the direction of L, the angular momentum. This change in angular momentum will not affect its magnitude but will affect its direction [80], causing the shaft and workpiece to bend and create a conical orbit as it is spinning. This effect, combined with the centripetal force of the workpiece, will cause the spindle to wobble and vibrate in a conical orbit. The amount of precession (gyroscopic effect) depends on the cross-coupling stiffness difference between axial and radial direction.

In order to understand vibration in rotating machinery, the Campbell diagram was developed to map a system's frequency response as a function of rotating speed. In an experimental setup, this is done by measuring the frequency response spectrum for a given interval of machine speeds and plotting a waterfall plot. An example of a waterfall plot from Lee et al. is shown in Figure 5.55.

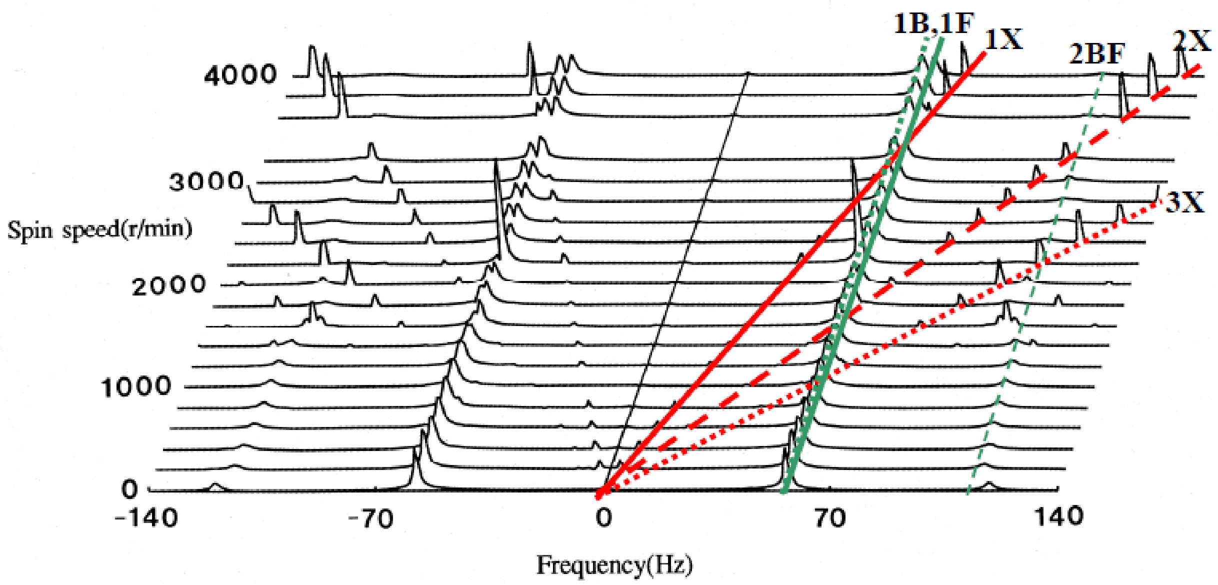

Figure 5.55 Example of a Campbell Diagram [81] [After Lee et al.(2010)]

In the waterfall plot, the X axis represents the vibration frequency (Hz) while the Y axis represents the spindle speed (RPM). The vertical Z axis, represents the vibration amplitude for a given frequency and spindle speed.

The red lines labeled 1X, 2X, and 3X represent the first, second, and third harmonics of the rotational frequency, respectively. They can be plotted using Equation 5.10.

$$y = N\frac{x}{60}$$

Equation 5.10 Nth Harmonic Line Of A Campbell Diagram

Where, *y* represents the spindle speed in RPM, while *x* is a vibration frequency in Hz. *N* is a positive integer. If there is a row of vibration amplitude peaks following one of these lines, it is said to be an *Nth* harmonic resonant vibration. The harmonic number which is synchronous to rotational speed, can give insight to the source of the vibration. The green lines in Figure 5.55 represent an asynchronous natural frequency of a structure on the rotating machine. By plotting the trends of vibration amplitude peaks, a designer can determine which spindle speeds to avoid or gain information on how the machine should be revised.

5.2.2 Effect of Aerostatic Bearings in Spindle Star Formation

In ultraprecision machining, the work-holding spindles typically use externally pressurized air bearings for their rotating shafts. Air bearings have very low friction when rotating, leading to low heat buildup and better dimensional accuracy [82]. At higher pressures, they also have a high load capacity and can boast a stiffness of several N/µm with limited cross-coupling effects [83]. When compared to hydrostatic bearings, air bearings are cleaner and do not require complex, high-friction sealing systems to contain the hydraulic oil. Due to their static characteristics, air bearings are the obvious choice for ultraprecision machining. Air bearings are not without problems and suffer from dynamic problems, such as air hammer instability due to the compressibility of air.

An externally pressurized, aerostatic bearing consists of a smooth shaft with a flange, and an outer ring with a system of orifices in which the air is pumped through. Figure 5.56 shows a hypothetical cutaway of the air-bearing spindle system in a diamond turning machine.

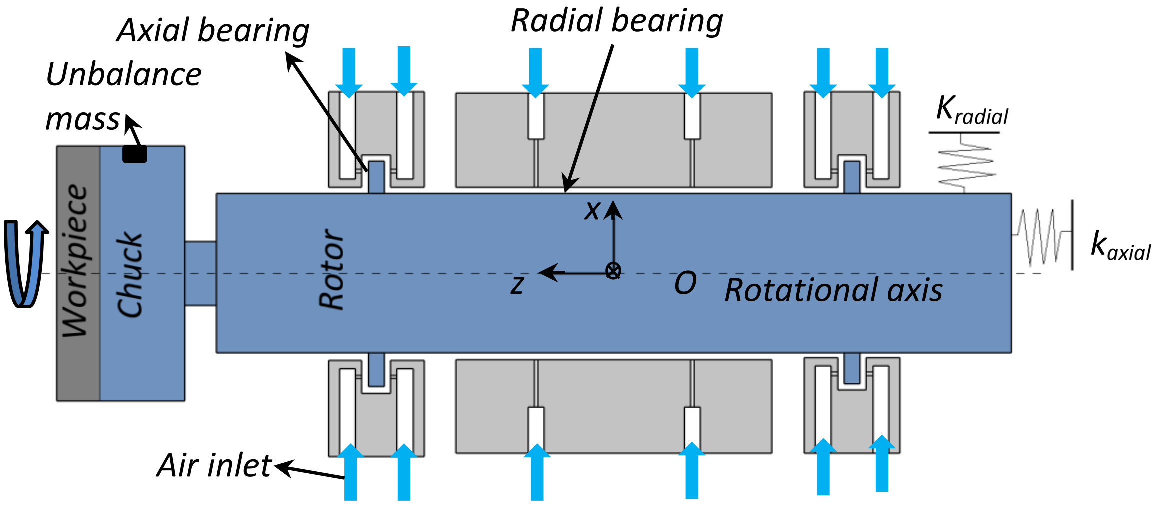

Figure 5.56 Example of an Air Bearing Spindle Cutaway

The distance of the shaft from the outer race is important to the stability and load capacity of the bearing. When the spindle shaft is not rotating, a displacement of the shaft due to external forces or vibration in the X or Z direction will create an uneven air gap between opposing sides of the bearing. For example, a displacement in the positive Z direction will cause the orifices in the positive Z direction to resist the movement due to a decrease of volume and increase of pressure. This follows Boyle's law (Equation 5.11) [84].

$$PV = C$$

Equation 5.11 Boyle's Law

This pushes the shaft back towards the negative Z direction, causing the orifices in the negative Z direction to resist. When this happens, the shaft extracts energy to reach an equilibrium position from the external air supply and vibrates at its natural frequency. This natural frequency is dependent on the apparent stiffness, and mass of the shaft. Air bearings have low levels of damping so the resonant peak closely aligns with the natural frequency. This phenomenon is called "air hammer instability". Air hammer instability is a phenomenon that is highly dependent on the orifice configuration, supply pressure and of course the natural frequency of the system and is present even when there is no rotation [82] [85] [86] [87].

The air-hammer instability can be exacerbated by the gyroscopic precession or whirling phenomena discussed earlier in Section 5.2.1. It can also occur due to external perturbations. When a vibration at a synchronous frequency is sustained over time by extracting energy from the external air supply, it is known as “assisted air hammer instability”. In this case, any displacement of the shaft is corrected by the shaft exciting itself to one of the closest harmonics of the system’s rotational damped natural frequency to conserve energy, in an attempt to return to its equilibrium position. It has been observed that for small displacements, the air film begins to act as if it were a spring element, and less like a damper element [88]. When the system has little or no damping, resonant frequencies are easily excited [82].

In all, there are several major contributions to the form error of the ultraprecision machined part. These can range from tool-workpiece interactions, structural vibration, vibration due to externally pressurized air bearings, or gyroscopic effects from the work-holding spindle.

5.2.3 Discovery & Detection of Spindle Star Error

The spindle star error is a form error that is believed to be caused by spindle movement [37] [40], resulting in a wavy surface in which the peaks and valleys form straight, radial spokes on the surface. These straight, radial spokes are constant throughout the surface and are not dependent on machine position. Although the spindle star pattern is not visible to the naked eye, the structured form error can be amplified in an optical system, causing imagining problems in a final application limiting its performance.

In these findings, the disturbance frequency was found to be constant over a range of spindle speeds, but is also not constant at other spindle speeds. In other words, the spindle star phenomenon has both synchronous and asynchronous components.

Using a force dynamometer, it has been observed that a distinct 400Hz frequency was found during the cutting operation when the force signal is analyzed using a Fast Fourier Transform (FFT) analysis in LabView 7.1. The FFT of a force measurement is shown below in Figure 5.57. To ensure accuracy in the results, 20,480 samples were taken at a rate of 10,240 samples per second.

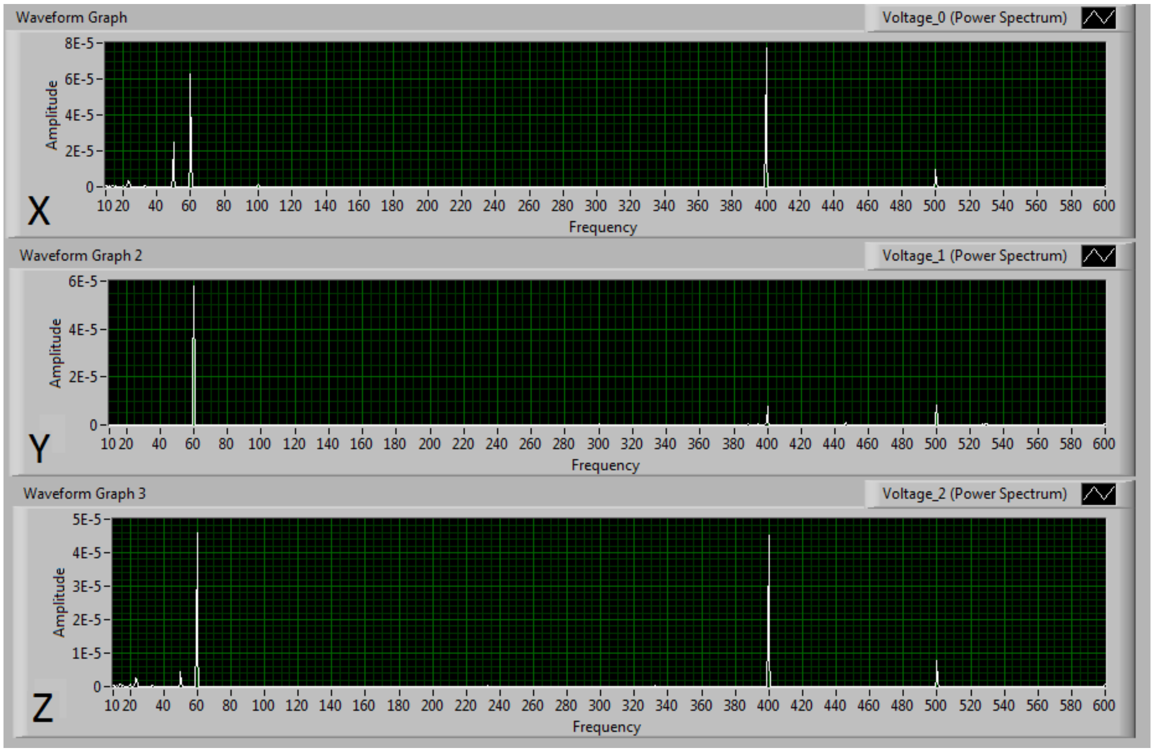

Figure 5.57 Example of 400Hz Disturbance in Force Dynamometer Reading at 1000RPM

In Figure 5.57, the cutting parameter used was a spindle speed of 1000RPM, feed rate of 5μm/rev and a depth of cut of 2μm. The X direction corresponds with the thrust force on the tool, while the Y and Z directions correspond with the feed and cutting force, respectively. Figure 3.7

shows the coordinate axes of the tool more clearly. The detection of 60Hz is not relevant as it corresponds with the line frequency given off by the charge amplifier used in the data acquisition system.

It has been observed that the number of spokes created by the disturbance frequency will change depending on the spindle speed. In these tests, different spindle speeds were used to produce an optical quality surface with a constant feed rate of 5μm/rev and 2μm depth of cut. An SCD tool with a 12mm nose radius and no modification to its cutting edge was used to produce these results. The disturbance frequency was found to be 400Hz or close to 400Hz in every test. Table 5.6 shows a summary of the initial tests performed to understand this phenomenon and Figure 5.58 to Figure 5.62 show the optical measurement of the machined surfaces under these conditions. Numbers of spokes are observable from 360° surface profile of these figures. The source and reason for low wavelength undulations on the surface profile will be discussed later. It is important to mention here that

Table 5.6 exactly represents Equation 5.10.

Table 5.6 Summary of Observed Disturbance Frequency and Spokes in Spindle Star

Disturbance frequency (Hz)	RPM (rev/min)	RPS (rev/sec)	Number of spokes, N
400	500	8.3	48.0
400	1000	16.7	24.0
408.4	1021	17.0	24.0
400	2000	33.3	12.0
400	3000	50.0	8.0

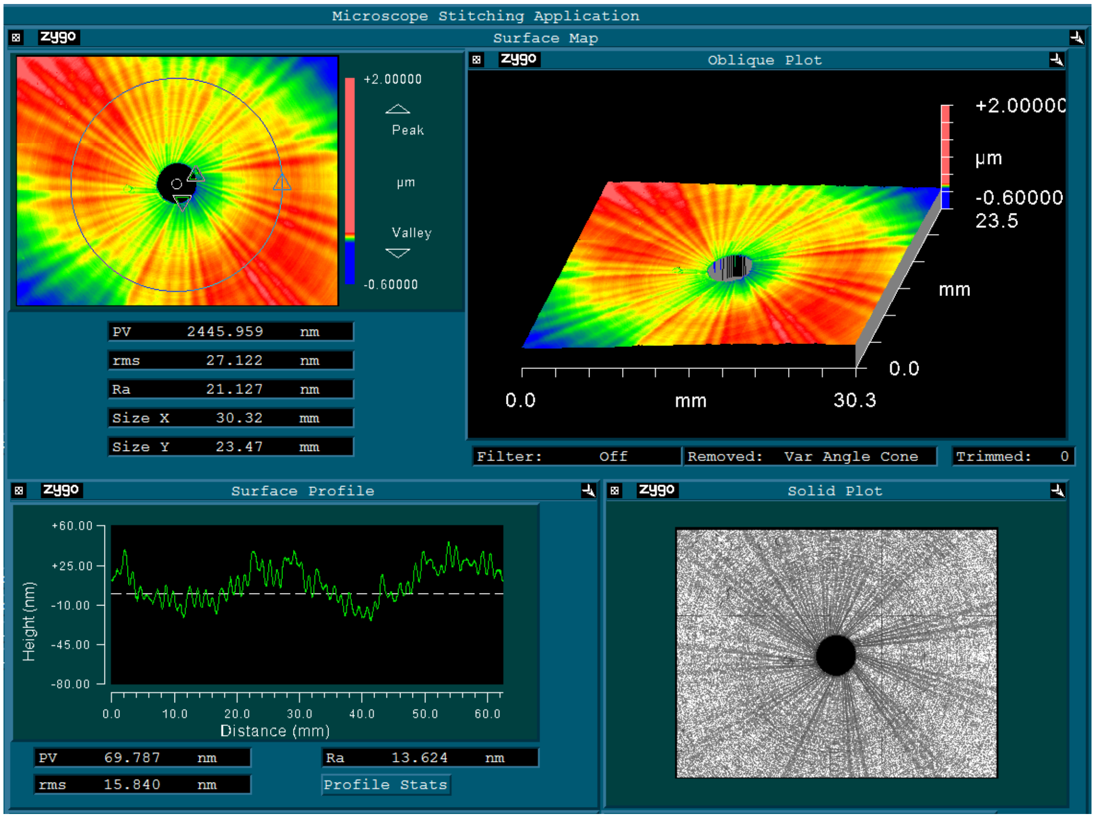

PV 2445.959 nm
rms 27.122 nm
Ra 21.127 nm
Size X 30.32 mm
Size Y 23.47 mm

Filter: Off
Removed: Var Angle Cone
Trimmed: 0

PV 69.787 nm
rms 15.840 nm
Ra 13.624 nm

Figure 5.58 Spindle Star at 500RPM, 10X Magnification, 48 Spokes

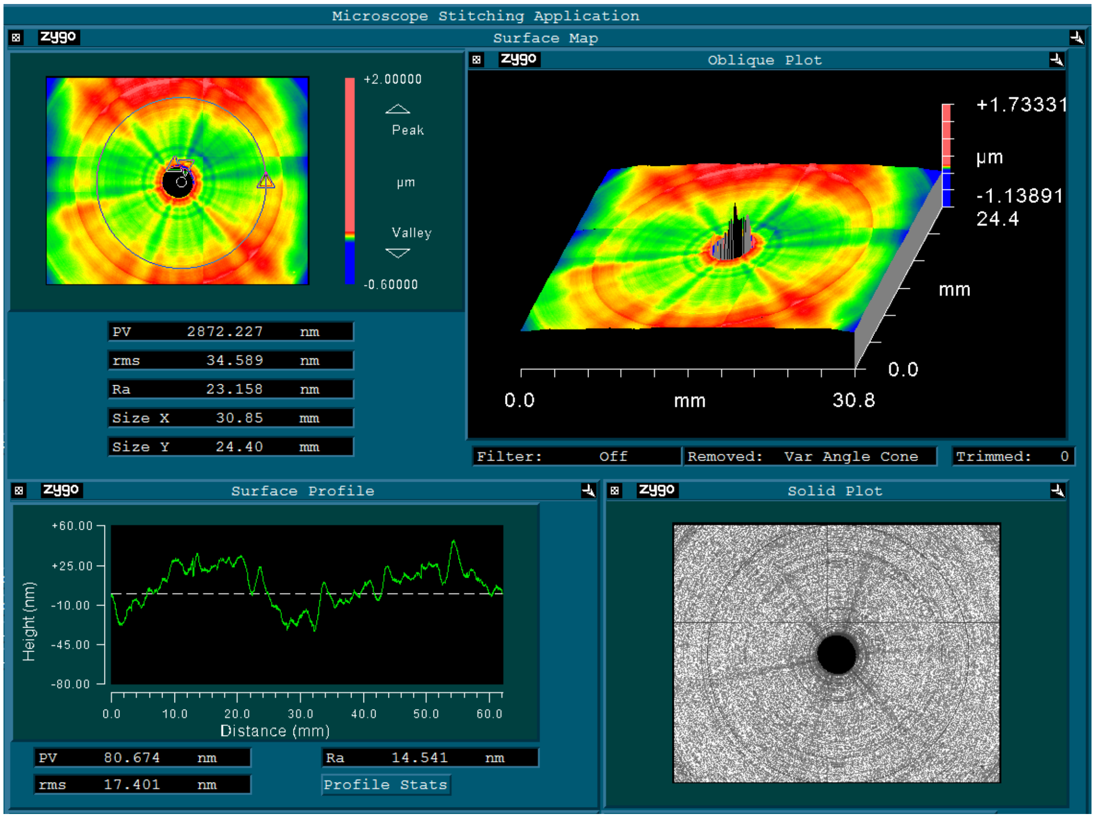

PV 2872.227 nm
rms 34.589 nm
Ra 23.158 nm
Size X 30.85 mm
Size Y 24.40 mm

Filter: Off
Removed: Var Angle Cone
Trimmed: 0

PV 80.674 nm
rms 17.401 nm
Ra 14.541 nm

Figure 5.59 Spindle Star at 1000RPM, 10X Magnification, 24 Spokes

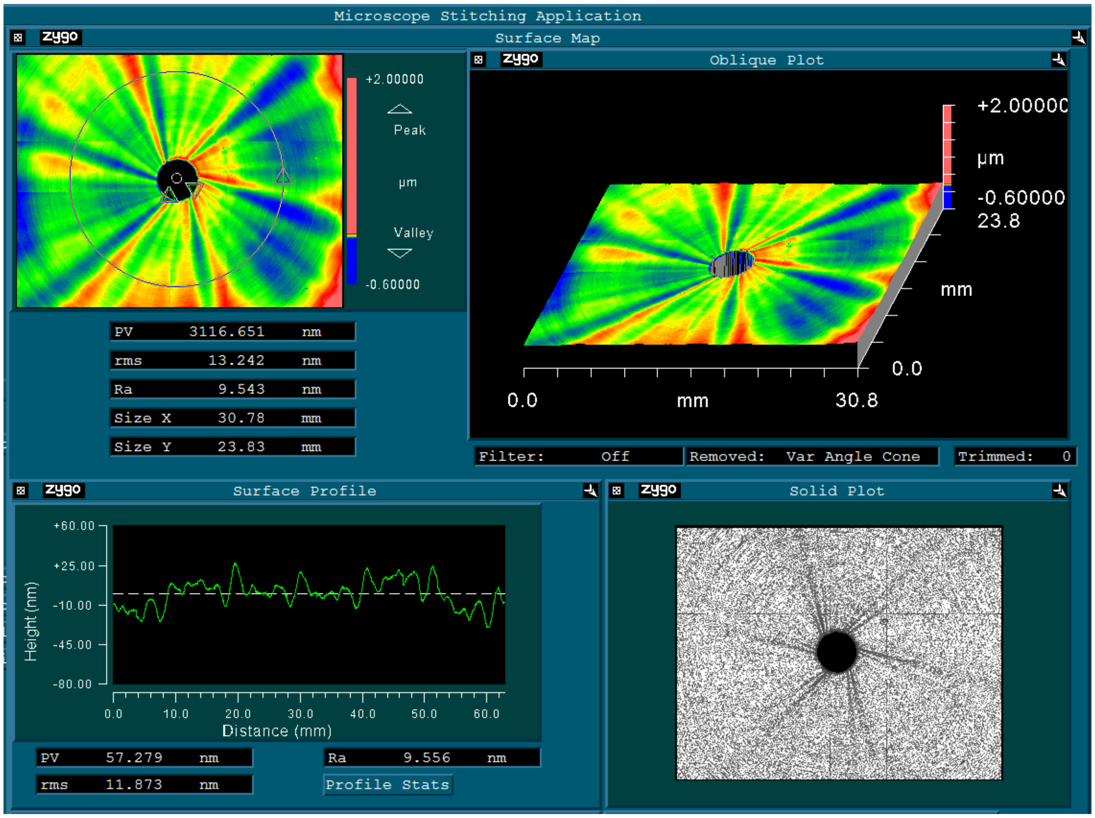

PV 3116.651 nm
rms 13.242 nm
Ra 9.543 nm
Size X 30.78 mm
Size Y 23.83 mm

Filter: Off
Removed: Var Angle Cone
Trimmed: 0

PV 57.279 nm
rms 11.873 nm
Ra 9.556 nm

Figure 5.60 Skewed Spindle Star at 1021RPM, 10X Magnification, 24 Spokes

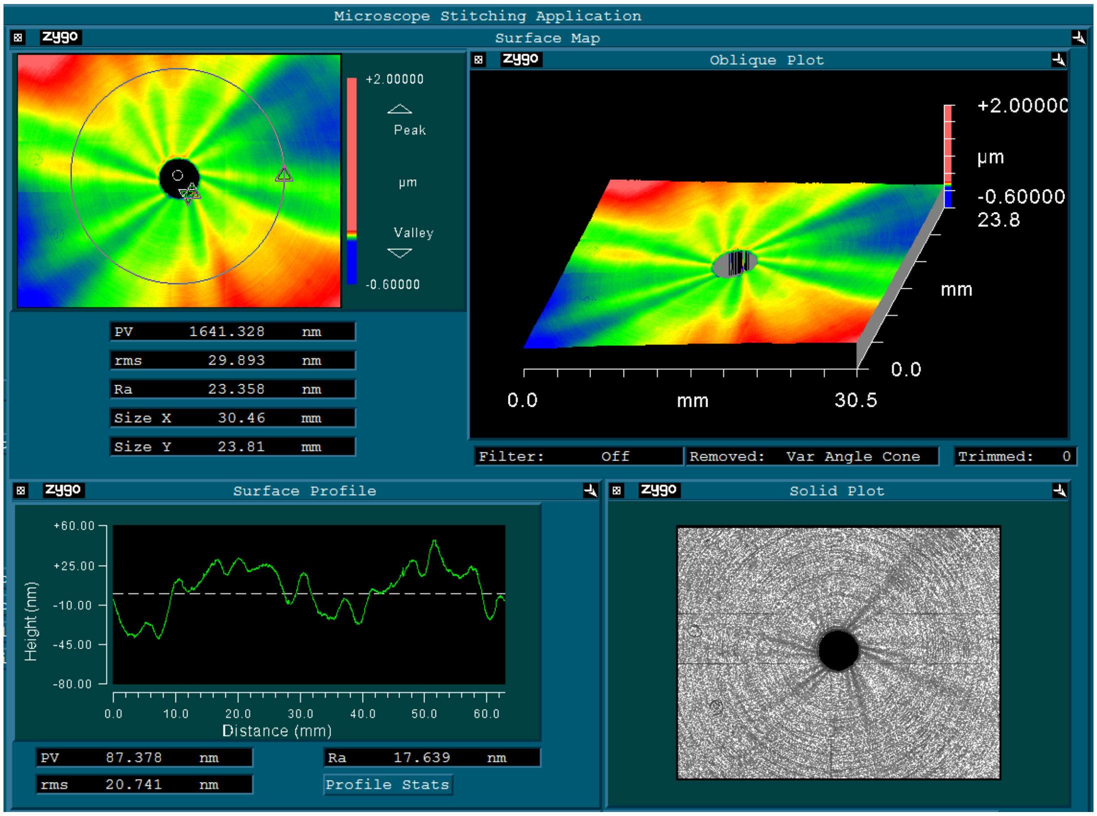

PV 1641.328 nm
rms 29.893 nm
Ra 23.358 nm
Size X 30.46 mm
Size Y 23.81 mm

Filter: Off
Removed: Var Angle Cone
Trimmed: 0

PV 87.378 nm
rms 20.741 nm
Ra 17.639 nm

Figure 5.61 Spindle Star at 2000RPM, 10X Magnification, 12 Spokes

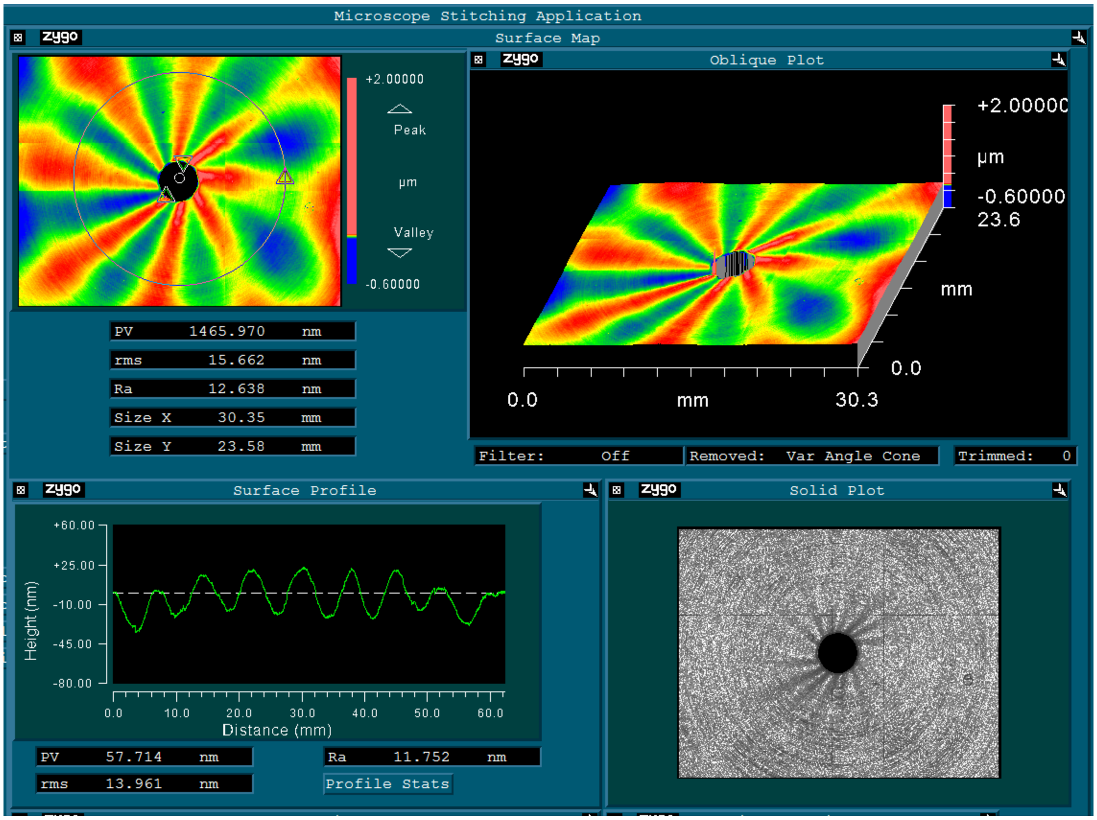

PV 1465.970 nm
rms 15.662 nm
Ra 12.638 nm
Size X 30.35 mm
Size Y 23.58 mm

Filter: Off
Removed: Var Angle Cone
Trimmed: 0

PV 57.714 nm
rms 13.961 nm
Ra 11.752 nm

Figure 5.62 Spindle Star at 3000RPM, 10X Magnification, 8 Spokes

5.2.3.1 Tool geometry and contact length in spindle star formation

Cutting tests were performed with different tools to determine the effects of process damping in an attempt to decrease the amplitude of the waviness. Three SCD tools were used with a spindle speed of 1000RPM, feed rate of 5µm/rev and a depth of cut of 2µm. All three tools produced the same 24-lobe pattern, corresponding with a disturbance frequency of 400Hz.These surfaces were scanned using the white-light interferometer. The annular Peak-To-Valley (PV) reading was taken from a circular profile 10mm in diameter from the center of the part. These results are summarized below in Table 5.7.

Table 5.7 Tools Used in Spindle Star Investigation

Tool	Nose Radius	Edge Preparation	Annular PV (nm)
1	12mm	None	80.693
2	12mm	Chemically Honed	87.061
3	0.5mm	None	82.137

The result was that these tools do not show a significant change in the PV amplitude of the spindle star error. Using CAD software, the geometric length of the line contact on the workpiece was estimated in Table 3.2. With a small contact length and low cutting forces, the damping effect of the different SCD tools is insignificant when compared to other factors in the cutting process and does not affect the amplitude of spindle star error.

The vibration frequency that causes spindle star error is also independent of the tool-workpiece contact. An experiment was performed where the RSA 6061 workpiece was cut using a 0.5mm nose radius tool at 1000RPM with a feed rate of 5µm/rev and a depth of cut of 2µm. The machine tool was then set to run the cutting tool about 2µm away from the freshly cut surface, called air cutting. A second test was performed with the same cutting parameters, but with a 12mm nose radius tool and at a spindle speed of 3000RPM. The FFT of the force dynamometer signals were extracted from LabVIEW and plotted below in Figure 5.63 and Figure 5.64. Both tests showed similar frequencies at 400Hz but with different force amplitudes. This means, the changes in tool nose radius and tool contact do not affect the disturbance frequency that causes spindle star error. Therefore, the tool-workpiece contact is not a major factor in determining the disturbance frequency of the spindle star phenomenon. These two results also suggest that the disturbance frequencies and its characteristics are independent of the cutting process and in fact is a part of the machine's dynamic behavior and the amplitude of such vibration increases with higher RPM.

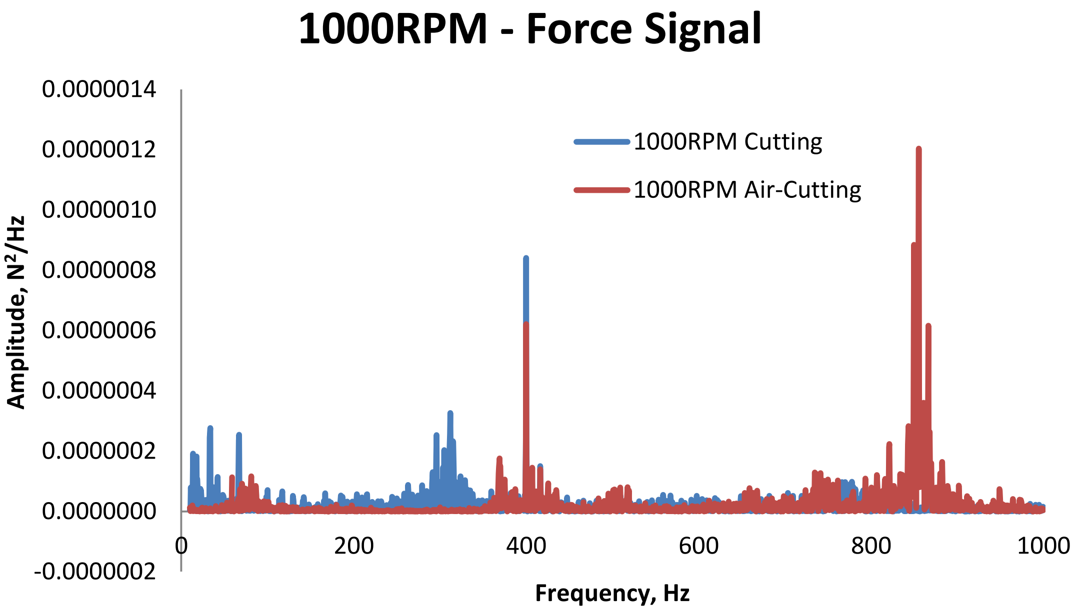

Figure 5.63 FFT of Force Signal in Cutting and Air Cutting, 1000RPM Spindle Speed, Tool Thrust Direction, 0.5mm nose radius tool

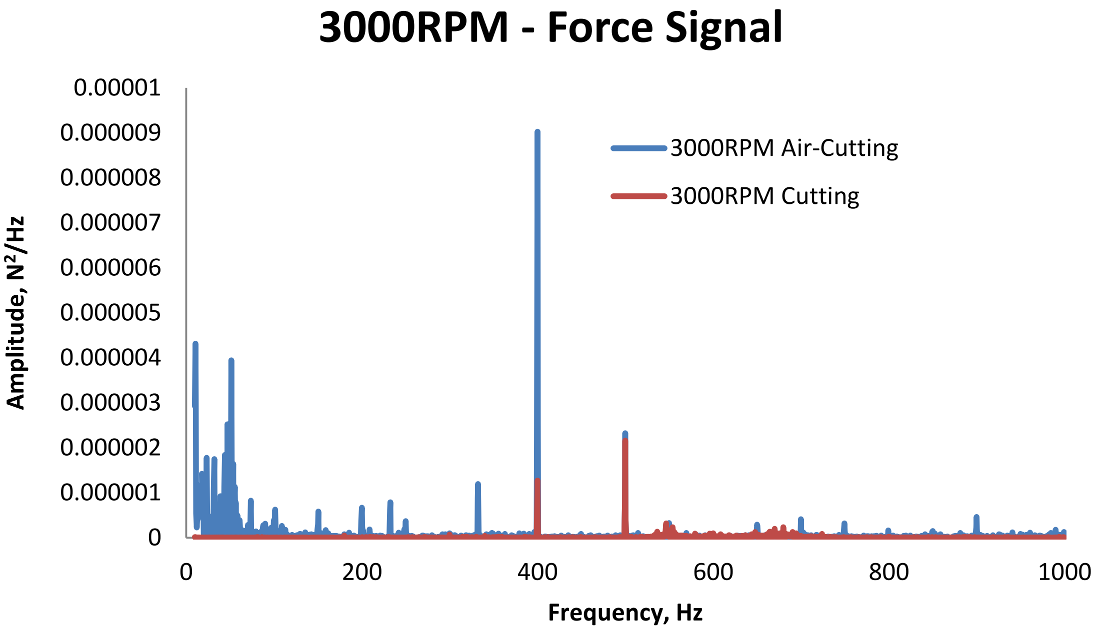

Figure 5.64 FFT of Force Signal in Cutting and Air Cutting, 3000RPM Spindle Speed, Tool Thrust Direction, 12mm nose radius tool

5.2.3.2 Consistent Spindle Star Disturbance Frequency

For a cutting test at 3000RPM, feed rate of 5µm/rev and a depth of cut of 2µm, three force measurements were taken one case was for when the tool is entering cut near the outer diameter, in the center of the part, and near the inner diameter of the part. The FFT data is shown below in Figure 5.65. Again, the 60Hz reading is irrelevant as it corresponds with the switching frequency of the charge amplifier used with the force dynamometer. These three measurements show the same disturbance frequency of 400Hz and 500Hz is present in generating the entire surface that can also be seen as spindle star on the finished workpiece with optical measurements as shown in Figure 5.62. These vibrations are consistent, even at the center of the workpiece.

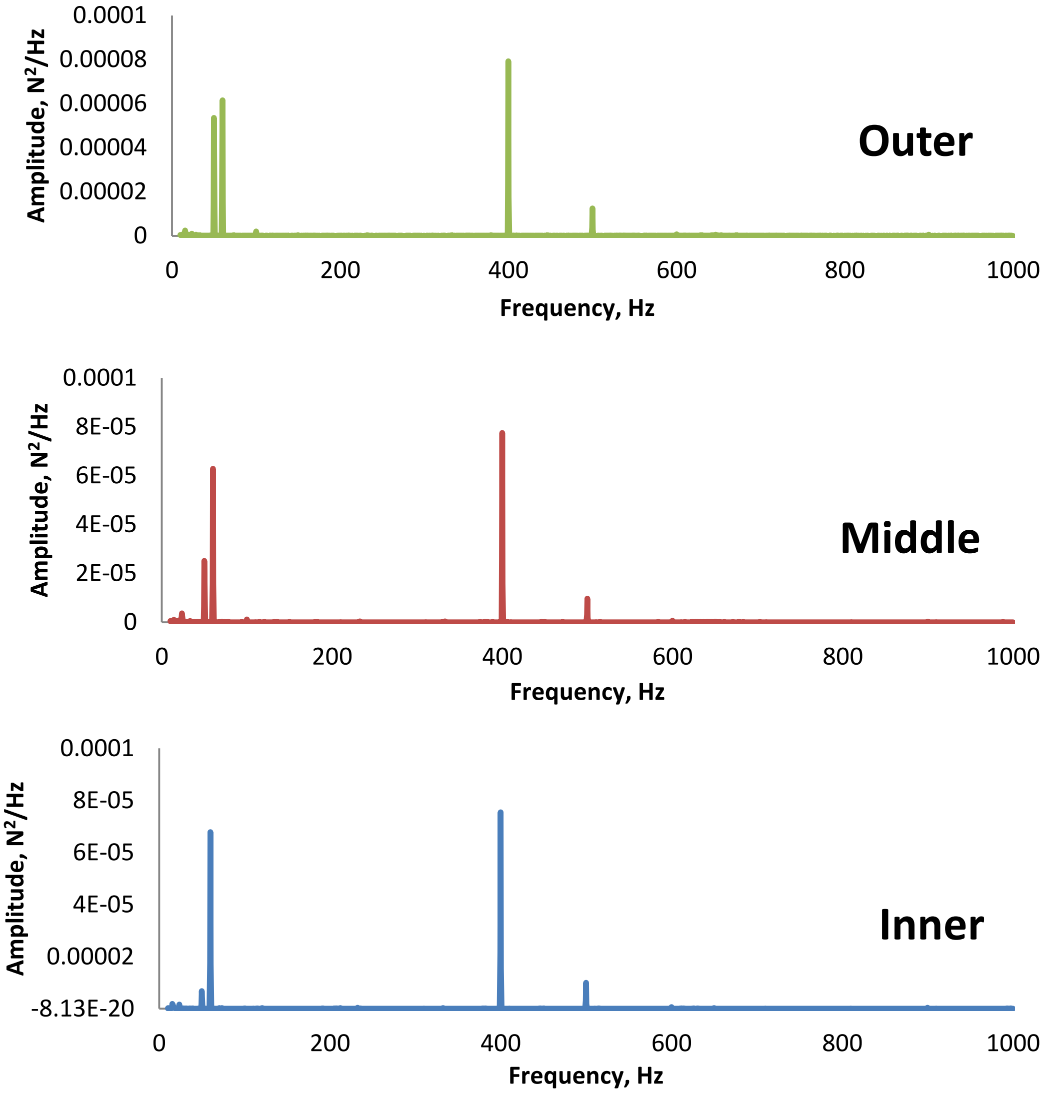

Figure 5.65 Force Measurement Near OD, Center, and ID, Respectively For 3000RPM

5.2.3.3 Material and its effect on spindle star

It was also observed that these vibrations are independent of the workpiece material. The aluminum workpiece contained a hole in its center in order to simplify machine setup. A copper workpiece, 25mm in diameter, was diamond turned at 1000rpm with a feed rate of 5µm/rev and a depth of cut of 2µm. An optical-quality finish was achieved, shown in Figure 5.66. This workpiece was scanned using the Zygo WLI. The WLI scan Figure 5.67 shows a spindle star pattern that extends to the very center of the workpiece with 24 lobes, a pattern identical to that of the aluminum workpiece. The spindle star error is independent of the workpiece material. It is also present from the outer diameter to the very center of the workpiece.

Figure 5.66 Diamond Turned Copper Workpiece

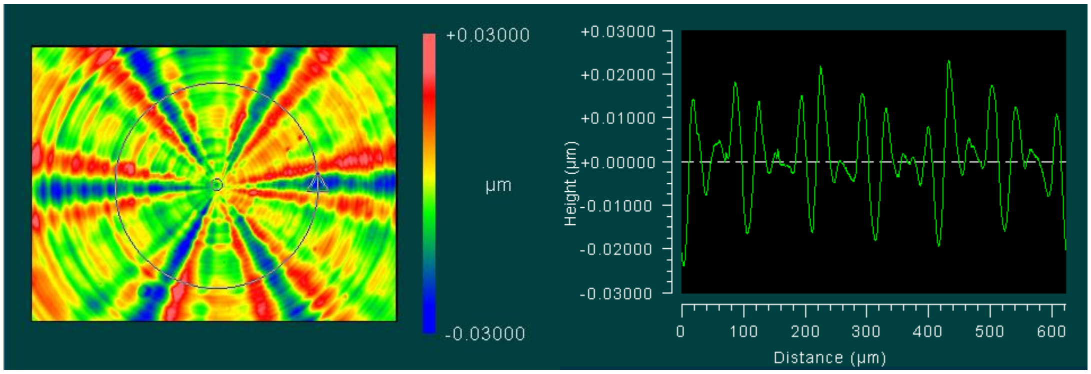

Figure 5.67 Spindle Star in Copper Workpiece, 1000RPM, 24 Spokes, 400X Magnification

5.2.4 Machine Component Modal Tests and Source of Spindle Star Error

The source of this spindle star error required an investigation of the individual machine components to isolate its source by performing a series of modal tests. A modal test requires the use of a force hammer to strike the component with a sharp impulse force. The force hammer is instrumented to measure the magnitude of the impulse force. An accelerometer is mounted to the component to measure the magnitude, and frequency of the vibration due to the sharp impulse force to measure the modal stiffness, damping ratio, and natural frequency of the component. As mentioned in Chapter 5.2.2, a perturbation in an air bearing will cause it to vibrate due to a pressure differential between opposing orifices. The modal test will then determine the frequency at which this stabilizing effect occurs.

Although the phenomenon is named “spindle star error”, there is a possibility that the source of the error is due to the vibration of the machine tool’s structure and or forced vibration by the control feedback loop. Sensitive accelerometers and small force hammers were used carefully to limit the number of components being excited by the force hammer. The CutPro 9 software from the Machining Automation Laboratories was used here to analyze the data. The equipment used is listed in Table 5.8.

Table 5.8 Equipment Used to Investigate The Source of Error

Instrument Type	Model
Force Hammer	PCB Piezotronics 086B01
Accelerometer	Kistler 8730A500M1
Data Acquisition	National Instruments NI 9234
Data Acquisition to USB Interface	National Instruments NI cDAQ 9172

The modal tests were performed at three locations on the machine. The first is the tool-side test where an accelerometer is glued to the front of the tool-holding clamp and the force hammer was used to strike the front face of the tool-holding fixture. The second test is the spindle-side test, where an accelerometer was mounted to the center of the spindle face and the force hammer was struck on the face of the spindle as close to the accelerometer as possible. The third location is the Z-axis slide, where an accelerometer is mounted to the Z-axis with the force hammer striking the back of the Z-axis slide. A series of tests were designed to help eliminate the source of the asynchronous error, identified as a vibration at approximately 400Hz.

The first set of modal tests was performed on the machine with all its components online to serve as a benchmark for vibration response for all components. Components will be isolated and taken offline in order to pinpoint the source of the spindle star error. A natural frequency of 384 Hz was detected at the spindle, and 411Hz was detected at the tool fixture. The MalTF program outputs are shown in Figure 5.68 and Figure 5.69 for tests on the spindle face and tool fixture, respectively. The signal coherence represents the correlation between the input and output system. If the coherence is below 0.8, in the frequency range that is being studied, then the result is considered to be invalid.

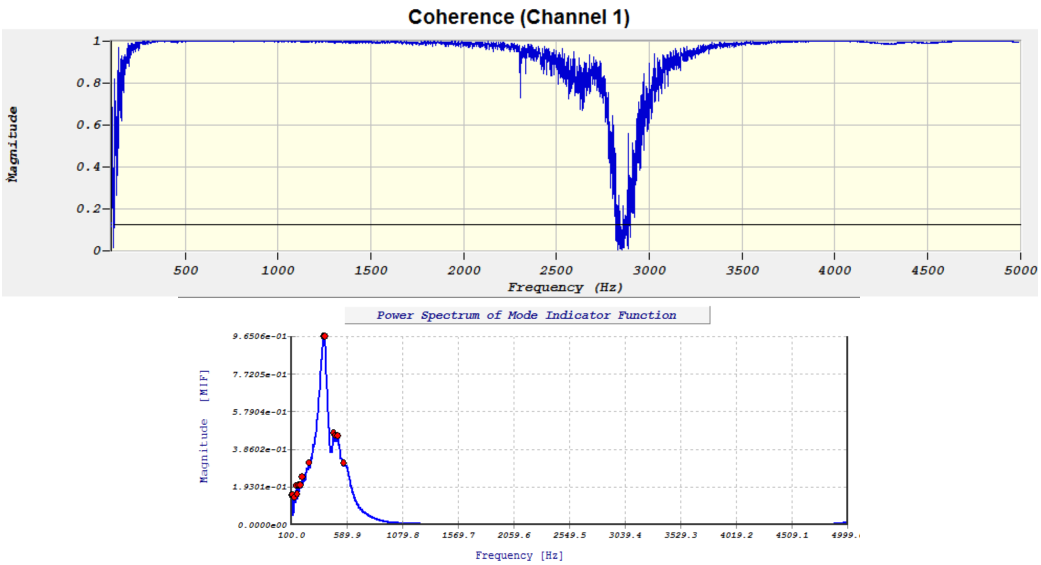

Figure 5.68 Signal Coherence and Frequency Response of Spindle Face, With All Machine Functions

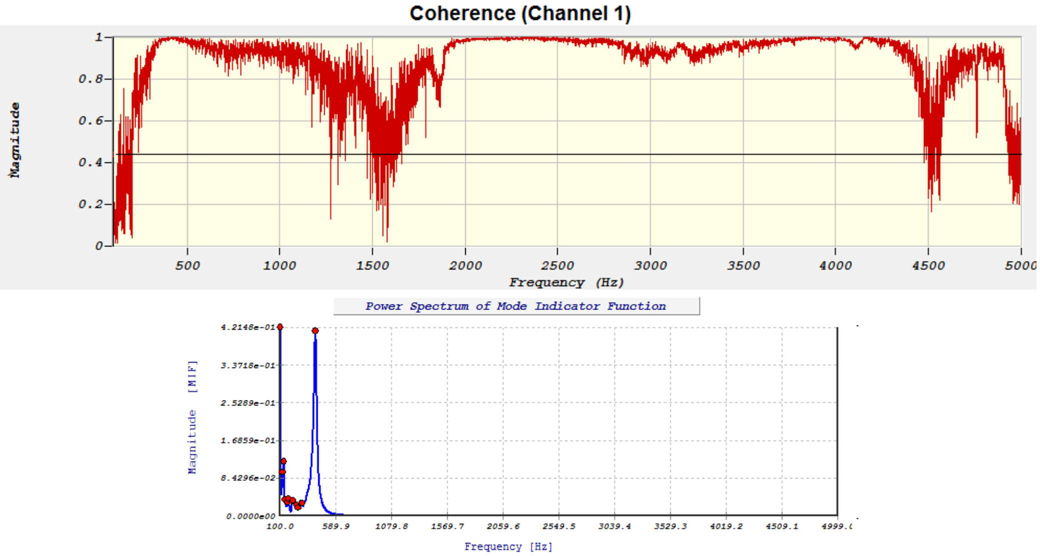

Figure 5.69 Signal Coherence and Frequency Response of Tool Fixture, With All Machine Functions

An extra test was performed with the accelerometer attached to the outer diameter of the spindle head to find the natural frequency of the spindle in the radial direction. The results are shown below in Figure 5.70. Two frequencies were detected at 392Hz and 465Hz.

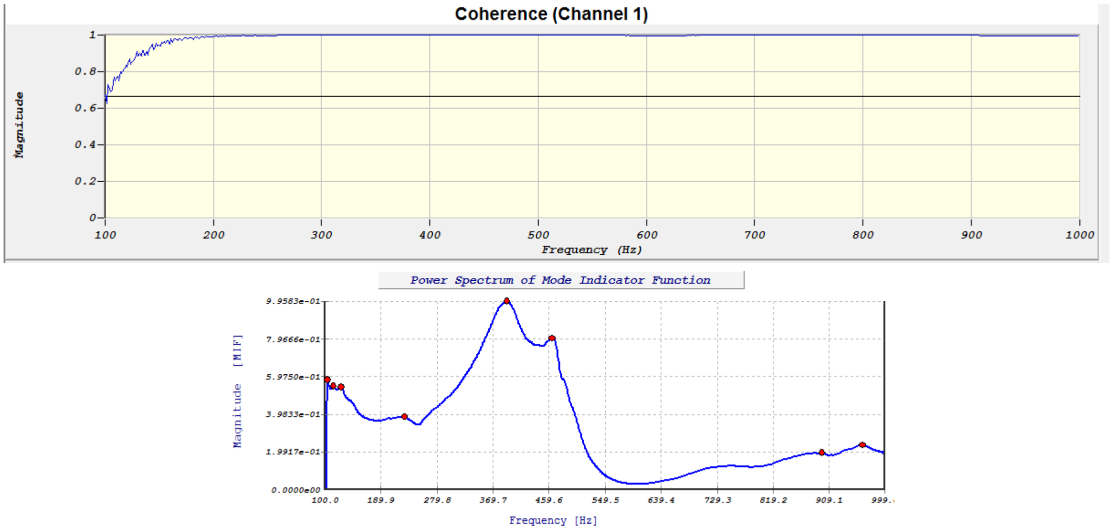

Figure 5.70 Signal Coherence and Frequency Response of Radial Direction of Spindle Face, With All Machine Functions

The second test required the use of the Precitech’s cylinder balancing utility to disable the linear motor control to the Y-axis. By doing this and repeating the modal test, disturbance from the controller compensating for movement in the Y-axis is eliminated. A modal test was not performed on the spindle as the disabling of the Y-axis does not affect the Z-axis and spindle. The detected natural frequency, shown in Figure 5.71, was identical to the previous test at 411Hz, eliminating the Y-axis controller as the cause of asynchronous motion.

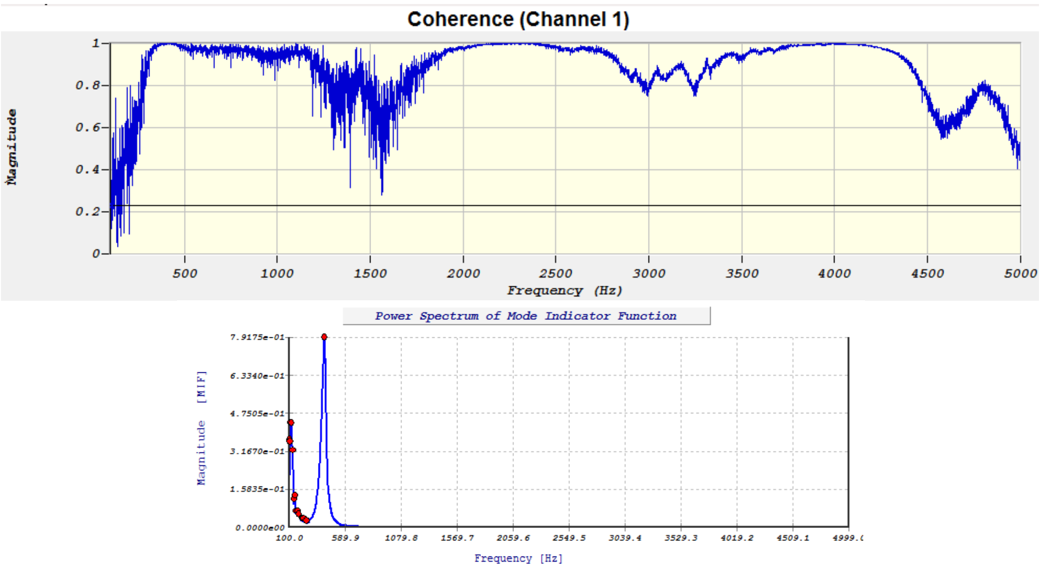

Figure 5.71 Signal Coherence and Frequency Response of Tool Fixture, With Y-Axis Disabled

The third test required the machine to be in “Emergency Stop” mode. When the emergency stop button is pressed, mechanical brakes are engaged on the Y-axis while the controller releases control to the X and Z-axes, allowing them to freely float on the machine’s hydrostatic bearings. A modal test was performed on the spindle face with a detected natural frequency of 385Hz. The modal test for the tool holding fixture detected a dominant frequency at 419Hz. The mechanical brakes increased the stiffness of the Y-axis, causing the natural frequency to shift upwards slightly. These results are shown in Figure 5.72 and Figure 5.73 for the spindle face and tool fixture of the machine tool, respectively.

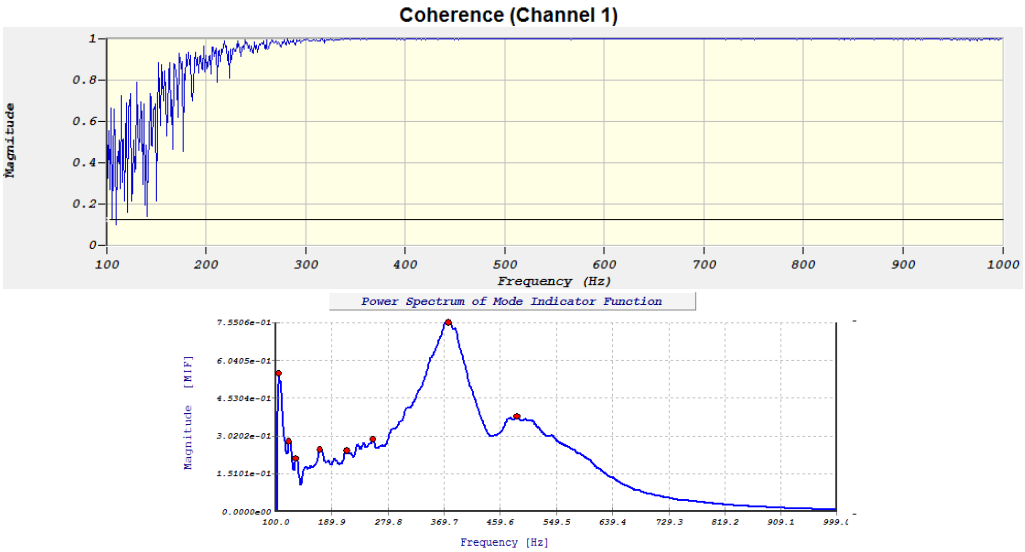

Figure 5.72 Signal Coherence and Frequency Response of Spindle Face, With Emergency Stop Engaged

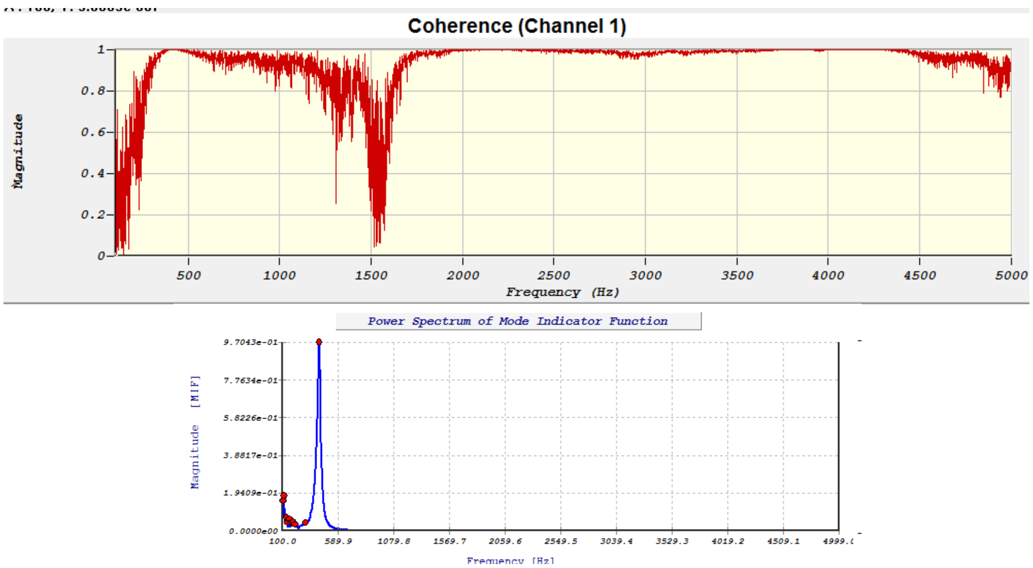

Figure 5.73 Signal Coherence and Frequency Response of Tool Fixture, With Emergency Stop Enabled

The Z-axis slide was also tested with an accelerometer mounted to the base of the Z-axis. A frequency of 396Hz was detected (Figure 5.74), but with poor coherence. The relatively small force hammer did not excite any frequencies in the structure other than a faint vibration from the spindle placed far away on top of the Z-axis slide. The source of the spindle star error is not caused by the rocking of the Z-axis on its hydrostatic ways.

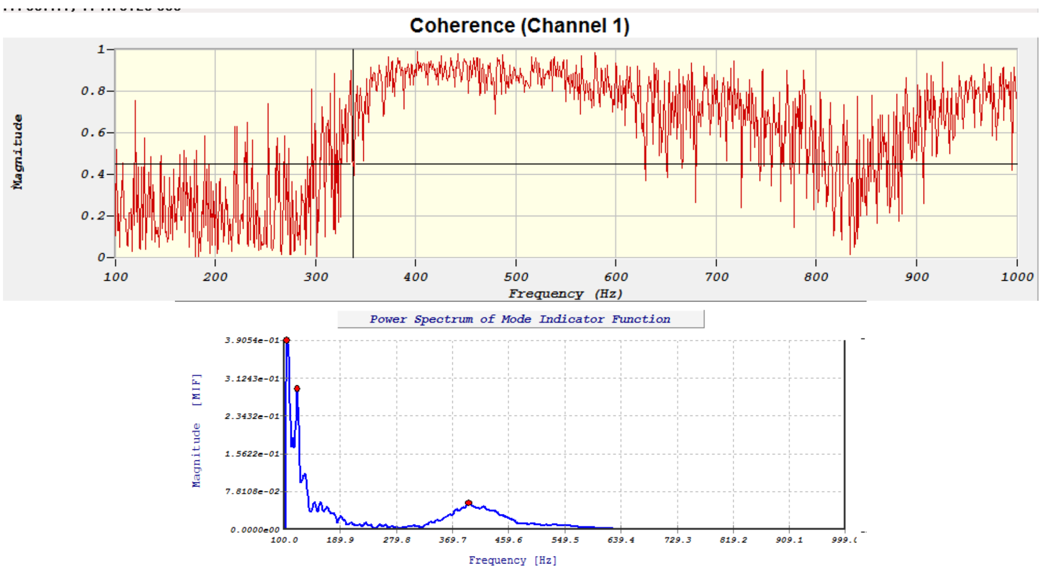

Figure 5.74 Signal Coherence and Frequency Response of Z-Axis Slide, With Emergency Stop Engaged

For the fourth series of tests, the air supply to the machine tool was shut off, disabling the air bearings in the spindle. The “Emergency Stop” mode continued on the machine, locking the Y-axis using mechanical brakes and disabling control to the linear motors in the machine. No changes were observed in the detected frequencies in the tool-holding fixture as compared to the previous tests. While testing the spindle face (Figure 5.75), two dominant frequencies were detected, at 384Hz and 629Hz. The dynamic stiffness associated with 384Hz is much higher without an air supply as the rushing air will no longer cushion the structure inside the spindle, the bearing surfaces inside the spindle are now in direct contact.

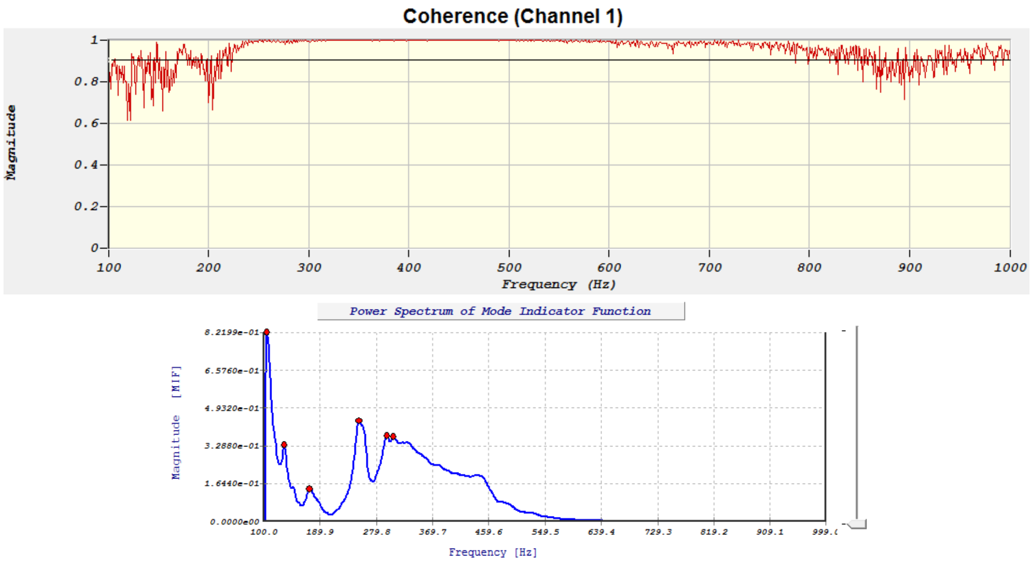

Figure 5.75 Signal Coherence and Frequency Response of Spindle Face, With Emergency Stop and No Air Supply

When the air supply is engaged, the rushing of air into the spindle body will excite a structure within the air bearing spindle at approximately 385Hz. Once the air supply has been disabled, the structure is no longer excited by the air, allowing the vibration of other components in the spindle to be detected. There is also no possibility of air hammer instability without an external air supply. The results of these modal tests are summarized below, in Table 5.9.

Table 5.9 Summary of Modal Tests

Test Condition	Test Location	Dominant Frequency (Hz)	Machine Features Eliminated	Modal Stiffness (N/µm)	Damping Ratio (%)
Machine Online	Spindle Face	384	None	66.201	11.503
	Tool Fixture	411		80.488	4.670
Y-Axis Disabled	Tool Fixture	408	Y-Axis Active Position Control	80.018	5.640
Emergency Stop	Spindle Face	385	Active Position Control, All Axes	41.173	14.151
	Tool Fixture	419		90.372	4.198
Air Supply Shutdown	Spindle Face, Two Peaks	390 683	Spindle Air Bearing	348.28 69.181	9.554 24.638

The source of the form error is due to a structure vibrating at its natural frequency in the air bearing spindle. When the air bearings are energized, the rushing air will excite the structure, causing it to vibrate at approximately 385Hz. When there is no air in the system, the air bearing falls and rests against the bearing outer race. This increases the stiffness significantly. This vibration will also cause the tool fixture to vibrate at its natural frequency at about 411Hz. The modal stiffness of the fixture is much higher than that of the spindle. Therefore, the largest contributor to the error leading to the spindle star surface is vibration of the spindle.

A 4kg steel mass was attached to the spindle to measure its effects on the natural frequency of the spindle. The results of the modal test are shown in Figure 5.76.

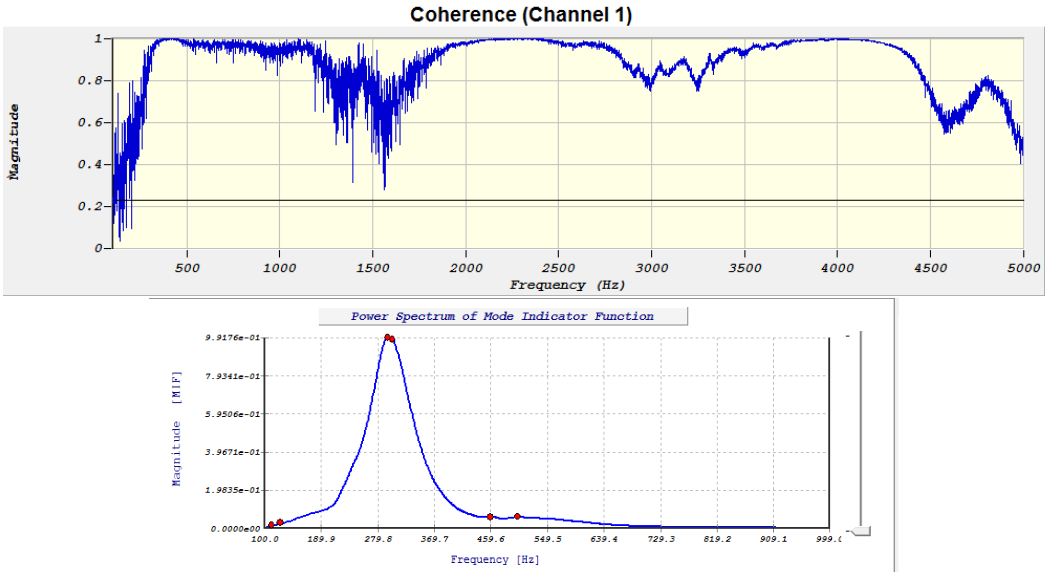

Figure 5.76 FRF and Coherence Graph for SP-90 Spindle with 4kg Mass

Due to the increase in mass, the spindle’s natural frequency was lowered to 310Hz from 385Hz. A cutting test was performed to determine the effects that the increased mass has on the resulting workpiece surface and the result is shown in the next section on Page 143.

5.2.5 Rotordynamic Analysis of Spindle Star Error

The disturbance frequency associated with spindle star error, to this point, has been assumed to be constant at 400Hz. An experiment was performed to attempt to create a phase lag of vibration between rotations of the spindle in order to kink or scramble the lobes of the spindle star pattern on the diamond turned surface. Table **5.10** lists the measurement equipment used in this section.

Table 5.10 Equipment Used In Rotordynamic Analysis of Air-Bearing Spindle

Instrument Type	Model
Force Dynamometer	Kistler 9256B1
Accelerometer	Kistler 8730A500M1 (500g) Kistler 8640A5 (5g)
Data Acquisition	National Instruments NI 9234
Data Acquisition to USB Interface	National Instruments NI cDAQ 9172
Surface Topography Measurement	Zygo NewView 5000 WLI

These cutting tests were performed with a 1.5mm nose radius tool with a feed rate of 5μm/rev and 2μm depth of cut on an aluminum workpiece. The disturbance frequency was detected using the Kistler force dynamometer in the tool thrust direction. A summary of the force dynamometer measurements is shown below (Table 5.11). To confirm the results, the freshly cut surfaces were scanned on the Zygo WLI, shown in Figure 5.77 to Figure 5.80. The FFT data from the tool thrust force measurements are below in Figure 5.81.

Table 5.11 Expected and Actual Disturbance Frequencies For Targeted Number Of Spindle Star Lobes

Spindle Speed (RPM)	Expected Disturbance Frequency	Expected Number of Lobes	Actual Disturbance Frequency	Actual Number of Spindle Star Lobes
3000	400Hz	8	400Hz	8
3200	400Hz	7.5	426.67Hz	8
3310	400Hz	7.25	441.33Hz	8
3429	400Hz	7	457.2Hz	8

The number of spindle star lobes stayed constant despite the change in spindle speed. Thus, the assumption that the disturbance frequency is constant at 400Hz is incorrect. Instead, the disturbance frequency will be close to 400Hz, changing to reflect the closest even integer harmonic of the rotational frequency. The rotational frequency is measured in revolutions per second, or RPS. A thorough investigation of the rotordynamic properties of the air bearing spindle is thus required.

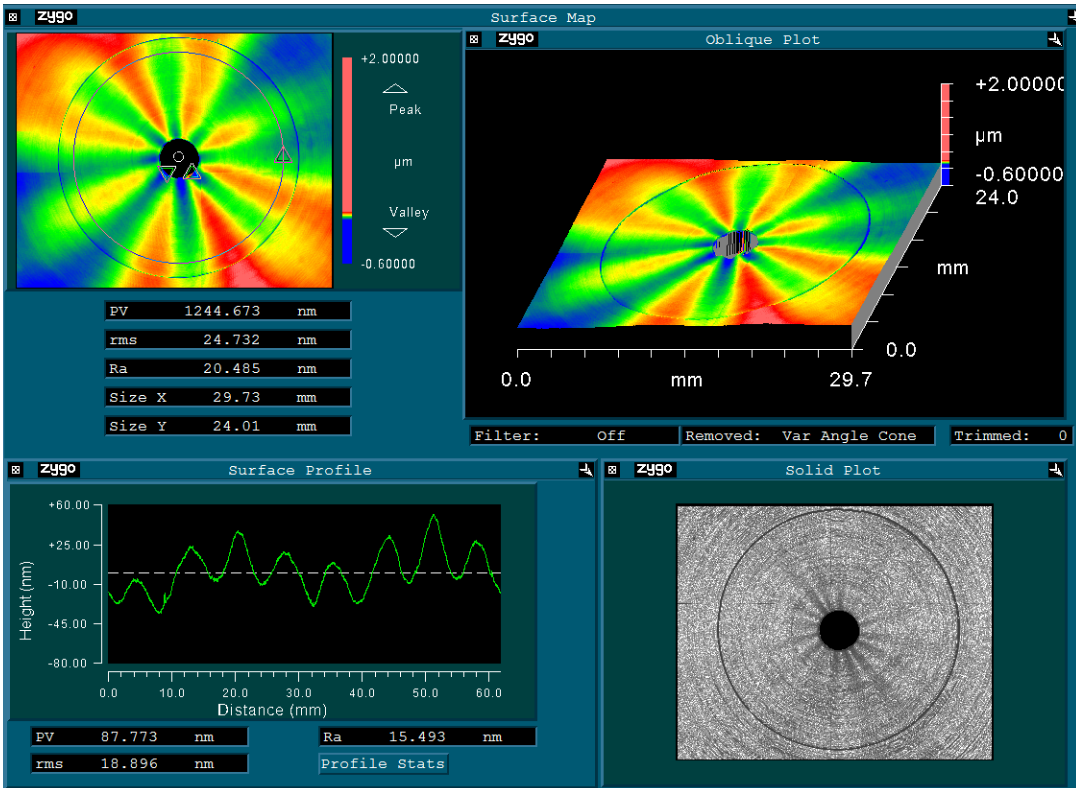

PV 1244.673 nm
rms 24.732 nm
Ra 20.485 nm
Size X 29.73 mm
Size Y 24.01 mm

Filter: Off
Removed: Var Angle Cone
Trimmed: 0

PV 87.773 nm
rms 18.896 nm
Ra 15.493 nm

Figure 5.77 Interferometer Measurement Showing 8 Lobes At 3000RPM

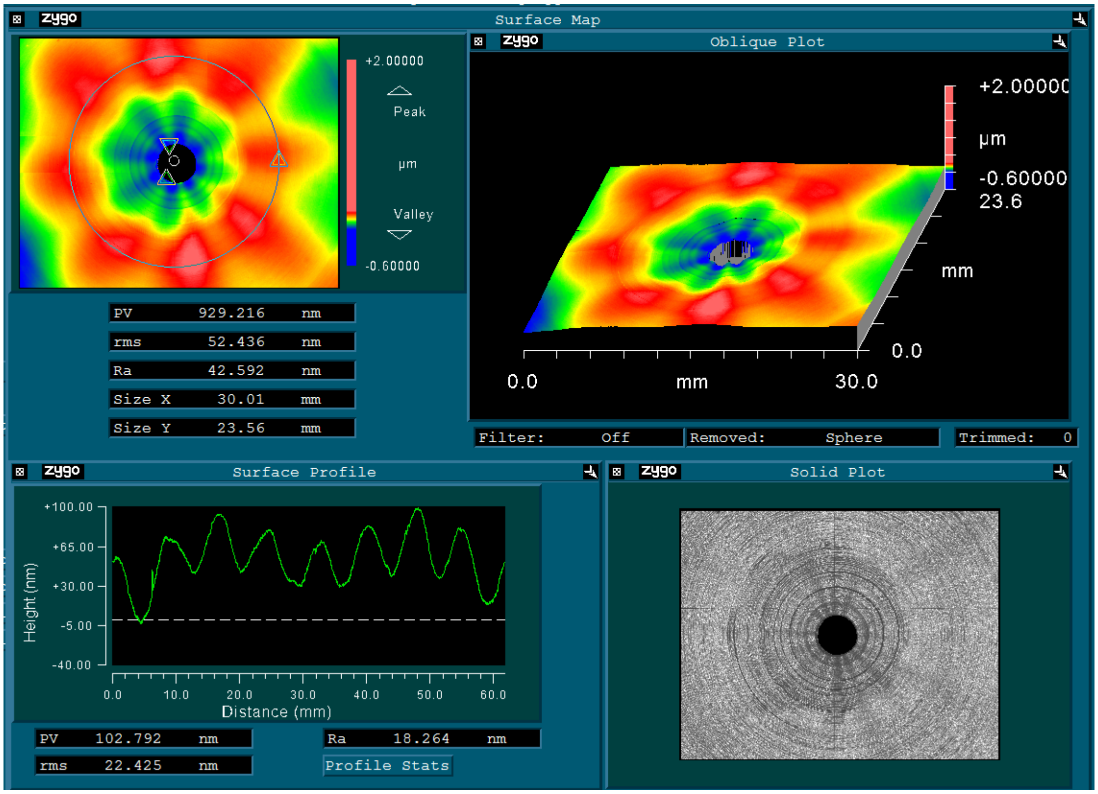

PV 929.216 nm
rms 52.436 nm
Ra 42.592 nm
Size X 30.01 mm
Size Y 23.56 mm

Filter: Off
Removed: Sphere
Trimmed: 0

PV 102.792 nm
rms 22.425 nm
Ra 18.264 nm

Figure 5.78 Interferometer Measurement Showing 8 Lobes At 3200RPM

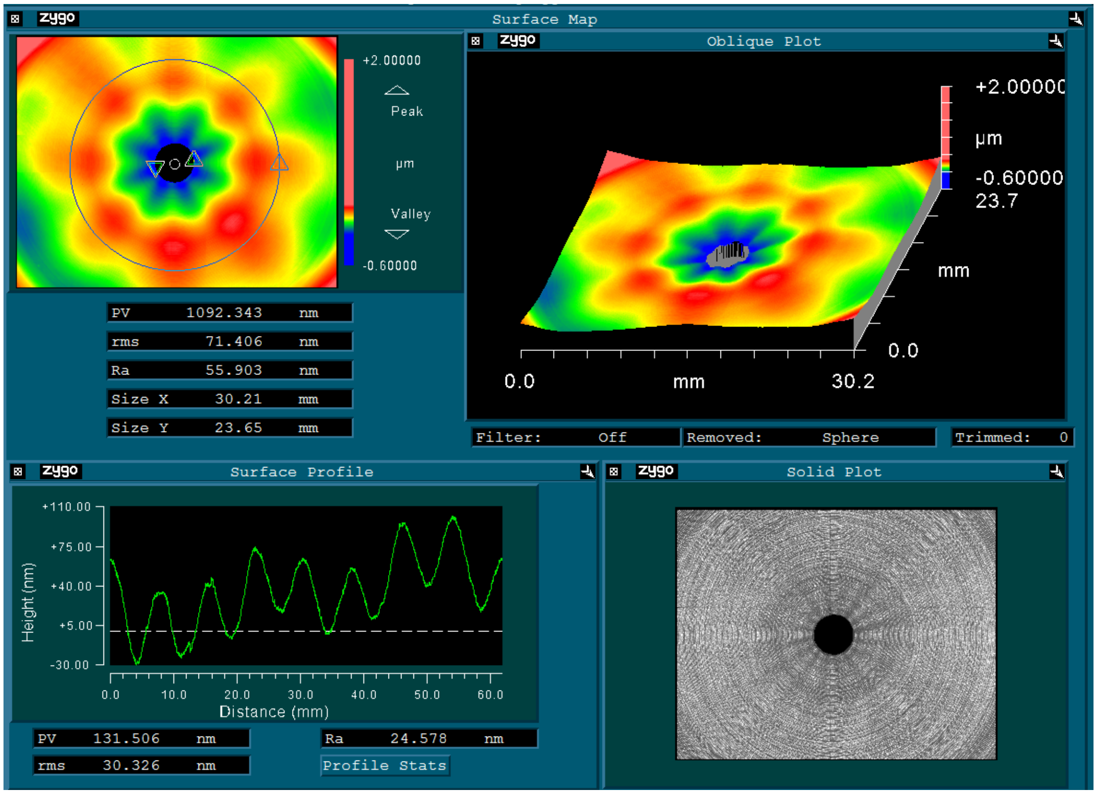

PV 1092.343 nm
rms 71.406 nm
Ra 55.903 nm
Size X 30.21 mm
Size Y 23.65 mm

Filter: Off
Removed: Sphere
Trimmed: 0

PV 131.506 nm
rms 30.326 nm
Ra 24.578 nm

Figure 5.79 Interferometer Measurement Showing 8 Lobes At 3310RPM

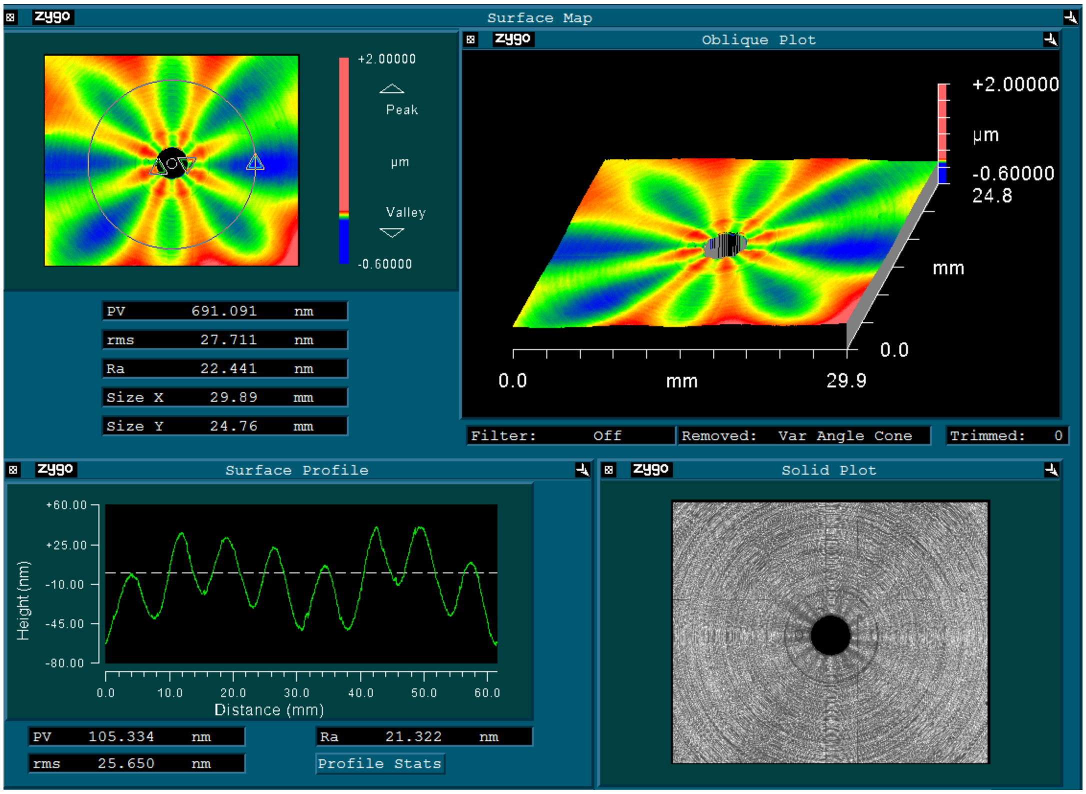

PV 691.091 nm
rms 27.711 nm
Ra 22.441 nm
Size X 29.89 mm
Size Y 24.76 mm

Filter: Off
Removed: Var Angle Cone
Trimmed: 0

PV 105.334 nm
rms 25.650 nm
Ra 21.322 nm

Figure 5.80 Interferometer Measurement Showing 8 Lobes At 3429RPM

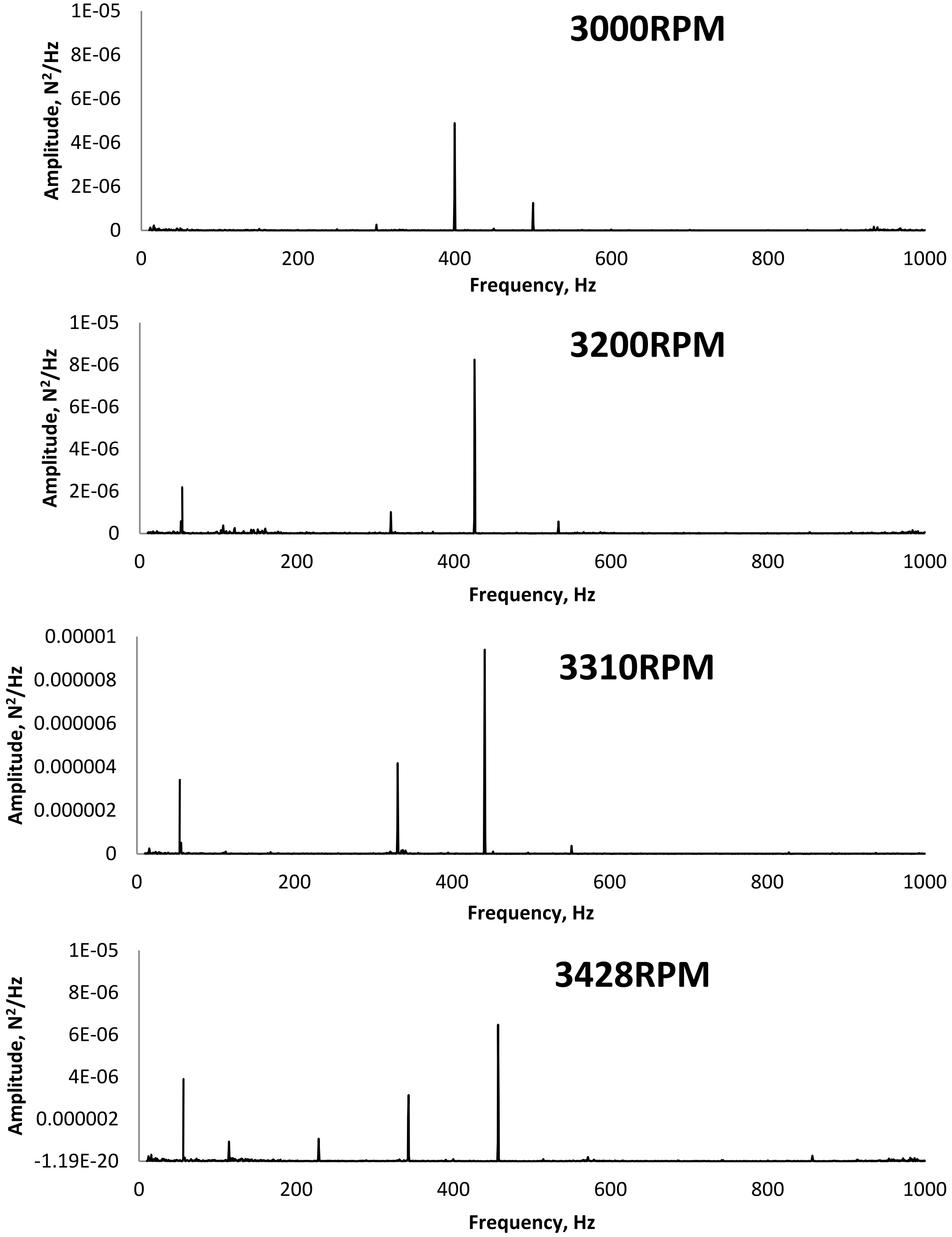

Figure 5.81 FFT of Tool Thrust Force For Four RPMs (5µm/rev feed rate and 2µm depth of cut)

It has been shown earlier that the disturbance frequency causing spindle star error is independent of the tool-workpiece contact and that it originates from the spindle. To further understand the dynamic properties of the air bearing spindle in SPDT, a rotordynamic analysis was performed. Analytical and numerical simulations were not performed due to the lack of information on the internal geometry of the spindle and air bearings. An experimental approach was taken instead. To generate the Campbell plot for rotodynamic analysis, cutting tests were performed with a feed rate of 5μm/rev and with a depth of cut of 2μm. Spindle speeds ranged from 400RPM to 3600RPM, with cutting tests performed in 200RPM intervals. The workpiece used was an RSA-6061 workpiece 60mm in diameter. A sharp SCD tool with 12mm nose radius was used to create these Campbell plots.

Table 5.12 summarizes the disturbance frequency and recorded number of spindle star spokes for all the cutting tests performed.

Table 5.12 Summary Of Spindle Star Frequencies With Changing Spindle Speed

Spindle Speed (RPM)	Rotational Frequency (RPS)	Disturbance Frequency (Hz)	Spindle Star Spokes
500	8.333	400	48
600	10	360	36
1000	16.667	400	24
1021	17.017	408.4	24
1100	18.333	440	24
1200	20	360	18
2000	33.333	400	12
2400	40	400	10
3000	50	400	8
3600	60	480	8

In the waterfall plots, a line can be drawn on the frequency-spindle speed plane using Equation 5.10, described earlier in Chapter 5.2.1. The accelerometer attached to the spindle represents all the frequencies generated by the spindle during operation, including electrical noise and turbulent air in the air bearing. Despite the presence of noise, Figure 5.82 shows a clear trend 1st harmonic excitation in the graph, as well as a range of large peaks ranging from 300Hz to 500Hz.

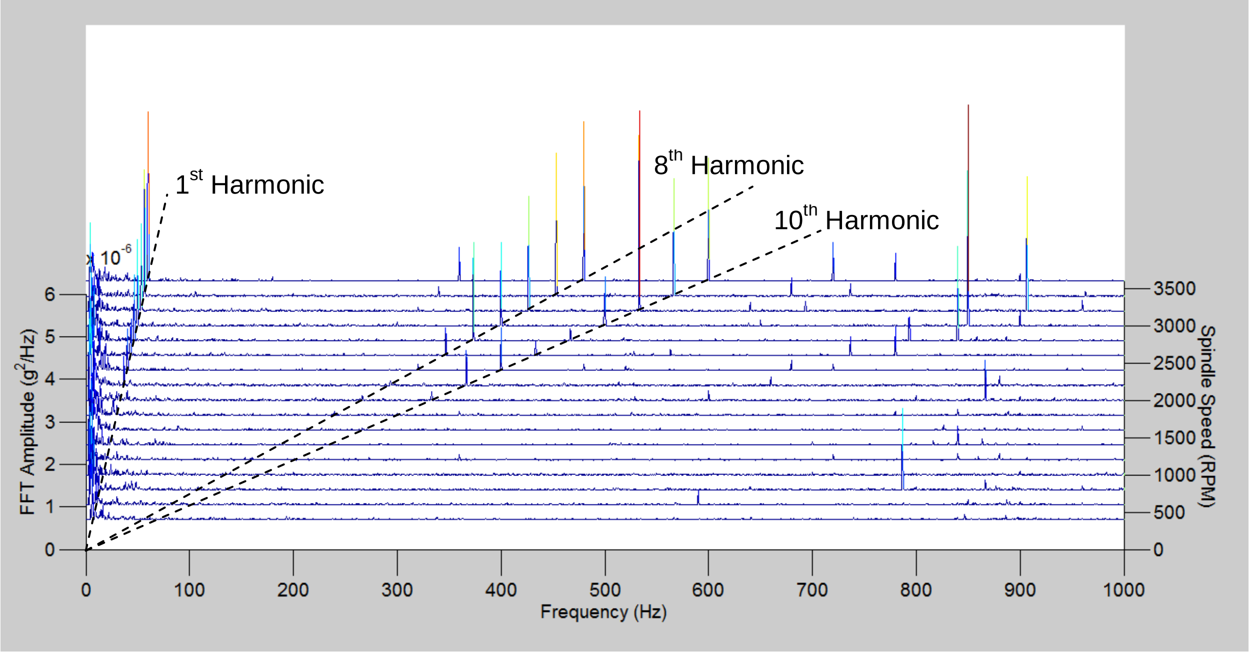

Figure 5.82 Waterfall Plot Of 500g Accelerometer FFT Mounted To Spindle Body, Radial Direction

An accelerometer was placed on the tool in the thrust direction. This accelerometer and the tool's force dynamometer represent the mechanical forces transmitted from the spindle, through the machine structure, and to the cutting tool itself. The waterfall plot of the accelerometer's FFT results is shown below, in Figure 5.83.

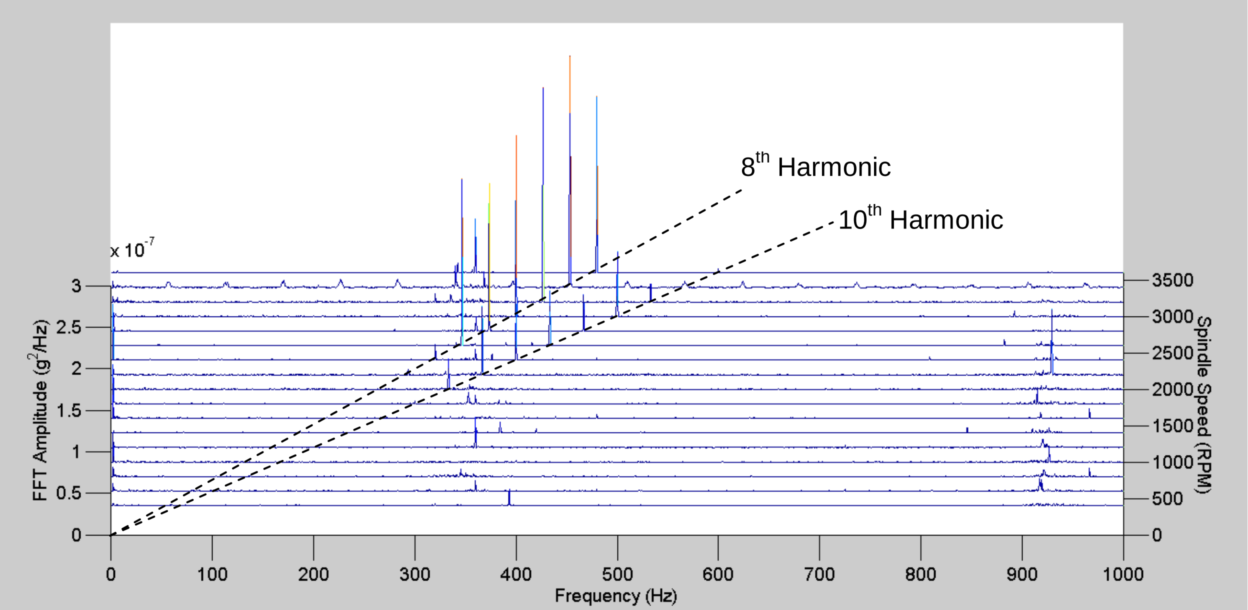

Figure 5.83 Waterfall Plot Of 5g Accelerometer FFT Mounted To Tool Holder, Axial Direction

In the Figure 5.83, one can see that most of the frequencies that make up the spindle star pattern fall within 300Hz to 500Hz. The 1st harmonic frequencies detected by the Kistler 8730A500M1 500g accelerometer was not detected by the Kistler 8640A5 5g accelerometer. If we isolate this region for spindle speed below 2000RPM (Figure 5.84), one can see that the peak frequencies often stay near 400Hz. Diamond turning is typically performed below 2000RPM, leading to the incorrect assumption that the spindle star phenomenon is an asynchronous spindle error. However, in all of these spindle speeds, the peak frequency creating the spindle star was always a harmonic of the spindle frequency.

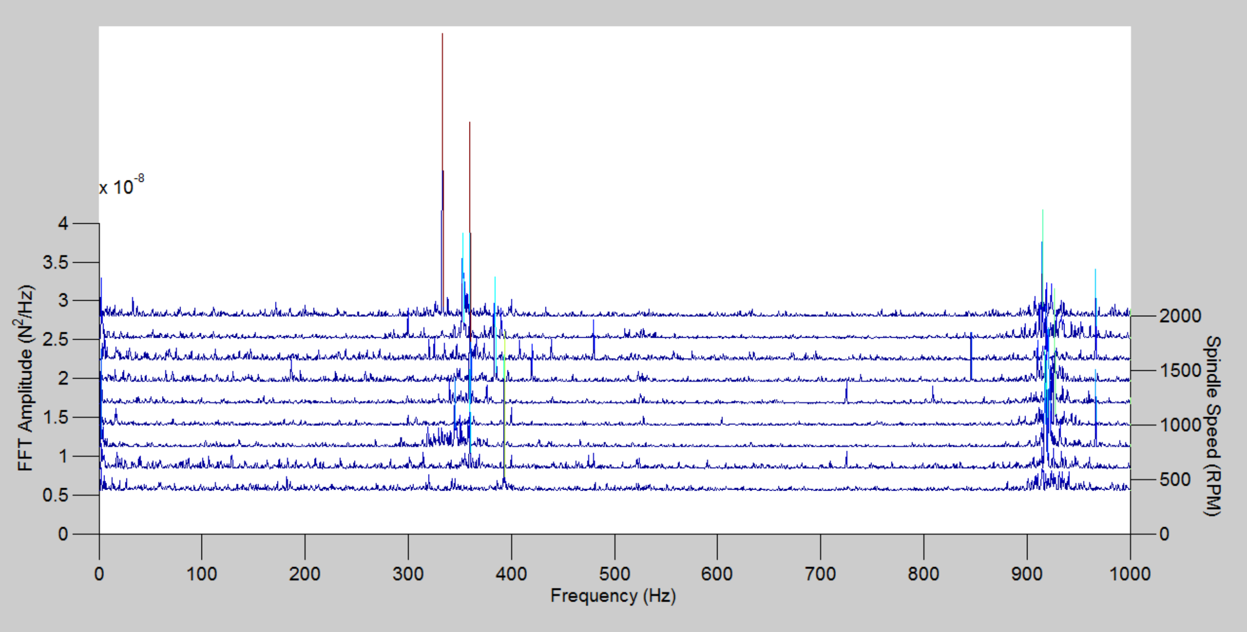

Figure 5.84 Waterfall Plot Of 5g Accelerometer FFT Mounted To Tool Holder, Axial Direction For Spindle Speed Under 2000RPM

The tool is mounted to a force dynamometer that measures the cutting forces. Due to the size effect, a change in the depth of cut will impart a large change in the cutting and thrust force. At low frequencies, there is a high amount of data leakage in the Fast Fourier Transform, creating a rough graph. This is due to the relatively low sensitivity of the force dynamometer compared to that of the accelerometers. The FFT of the tool thrust force measurements is shown below in Figure 5.85.

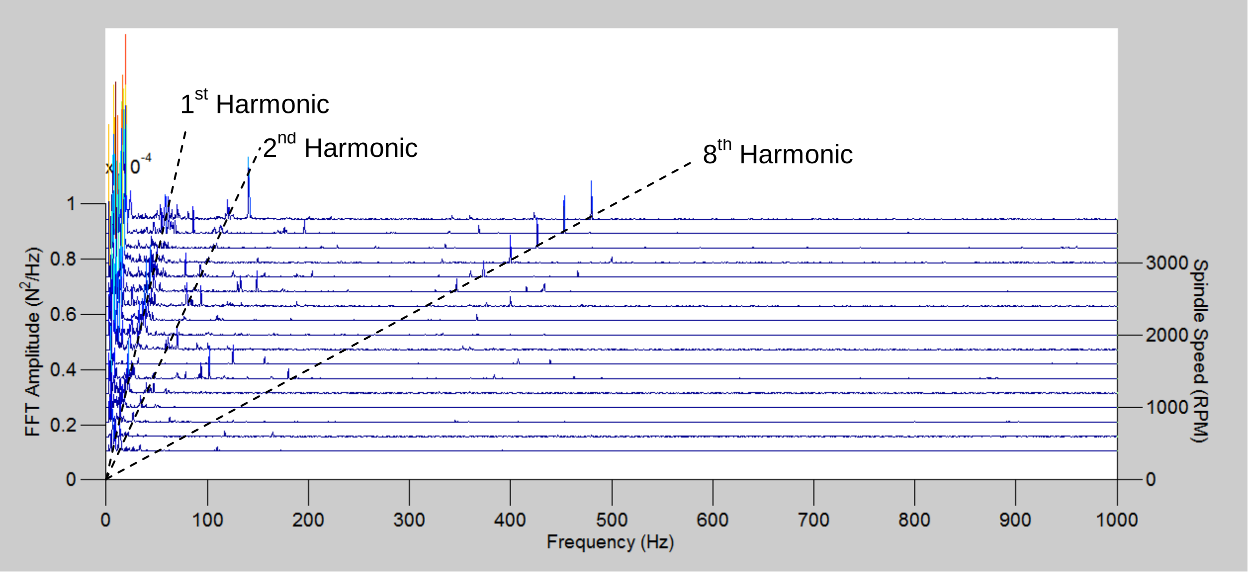

Figure 5.85 Waterfall Plot Of Force Dynamometer FFT, Spindle Axial Direction, Tool Thrust Direction

The trends indicating 1st harmonic, 2nd harmonic, and a weaker 3rd harmonic are observable in Figure 5.85. There is also a series of peaks at the 8th harmonic between 300Hz and 500Hz when the spindle speed is past 2800RPM. This 8th harmonic appears on the surface as a spindle star with 8 lobes. By analyzing the frequency domain of a force or accelerometer measurement, the spindle star lobe pattern can be determined and serve as a useful tool for online monitoring of the spindle star error.

The force dynamometer, when cutting, gave the most complete picture of vibration in SPDT. It detected the low frequency vibrations associated with the 1st, 2nd, and 3rd harmonic, but also the higher frequency vibrations associated with the spindle star pattern. When air-cutting, the tool is moved away from the workpiece but the machine continues to move through its program as if it were cutting material. From the results shown in Figure 5.86, the force dynamometer only detected the 8th, 10th, and higher harmonics of the spindle frequency. This further confirms that the disturbance frequency associated with spindle star is not affected by the tool-workpiece contact.

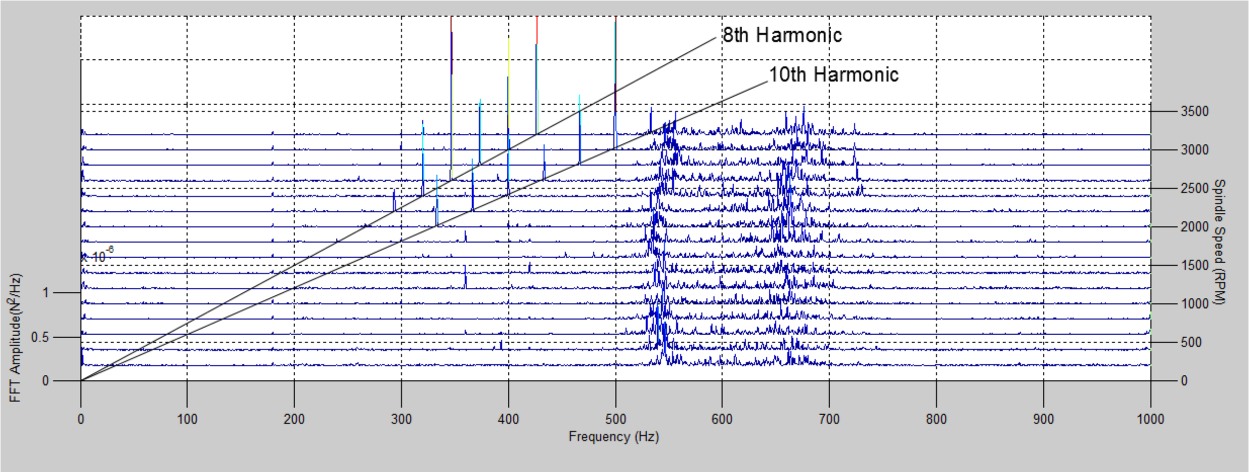

Figure 5.86Waterfall Plot Of Force Dynamometer FFT, Axial Direction, Air Cutting

It has also been observed that the spindle star error can be manipulated by adding mass to the spindle. The same RSA 6061 workpiece was mounted to a steel workpiece holder, weighing 4kg. This changed the natural frequency of the spindle down to 310Hz, determined by a modal test in Chapter 5.2.4. A cutting test was performed at 1000RPM, 5µm/rev feed rate, with a 2µm depth of cut. The added mass changed the disturbance frequency from 400Hz to 300Hz, as seen by the force dynamometer in Figure 5.87.

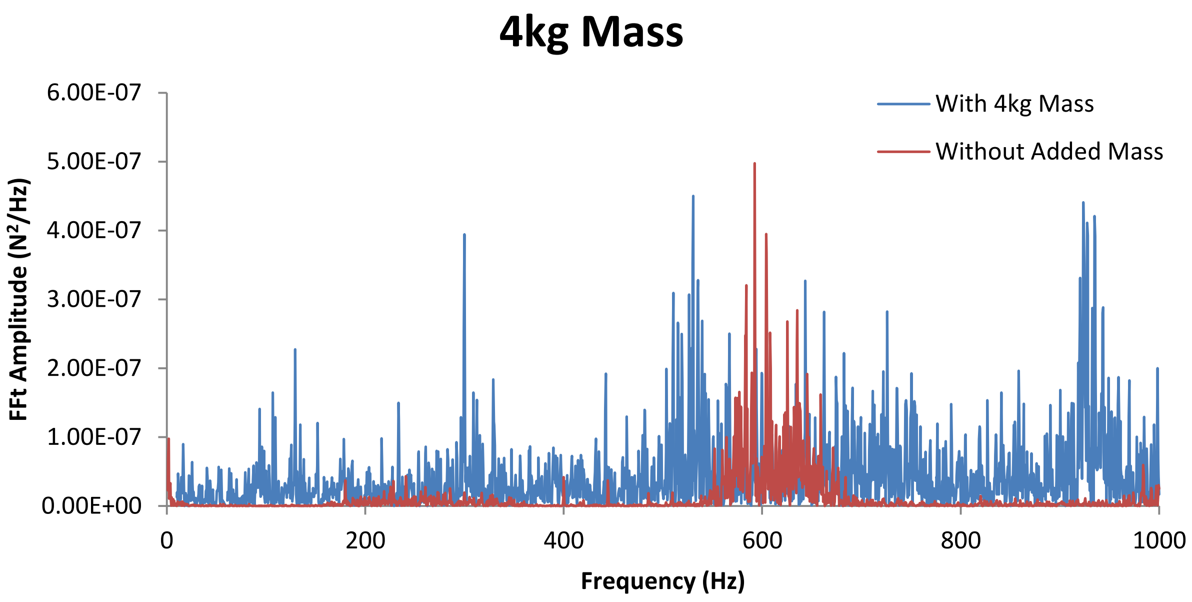

Figure 5.87 FFT of Tool Thrust Force For Cutting Test With 4kg Mass

The change from 400Hz to 300Hz changed the number of spindle star lobes from 24 to 18 at a rotational frequency of 16.667Hz according to Equation 5.10. The workpiece, scanned using the Zygo WLI (Figure 5.88) confirms this.

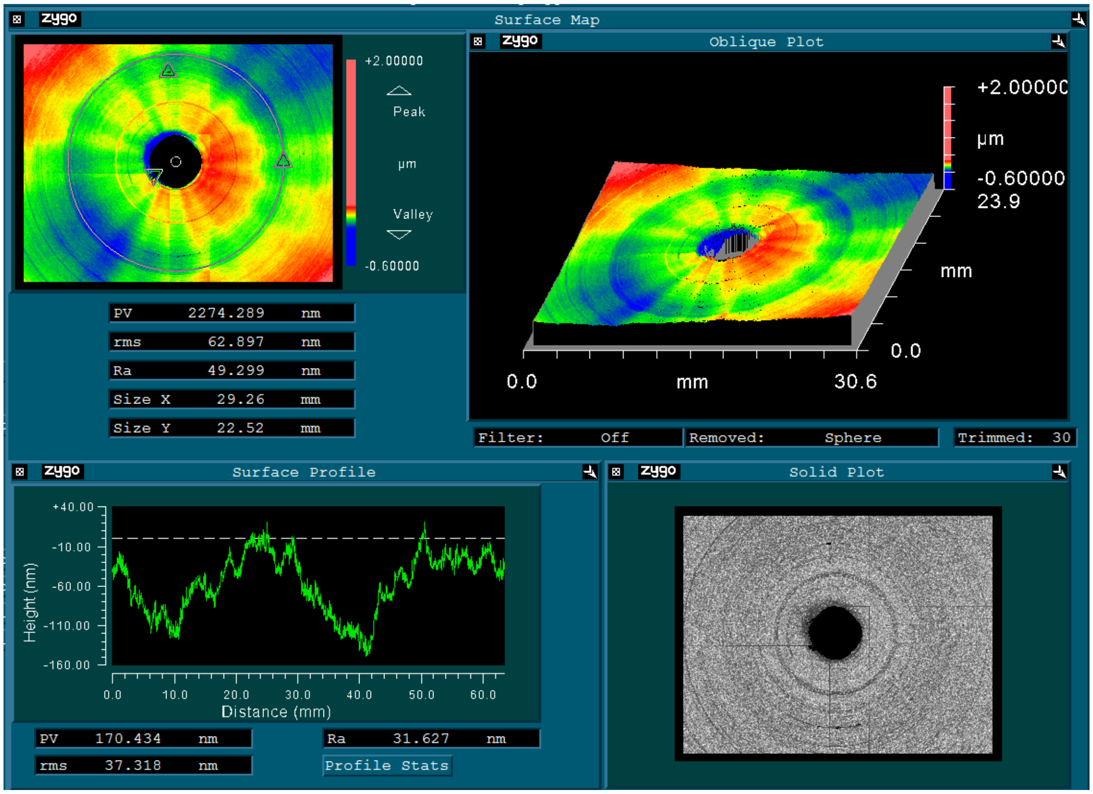

PV 2274.289 nm
rms 62.897 nm
Ra 49.299 nm
Size X 29.26 mm
Size Y 22.52 mm

Filter: Off
Removed: Sphere
Trimmed: 30

PV 170.434 nm
rms 37.318 nm
Ra 31.627 nm

Figure 5.88 Interferometer Measurement Showing 18 Lobes At 1000RPM With 4Kg Mass Installed

This result demonstrates that the spindle star pattern can be manipulated by adding mass. This also opens the possibility of manipulation of the spindle star pattern by increasing damping. The increased mass, and consequently, increased inertia, did not significantly improve the PV of the surface. Using a 10mm diameter circular profile on the part, the PV was 193nm. From Table 5.7, we can see that at 1000RPM, the average PV typically falls between 80nm to 88nm for a lightweight workpiece.

5.2.6 Causes of Spindle Star Error

There are disturbance frequencies that have the most influence on the flatness and form error of the part. These errors can be seen as trends in the waterfall plot for the force dynamometer in the thrust direction (Figure 5.85) and in the interferometer scans for all tests. The greatest contributors to the form errors are the 1st and 2nd harmonics of the rotational frequency, creating 1-2 lobes on the resulting surface. The next contributor is the spindle star error, an error that ranges from the 8th through to the 48th harmonic of the rotational frequency.

Using a scan from the Zygo WLI (Figure 5.89), the frequency that affects the surface can be clearly seen by taking a circular profile centered on the part. In Figure 5.89, the circular profile is bowed, showing an example where both the first harmonic and eight harmonic contribute to the flatness of the part when turned at 3000RPM.

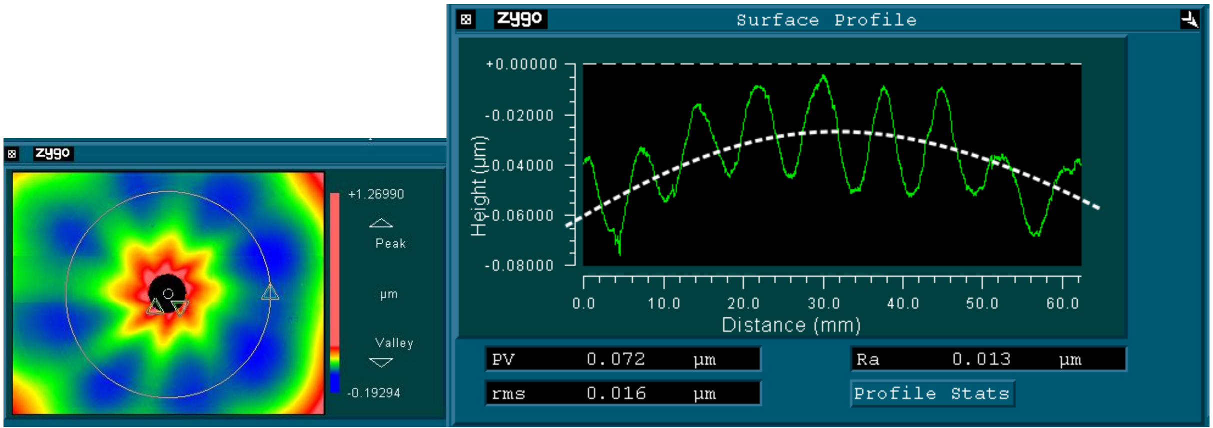

PV 0.072 µm

rms 0.016 µm

Ra 0.013 µm

Figure 5.89 Interferometer Scan Of RSA 6061 Surface At 3000RPM Showing Strong 1st And 8th Harmonic Vibration

A similar part turned at 500RPM was also scanned using the Zygo WLI (Figure 5.90). It showed less magnitude in spindle star error (48th harmonic) and more error in its 2nd harmonic error. The slower speed reduced the spindle star error but did not improve the 2nd harmonic error. This can be seen from the PV of the surface profile of both of these parts.

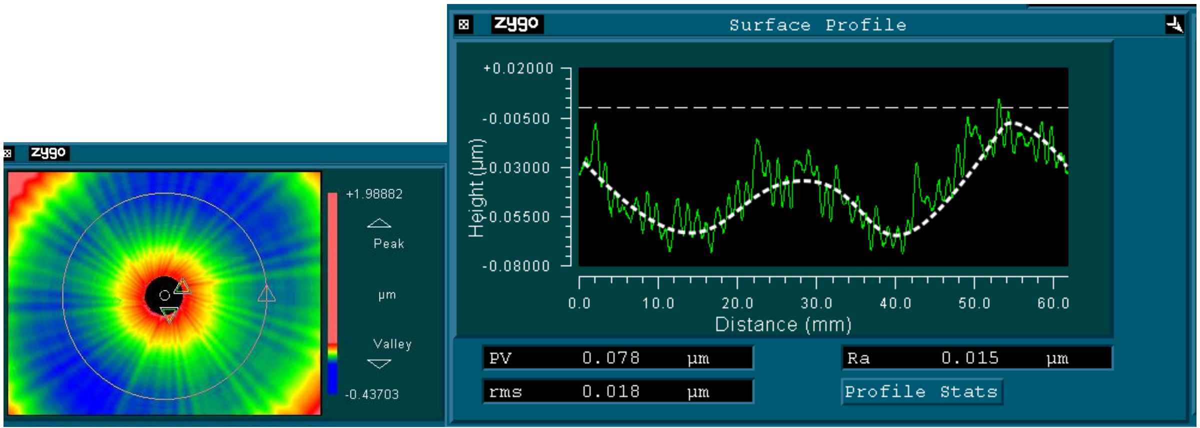

PV 0.078 µm

rms 0.018 µm

Ra 0.015 µm

Figure 5.90 Interferometer Scan Of RSA 6061 Surface At 500RPM Showing Strong 2nd And 48th Harmonic Vibration

The 1st and 2nd harmonic errors are caused by spindle imbalance. Van Osch et al. published a vibration troubleshooting chart [77], stating that a common fault in rotordynamic system is the misaligned, bent shafts with imbalance typically cause 1st and 2nd harmonic frequencies. These vibrations were detected using accelerometers and force dynamometers in Section 5.2.5. The machine balance procedure created an improvement in vibration by adjusting the balancing set screws around the spindle chuck. The procedure can be found in Section 3.3.2. The vibration peak-to-valley acceleration decreased from 0.034g to 0.001g, as seen in Figure 5.91.

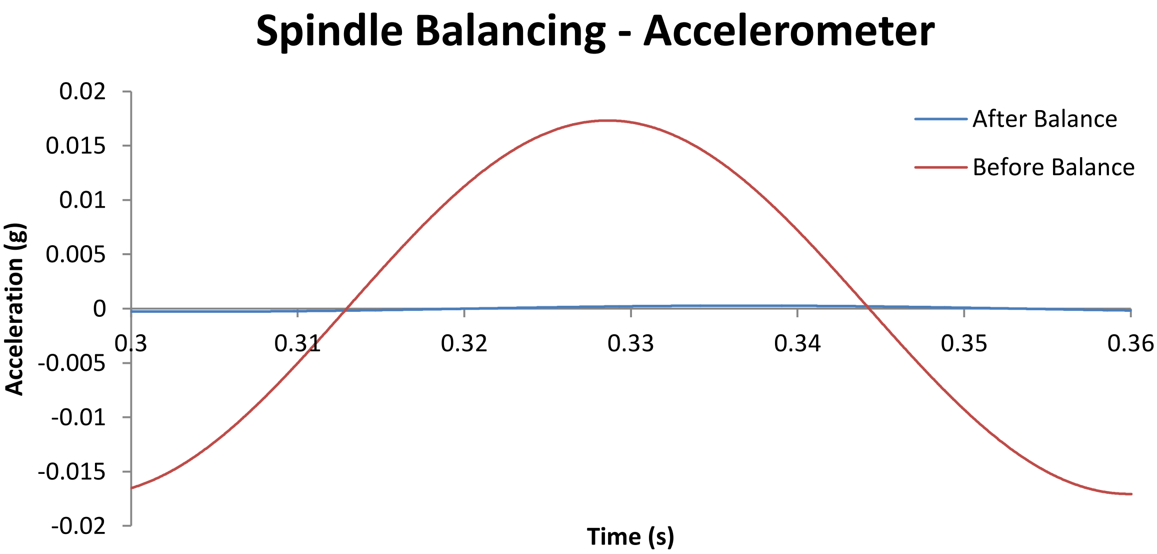

Figure 5.91 Spindle Balancing Results, Before And After Machine Balance Procedure

Two parts were machined out of RSA 6061 with a spindle speed of 3000RPM, feed rate of 5µm/rev, and a depth of cut of 2µm. One part was machined before the machine balancing procedure while the second was machined afterwards. From the Zygo WLI images in Figure 5.92 and Figure 5.93, balancing the machine reduced the surface profile PV from 174nm to 92nm. Both of the surface profile lines have a radius of 10mm. The waviness corresponding to the 1st harmonic frequency decreased after the machine balancing procedure. The 8 spindle star lobes are still prominent on the surface. The balancing procedure is limited by the arrangement of the balancing screws as only single plane of balancing can be performed. The true location and magnitude of the shaft imbalance is unknown and cannot be compensated using the balancing screws alone.

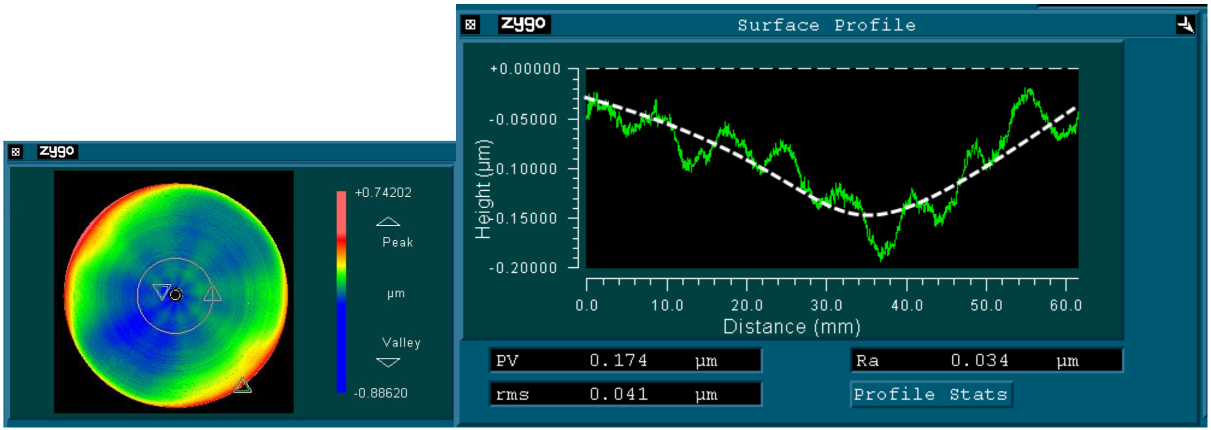

PV 0.174 µm

rms 0.041 µm

Ra 0.034 µm

Figure 5.92 Part Machined at 3000RPM, Before Machine Balance Procedure, 1st Harmonic Highlighted

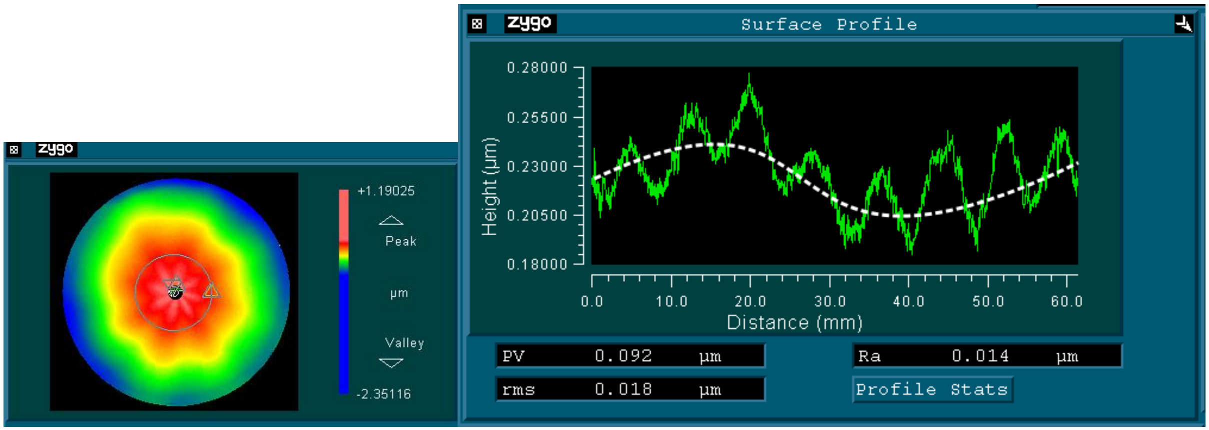

PV 0.092 µm

rms 0.018 µm

Ra 0.014 µm

Figure 5.93 Machined at 3000RPM, After Machine Balance Procedure, 1st Harmonic Highlighted

The disturbance frequency associated with spindle star error for all the spindle speeds used in this study all fell between 300Hz to 500Hz. This region is also close to the natural frequency of the spindle in both the axial and radial direction. The modal test (performed in Chapter 5.2.4), showed that the natural frequency of the spindle in the axial direction is 385Hz. The frequency response function (FRF) of the spindle in the radial direction shows two peaks, one at 392Hz and another at 465Hz. The FRF from these modal tests are shown again in Figure 5.94 and Figure 5.95.

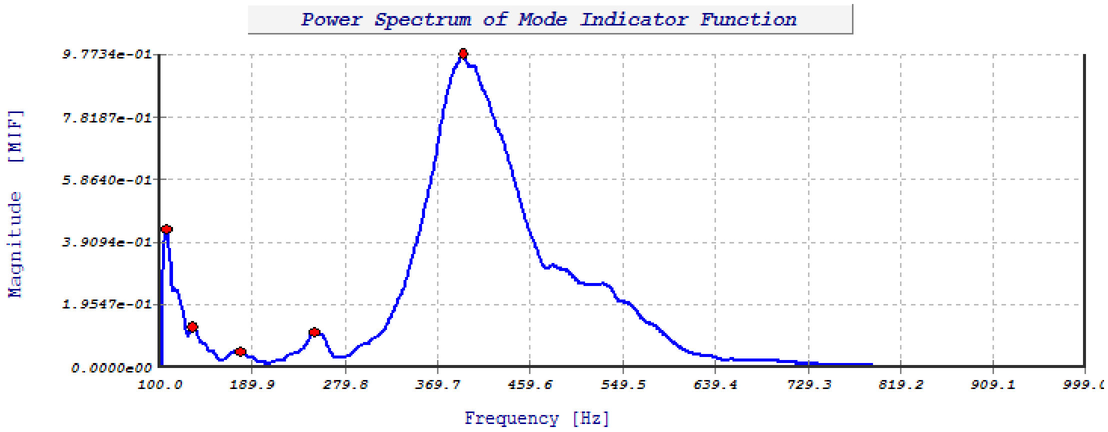

Figure 5.94 FRF of Spindle, Axial Direction

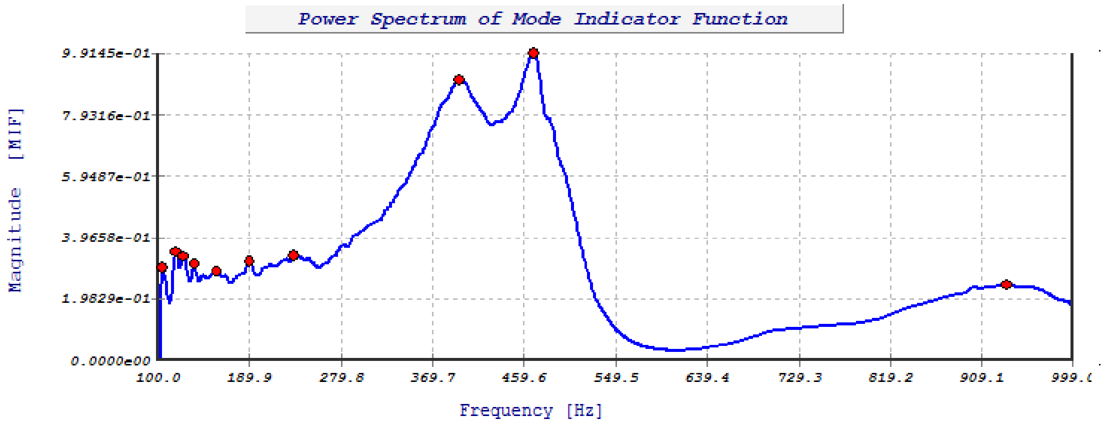

Figure 5.95 FRF of Spindle, Radial Direction

When performing the modal test, the spindle is struck with an instrumented force hammer. The accelerometer attached to the spindle measures the spindle's response to the hammer strike. In this case, the spindle is responding by vibrating as its air bearings absorb the blow as it is undergoing assisted air hammer instability. Air hammer instability is also present even when the spindle is not moving. A measurement was made with the accelerometers without the use of the force hammer this test was used to determine the frequency of the air hammer instability. The FFT of the accelerometer measurements are shown in Figure 5.96 and Figure 5.97.

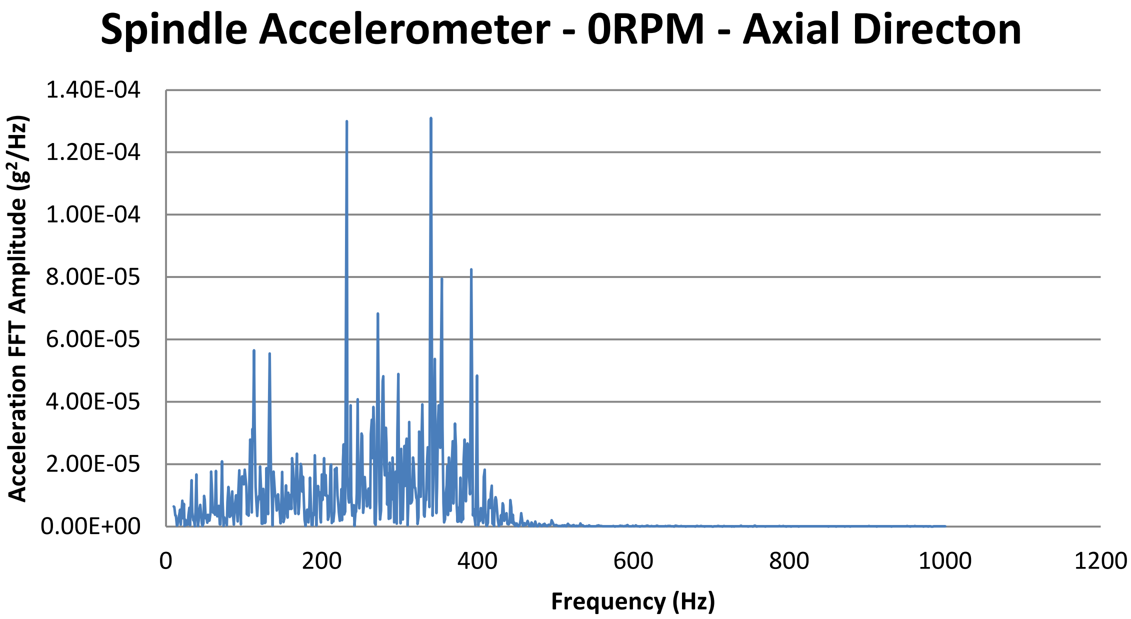

Figure 5.96 FFT of Accelerometer, Spindle Axial Direction With No Rotation

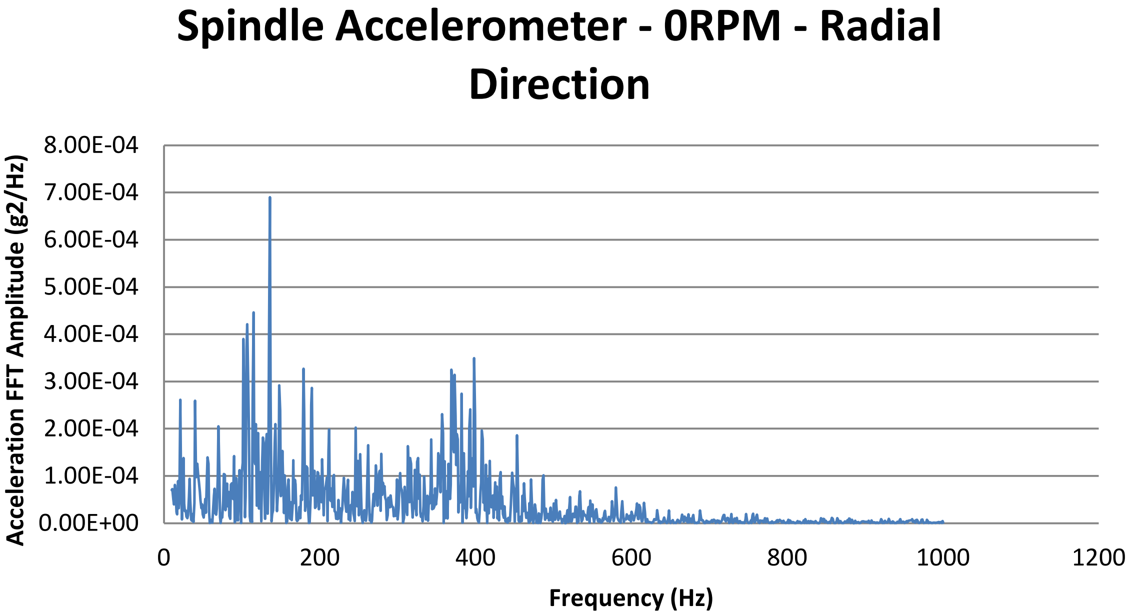

Figure 5.97 FFT Of Accelerometer, Spindle Radial Direction With No Rotation

When the spindle is not rotating, the accelerometer signals are still not zero. This is because of the air hammer instability of the air bearings which causes the spindle to vibrate. An FFT analysis on these signals reveals that they are vibrating at frequencies below 600Hz due to air hammer instability. Once the spindle begins rotating, the air hammer instability turns to assisted air hammer instability. During assisted air hammer instability, the spindle begins to vibrate at a frequency that is excited by the rotational frequency and is also extracting energy from the external air supply which equalizes any pressure differential between the opposing air bearing orifices.

The spindle star error was measured in several workpieces, summarized in Figure 5.98. The height of the spindle star lobes increase linearly with spindle speed. For these tests, a 12mm nose radius tool was used with a constant feed rate of 5µm/rev and a depth of cut of 2µm.

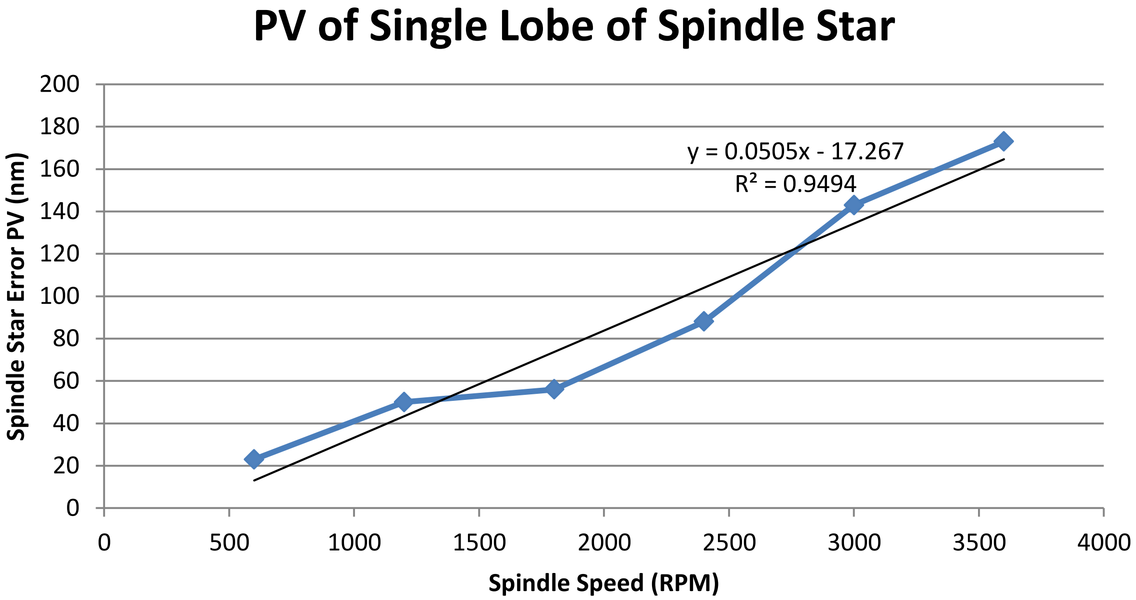

Figure 5.98 Spindle Star Lobe PV Increasing With Spindle Speed

The increasing magnitude of spindle star error with spindle speed is due to the decreased damping in the air bearing at high spindle speeds [82]. The angular momentum increases with the increased rpm for a given rotor which has directional vector acting along the axis of rotation (depth of cut direction). These two factors cause vibration with large amplitude to occur. The spindle operates well below its first fundamental frequency, as seen in Section 5.2.4. By increasing spindle frequency, the vibration amplitude will also increase due to gyroscopic effects and precession. This will exacerbate the spindle star error as it will cause assisted air hammer instability, as seen with the increase of spindle star error PV with spindle speed. Increasing workpiece mass, as demonstrated in section 5.2.4 has lowered the system's natural frequency, but vibration amplitude increased, creating a wavier surface by increasing the amount of precession from the overhang mass. When operating in a sub-critical regime, the only way to decrease vibration amplitude and improve (or eliminate) form error is to apply external damping.

5.2.7 Rotordynamic and Assisted Air-Hammer Instability: A Conclusive Summary

This analysis has found many important findings. Exploratory tests in Section 5.2.3 found that the tool geometry and edge preparation does not affect the magnitude of the spindle star error. The error exists even when air-cutting; leading to a conclusion that tool-workpiece contact has a minimal effect on the magnitude of spindle star error and no effect on the number of lobes. The spindle star error was also found to be consistent throughout the whole workpiece, but is most easily detected near the center of the part. Section 5.2.3.3 showed that the workpiece material also has no impact on the number of lobes in the spindle star error. A thorough investigation using modal tests in Section 5.2.4 confirmed that the spindle star error is due to vibration generated by the rotation of the spindle and is affected by the properties of the air bearings.

Air bearings are excellent for SPDT due to their high stiffness, load capacity, and low friction. They have some dynamic problems, as outlined in Section 5.2.2 such as decreased damping and assisted air hammer instability at high rotational speeds. The spindle star error is caused by spindle imbalance with a cantilevered workpiece mass, causing assisted air hammer instability. Spindle imbalance results in circular orbital movement of the spindle at 1st harmonic where the overhang mass results in a tilting motion to that orbit leading to an orbital movement of the rotor. All these factors work together to create a gyroscopic precession which eventually the air bearing tries to compensate at the natural frequency of the spindle leading to the assisted air hammer instability. The rotating spindle and gyroscopic effects creates a forced vibration problem, with Equation 5.12 below. In this equation, M represents mass, C represents damping, and *K* represents the stiffness of the system. The function $f_{vib}(t)$ represents the forcing function, such as the input force from rotating imbalance.

$$M\ddot{x} + C\dot{x} + Kx = f_{vib}(t)$$

Equation 5.12 General Second-Order Equation for Mechanical Vibrations

In Section 5.2.1, this general equation was solved using sine and cosine functions for simple harmonic motion. Due to the characteristics of air bearings and Boyle's Law (Equation 5.11), the spring rate (cross-coupling stiffness) is non-linear and hysteresis effects may not be uniform for tension and compression. This results in a different natural frequency for the first and second half-cycle of vibration representing the tension and compression phase of a single cycle of vibration. The resulting motion, $x(t)$, is no longer simple harmonic motion, but is represented by a Fourier series in Equation 5.13, solved by Dimarogonas et. al. [89].

$$x(t) = a_0 + \sum_{k=1}^{\infty} (a_k \sin k\omega t + b_k \cos k\omega t)$$

Equation 5.13 Fourier Series Solution for Mechanical Vibrations

From Equation 5.13, it can be seen that the system has an infinite number of natural frequencies, multiples of the circular frequency of a full cycle ω, 2ω, 3ω… In forced vibration, such as that of a rotating imbalance, the circular frequency will match the rotational frequency. In a physical sense, a shaft with a rotating imbalance will cause it to vibrate at the rotational frequency as well as its harmonic frequencies. This forces the number of spindle star lobes to be an integer.

The frequency response function (FRF) of the system is governed by the mass, stiffness, and damping of the system. These attributes are heavily influenced by the dynamics of the air bearings that support the spindle shaft. The forced vibration from rotation (with all harmonics frequencies) will cause the spindle shaft to respond according the FRF, favoring frequencies close to the natural frequency of the spindle shaft that was found in Section 5.2.4 in the axial direction. These trends can be seen in Figure 5.99. The vibration data shown in Figure 5.99 was taken from Figure 5.85 while the FRF was taken from Figure 5.72, multiplied by 100 for visibility on the graph.

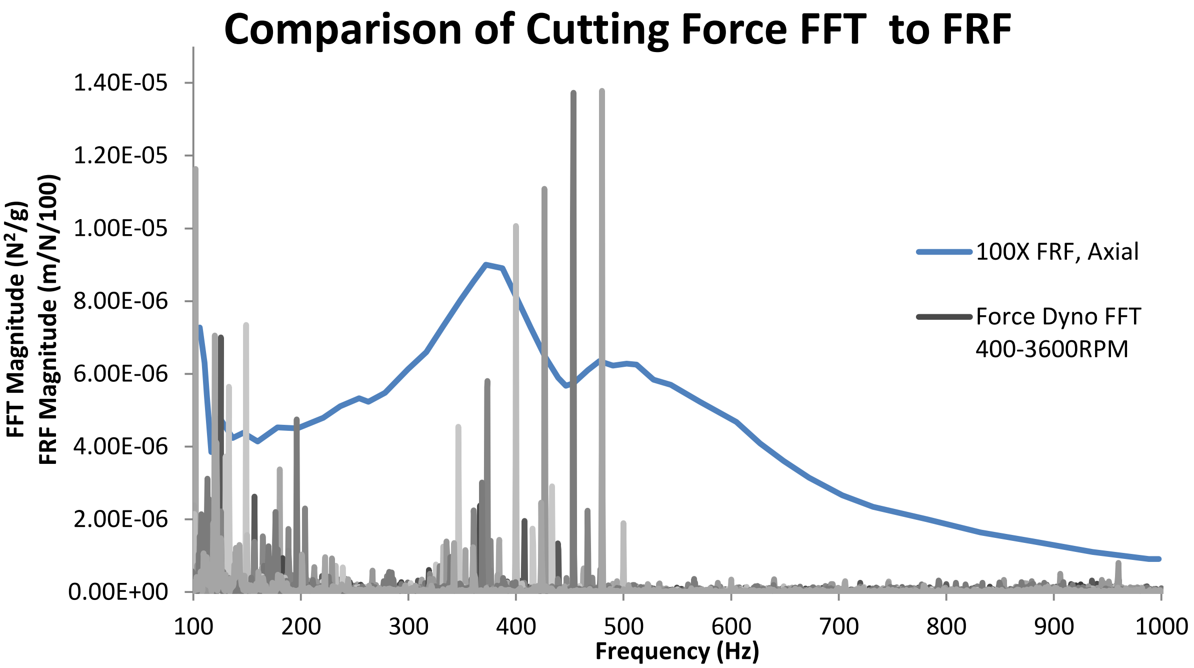

Figure 5.99 Vibration Data Overlaid on FRF of Spindle, Axial Direction

Figure 5.99 shows that the frequencies detected during cutting that causes spindle star error are higher than the peak frequencies detected by the modal test. This is due to the increase of air bearing stiffness with spindle speed, a phenomenon also observed by Kozanek et al. [88]. The increased stiffness will increase the natural frequency of the system, governed by the equation:$\omega = \sqrt{k/_{m}}$. Another important point is that the amplitude of the spindle star error will increase with spindle speed. The PV of a single spindle star lobe was seen to increase linearly according to Figure 5.98 due to the decreasing damping effect of air bearings with spindle speed

[88]. The overall PV of the surface is dominated by how well the spindle chuck has been balanced.

The analysis performed in Section 5.2 leads to the following conclusions:

a. Air-hammer can be inherent to an air-bearing system due to imbalance. This imbalance is practically impossible to eliminate; however, it can be minimized.
b. When rotating, this imbalance leads to whirl at the rotational frequency
c. The cantilevered mass or the cutting force may excite the system and may result in a 2nd mode of conical orbital vibration (gyroscopic effect)
d. Air-hammer instability vibrates the spindle with system rotational natural frequencies.
e. This axial movement from air hammer instability leaves a frequency signature on the machined surface
f. There are two peaks and two valleys on the surface which will dominate near the periphery and diminish near center (Abbe's principle of error) of the face turned workpiece
g. From optical metrology, the effect of air hammer instability is more visible near the center of the part where the precession has minimum influence. The spoke pattern is clear at the center of the part. The same pattern may be missed near the outside of the part due to the wide space each lobe encompasses and small field of view of the optical microscope.
h. Due to inherent rotordynamic nature of a system, it is possible to characterize a rotating air-bearing spindle to extrapolate its behavior during cutting.

i. Spindle star is a synchronous error and is also a function of rotation and can be predicted using Campbell’s rotordynamic analysis.
j. Inherent nature of rotordynamics and air hammer instability can be monitored and predicted by online cutting forces (thrust force) and offline accelerometer measurements

Chapter 6. Conclusions

The focus of this research is to gain an understanding of the four major factors that affect the surface finish in SPDT. By understanding the factors that affect surface finish and how they are related to each other, higher quality ultra-precision machined parts can be made without post-polishing work. This is advantageous as it eliminates an entire process step and allows for the creation of geometries that were previously not possible. Another way to increase the productivity of SPDT is to increase the spindle speed and cutting speed to decrease cycle time.

The material microstructure is important for SPDT. Studies using 99.9% pure aluminum alloy showed that a material microstructure with a high dislocation density and fine grain structure is best for diamond turning. In this study, it has been found that an aluminum 6061 alloy also follows the same trend. The hard, alloying particles of the aluminum 6061 must also be finely dispersed to avoid scratches and pull-outs. The material that yielded the best surface finish was a rapidly solidified aluminum, RSA-6061.

High quality cutting tools will also greatly improve the surface finish in diamond turning. Two tools were compared, a tool with a chemically etched edge, and an unmodified tool to apply a prepared edge on the tool. The chemical etching was performed in an attempt to create a rounded cutting edge without any defects to extend tool life. In the study, single-crystal diamond (SCD) tools were measured using a confocal laser scanning microscope to measure their cutting edge radii. When new, the cutting edge radius of a sharp SCD tool was found to be 95nm. The chemically etched tool had a stepped profile instead of a rounded one. The stepped profile had a cutting edge radius made up of two radiuses of 100nm each. These tools were tested until they produced surfaces with unacceptable quality. After the cutting tests, the tools were cleaned and inspected again, with both tools having a cutting edge radius of about 290-300nm. After cleaning, both tools were able to continue producing surfaces with good surface finish. This is because the primary cause of tool wear and high surface roughness in SPDT is through built-up-edge (BUE) formation. BUE was found on the surface of the tool after use. Surfaces generated with a tool with BUE showed deep scratches as the BUE, made of strain-hardened workpiece material, adheres itself to the tool and scratches the workpiece. The main issue of maintaining good surface finish in diamond turning aluminum is the formation of BUE and avoiding the conditions which generate side flow.

The chemically etched tool had a shorter useful tool life than the unmodified one. However, the etched tool did not require a long break-in period to achieve a good surface finish. The chemically etched tool did not last as long as the cutting edge was not a rounded cutting edge, but was a stepped edge instead. Inspections of an SCD tool can now be performed using a modern confocal laser scanning microscope. These microscopes are much more robust and are less costly than the older methods of SCD tool inspection using an SEM or AFM. More work will be needed to produce a SCD tool with proper edge preparation. In summary good, consistent surface roughness was achieved through a combination of appropriate workpiece material, high quality tools, and the control of BUE and side flow.

When machining, relative tool-workpiece vibration is important as it impacts surface finish and form error. Unwanted vibrations through the machine tool can cause parts to be scrapped and can damage cutting tools. The largest contributor to form error is a form error in the 1st or 2nd harmonic of the spindle frequency. This corresponds with imbalance in the air bearing spindle. By balancing the machine, this error was greatly reduced, but cannot be completely eliminated. When machining, a disturbance frequency was detected using a force dynamometer. This frequency corresponds to the number of lobes in the spindle star error when the workpiece is scanned using a white light interferometer. A rotordynamic analysis on the spindle showed that the disturbance frequency causing spindle star closely follows the rotational frequency while keeping close to the frequency of air hammer instability in the spindle. An increase in workpiece mass will change the spindle dynamics by reducing the system’s natural frequency and increasing vibration amplitude. The spindle’s operating frequency is well below its first natural frequency. Increasing spindle speed will decrease the damping ratio of the spindle’s air bearings. This causes increased vibration amplitude due to imbalance and exacerbating assisted air hammer instability.

The second largest contributor to form error is the spindle star error. The air-bearing spindle vibrates due to precession and rotary imbalance. The air bearing undergoes assisted air hammer instability, vibrating at a multiple of the rotating frequency, but close to the natural frequency of the shaft-bearing system. In a physical system, imbalance and gyroscopic forces cannot be practically eliminated.

Form error is not heavily influenced by the tool-workpiece contact, as the use of different tools did not change the vibration amplitude. The major source of form error is not through asynchronous error, but it is an error that has elements of being both synchronous, as it follows spindle frequency, but also asynchronous, as it will fall within a narrow range of frequencies which result in an integer number of radial star patterns.

Chapter 7. Future Work and Recommendations

The research in this thesis answered some questions while at the same time, many new, unanswered questions were uncovered.

In the area of improving SCD tools, the chemically etched tool did not round the cutting tool, but instead, created a stepped cutting edge. Further development of SCD tool honing to produce a slightly rounded cutting edge is required. SCD tools typically ‘wear out’ by the presence of BUE. Research in ways to prevent BUE, such as by the use of a different coolant or workpiece alloy is required.

Further work is being done to reduce the effect of spindle star by using a combination of specially designed tool geometries and cutting parameters. When spindle speeds are relatively low, the spatial distance between spindle star lobes becomes small. A large, wide tool with a flat end can promote burnishing of the surface, eliminating the high spots of the spindle star lobes. This solution will only be applicable for planar surfaces or cases where the nose radius of the tool can be matched to the part radius.

In the ultra-precision machine tool, the air bearing design needs to be changed to improve their damping characteristics at high spindle speeds. External damping can also help in reducing vibration amplitude. Pursuing research in these directions will allow SCD tools to have a longer tool life and improve the quality of parts produced using SPDT and reduce manufacturing costs.

It was also observed that the number of lobes reduces with the increase in RPM. This may possibly open a new technique of “ultra-high speed, ultra-precision diamond turning.” For example, it was observed that the SP-90 spindle has its highest disturbance frequency at 500Hz. Thus if it was possible to diamond turn a sample above 30,000rpm (500Hz rotational frequency); this can open new possibilities of extremely high speed production with minimum form error. However, SP-90 spindle RPM is limited to 10,000rpm and passing the critical frequency range to reach that speed can be a challenge. More research is required to develop and realize this possibility.

References

[1] O. Riemer and K. Rickens, *Review of Ultra Precision Machining Capabilities, Precision Engineering at CERN: Future Challenges and Opportunities,* Bremen: IWT Stiftung Institut Fur Werkstofftechnik.

[2] M. Tauhiduzzaman and S. C. Veldhuis, *Enhancing the Surface Finish of Single Point Diamond Turning*, McMaster University, 2011.

[3] S. Takasu, M. Masuda, T. Nishiguchi and A. Kobayashi , "Influence of Study Vibration with Small Amplitude Upon Surface Roughness in Diamond Machining," *Annals of the CIRP*, vol. 34, no. 1, pp. 463-467, 1985.

[4] D. Dornfeld, S. Min and Y. Takeuchi, "Recent Advances in Mechanical Micromachining," *CIRP Annals*, vol. 55, no. 2, pp. 745-768, 2006.

[5] P. Tom Solon, "Fundamentals of Ultrapecision Machining," Machine Design.com, Hollis, 2012.

[6] A. Sohn, L. Lamonds and . K. Garrard, "Modeling of Vibration in Single-Point Diamond Turning," *Proceedings of the ASPE, American Society of Precision Engineering,* no. 21st Annual Meeting, pp. 15-20, 2006.

[7] M. Tauhiduzzaman and S. Veldhuis, "Effect of Material Microstructure and Tool Geometry on Surface Generation in Single Point Diamond Turning," *Precision Engineering,* vol. 38, no. 3, pp. 481-491, 2014.

[8] T. C. Childs, D. Dornfeld, D. Lee, S. Min, K. Sekiya, R. Tezuka and Y. Yamane, "The Influence of Cutting Edge Sharpness on Surface Finish in Facing With Round Nosed Cutting Tools," *CIRP Journal of Manufacturing Science and Technology,* vol. 1, no. 2, pp. 70-75, 2008.

[9] S. Tahaaki and U. Kanji, Fundamentals of Machining, Japan: KOURITU Book Publication, 1984.

[10] S. To, W. B. Lee and C. Y. Chan, "Ultraprecision Diamond Turning of Aluminum Single Crystals," *Journal of Materials Procesing Technology,* vol. 63, pp. 157-162, 1997.

[11] R. G. Jasinevicius, J. G. Duduch, A. J. V. Porto and B. M. Purquerio, "Critical Aspects on the Behavior of Material from the Mechanical Tool-Workpiece Interaction in Single Point Diamond Turning," *Journal of the Brazilian Society of Mechanical Sciences,* vol. 21, no. 3, 1999.

[12] Y. Furukawa and N. Moronuki, "Effect of Material Properties on Ultra Precise Cutting Processes," *Annals of the CIRP* , vol. 37, no. 1, pp. 113-116, 1988.

[13] L. Goncharova, "Mechanical Properties of Metals," University of Western Ontario, 2008. [Online]. Available: http://www.physics.uwo.ca/~lgonchar/courses/p2800/Chapter6_Mechanical_Handouts.pdf. [Accessed 30 April 2014].

[14] T. W. Morris, N. E. David, N. J. Christopher, P. Temple-Smith, K. S. W. Klaus WE and D. C. John, "Friction stir welding". Great Britain Patent GB2306366, 07 May 1995.

[15] NASA, "Space Shuttle Technology Summary - Friction Stir Welding," NASA, 2001. [Online]. Available: http://www.nasa.gov/centers/marshall/pdf/104835main_friction.pdf. [Accessed 12 May 2014].

[16] G. Liu, L. E. Murr, C.-S. Niou, J. C. McClure and F. R. Vega, "Microstructural Aspects Of The Friction-Stir Welding Of 6061-T6 Aluminum," *Scripta Materialia,* vol. 37, no. 3, pp. 355-361, 1997.

[17] J. Perett, J. Martin, P. L. Threadgill and M. Ahmed, "Recent developments in friction stir welding of thick section aluminium alloys," March 2007. [Online]. Available: http://www.twi-global.com/technical-knowledge/published-papers/recent-developments-in-friction-stir-welding-of-thick-section-aluminium-alloys-march-2007/. [Accessed 12 May 2014].

[18] "RS Alloys Optics," RSP Technlology, [Online]. Available: http://www.rsp-technology.com/RSP%20Technology%20-%20Optics.pdf. [Accessed 29 January 2014].

[19] Y. Altintas, M. Eynian and H. Onozuka, "Identification of Dynamic Cutting Force Coefficients and Chatter Stability With Process Damping," *CIRP Annals - Manufacturing Technology,* vol. 57, no. 1, pp. 371-374, 2008.

[20] J. Rech, "Influence Of Cutting Edge Preparation On The Wear Resistance In High Speed Dry Gear Hobbing," *Wear,* pp. 505-512, 2006.

[21] J. Rech, Y. C. Yen, M. J. Schaff, H. Hamdi, T. Altan and K. D. Bouzakis, "Influence of Cutting Edge Radius On The Wear Resistance Of PM-HSS Milling Inserts," *Wear,* vol. 259, pp. 1168-1176, 2005.

[22] K. C. Feng Qin, "Cutting Edge Radius Effects on Diamond Coated Tools," *Transactions of NAMRI/SME,* vol. 37, pp. 653-660, 2009.

[23] D. Biermann and A. Baschin, "Influence of Cutting Edge Geometry And Cutting Edge Radius On The Stability Of Micromilling Processes," *German Academic Society For Production Engineering,* vol. 3, pp. 375-380, 2009.

[24] J. K. Min, J. K. Lee, Y. Hwang, D. H. Cha, H. J. Kim and J. H. Kim, "Experimental Study Of The Diamond Turning Characteristics Of Tungsten Carbide (Co 0.5%) When Using a Chamfered Diamond Bite," *Journal Of The Korean Physical Society,* vol. 61, no. 9, pp. 1390-1394, 2012.

[25] Y. Kobaru, E. Kondo and R. Iwamoto, "Ultra-Precision Cutting of Single Crystal Silicon using Diamond Tool with Large Top Corner Radius," *Key Engineering Materials,* Vols. 523-524, pp. 81-86, 2012.

[26] M. Masuda, Y. Maeda, T. Nishiguchi and M. Sawa, "A Study On Diamond Turning of Al-Mg Alloy - Generation Mechanism of Surface Machined With Worn Tool," *Annals of the CIRP,* vol. 38, no. 1, pp. 111-114, 1989.

[27] D. A. Lucca and Y. W. Seo, "Effect Of Tool Edge Geometry on Energy Dissipation in Ultraprecision Machining," *Annals of the CIRP* , vol. 42, no. 1, pp. 83-86, 1993.

[28] N. Kawasegi, T. Niwata, N. Morita, K. Nishimura and S. Hideki, "Improving Machining Performance Of Single-Crystal Diamond Tools Irradiated By A Focused Ion Beam," *Precision Engineering,* vol. 38, pp. 174-182, 2014.

[29] R. A. G. Zareena and S. C. Veldhuis, "Extension of Ultraprecision Machining To Titanium Alloys," McMaster University, Hamilton, ON, 2010.

[30] S. C. Fawcett, "Small Amplitude Vibration Compensation for Precision Diamond Turning," *Precision Engineering,* vol. 12, no. 2, pp. 91-96, 1990.

[31] W. L. C.F. Cheung, "Study of Factors Affecting the Surface Quality in Ultra-Precision

Diamond Turning," *Materials and Manufacturing Processes,* vol. 15, no. 4, pp. 481-502, 2000c.

[32] W. C.F. Cheung, "A Multi-Spectrum Analysis of Surface Roughness Formation in Ultra-Precision Machining," *Precision Engineering,* vol. 24, pp. 77-87, 2000b.

[33] C. F. Cheung and W. B. Lee, "A Theoretical and Experimental Investigation of Surface Roughness Formation in Ultra-Precision Diamond Turning," *International Journal of Machine Tools and Manufacture,* vol. 40, no. 7, pp. 979-1002, 2000a.

[34] S. J. Zhang and S. To, "A Theoretical and Experimental Investigation in Multimode Tool Vibration With Surface Generation in Ultra-Precision Diamond Turning," *International Journal of Machine Tools & Manufacture,* vol. 72, pp. 32-36, 2013 .

[35] P. Meyer, *A Framework for Enhancing the Accuracy of Ultra-Precision Machining,* Hamilton: Mcmaster University, 2010.

[36] H. Wang, S. To and C. Y. Chan, "Investigation on the Influence of Tool-Tip Vibration on Surface Roughness and its Representative Measurement in Ultra-Precision Diamond Turning," *International Journal of Machine Tools and Manufacture,* vol. 69, pp. 20-29, 2013.

[37] R. Bittner, "Tolerancing of Single Point Diamond Turned Diffractive Optical Elements and Optical Surfaces," *Journal of the European Optical Society,* no. Rapid Publications 2, 2007.

[38] H.-S. Kim and E.-J. Kim, "Feed-Forward Control of Fast Tool Servo for Real-Time Correction of Spindle Error in Diamond Turning of Flat Surfaces," *International Journal of Machine Tools and Manufacture,* vol. 43, no. 12, pp. 1177-1183, 2003.

[39] R. C. Juergens, R. Hamilton Shepard III and J. P. Schafer, "Simulation of Single Point Diamond Turning Fabrication Process Errors," *Proc. of SPIE ,* vol. 5174, pp. 93-104, 2003.

[40] H. Khanfir, M. Bonis and P. Revel, "Improving Flatness in Ultraprecision Machining by Attenuating Spindle Motion Errors," *International Journal of Machine Tools and Manufacture,* vol. 45, no. 7-8, pp. 818-848, 2005.

[41] S. J. Zhang, S. To, C. F. Cheung and H. T. Wang, "Dynamic Characteristics Of an Aerostatic Bearing Spindle And Its Influence On Surface Topography In Ultra-Precision Diamond Turning," *International Journal of Tools & Manufacture,* vol. 62, pp. 1-12, 2012.

[42] Precitech , *Freeform 700 Series Installation & Maintenance Manual,* 2002.

[43] Alfred Jäger GmBH, "Alfred Jäger air bearing spindle," 29 November 2011. [Online]. Available: https://www.youtube.com/watch?v=g6ZkF2Vv1S0. [Accessed 28 April 2014].

[44] D. McMullan, "Scanning electron microscopy 1928–1965," *Scanning,* vol. 17, no. 3, pp. 175-185, 1995.

[45] Austrialian Microscopy & Microanalysis Research Facility, "Troubleshooting: edge effect, charging, sample damage," 12 May 2014. [Online]. Available: http://www.ammrf.org.au/myscope/sem/practice/principles/troubleshooting.php. [Accessed 27 May 2014].

[46] S. Asai, Y. Taguchi, K. Horio, T. Kasai and A. Kobayshi, "Measuring The Very Small Cutting-Edge Radius For A Diamond Tool Using A New Kind Of SEM Having Two Detectors," *Annals of the CIRP,* vol. 39, no. 1, pp. 85-88, 1990.

[47] "AFM/SPM Principles," Agilent Technologies, 10 September 2012. [Online]. Available: http://www.afmuniversity.org/index.php/2011-07-25-05-54-22/afmspm-principles.

[Accessed 22 May 2014].

[48] W. Gao, T. Motoki and S. Kiyono, "Nanometer Edge Profile Measurement Of Diamond Cutting Tools By Atomic Force Microscope With Optical Alignment Sensor," *Precision Engineering,* vol. 30, pp. 396-405, 2006.

[49] T. Asai, S. H. Jang, Y. Arai and W. Gao, "Edge Profile Measurement of Micro-Cutting Tools On A Diamond Turning Machine," in *Proc. of SPIE Vol. 7544*, 2010.

[50] E. Brinksmeier and R. Glabe, "Elliptical Vibration Cutting of Steel with Diamond Tools," in *Proc. of the 14th Annual ASPE Meeting*, Monterey, CA, USA, 1999.

[51] E. Weeks, "Confocal microscopy of colloids," [Online]. Available: http://www.physics.emory.edu/faculty/weeks//confocal/. [Accessed 25 August 2014].

[52] N. S. Claxton, T. J. Fellers and M. W. Davidson, "Laser Scanning Microscopy," Department of Optical Microscopy and Digital Imaging, National High Magnetic Field Laboratory, Florida State University, [Online]. Available: http://www.olympusconfocal.com/theory/LSCMIntro.pdf. [Accessed 22 August 2014].

[53] T. J. Fellers and M. W. Davidson, "Introduction to Confocal Microscopy," Olympus Corporation, 2009. [Online]. Available: http://www.olympusfluoview.com/theory/confocalintro.html. [Accessed 26 August 2014].

[54] W. J. Callister, Materials Science And Engineering, An Introduction, Fourth Edition, John Wilen & Sons, Inc, 1997.

[55] Kistler Group, *Kistler 9256B1.*

[56] Kistler Instrument AG, *Kistler 87330A Miniature K-Shear Accelerometers,* Amhurst, NY: Kistler Instrument Corporation, 2008.

[57] Kistler Instrument AG, *Miniature PiezoBeam Accelerometer,* Winterthur: Kistler Instrument Corporation, 2011.

[58] C. J. Rick L., *Specifications Impulse Hammer Model No. 086B01,* PCB Piezotronics, 1992.

[59] National Instruments, "NI 9215 Module Packages," [Online]. Available: http://sine.ni.com/nips/cds/view/p/lang/en/nid/208793. [Accessed 2 May 2014].

[60] National Instruments, "Operating Instructions and Specifications NI 9234," August 2008. [Online]. Available: http://www.ni.com/pdf/manuals/374238c.pdf. [Accessed 2 May 2014].

[61] National Instruments, "Low-Cost E Series Multifunction DAQ," National Instruments, 2008. [Online]. Available: http://www.ni.com/pdf/products/us/4daqsc202-204_ETC_212-213.pdf. [Accessed 3 August 2014].

[62] MAL Inc., *User Manual for CutPro 9.0,* Vancouver, Canada, 2012.

[63] Zygo Corporation, *Owner's Manual, Zygo NewView 5000.*

[64] J. Chae, S. Park and T. Freiheit, "Investigation of Micro-Cutting Operations," *International Journal of Machine Tools and Manufacture,* vol. 46, pp. 313-332, 2006.

[65] A. P. Markopoulos, "Cutting Mechanics and Modeling," in *Finite Element Method in Machining Process*, SpringerBriefs in Applied Sciences and Technology, 2013, pp. 11-27.

[66] M. C. Shaw, Metal Cutting Principles, Second Edition, USA: Oxford University Press, 2005.

[67] H. A. Kishawy and M. A. Elbestawi, "Effects of Process Paramaters on Material Side Flow During Hard Turning," *International Journal of Machine Tools & Manufacture,* vol. 39, pp.

1017-1030, 1999.

[68] K. Liu and S. N. Melkote, "Effect Of Plastic Side Flow On Surface Roughness In Micro-Turning Process," *International Journal Of Machine Tools and Manufacture,* vol. 46, no. 14, pp. 1778-1785, 2006.

[69] X. Liu, R. E. Devor and S. G. Kapoor, "An Analytical Model for the Prediction of Minimum Chip Thickness in Micromachining," *Journal of Manufacturing Science and Engineering,* vol. 128, no. 2, pp. 474-481, 2005.

[70] H. H. Kim, S. H. Cho and C. Kang, "Evaluation of Microstructure and Mechanical Properties by Using Nano/Micro-Indentation and Nanoscratch During Aging treatment of Reho-Forged Al 6061 Alloy," *Materials Science and Engineering,* vol. 486, no. (1-2), pp. 272-281, 2008.

[71] I. Bucher, "Circle Fit," MATLAB Central, 26 July 2004. [Online]. Available: http://www.mathworks.com/matlabcentral/fileexchange/5557-circle-fit. [Accessed 17 August 2014].

[72] E. W. Weisstein, "Archimedes' Spiral," [Online]. Available: http://mathworld.wolfram.com/ArchimedesSpiral.html. [Accessed 17 April 2014].

[73] National Aeronautics and Space Administration, Science Mission Directorate, "Visible Light," 2012. [Online]. Available: http://missionscience.nasa.gov/ems/09_visiblelight.html. [Accessed 26 August 2014].

[74] W. J. Palm, Mechanical Vibration, Wiley, 2006.

[75] S. Y. Yoon, Z. Lin and P. E. Allaire, "Introduction To Rotordynamics," in *Control of Surge in Centrifugal Compressors by Active Magnetic Bearings,* Springer, 2013, pp. 17-55.

[76] ANSYS Inc., "Rotordynamic Analysis Guide," November 2009. [Online]. Available: http://orange.engr.ucdavis.edu/Documentation12.1/121/ans_rot.pdf. [Accessed 18 July 2014].

[77] M. E. van Osch and B. M. van Esch, "Rotor Dynamics of a Centrifugal Pump," Technical University Eindhoven, Eindhoven, Netherlands, 2006.

[78] R. G. Budynas and K. J. Nisbett, Shigley's Mechanical Engineering Design, New York: McGraw-Hill, 2008.

[79] E. Swanson, C. D. Powell and S. Weissman, "A Practical Review of Rotating Machinery Critical Speeds and Modes," *Sound and Vibration,* pp. 10-17, 2005.

[80] R. Nave, "Vector Properties of Rotational Quantities," Department of Physics and Astronomy, Georgia State University, [Online]. Available: http://hyperphysics.phy-astr.gsu.edu/hbase/rotv2.html. [Accessed 31 July 2014].

[81] C.-W. Lee, "Campbell Diagram Waterfall Plot," Center for Noise and Vibration Control, Department of Mechanical Engineering, KAIST, Daejeon, South Korea, 2010.

[82] J. S. Jacob, J. J. Yu, D. E. Bently and P. Goldman, "Air-Hammer Instability of Externally Pressurized Compressible-Fluid Bearings," *Proc. ISCORMA-1,* pp. 20-24, 2001.

[83] M. Arghir, "Theoretical and Experimental Analysis of Hybrid Aerostatic Bearings," Université de Poitiers,, Poitiers, France, 2013.

[84] J. P. F. A.-B. a. D. R. Tobias Waumans, "Aerodynamic journal bearing with a flexible, damped support operating at 7.2 million DN," *J. Micromech. Microeng,* vol. 21, pp. 1-12, 2011.

[85] K. J. Stout and S. M. Barrans, "The Design of Aerostatic Bearings For Application to Nanometre Resolution Manufacturing Machine Systems," *Tribology International,* vol. 33, pp. 803-809, 2000.

[86] F. Y. W. Ilmar F. Santos, "Lateral Dynamics and Stability Analysis of a Gas Compressor Supported by Hybrid and Active Lubricated Multirecess Journal Bearing," in *J. of the Braz. Soc. of Mech. Sci. & Eng.*, Ouro Preto. MG. Brazil, 2006.

[87] Y. K. Y. K. T. Aoyama, "Numerical and Experimental Analysis for the Small Vibration of Aerostatic Guideways," *Annals of the CIRP,* vol. 55, pp. 1-4, 2006.

[88] J. Kozanek, J. Simek, P. Steinbauer and A. Bilkosky, "Identification of Stiffness and Damping Coefficients of Aerostatic Journal Bearing," *Engineering MECHANICS,* vol. 16, no. 3, pp. 209-220, 2009.

[89] A. D. Dimarogonas, S. A. Paipetis and T. G. Chondros, "The Problem of Stablity," in *Analytic Methods in Rotor Dynamics, Second Edition*, Dordrecht Heidelberg New York London, Springer , 2013, pp. 28-31.

[90] A. Davis and F. Kuhnlenz, "Optical Design using Fresnel Lenses, Basic Principles and some Practical Examples," Optik & Photonik, WeinHeim, 2009.

[91] R. Nave, "Lens-Maker's Formula," HyperPhysics, [Online]. Available: http://hyperphysics.phy-astr.gsu.edu/hbase/geoopt/lenmak.html. [Accessed 30 August 2014].

[92] C. F. Cheung and W. B. Lee, "Characterisation of Nanosurface Generation in Single Point Diamond Turning," *International Journal of Machine Tools and Manufacture,* vol. 41, no. 6, pp. 851-875, 2001.

[93] F. Wardle, "Recent Developments In Air Bearing Spindles Are Redefining The Boundaries Of High Precision Machining," 2014. [Online]. Available: http://www.loadpointbearings.com/knowledge-base/news/recent-developments-in-air-bearing-spindles-are-redefining-the-boundaries-of-high-precision-machining/. [Accessed April 2014].

[94] C. D. P. S. W. Erik Swanson, "A Practical Review of Rotating Machinery Critical Speeds and Modes," *Sound and Vibration,* pp. 10-17, 2005.

[95] H. Khanfir, M. Bonis and P. Revel, "Improving Flatness in Ultraprecision Machining by Attenuating Spindle Motion Errors," *International Journal of Machine Tools and Manufacture,* vol. 45, no. 7-8, pp. 818-848, 2005.

[96] "The design of aerostatic bearings for application to nanometre resolution manufacturing machine systems," *Tribology International,* vol. 33, p. 803–809, 2000.

Appendix 1: Codes

A1. MATLAB Circle Fitting Code

A circle-fitting program was used to fit points from the Olympus OLS4000 LEXT in order to determine the cutting edge radius of the SCD tools. It was used in this study under the BSD license, thanks to Izhak Bucher.

http://www.mathworks.com/matlabcentral/fileexchange/5557-circle-fit

```
function   [xc,yc,R,a] = circfit(x,y)
%
%   [xc yx R] = circfit(x,y)
%
%   fits a circle  in x,y plane in a more accurate
%   (less prone to ill condition )
%  procedure than circfit2 but using more memory
%  x,y are column vector where (x(i),y(i)) is a measured point
%
%  result is center point (yc,xc) and radius R
%  an optional output is the vector of coeficient a
% describing the circle's equation
%
%   x^2+y^2+a(1)*x+a(2)*y+a(3)=0
%
%  By:  Izhak bucher 25/oct /1991,
    x=x(:); y=y(:);
   a=[x y ones(size(x))]\[-(x.^2+y.^2)];
   xc = -.5*a(1);
   yc = -.5*a(2);
   R  =  sqrt((a(1)^2+a(2)^2)/4-a(3));

%Input XData, YData as 2 vectors for X and Y
[xfit, yfit, Rfit] = circfit(XData,YData);

plot(XData,YData,'b.')
hold on
rectangle('position',[xfit-Rfit,yfit-Rfit,Rfit*2,Rfit*2],...
    'curvature',[1,1],'linestyle','-','edgecolor','r');
title(sprintf('Best fit: R = %0.1f; Ctr = (%0.1f,%0.1f)',...
    Rfit,xfit,yfit));
plot(xfit,yfit,'g.')
xlim([xfit-Rfit-1,xfit+Rfit+1])
ylim([yfit-Rfit-1,yfit+Rfit+1])
axis equal

% Copyright (c) 1981, Izhak Bucher
% All rights reserved.
%
% Redistribution and use in source and binary forms, with or without
% modification, are permitted provided that the following conditions are
```

```
% met:
%
%     * Redistributions of source code must retain the above copyright
%       notice, this list of conditions and the following disclaimer.
%     * Redistributions in binary form must reproduce the above copyright
%       notice, this list of conditions and the following disclaimer in
%       the documentation and/or other materials provided with the distribution
%
% THIS SOFTWARE IS PROVIDED BY THE COPYRIGHT HOLDERS AND CONTRIBUTORS "AS IS"
% AND ANY EXPRESS OR IMPLIED WARRANTIES, INCLUDING, BUT NOT LIMITED TO, THE
% IMPLIED WARRANTIES OF MERCHANTABILITY AND FITNESS FOR A PARTICULAR PURPOSE
% ARE DISCLAIMED. IN NO EVENT SHALL THE COPYRIGHT OWNER OR CONTRIBUTORS BE
% LIABLE FOR ANY DIRECT, INDIRECT, INCIDENTAL, SPECIAL, EXEMPLARY, OR
% CONSEQUENTIAL DAMAGES (INCLUDING, BUT NOT LIMITED TO, PROCUREMENT OF
% SUBSTITUTE GOODS OR SERVICES; LOSS OF USE, DATA, OR PROFITS; OR BUSINESS
% INTERRUPTION) HOWEVER CAUSED AND ON ANY THEORY OF LIABILITY, WHETHER IN
% CONTRACT, STRICT LIABILITY, OR TORT (INCLUDING NEGLIGENCE OR OTHERWISE)
% ARISING IN ANY WAY OUT OF THE USE OF THIS SOFTWARE, EVEN IF ADVISED OF THE
% POSSIBILITY OF SUCH DAMAGE.
```

A2. LabVIEW Code

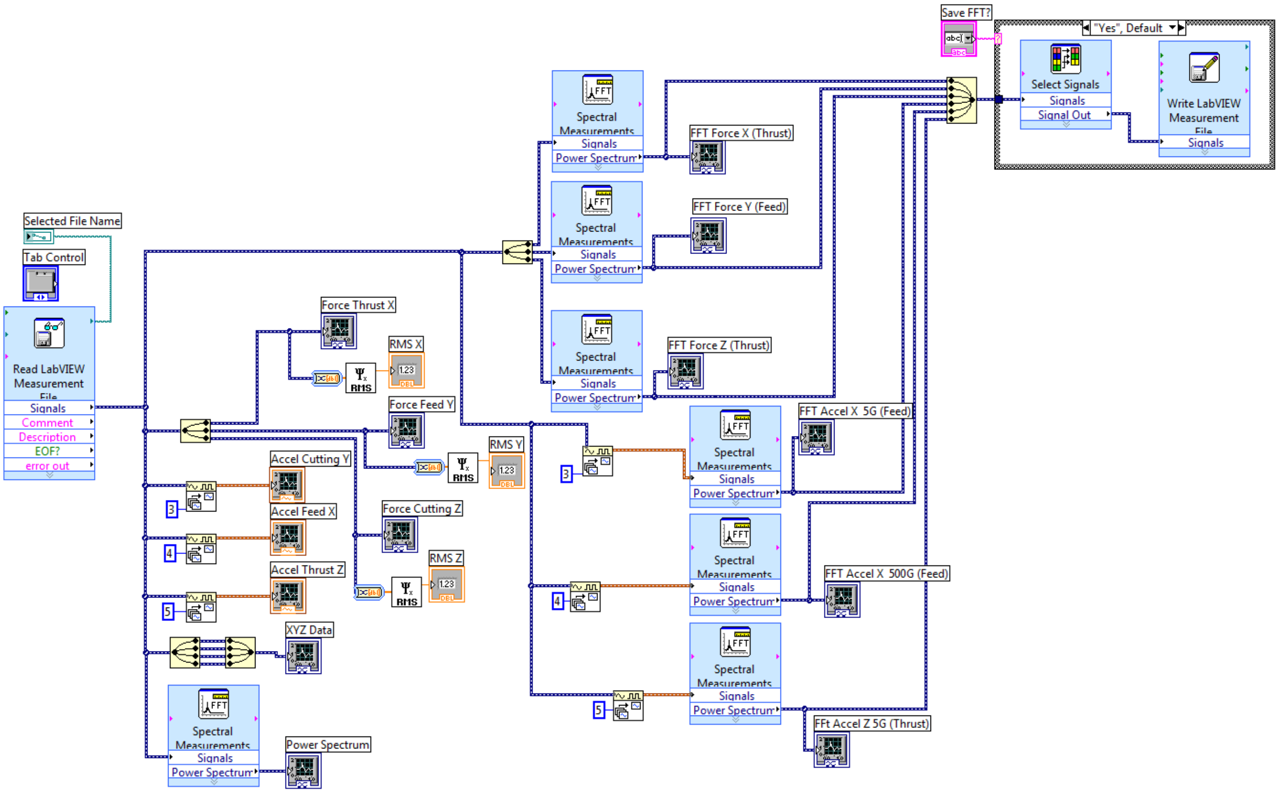

Figure A1.0.1 LabVIEW Code For Reading LVM File With 3 Force Channels, 3 Accelerometer Channels

A3. Precitech CNC Program Code

```
G90             %Machine Absolute mode
G71             %Set Metric System
G01 B-1.9500    %Move B-Axis, align spindle axis with machine axis
G00 Y-67.700    %Set Tool Height
G00 X-120.      %Safe X distance from part
G00 Z10.        %Safe Z distance from part
M07.1           %Coolant, Line 1 ON
G97 M3 S1000.   %Spindle ON, CW, 1000RPM
G04 F15.        %15 Sec delay for spindle speed to stabilize
G01 Z-0.002 F20.%Move Tool into workpiece, 2 microns DoC
G01 X0. F5      %Feed tool across part, facing flat surface, 5mm/min
G00 Z10.        %Move part away from surface
M05             %Spindle OFF
M09             %Coolant OFF
m30             %End of program
```

Appendix 2: Detailed Procedure and Case Study: Fresnel Lens

The strength for single point diamond turning (SPDT) is that SPDT can produce parts with nanometer-level accuracy and high quality surface finish. The advanced CNC ultraprecision machine tools also have the capability to produce parts with a complex geometry. The Fresnel lens is a perfect way to demonstrate the capabilities of diamond turning.

A2.1 Fresnel Lens Design

A Fresnel lens is used as a lightweight, thinner alternative to a conventional optical element. Traditionally, a Fresnel lens is manufactured by pressing glass into a mold, requiring a draft angle and rounded corners to allow the part to be released from the mold. The mold must be roughed using a machine tool and hand polished, a process that cannot guarantee the accuracy of the final part. This is especially important in the optics industry, where deviations of more than 0.5μm are considered to be large imperfections. The advantage of directly manufacturing a Fresnel lens using SPDT is that no draft angle is required, increasing lens efficiency and allowing for sharp corners and edges on the lens. Each concentric facet of the Fresnel lens can now be created with a curved radius instead of a simple slope facet, further increasing lens efficiency.

Following a Fresnel lens design guide by Davis and Kuhnlenz [90], a Fresnel lens was designed and manufactured at the MMRI Micro Manufacturing Laboratory (MML) for demonstration purposes. The material used is PMMA, or acrylic plastic. The workpiece is a flat disk, 100mm in diameter and 4mm thick.

Table A2.0.1 Specifications for MML Demonstration Fresnel Lens

Property	**Variable Name**	**Value**
Lens to Object Distance (mm)	s1	125
Magnification	M	2
Distance from Object to Observer (mm)	L	450
Refractive Index, Acrylic	n	1.49
Visible Object Size (mm)	h1	20

The focal length can be determined using the Newtonian thin lens equation.

$$f = \frac{s_1}{(1 - \frac{1}{m})}$$

The lens diameter can then be calculated using this formula provided by the Fresnel lens design guide.

$$\phi = \frac{mh}{\left(1 + \frac{m\, s_1}{l - s_1}\right)}$$

We can then use the thin lens approximation to find the required radius of curvature of each lens facet using the lens-maker's formula for a thin lens [91]. This formula has been modified to assume that the lens is single-sided, one side is plano.

$$\frac{1}{f} \approx (n - 1)\left[\frac{1}{R_1}\right]$$

Using a pitch size of 2mm for each lens facet, the lens can then be modeled in SolidWorks 2013.

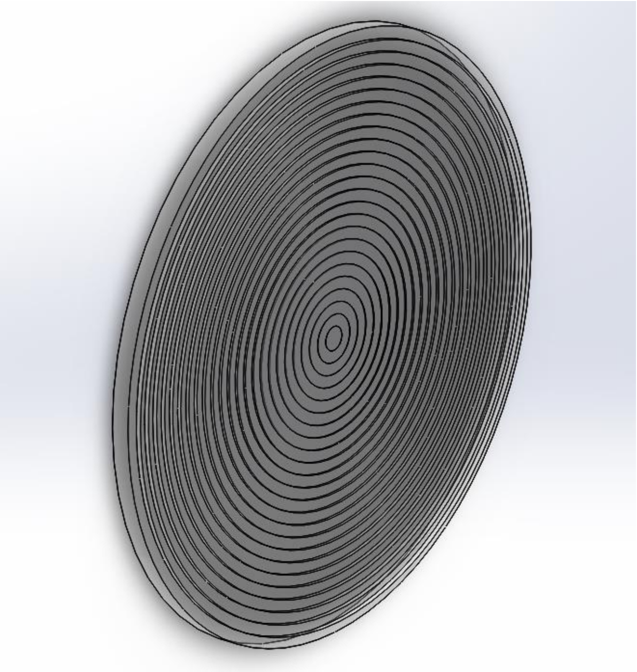

Figure A2.0.2 Fresnel Lens, Modeled in SolidWorks 2013, Student Edition

A2.2 Fresnel Lens Manufacturing

To create the lens, computer-aided-manufacturing (CAM) software was used to generate the G-code for use in the machine tool. A tool with a nose radius of 0.318mm was used to cut the workpiece. The roughing pass used a depth of cut of 10µm, spindle speed of 1000RPM and a feed rate of 10µm/rev. Due to the large file size of the generated G-code, the rotary buffer was used in the machine tool.

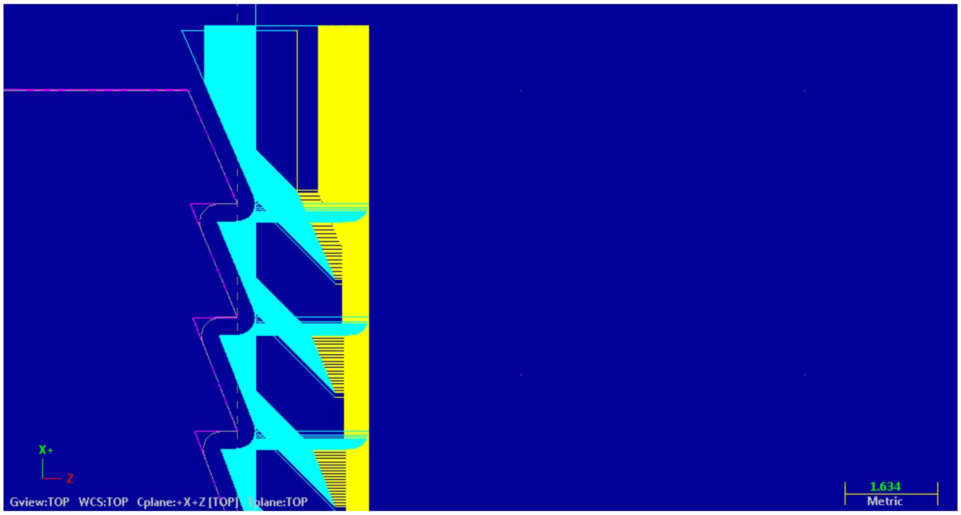

Table A2.30.2 MasterCAM Screenshot of Toolpath

The blank workpiece was setup on the Precitech 700G machine tool and the generated program was transferred to the machine’s controller. The lens was successfully manufactured, requiring 6 hours of machine time.

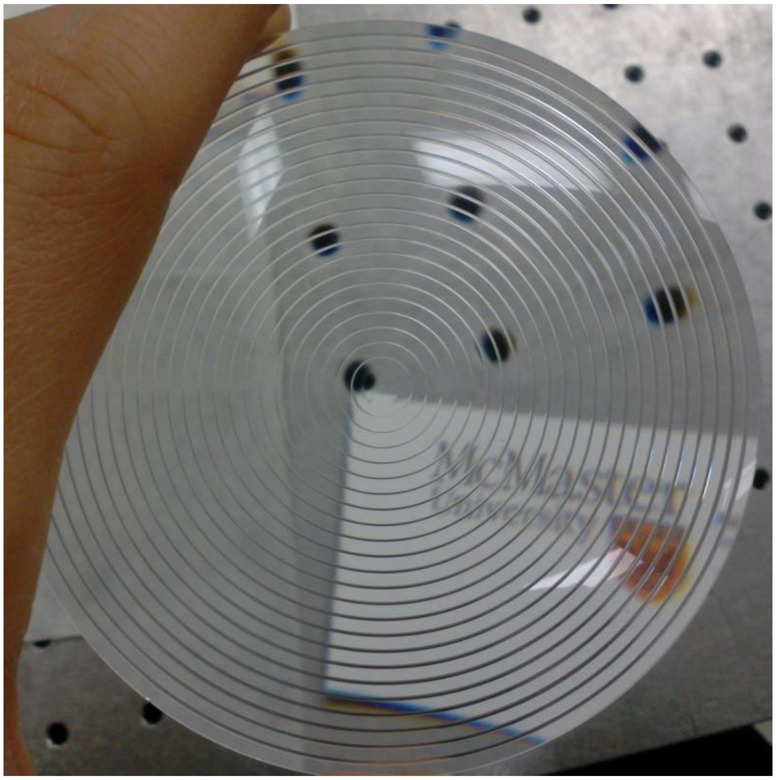

Figure A2.4.0.3 Demonstration Fresnel Lens, McMaster University MML

The directly manufactured lens is based on a simple, spherical magnifier, split into 2mm Fresnel lens elements. Further work can reduce the spherical aberration by implementing a Fresnel lens with aspheric geometry. This is an example of the type of ultraprecision lenses that are possible with SPDT that are otherwise extremely difficult with traditional methods of manufacturing lenses.